Low-Concentrating, Stationary Solar Thermal Collectors for Process Heat Generation

Ph.D. Thesis

Stefan Hess

2014

De Montfort University Leicester

Institute of Energy and Sustainable Development IESD

Fraunhofer Institute for Solar Energy Systems ISE

Division Solar Thermal and Optics

Low-Concentrating, Stationary Solar Thermal Collectors for Process Heat Generation

Stefan Hess

A thesis submitted in partial fulfillment of the requirements of De Montfort University for the degree Doctor of Philosophy (Ph.D.)

Freiburg, December 2014

Stefan Hess

Low-Concentrating, Stationary Solar Thermal Collectors for Process Heat Generation

Abstract

The annual gain of stationary solar thermal collectors can be increased by non-focusing reflectors. Such concentrators make use of diffuse irradiance. A collector's incidence angle modifier for diffuse (diffuse-IAM) accounts for this utilization. The diffuse irradiance varies over the collector hemisphere, which dynamically influences the diffuse-IAM. This is not considered by state-of-the-art collector models. They simply calculate with one constant IAM value for isotropic diffuse irradiance from sky and ground.

This work is based on the development of a stationary, double-covered process heat flat-plate collector with a one-sided, segmented booster reflector (RefleC). This reflector approximates one branch of a compound parabolic concentrator (CPC). Optical measurement results of the collector components as well as raytracing results of different variants are given. The thermal and optical characterization of test samples up to 190 °C in an outdoor laboratory as well as the validation of the raytracing are discussed.

A collector simulation model with varying diffuse-IAM is described. Therein, ground reflected and sky diffuse irradiance are treated separately. Sky diffuse is weighted with an anisotropic IAM, which is re-calculated in every time step. This is realized by generating an anisotropic sky radiance distribution with the model of Brunger and Hooper, and by weighting the irradiance from distinct sky elements with their raytraced beam-IAM values. According to the simulations, the RefleC booster increases the annual output of the double-covered flat-plate in Würzburg, Germany, by 87 % at a constant inlet temperature of 120 °C and by 20 % at 40 °C. Variations of the sky diffuse-IAM of up to 25 % during one day are found. A constant, isotropic diffuse-IAM would have undervalued the gains from the booster by 40 % at 40 °C and by 20 % at 120 °C. The results indicate that the gain of all non-focusing solar collectors is undervalued when constant, isotropic diffuse-IAMs calculated from raytracing or steady-state test data are used.

Process heat generation with RefleC is demonstrated in a monitored pilot plant at working temperatures of up to 130 °C. The measured annual system utilization ratio is 35 %. Comparing the gains at all inlet temperatures above 80 °C, the booster increases the annual output of the double-covered flat-plates by 78 %. Taking all inlet temperatures, the total annual gains of RefleC are 39 % above that of the flat-plates without reflectors.

A qualitative comparison of the new simulation model results to the laboratory results and monitoring data shows good agreement. It is shown that the accuracy of existing collector models can be increased with low effort by calculating separate isotropic IAMs for diffuse sky and ground reflected irradiance. The highest relevance of this work is seen for stationary collectors with very distinctive radiation acceptance.

Declaration

I declare that the content of this submission is my own work. The contents of the work have not been submitted for any other academic or professional award. This thesis is submitted according to the conditions laid down in the regulations.

Furthermore, I declare that the work was carried out as part of the course for which I was registered at De Montfort University, United Kingdom from October 2008 until September 2014.

I draw attention to any relevant considerations of rights of third parties.

Acknowledgements

I thank my supervisor Prof. Victor Ian Hanby for his wise and motivating guidance of this work. His knowledge and great sense of humor highly contributed to make my external doctorate at DMU with the annual stays in Leicester a positive and enriching experience. Prof. Ursula Eicker and Dr. Michael Hermann supported me during the initial phase of this dissertation project.

The research reported here is based upon the collector development project RefleC, which I carried out at Fraunhofer ISE together with students and the industry partner Wagner & Co. Solartechnik GmbH. I am very thankful to Prof. Matthias Rommel for his trust and encouragement to start working on a doctorate.

The committed support of students and colleagues to the RefleC project highly contributed to the quality of this thesis. Paolo Di Lauro did many of the raytracing-simulations, using the OptiCad collector model I had set up before. He helped to measure the collector test samples, set up the sun position calculation tool used in this work and was always open for discussions on the IAM. Stefanie Rose carried out most optical measurements of the material samples. Christoph Raucher did a great job implementing the first version of the anisotropic collector simulation model in Fortran. Axel Oliva performed system simulations for the dimensioning of the pilot plant and Michael Klemke carefully calibrated and installed the monitoring equipment. Christoph Thoma instructed me to work with the medium temperature collector test stand and was always helpful in case of questions. I also would like to thank all the other great people at ISE and Wagner who contributed to this work.

I had the honor to briefly discuss some of my ideas with Prof. Roland Winston, Dr. Bengt Perers, Prof. Björn Karlsson, Prof. Manuel Collares-Pereira and Dr. Alfred Brunger. I am very thankful for their feedback and for helpful literature.

RefleC was funded by the German Federal Ministry for the Environment, Nature Conservation and Nuclear Safety (BMU). The work in hand was funded by a Ph.D. scholarship of the Reiner-Lemoine-Stiftung. This important support gave me the freedom for independent research and to continue monitoring the RefleC pilot plant after the financed RefleC project had ended.

This work would not have been finalized without the love, support and understanding of my friends and family. In hard times, you listened and kept me going. In good times, you were happy with me. I am very grateful for having you in my life.

Content

Nomenclature

Latin Symbols

Symbol	Unit	Meaning
a	$-$	Aperture half-width of concentrator entrance
a'	$-$	Aperture half-width of concentrator exit
a_0	$-$	Coefficient of the Brunger distribution
a_1	$-$	Coefficient of the Brunger distribution
a_2	$-$	Coefficient of the Brunger distribution
a_3	$-$	Coefficient of the Brunger distribution
A_1	m^2	Area normal to direction of irradiance
A_2	m^2	Area turned away by θ from normal of irradiance
A_{ap}	m^2	Aperture area (index R = reflector, fp = flat plate, u = upper reflector, l = lower reflector)
A_{gr}	m^2	Gross area
A_r	m^2	Receiver area
b_0	$-$	Parameter of Souka/Safwat IAM function
c_1	$W/(m^2K)$	Heat loss coefficient of the first order
c_2	$W/(m^2K^2)$	Heat loss coefficient of the second order
c_{eff}	$J/(m^2K)$	Effective heat capacity of the collector (material and fluid)
$c_{p,fl}$	$J/(kg\,K)$	Specific heat capacity of the collector fluid
$\bar{c}_{p,fl}$	$J/(kg\,K)$	Mean specific heat capacity of the collector fluid
C_{geo}	$-$	Geometric concentration ratio
C_{rad}	$-$	Concentration ratio for radiation
f	m	Focal length
f_a	$1/a$	Annuity factor
$f_{acc,iso}$	$-$	Concentrator acceptance factor for isotropic irradiance
f_b	$-$	Fraction of beam irradiance
f_d	$-$	Fraction of diffuse irradiance $(1 - f_b)$
F'	$-$	Collector efficiency factor
G	W/m^2	Global (hemispherical) irradiance on horizontal (GHI)
G_0	W/m^2	Extraterrestrial irradiance on horizontal
G_b	W/m^2	Beam irradiance (horizontal)

Nomenclature

Symbol	Unit	Meaning
G_{bn}	W/m²	Beam irradiance perpendicular to sun direction (DNI)
G_{bt}	W/m²	Beam irradiance (tilted plane)
G_d	W/m²	Diffuse irradiance on horizontal (DHI)
G_{dt}	W/m²	Diffuse irradiance on tilted plane ($G_{st} + G_{rt}$)
G_{rt}	W/m²	Diffuse ground irradiance (tilted plane)
G_{sc}	W/m²	Solar Constant (1367 ± 23 W/m²)
G_{st}	W/m²	Diffuse sky irradiance (tilted plane)
$G_{st,Br}$	W/m²	Diffuse sky irradiance from Brunger distribution
G_t	W/m²	Global (hemispherical) irradiance (tilted plane)
i	–	Day of the year
$I(\theta_s, a_3)$	–	Function within Brunger model
I_{ap}	W	Integral intensity at concentrator aperture area
I_r	W	Integral intensity at concentrator receiver area
k	–	Fraction of diffuse irradiance on horizontal
k_t	–	Atmospheric clearness Index
K	–	Extinction coefficient of solid, transparent material
K_b	–	IAM for beam irradiance G_{bt}
K_d	–	IAM for isotropic diffuse irradiance from collector hemisphere ($G_{st} + G_{rt}$)
K_h	–	IAM for global hemispherical irrad. ($G_{bt} + G_{st} + G_{rt}$)
K_{inv}	EUR/(m²)	Investment costs per unit area
K_{main}	EUR/(m²a)	Maintenance costs per year and unit area
K_{op}	EUR/(kWh)	Operational costs per kWh useful solar gain
K_r	–	IAM for diffuse irradiance from the ground G_{rt}
K_s	–	IAM for diffuse irradiance from the sky G_{st}
K_{sol}	EUR/(kWh)	Solar heat generation costs
$L(\theta_h, \phi_h)$	W/(m²sr)	Sky radiance in direction (θ, ϕ)
$\dot{m}$	kg/(m²h)	Specific mass flow rate per m^2 of aperture area
m_{coll}	–	Number of collectors (parallel)
$\dot{M}$	kg/h	Absolute mass flow rate
n	–	Refractive index
n	–	Number of measured values for error calculation
$n_{\phi,h}$	–	Number of steps in direction ϕ_h
$n_{\theta,h}$	–	Number of steps in direction θ_h
n_{air}	–	Refractive index air (optically thinner medium)

Symbol	Unit	Meaning
n_{cov}	–	Refractive index cover (optically denser medium)
n_{coll}	–	Number of collectors (serial)
$n_{coll,S}$	–	Projection of collector normal vector onto south axis
$n_{coll,W}$	–	Projection of collector normal vector onto west axis
$n_{coll,Z}$	–	Projection of collector normal vector onto zenith axis
$\vec{n}_{0,coll}$	–	Normal unit vector of the collector plane
n_{long}	–	Number of longitudinal IAM values in external file
n_{trans}	–	Number of transversal IAM values in external file
p	–	Capital interest rate
$\dot{q}_{gain}$	W/m^2	Collector gain per aperture area (stationary)
$\dot{q}_{loss}$	W/m^2	Thermal losses heat flow
$\dot{q}_{rad}$	W/m^2	Radiative solar gains heat flow
Q_{sol}	kWh/(m^{2}a)	Usable solar heat per year and unit area
$\dot{q}_{use}$	W/m^2	Thermal collector output (dynamic, with capacity)
$\dot{Q}_{use}$	W	Thermal collector (field) output (with capacity)
r	–	Parameter of Ambrosetti IAM function
r_S	m	Sun radius $(6.95 \cdot 10^8)$
r_{SE}	m	Median orbital radius of earth around sun $(1.50 \cdot 10^{11})$
s_S	–	Projection of solar unit vector onto south axis
s_W	–	Projection of solar unit vector onto west axis
s_Z	–	Projection of solar unit vector onto zenith axis
$\vec{s}_0$	–	Solar unit vector
$\vec{s}_{0,l}$	–	Projection of solar unit vector into longitudinal plane
$\vec{s}_{0,t}$	–	Projection of solar unit vector into transversal plane
T	a	Technical service life of booster reflectors in years
T_a	K	Ambient temperature
T_f	K	Mean collector (field) fluid temperature
T_{in}	K	Fluid inlet temperature
$T_{on,RK}$	°C	Activation temperature of stagnation cooler
T_{out}	K	Fluid outlet temperature
T_p	K	Mean absorber plate temperature
T_{stag}	K	Stagnation temperature
T_{tre}	°C	Temperature threshold to switch storage charging
Δt	s	Width of timestep in TRNSYS

Nomenclature

Symbol	Unit	Meaning
$\Delta T/G$	$(m^2 K)/W$	Reduced temperature difference
U_{loss}	$W/(m^2 K)$	Heat loss coefficient of the collector
$\dot{v}$	l/h	Volume flow
y_{ci}	$[y_{ci}]$	Calculated value for error calculation
y_{mi}	$[y_{mi}]$	Measured value for error calculation

Greek Symbols

Symbol	Unit	Meaning
α	–	Absorptance
α_D	rad	Divergence of sunlight (0.54° or 0.0094 rad)
β	rad	Collector tilt or slope from horizontal
γ	rad	Collector azimuth angle from south (west positive)
δ	rad	Concentrator shading angle for beam irradiance
ε	–	Emittance
η	–	Collector efficiency
η_0	–	Conversion factor at perpendicular beam irradiance
$\eta_{0,b}$	–	Conversion factor for pure beam irradiance
$\eta_{0,h}$	–	Conversion factor for hemispherical irradiance
θ	rad	Incidence angle
$\theta(\theta_s, \phi_s)$	rad	Incidence angle of sun on aperture
$\theta(\theta_h, \phi_h)$	rad	Incidence angle of sky element on aperture
θ_a	rad	Acceptance half-angle of concentrator
$\theta_{a,V}$	rad	Acceptance half-angle of V-trough
$\Delta\theta_{diff}$	rad	Angular step width of diffuse integration in Type 154
θ_h	rad	Zenith angle of sky element
$\Delta\theta_h$	rad	Angular width of sky element at θ_h
θ_h^*	rad	Zenith angle of ground element
$\Delta\theta_h^*$	rad	Angular width of ground elem. at θ_h^*
θ_l	rad	Projection of θ into longitudinal plane
$\theta_{p,NS}$	rad	South projection angle
θ_r	rad	Angle of reflection
θ_s	rad	Zenith angle of the sun
θ_t	rad	Projection of θ into transversal plane
θ_{trunc}	rad	Truncation angle of a CPC

Symbol	Unit	Meaning
λ	m	Wavelength
ρ	–	Reflectance (total, hemispherical)
ρ_{diff}	–	Diffuse reflectance (share reflected diffuse)
ρ_{fl}	kg/m^3	Density of collector fluid
ρ_{grd}	–	Reflectance of the ground
ρ_{spec}	–	Specular reflectance (share reflected specular)
$(\rho\tau\alpha)_e$	–	Effective reflectance-transmittance-absorptance product (effective optical loss factor)
σ	rad	Standard deviation (of scattered rays after reflection)
σ_{ori}	rad	Standard deviation from macroscopic (shape) errors
σ_{refl}	rad	Standard deviation from microscopic surface errors
σ_{sun}	rad	Standard deviation from solar irradiation direction
τ	–	Transmittance
$(\tau\alpha)_e$	–	Effective transmittance-absorptance product
ϕ	rad	Sun azimuth angle from collector (west positive)
ϕ_s	rad	Sun azimuth angle from south direction (west positive)
ϕ_h	rad	Azimuth of sky element (west positive)
$\Delta\phi_h$	rad	Angular width of sky element at ϕ_h
ϕ_h^*	rad	Azimuth of ground element (west pos.)
$\Delta\phi_h^*$	rad	Angular width of ground element at ϕ_h^*
$\varphi_{s/2}$	rad	Opening half angle of the sun (0.27°)
ψ	rad	Opening half angle of a V-trough
Ψ	rad	Angular distance from sun to sky element
Ω	sr	Angular width of sky element

Abbreviations

a	annum (year)
a.m.	ante meridiem
AM	Air mass
AR	Anti-reflective, i.e. with reduced reflectivity
ASA	Advanced security appliance (hardware-firewall)
ASTM	American Society for Testing and Materials
approx.	approximately
App.	Appendix
BMWi	German Federal Ministry for Economic Affairs and Energy
BSW	German Solar Industry Association

CPC	Compound Parabolic Concentrator
CSR	Circumsolar ratio
d	day
DGS	German Solar Energy Society
DNI	Direct normal irradiance
EU	European Union
Eq.	Equation
ETC	Evacuated tube collector
ETFE	Ethylene tetrafluoroethylene
FEP	Fluorinated ethylene propylene
Fortran	Formula translation (programming language)
GHI	Global hemispherical irradiance on horizontal plane
h	hour
IAM	Incidence angle modifier
IEA	International Energy Agency
IR	Infrared wavelengths of solar spectrum
ISE	Fraunhofer Institute for Solar Energy Systems
LED	Light emitting diode
L/H	Ratio of booster reflector length to receiver flat-plate height
MBE	Mean bias error
min	minute
MID	Magneto-inductive flow meter
MTTS	Medium temperature collector test stand
NREL	National Renewable Energy Laboratory
p.m.	post meridiem
prim.	Data plotted to the primary (left) axis
PE	Polyethylene
PFA	Perfluoroalkoxy alkanes
PHC	Process heat collector
PTFE	Polytetrafluoroethylene
RMSE	Root mean square error
s	second
sec.	Data plotted to the secondary (right) axis
SHC	Solar Heating and Cooling (Program)
SPH	Solar thermal process heat(ing)
ST	Solar thermal
TMY	Typical meteorological year
TRNSYS	Transient system simulation software
US	United States of America
UTC	Coordinated Universal Time
UV	Ultraviolet wavelengths of solar spectrum
Vis	Visible wavelengths of solar spectrum

1 Introduction

The field of solar thermal heat generation is briefly introduced. The context of this work, its approach, structure and intended contribution to knowledge are described. An overview on solar thermal process heating is given and the state of the art in the development of low-concentrating, stationary solar thermal process heat collectors is discussed.

The transition towards a sustainable energy supply is a global challenge. Not only against the background of scarce fossil and nuclear resources, but also due to the rapidly progressing climate change it is imperative to develop and improve technologies for renewable energy utilization. Apart from gravity forces, the sun's photons are the only external energy source available to our planet, so direct use of solar energy is obvious. Solar thermal (ST) systems are often applied in combination with other heating technologies, which compensate for the fluctuating solar resource. They generate heat on-site and can significantly reduce the dependence on conventional energy carriers.

Solar Heat Worldwide: Weiss and Mauthner (2014) annually provide an overview on the worldwide ST market. According to them, by the end of 2012 a ST collector area of 384.7 million m^2 was in operation, corresponding to 269.3 GW_{th} total power (conversion factor 0.7 kW_{th}/m^2). Compared to 2011, the newly installed capacity grew by 9.4 % in 2012. China (44.7 GW_{th}) and Europe (3.7 GW_{th}) were the main markets; they together account for 92 % of all newly installed collector area. For 2013, Weiss and Mauthner estimate that ST systems of overall 471 million m^2 collector area produced a total energy of 281 TWh_{th}. So in 2013 ST systems produced about 80 % more energy than photovoltaic systems (about 160 TWh_{el}). ST electric power generation accounted for 5 TWh_{el}.

Only a very small share of the installed area (about 1 % or 4 million m^2) provided heat for district heating, thermally driven solar cooling or process heat.

Figure 1.1: The most widespread ST technology is thermo-siphon systems with evacuated tubes for domestic hot water preparation. Picture: SUNNY (2014)

1.1 This Work

1.1.1 RefleC Project

The company Wagner & Co. Solartechnik GmbH developed together with the Fraunhofer Institute for Solar Energy Systems ISE a stationary, double-covered ST flat-plate collector with external reflectors for process heat generation. From August 2007 to December 2010, this project was funded by the German Federal Ministry for the Environment, Nature Conservation and Nuclear Safety (funding reference FK 0329 280 C). Figure 1.2 shows the initial collector concept.
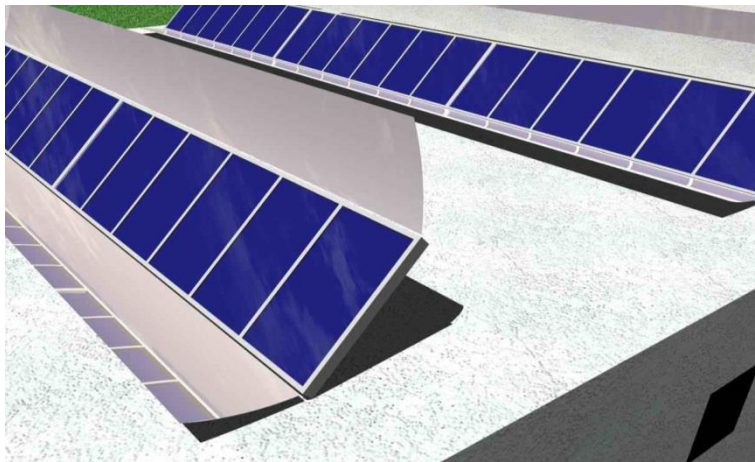

Figure 1.2: Computer graphic of the initial RefleC collector concept. Sloped collector rows with CPC-reflectors are installed on the flat roof of an industrial building.

The RefleC collector finally developed is shown in Figure 1.3. As desired, it has significantly higher annual energy gains than double covered flat-plates, especially at working temperatures above 80 °C. The design offers a very good utilization of roof area. It can be optimized for certain locations, temperature levels and heat demand profiles.

Figure 1.3: RefleC prototype at pilot plant laundry Laguna in Marburg an der Lahn

The work in hand addresses questions that arose from development and optimization of the RefleC collector. Research from within and after the funded project duration is reported and general conclusions for assessment and optimization of stationary solar thermal process heat collectors with reflectors are drawn.

1.1.2 Structure, Approach and Contribution to Knowledge

Structure: The scheme in Figure 1.4 illustrates the different fields of research which were interrelated to conduct the research presented in this thesis.
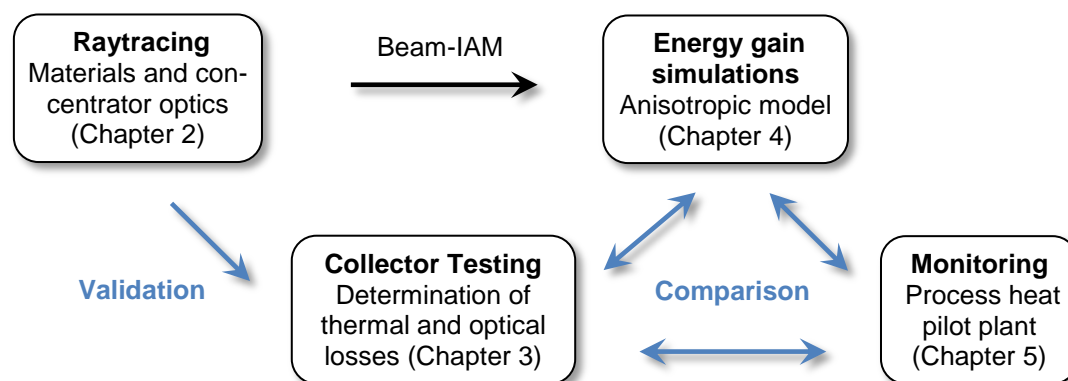

Figure 1.4: Approach and structure of the work with interaction between the different research fields and tools.

The work is structured in six chapters. Four of these chapters are complemented by further related information presented in an appendix. Each chapter starts with a short paragraph summarizing its content and role within the thesis.

Approach: This work is inspired by the question to which extent diffuse irradiance contributes to the instantaneous and annual output of low-concentrating, stationary solar thermal collectors. This is investigated by raytracing, collector tests, energy gain simulations and monitoring of a pilot plant. The results are compared to the state of the art, discussed, and recommendations are given on how collector tests and simulations could account for the contribution of diffuse irradiance more accurately.

The results of this work were found to be especially relevant for highly incidence-angle-selective collectors with higher working temperatures, as in process heat applications. Thus, as an introduction, solar thermal process heating as well as the mentioned collector types are shortly introduced. After this, as a basis for the research, measurement results of optical parameters of collector components are given. A raytracing model is described, and the correct representation of the material properties by raytracing is shown. Simplifications are mentioned and discussed. Outdoor collector test results are used to validate the raytracing simulations. This ensures that beam-IAM curves generated by raytracing can be applied in annual energy gain simulations. The outdoor tests of different collector samples are further used to determine their thermal efficiency curve,

to assess certain theoretically expected effects of the booster reflectors, and to optimize the RefleC collector. A collector simulation model for the calculation of annual and instantaneous collector gains in TRNSYS is developed. This model has three optical modes: Diffuse irradiance can be treated as isotropic, separately isotropic for sky and ground, or separately with an anisotropic sky. The model is applied to both the final RefleC collector and its double-covered receiver flat-plate without reflectors. The differences resulting from the three optical modes are analyzed. Finally, RefleC and its flat-plate receiver are monitored in a solar process heat pilot plant. The results from the collector tests, the TRNSYS simulations, and the pilot plant are compared in order to draw general conclusions with respect to the research questions stated above.

Contribution to knowledge: In practice, the research presented in this work contributed to the development of the new RefleC collector. This collector has significant advantages compared to the state of the art.

A significant theoretical contribution to solar thermal research is the assessment of the impact of anisotropic sky irradiance on instantaneous diffuse-IAM values and on simulated collector output. Two extremes, the RefleC collector with very selective radiation acceptance, and the double covered flat plate with very broad acceptance, have been tested and simulated. For both collectors an undervaluation of the annual gains by state-of-the-art isotropically calculated diffuse-IAMs was found. It is concluded that the results of this work are relevant for all non-focusing ST collector types.

1.2 Solar Thermal Process Heating

Though the focus of this work is on low-concentrating ST collectors, in this section a short introduction to solar thermal process heating (SPH) is given. Its potential, current state and future perspectives are discussed. Further readings are recommended as well.

As implied above, the vast majority of ST systems are currently used for domestic hot water preparation in the residential sector. According to Weiss and Mauthner (2014, p. 6), about 87 % of the worldwide collector area serves for this purpose. In comparison to these systems, SPH is usually more complex. There is a high discrepancy between the SPH potential and the number of systems installed for industry and service applications.

1.2.1 Process Heat Demand

To give an insight into the relevance of process heat in a highly industrialized country, the final energy demand of Germany is analyzed in more detail in Figure 1.5. Therein, the transport sector has no process heat demand at all. In private households, a share of 6 % of the energy demand is process heat (used e.g. for cooking or washing).
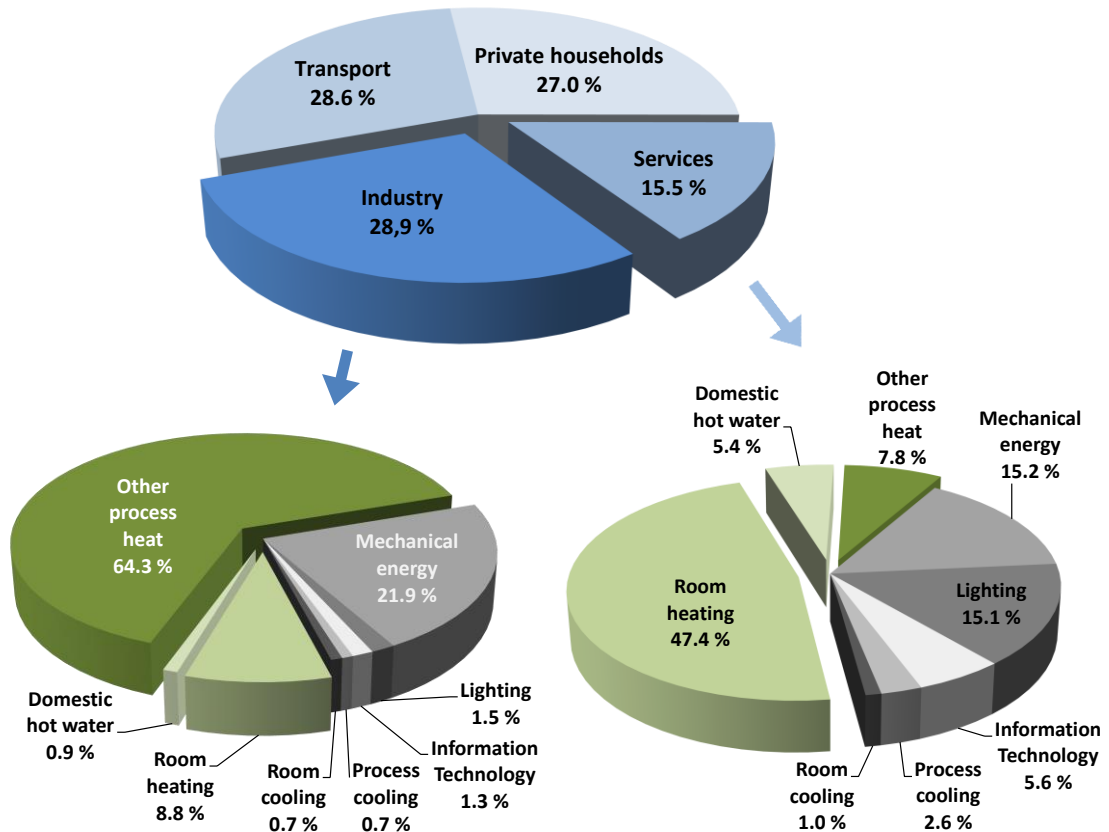
Figure 1.5: Distribution of Germany's final energy consumption in 2012 (top) with a closer look into the industry (left) and service sector (right). Values calculated based on data of the BMWi (2014, spreadsheets 7 and 7a).

The subdivision in Figure 1.5 reveals that, as expected, the majority of process heat is consumed by industry. This sector accounts for 28.9 % of Germany's final energy demand. It is remarkable that almost three quarters of its demand is heat. In the service sector, the share of process heat demand is relatively low, but many applications demand low temperature levels (e.g. washing processes for cars or laundry), which is favorable for ST. Process heating in the German industry and service sector accounted for 19.8 % or 494 TWh of totally 2,499 TWh consumed in 2012. In industry, this demand was mainly covered by gas (48 %), coal (19 %), and district heating (9 %). In the service sector, oil (23 %) is still also an important source besides gas (51 %) and district heating (12 %). In both sectors only about 8 % of the heat demand was supplied by grid electricity, about 6 % was supplied by renewable energy utilization on site (BMWi 2014).

According to Weiss and Biermayr (2009, p. 96), the European energy consumption can be divided into electricity and transport (51 %), heat above 250 °C (15 %), and heat below 250 °C (34 %). Sanner et al. (2011, p. 8) show that 44 % of the EU's overall heat demand is caused by industry, with about two thirds of the heat required above 250 °C and about one third below. Comparing these figures reveals that almost the whole high temperature heat demand above 250 °C is caused by industry. Since temperatures below 250 °C are technically more feasible for solar thermal heat generation, Figure 1.6 allows for a closer look into the different types of end energy use in this temperature range.
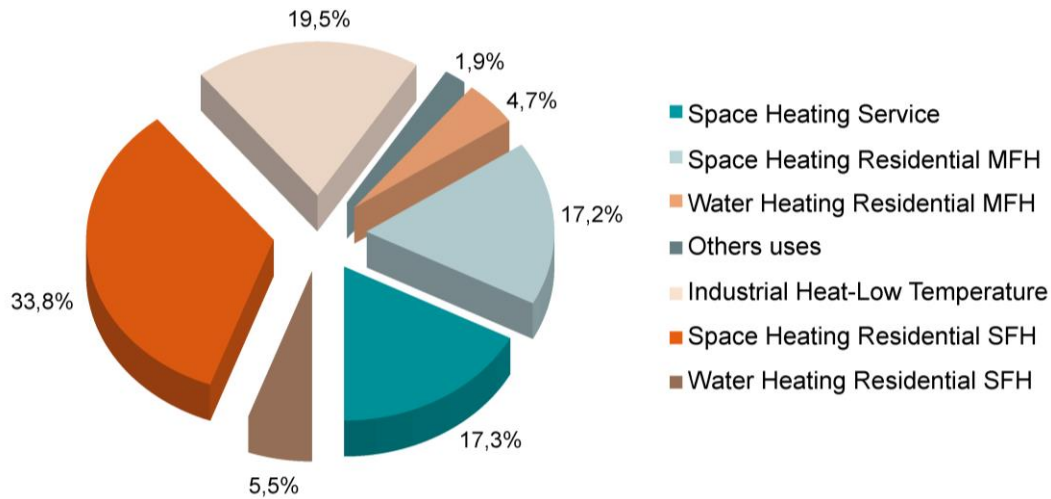
Figure 1.6: Heat demand of the EU below 250 °C by type of use (SFH = single family house, MFH = multifamily house (Sanner et al. 2011, p. 8))

The heat demand structure below 250 °C clearly shows that ST systems with their current main application field of domestic hot water generation can only cover a small share of the energy demand below 250 °C. In order to achieve a significant contribution, they also have to provide space heating and solar thermal process heat (SPH) in the industry and the service sector.

1.2.2 Potential Contribution of Solar Thermal Systems

Several national and international projects identified a high potential of ST systems to generate process heat. The early studies in the field are POSHIP (Schweiger et al. 2000 ; Schweiger 2001), PROCESOL II (Aidonis et al. 2005) and PROMISE (Müller et al. 2004). Among others, the sectors of food and beverage, textiles, paper, metal treatment, machinery and wood and tobacco processing were identified to be promising.

A potential study of the IEA-SHC Task 33 *Solar Heat for Industrial Processes* summarized the main outcomes of existing potential studies. Vannoni et al. (2008) roughly estimated that a share of 3.8 % of the industrial heat demand within EU 25 could be generated by state of the art ST systems. Non-industrial process heat demand was not considered in this study. In 2012, the overall energy consumption of the EU 28 was 19579 TWh (Eurostat 2014b), with a share of 25.6 % in industry and 13.5 % in services (Eurostat 2014a).

Only considering industry, the SPH potential within Europe estimated by Vannoni et al. corresponds to about 190 TWh/a, or approx. 423 million m^2 (assuming solar gains of $450\ kWh/(m^2a)$ and assuming that the potential in the new EU member countries is similar than in EU 25). The magnitude of this potential gets clear when it is compared to the cumulated collector area installed in the EU, which was about 61 million m^2 by 2012 (calculated according to (Weiss and Mauthner 2014, p. 8) from 42.8 GW$_{th}$ installed with a factor of 700 W/m^2).
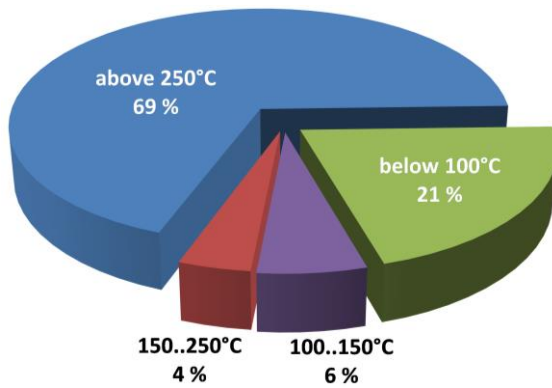
Figure 1.7: Industrial heat demand in Germany per temperature range (Lauterbach et al. 2011b)

To estimate the potential of ST technologies for process heat generation, consideration of the required temperature levels is essential. Lauterbach et al. (2011b) show in a study for Germany, that 69 % of the industrial heat is demanded at temperatures above 250 °C (cp. Figure 1.7). At temperatures below 100 °C, 21 % of the heat can be provided and further 6 % between 100 and 150 °C. It is remarkable that only 4 % of the demand occur between 150 and 250 °C. In their estimation of the SPH potential in Germany, Lauterbach et al. (2011b) focused on the industry (cp. Figure 1.5, left). In a first step, they identified nine promising industry sectors and summarized their heat demand below 250 °C, including the demand for domestic hot water and space heating. The demand above 250 °C was excluded from the study, because it was assumed that in Germany it would not be possible to provide these temperature levels with ST technologies at reasonable costs. For these boundary conditions, a theoretical potential of 130 TWh/a was estimated. Furthermore, Lauterbach et al. assumed that 60 % of the theoretical potential could not be realized due to the priority of energy efficiency measures, the necessity of electrical heat supply (e.g. for plastic products) or restrictions in terms of available roof area. For the remaining potential they suggest an average solar fraction of 30 %. These restrictions result in a technical potential of 3.1 % of Germany's overall industrial heat demand, i.e. 15.6 TWh/a or 35 million m^2 (Lauterbach et al. 2011b). This is approx. 10 % of the industrial heat demand below 250 °C.

Lauterbach et al. extended their study to 11 industrial sectors and up to 300 °C, which lead to an increased potential of 3.3 % (16 TWh/a). They conclude that the food and beverage sector shows the highest potential, mainly because of the often favorable temperature level below 100 °C. A detailed description of the industrial sectors analyzed and of the required temperature levels of different industrial processes can be found in (Lauterbach et al. 2012) and (Lauterbach 2014).

1.2.3 State of the Art, Perspectives and Further Readings

Installations worldwide: Despite the high technical potential, SPH is still in its infancy. It is difficult to get reliable data on the collector area installed in SPH applications, since current statistics usually do not count them separately. Following a bottom up approach, in the framework of the current IEA-SHC Task 49 *Solar Heat for Production and advanced Applications,* an online platform listing the worldwide existing SPH plants was set up. It was made publicly accessible in March 2014. ST companies and SPH customers can enter their technical and financial plant data as well as lessons

learned. At the beginning of September 2014, 134 SPH plants from all over the world with an overall collector area of 126,421 m² (corresponding to 88.5 MW$_{th}$) were listed. Among them, 19 plants were above 1000 m² and 29 between 500 and 1000 m² (AEE INTEC 2014). Since the database was set up recently, it can be expected to grow further when more actors in the field of SPH know about it.

Challenges: Currently, there are still high technical and economic barriers for an increased marked deployment of SPH systems. Technically, a very high variety of system designs is possible, because a high variety of processes can be supported. Thus, SPH systems usually need a high effort for planning and installation, especially in countries where the processes are on a high technological level. In this case, SPH systems are usually much more complex than ST systems for domestic purposes, since they have to be planned sector specific and individually. Due to the higher complexity of the systems, there is also often a lack of knowledge about technical concepts for solar heat integration and about SPH system hydraulics and control. No easy to handle software tools for SPH system design and optimization are available. This leads to considerable uncertainties about the solar gains to be expected from a certain design variant.

Economically, SPH generation is also a challenge. In larger industries, usually the most important decision criterion for an investment is its amortization period. Very often time frames of below five years are expected, which is hard to achieve for SPH systems. Thus, for the successful realization of a SPH project, also energy efficiency measures, often offering significantly lower amortization times than SPH systems, should be considered. To be attractive against this background, the planning, installation and component selection of SPH systems must be very cost-effective. Furthermore, interactions between the SPH system and the existing heat supply have to be considered. The instantaneous solar gains and also the service lifetime of a SPH plant can vary significantly when heat demand, mass flow or temperature level at the solar heat integration point are changing. Thus, the assessment of possible long-term effects on the thermal load at an integration point is another crucial aspect for ST process heating.

Selected further readings: SPH had been of interest in ST research for decades. Dedicated book chapters addressing this application field can be found e.g. in (Goswami et al. 1999), (Tiwari 2002), (Kalogirou 2004) and (Duffie and Beckman 2013). The potential study of Schweiger et al. (2000) mentioned above also contains a state of the art review for Spain and Portugal. Karagiorgas et al. (2001) analyzed 10 SPH systems, which have been installed during the 1990s in Greece. A list of suitable processes can be found in (Kalogirou 2003), who also comments on difficulties and framework conditions for SPH. Smyth and Russell (2009) analyzed the potential of ST and photovoltaic systems for the global wine production. Solar cooling of industrial processes has been successfully demonstrated by Motta (2010). For Australia, the state of the art in SPH has been analyzed by Fuller (2011). A contracting-financed project integrating SPH in a

gas pressure regulating station was realized by Heinzen et al. (2011). Economic assessments of SPH in Central Europe can be found in (Lauterbach et al. 2011a) and (Faber et al. 2011). Norton (2012) published a comprehensive literature survey on the field of SPH. Recently, SPH was also included in the handbook for planners and installers of the German Solar Energy Society DGS (Kasper et al. 2012). Feasibility analyses for Tunisia are presented by Calderoni et al. (2012) and Frein et al. (2014). Silva et al. (2014) did a study on SPH for vegetable preservation in Spain.

The EU-funded project *Solar Process Heat* (SoPro) was one of the first publicly funded projects addressing barriers for SPH on an international level. It supported the market deployment in six European regions. In sum, 90 energy screenings of industrial companies were carried out. Checklists were developed, training seminars were held and the chances and barriers for SPH contracting have been analyzed. Based on a process-specific approach, simplified design guidelines for SPH systems for four common applications were developed (Hess and Oliva 2010). These applications are heating of water for washing or cleaning, heating of make-up water, heating of baths or vessels and drying with air collectors. It was shown that SPH systems supporting open loop processes at low temperature levels can have significantly higher annual gains than standard ST systems in the domestic sector. The work within SoPro triggered 10 new SPH installations within the regions (Egger 2011). The summarized project results together with practical examples for application of the simple system dimensioning methodology are presented in (Hess et al. 2011).

Following a sector-specific approach, Schmitt et al. (2012a) presented a branch-concept for SPH integration in breweries. A guideline for planners for this sector was published as well (Schmitt et al. 2012b). Based on this work, generalized technical solar heat integration concepts were developed (Schmitt 2014). Lauterbach (2014) developed a preliminary design methodology for SPH systems.

Selected recent examples for scientifically monitored commercial solar process heat plants are the Hofmuehl brewery with a system utilization ratio of about 20 % (Wutzler et al. 2011), the Alanod demonstration plant for direct steam generation (Krueger et al. 2011) as well as the electroplating company Steinbach & Vollmann, where in the course of system optimization an innovative storage charging concept was implemented (Schramm and Adam 2014).

Lauterbach et al. (2014) monitored the Hütt brewery. By incorporating the measured ambient temperature, irradiance, process load profiles and system operation data in a TRNSYS simulation, the authors found a very good correlation between the measured and simulated performance of the flat-plate SPH system applied. Recently, SPH systems for brick manufacturing (Vittoriosi et al. 2014) and meat production (Cotrado et al. 2014) were installed and are monitored.

Visions and research priorities: In spite of the barriers described above, stakeholders have very high expectations for SPH. The German solar industry association BSW sees SPH below 100 °C in its *Fahrplan Solarwärme* as a strategic focus issue with decisive importance for market deployment of ST. With a joint effort of the whole ST sector, the BSW has set the ambitious target of 1.500 SPH plants installed in Germany by the year 2020 and perspectively more than 28.000 by 2030 (Ebert et al. 2012, p. 11).

The International Energy Agency IEA states in its *Technology Roadmap for Solar Heating and Cooling*, that ST systems globally could supply 20 % of the industrial heat demand below 120 °C until 2050 (IEA 2012, p. 22).

Based upon a *Common Vision for the Renewable Heating and Cooling Sector in Europe* (Sanner et al. 2011), the European Technology Platform on Renewable Heating and Cooling published *Strategic Research Priorities* for ST collectors until 2020 and beyond (Stryi-Hipp et al. 2012, p. 45). In their *Strategic Research and Innovation Agenda* for the renewable heating and cooling sector, the platform members defined research and innovation priorities for SPH collectors and systems (Sanner et al. 2013, p. 53).

They further detailed their suggestions in a *Solar Heating & Cooling Technology Roadmap*, containing technological and non-technological measures for SPH until 2020 with objectives and milestones. Among else, they recommend the development of mid temperature collectors with improved efficiency, self-carrying and modular collector structures for large-scale collector arrays on industrial roofs, as well as improved reflector materials for concentrating collectors (Ivancic et al. 2014, pp. 26-28).
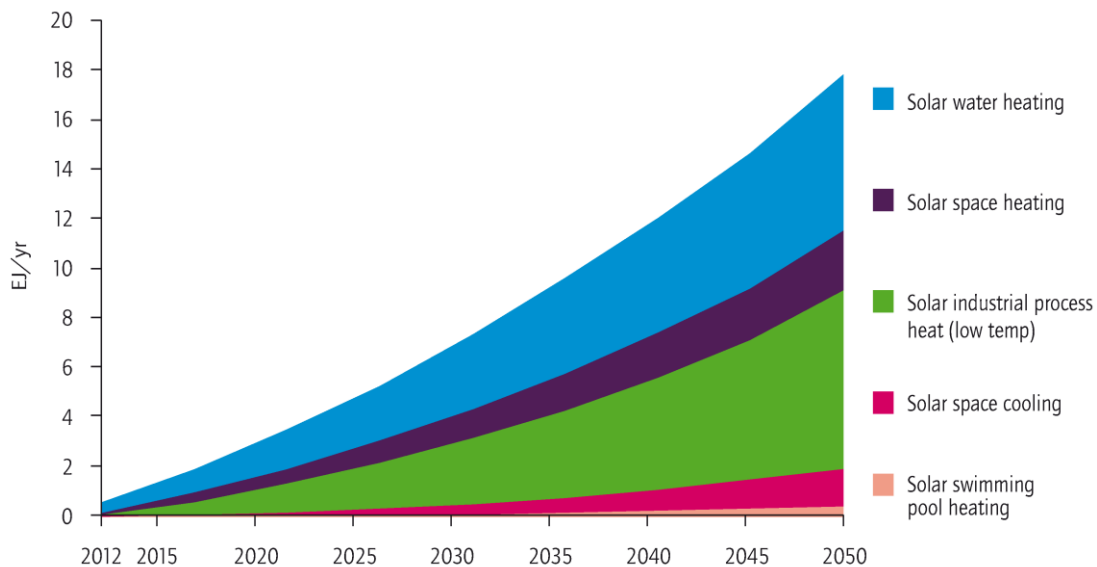

Figure 1.8: Vision of the International Energy Agency IEA for ST until 2050. ST technologies could supply 15.5 EJ or about 16 % to the predicted worldwide heating and cooling demand. In this scenario, SPH below 120 °C contributes 7.2 EJ (IEA 2012, p. 22).

1.3 Stationary Process Heat Collectors

1.3.1 Collector Categories

The purpose of a solar thermal collector is to convert solar irradiance incident on its aperture area[1] into useful heat. To efficiently generate temperatures above 100 °C a high variety of collector designs and materials is applied. The existing concepts can be categorized according to different criteria: Stationary (i.e. non-tracking), seasonally-tilted, one-axis tracked and two-axis tracked collectors are built. When the flux density of irradiance onto an absorber is enhanced by concentrators, high concentrating focusing collectors differ from the low-concentrating and are usually non-focusing. Thermally, non-evacuated collectors have to be distinguished from evacuated ones. Different heat transfer fluids such as water, water-glycol mixture, air, thermal oil or molten salt are used.

The term **process heat collector (PHC)** is not a clear definition, since process heat as defined above can be generated by all ST collector types. But since this term is mainly used in collector development, within this work it describes collectors, which are designed and optimized for output temperatures in the mid-temperature range (100 to 250 °C) or the high temperature range (above 250 °C). In Figure 1.9, a suggestion of performance criteria to fulfill are shown. Here, from the perspective of collector development, the single-covered flat-plate is not a process heat collector.
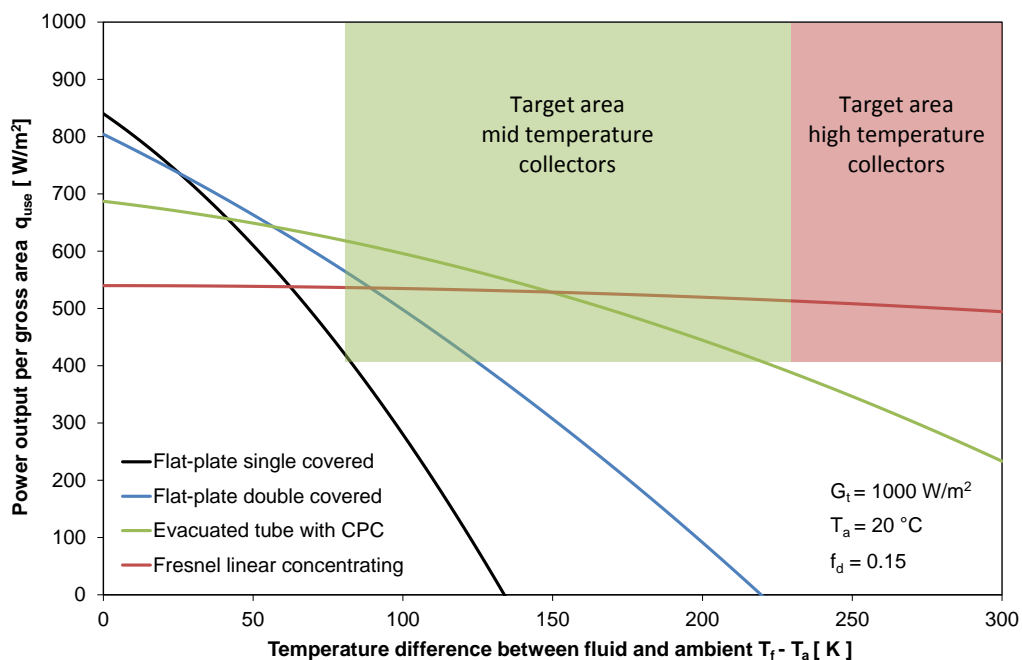

Figure 1.9: Collector output curves at reference conditions with suggested performance criteria for process heat collectors as discussed within Task 49, based on Fischer (2012). The symbols used are explained in section 3.2.1 and in the nomenclature.

---

[1] Theoretical reference area of solar thermal collectors, usually the projected area parallel to the absorber, through which radiation can reach the absorber (cp. A_{ap} in Figure 2.6)

1.3.2 Standard Flat-plates and Evacuated Tube Collectors

Flat-plate collectors: Standard-flat-plate collectors are the most common collector type in Europe (Weiss and Mauthner 2014, p. 11). Due to the low difference between gross and aperture area they collect much beam irradiance per gross area and make good use of diffuse irradiance. They are stationary mounted, simply constructed and need low maintenance. Figure 1.10 shows the construction of a non-evacuated standard flat-plate.

1. Selective coating
2. Absorber
3. Absorber pipe
4. Insulation
5. Rear panel
6. Header pipe
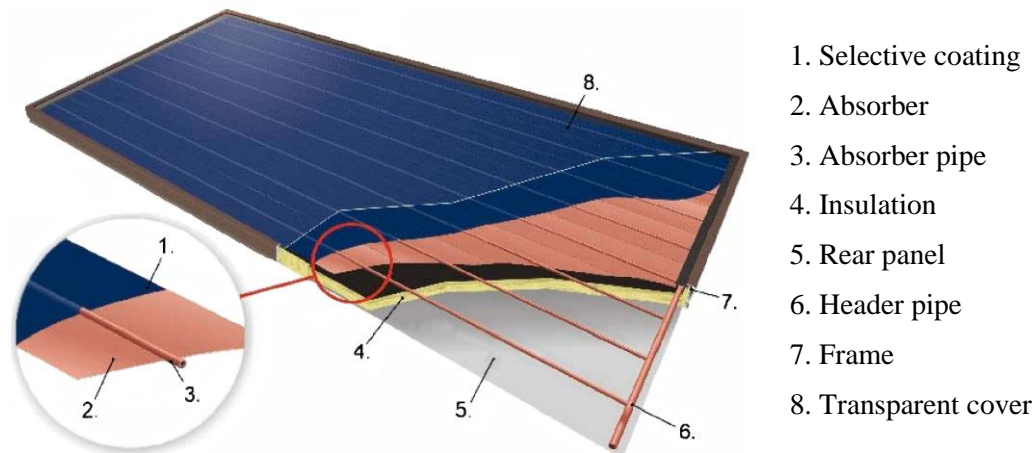7. Frame
8. Transparent cover

Figure 1.10: Components of a standard flat-plate collector, based on (Rommel 2005)

Good thermal conduction is needed to effectively transfer the heat generated on the absorber to the absorber pipes and finally to the heat carrier fluid of the solar loop. Figure 1.11 shows the main loss mechanisms of a standard flat-plate at non-perpendicular irradiance under operation conditions. The values are only indicatively and vary highly for different constructions, temperatures and locations.
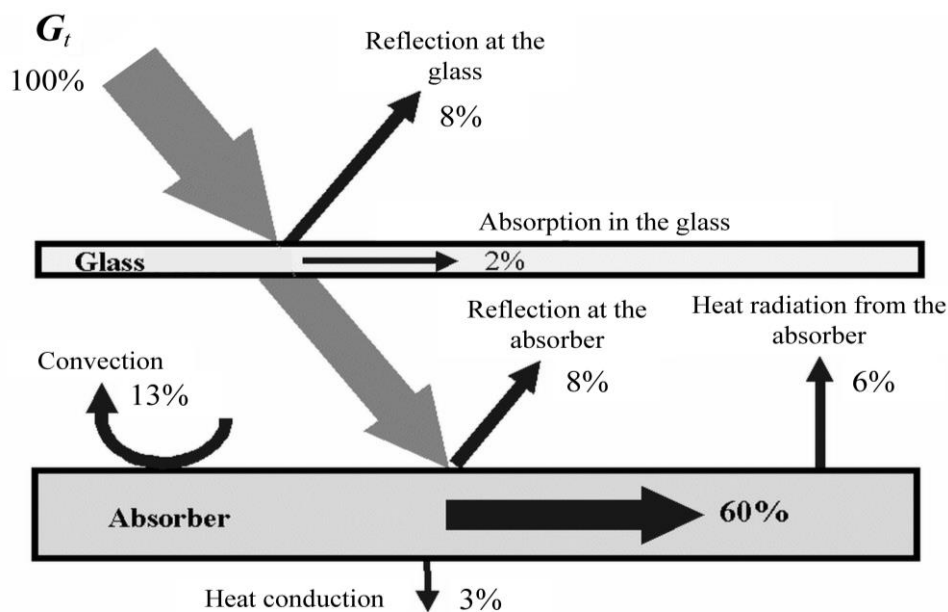

Figure 1.11: Simplified illustration of the loss mechanisms of a standard flat-plate Collector, adapted from Quaschning (2007)

Evacuated tube collectors: Currently, the solar thermal industry manufactures a large variety of evacuated tube collector concepts. The so called *Sydney tube* (also *Twin-glass tube* or *Thermo flask tube*), shown in Figure 1.12 is the most common tube. Most evacuated tube collectors can be characterized as follows:

- A collector consists of a row of parallel glass tubes.
- A vacuum ($< 10^{-2}$ Pa) inside every single tube extremely reduces conduction heat losses and eliminates convection.
- The upper end of the tubes is connected to a header pipe, through which the heat carrier fluid of the solar loop flows.

At Sydney tubes, the vacuum is located between the inner and the outer glass tube. A selectively coated absorber surface (cp. section 2.3.3) covers the outside of the inner tube. Due to the position within the vacuum, the coating usually has a high thermal stability. After evacuating the gap between the tubes, the so called *getter*, made from barium, is evaporated inductively. The emerging barium film on the lower end of the tube absorbs any CO, CO_2, N_2, O_2 and H_2O released during storage or operation of the evacuated tube. In this way the vacuum is enforced and long-term stabilized. If the silver color of the getter gets grey like in Figure 1.12, the vacuum is lost.

A heat conduction sheet transfers the heat absorbed by the inner glass tube to collector pipes (usually copper). In direct flow tubes, the fluid of the solar loop flows thorough these copper pipes, which are usually bended to a u-shape and clamped to the heat transfer sheet (cp. Figure 1.12). In direct flow tubes, the tubes are usually hydraulically parallel and brazed to the collector header pipes (one header for return flow, one for flow). The return flow streams down the Sidney-tubes within one half of the bended, so called *u-tube* pipes, and up again in the other half, being heated on both ways. Collected by the header, it forms the collector flow. Also direct flow configurations with coaxial pipes are offered. In this case, the return flow flows down within the inner pipe and up again in the outer pipe, which is centrally placed within the heat conduction sheet.
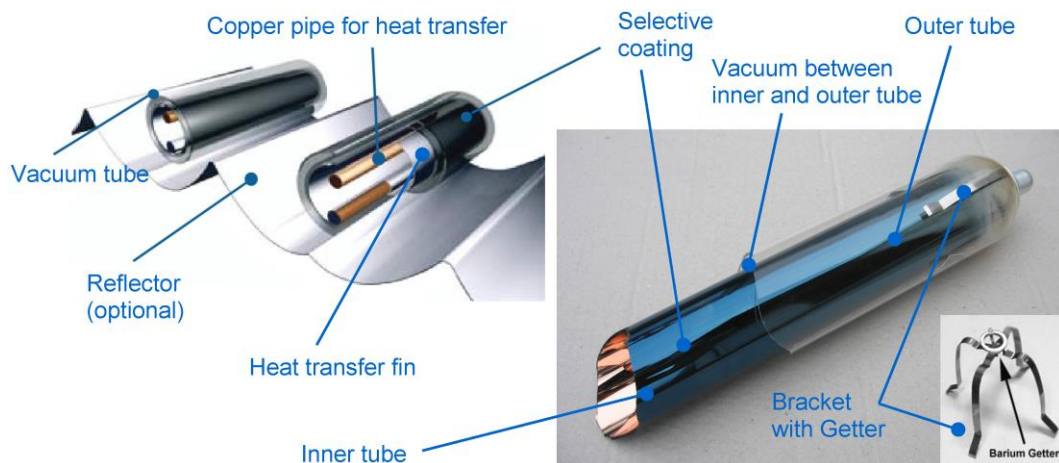

Figure 1.12: Components of a Sydney tube collector (Weiss and Rommel 2008, p. 8)

In heat-pipe collectors, collector pipes and solar loop are hydraulically disconnected. A working fluid evaporates within the collector pipes at low temperatures and condenses at the top of the pipe. The condensers are thermally connected to the header pipe, either dipping into the solar fluid (referred to as *wet connection*) or clamped to the header pipe and using heat conduction paste (*dry connection*).

1.3.3 Low-Concentrating, Stationary Collectors

Reflectors are applied to increase the energy gain of ST collectors by re-directing or concentrating solar irradiance onto an absorber. Focusing reflectors concentrate irradiance onto a focal point or line. Such collector types have to track the sun to keep the focus on the absorber. To avoid tracking, reflectors must be shaped in a way that the radiant flux density onto the absorber is increased for a certain range of incidence angles. Such reflectors are called non-focusing or non-imaging concentrators. With these concepts, only small concentration ratios are reasonable. Thermally, it is important to distinguish between reflector concepts, which are placed outside the thermal sealing of a collector (cp. Figure 1.13) or within (cp. Figure 1.14). Placing the reflectors inside protects them from hail, dust and water. But at such concepts conduction and convection occur within the whole casing, so the loss reduction related to the aperture area is usually smaller.

This section intends to reflect the state of the art of low-concentrating, stationary collectors, focusing on flat-plate based concepts that were theoretically optimized, characterized in laboratories, annually simulated or annually measured. The technical terms used are explained in the following chapters, mainly in section 2.4.1. Further literature with relevance for this work is referenced within the respective chapters.

The use of external so called *booster reflectors* for ST collector arrays (cp. Figure 1.13) has been investigated since the 1950s, when Tabor (1958) projected the incidence angle of beam irradiance into a vertical north-south plane and determined necessary acceptance angles of stationary concentrators.

Perers and Karlsson (1993) presented a simplified model to calculate the additional energy gain of flat-plate collectors equipped with flat or CPC booster reflectors. In Studsvik, Sweden, they measured the annual gain of a flat-plate equipped with optimized flat booster reflector and of an identical reference flat-plate without reflector. The flat-plates were double-covered with white glazing (i.e. low iron content) and a Teflon foil, and the length of the flat reflector in front of the flat-plates was 1.25 the height of the flat-plates (ratio L/H = 1.25). The reflectors extended the length of the flat-plates by one meter in the east-west direction to minimize end losses. After four operating seasons they measured an annual output increase due to the reflector of 30 %. In a simulation study, they applied reflectors of $\rho = 0.8$ ($\rho_{spec} = 0.6$) to the described flat-plate collectors and calculated the annual gain for $T_f = 70\ °C$ in Stockholm, Swe-

den. For L/H = 1.25, a collector with CPC-booster achieved 15 % higher output than with a flat booster. For L/H = 2, the authors expect additional gains of 50 % by a CPC booster. Perers (1995) further optimized different flat and CPC booster geometries for the flat-plate mentioned above. Assuming costs of ground area and a cost-range for the reflectors, he calculated an investment cost reduction of up to 25 % per delivered kWh for the Stockholm climate, when flat booster reflectors with optimal ratio of L/H = 1.5 are applied. In the study, the maximum yield per ground area was achieved by flat boosters; the maximum yield per receiver flat-plate area was achieved by a CPC.

Figure 1.13: Flat-plate collector field with trapezoidal corrugated aluminum sheet booster reflectors supplying a hospital in Östhammer, Sweden.
Picture: Björn Karlsson, cp. (Rönnelid and Karlsson 1999, p. 347).

Hellstrom et al. (2003) investigated the impact of different flat booster reflector materials on the additional annual energy gain of a standard flat-plate with solar transmittance of 0.90 in Stockholm. For L/H = 2.06, the optimized concepts were assessed at mean temperatures of 70 °C. A PVF2-coated aluminium sheet increased the annual gain by 25.7 %, anodized aluminium by 32.7 %, and silver coated glass by 36.4 %. The relative improvement increased with increasing operation temperatures. Rönnelid and Karlsson (1999) showed that v-corrugation of flat booster reflectors can further increase the annual beam irradiance onto the flat-plate by approx. 10 % and the annual output by approx. additional 3 % compared to a flat booster (for L/H = 2).

In Figure 1.14, a concept with internal CPC reflectors is shown. Efficiency test results of the collector alternately covered with solar glass, honeycomb transparent insulation material (TIM) and with additional Teflon foil can be found in (Carvalho et al. 1995).

Carvalho et al. (1995) compared different variants of their collector to other collector types by simulations for Lisbon, Portugal. They found their single covered, north-south orientated collector to achieve a higher annual solar fraction than a selective flat-plate or an evacuated tube collector (ETC) at daily heating 900 l water from ambient temperature to 60 °C. The authors further recommend their collector for seasonal applications.

1. Aluminum frame
2. EPDM gasket
3. Polyurethane insulation
4. Absorber fin with selective coating on both sides
5. Back sheet
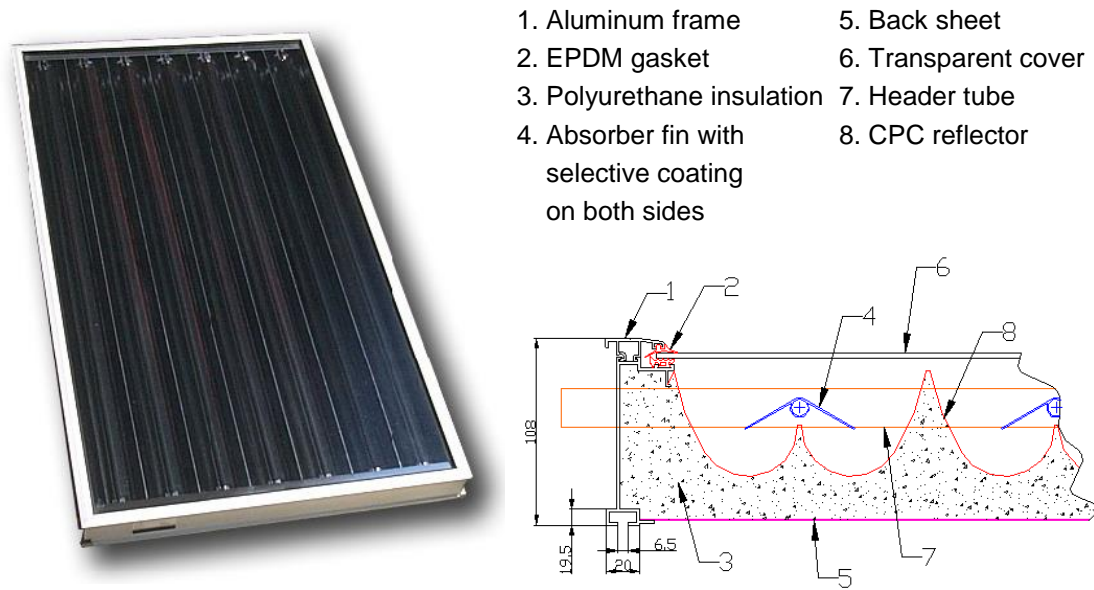6. Transparent cover
7. Header tube
8. CPC reflector

Figure 1.14: AoSol CPC collector with "inverted v"-absorber.
For highest gains the collector is orientated east-west. $C_{geo} = 1.12$, $\theta_a = 56{,}4°$,
$A_{ap} = 1.98 \text{ m}^2$. Parameters from Pereira et al. (2003). Pictures: Manuel Collares Pereira

Supporting a single-stage adsorption chiller at 90 °C in Lisbon, the single-covered variant achieved higher gains than a selective flat-plate. Carvalho et al. (1995) further state, that the double covered variant would have a better cost/performance ratio than an ETC in this application. Detailed analytical solutions for the optical parameters of "inverted v"-absorbers can be found in (Fraidenraich et al. 2008).

Rönnelid et al. (1996) constructed a flat-plate with internal, symmetric v-trough concentrator with a flat absorber. Laboratory heat loss tests revealed that a low-emitting reflector and an additional 25 μm FEP Teflon film reduced the heat losses by about 20 %. But the optimized CPC concept with $C_{geo} = 1.56$, $\theta_a = 35°$ and a truncation ratio of 0.4, had only approx. 5 % higher annual gains than a standard flat-plate, when it was orientated east-west and simulated in Stockholm at $T_f = 70 \text{ °C}$ (read from graph in (Rönnelid and Karlsson 1996, p. 178)). So for an annual load the additional costs for manufacturing internal reflectors of this kind might not be justified. A very similar collector had been investigated by Fasulo et al. (1987), who could significantly reduce convection losses by covering the flat absorbers with transparent foil, but the overall efficiencies of the concept were rather low and no annual energy gain simulations have been reported. Buttinger et al. (2010) investigated a flat-plate collector with internal CPC and tubular absorber. A prototype with krypton gas filling and very low pressure of 0.01 bar showed efficiencies of about 50 % at $G = 1000 \text{ W/m}^2$ with $f_d = 0.1$.

In order to replace collector components by cheaper reflector area, the collector concept shown in Figure 1.15 was developed for high latitudes.
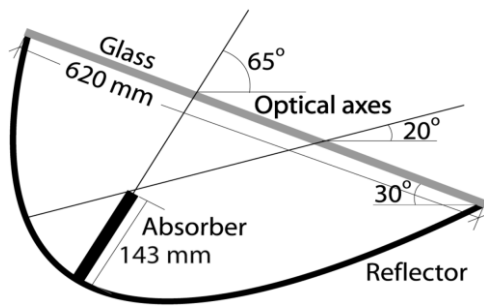
Figure 1.15: Construction principle of the *MaReCo* (Maximum Reflector Collector) with stand-alone MaReCo field of $A_{ap} = 500$ m^2 and row length of 40 m constructed in 1999 supporting a bio fuel burner in Torsåker, Sweden. Left picture from (Adsten et al. 2004, p. 201), right picture from (Adsten 2002, p. 41).

The reflector consists of two parabolic and one circular segment and directs irradiance onto a flat, bifacial coated absorber. Though having lower annual gains than a reference flat-plate, Adsten et al. (2005) estimate the roof-integrated MaReCo and the stand alone MaReCo to have a better annual cost/performance ratio than a flat-plate collector generating heat at $T_f = 75\,°\mathrm{C}$. Further development of the concept and its theory can be found in (Brogren 2004). The IAM of asymmetric reflectors is investigated in detail by outdoor measurements in (Helgesson 2004). A similar concept with bifacial absorber orientated parallel to the glazing is presented in (Tripanagnostopoulos et al. 2000).

The company SRB Energy developed a bifacial vacuum flat-plate collector, which can be equipped with two semicircular or CPC-shaped reflectors (cp. Figure 1.16). The reflectors are stationary and not covered. According to the company, the vacuum inside the flat-plate is between 10^{-6} to 10^{-9} mbar and is expected to last for the whole service life of the collector. This shall be achieved by a metal alloy getter being regenerated when heated by the sun, which shall cause diffusion

Figure 1.16: SRB collector at the Intersolar Europe 2011 in Munich. Picture: S. Hess

of atoms and molecules into the getter material. The collector is expected to work efficiently with in the medium temperature range also at low irradiance (Burckhart et al. 2014).

Many stationary, low concentrating collector concepts are based on evacuated tubes. As well as at flat-plates, one can distinguish between concepts where the reflector is placed within the evacuated tube or outside. Mills et al. (1994) optimized asymmetric, external CPC reflectors of ETCs for certain load profiles using ray-tracing and TRNSYS simulations. Muschaweck et al. (2000) used numerical optimization and raytracing to optimize such collectors for tubular ETC collectors. They found that east-west-orientated, asymmetric truncated CPC reflectors usually have a better ground use than collectors with symmetrical reflectors.

Nkwetta and Smyth (2012) designed two variants of external, truncated CPC reflectors for an evacuated heat-pipe tubular collector with flat absorber. The first variant is a CPC for flat radiation exit aperture, at which the standard-tube with the single-side coated absorber sheet (SSACPC) is placed. At the second variant, the absorber is rotated by 90° (now perpendicular to the aperture) and coated on both sides (DSACPC). Both variants have $\theta_a = 30°$ and $C_{geo} = 1.85$, so the DSACPC has twice the aperture of the SSACPC. The authors measured both variants under an indoor solar simulator. The conversion efficiency of the DSACPC was found to be only slightly below that of the SSACPC, with considerably lower heat loss coefficients. External, north-south symmetric CPC reflectors for evacuated tubes (XCPC) were presented by Kim et al. (2013). Working at comparably high concentration, efficiencies of above 40 % at temperatures above 200 °C were measured for such modules.

Duff et al. (2004) presented the integrated CPC-reflector evacuated solar collector (ICPC) running a double-effect absorption chiller. The inner bottom half of an evacuated glass tube is silvered and reflects the irradiance to a fin absorber attached to a coaxial counter flow absorber tube. Detailed monitoring of the system performance is ongoing (Duff and Daosukho 2011). An improved ICPC design with a flat, bifacial absorber perpendicular to the aperture, similar to the DSACPC-geommetry in (Nkwetta and Smyth 2012), was presented by Jiang and Winston (2014).

Nkwetta et al. (2012) introduced a CPC concentrator for a tubular absorber of 15 mm diameter, which is placed inside an evacuated tube of 100 mm outer diameter. In a ray-tracing analysis, under the simplification of ideal specular reflection and 100 % absorptance of the absorber, the construction with $\theta_a = 20°$ and $C_{geo} = 1.95$ offered a mean optical efficiency close to 0.8 within its acceptance angle. Nkwetta et al. (2013) performed outdoor-efficiency tests of this tube alternatively with heat-pipe or direct coaxial flow absorber, and with or without evacuation. The conversion factor with evacuation was higher than without for both absorber variants, and best efficiencies at higher working temperatures were found for the evacuated tube with heat-pipe absorber.

2 Optical Investigations

The main subject of this work is the utilization of anisotropic diffuse sky radiance by low-concentrating solar thermal collectors. Thus, this chapter starts with a background on solar irradiance. The concept of the incidence angle modifier and its determination for certain design variants of the RefleC collector by raytracing is explained. The parameterization of RefleC in the raytracing-model is discussed based on measured material properties. Finally, the reflector design is explained and raytracing results relevant for the following investigations are given.

2.1 Solar Irradiance

2.1.1 Components and Characteristics

Non-focusing solar thermal collectors make use of beam and diffuse radiation. Both types of irradiance vary during day and year with changing sun position and weather conditions. Figure 2.1 illustrates the different irradiance components incident on a low-concentrating, stationary collector.
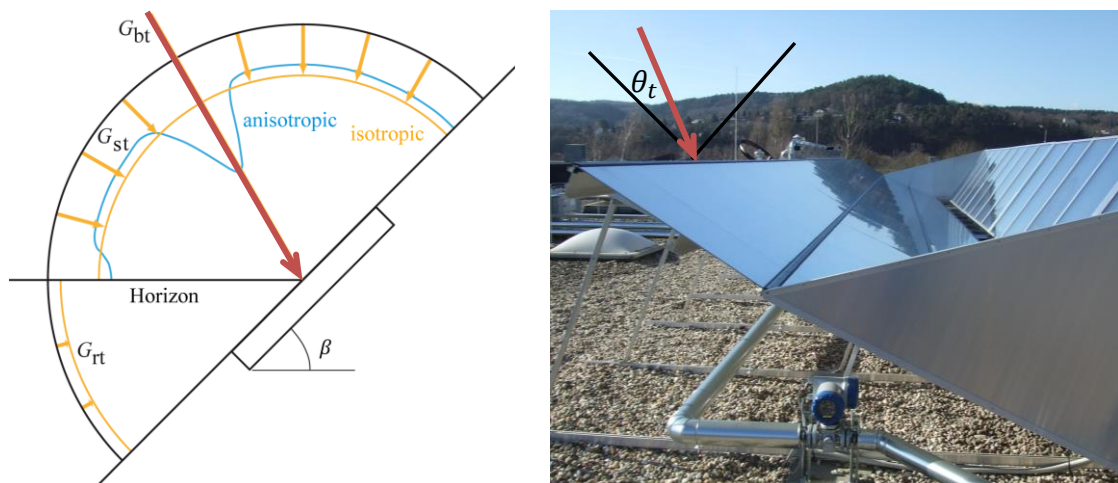

Figure 2.1: Solar irradiance components on an aperture plane with tilt angle β. Left: The yellow arrows and circular segments symbolize the simplified assumption of an isotropic nature of sky and ground reflected radiance. The blue curve shows a realistic, anisotropic intensity distribution of diffuse sky radiance for a sunny day, with brightening around sun and horizon. Right: RefleC with longitudinal direction along the reflector trough. In the transversal, the radiation acceptance is very distinctive (cp. Figure 2.11). The positive transversal incidence angle component θ_t on the aperture is indicated (cp. Figure 2.8).

Beam irradiance G_{bt} on the tilted aperture plane reaches the collector from a solid angle of approx. 6° diameter (cp. section 2.1.2) with the sun at its centre. Diffuse irradiance from the sky G_{st} originates from the whole sky dome visible from the aperture (excluding the disk of approx. 6°). Ground reflected irradiance G_{rt} reaches the aperture from directions below the horizon with transversal incidence angles $\theta_t = [-90; -90 + \beta]$.

Table 2.1 gives an overview on the terms used within this work to distinguish between radiation sent out and received as well as between instantaneous power and energy.

Table 2.1: Terms for solar radiation as suggested by Iqbal (1983, p. 41). All terms refer to the integrated power of the whole solar radiation spectrum.

Term	Unit	Meaning
Radiation	-	Used qualitatively to distinguish irradiance components
Radiance	$W/(m^2 sr)$	Emitted solar radiant flux within a unit solid angle
Irradiance	W/m^2	Incident solar radiance per unit aperture area
Irradiation	kWh/m^2	Integrated irradiance within time interval per aperture area

In the following, details on characteristics and calculation of the solar irradiance components as well as their use in simulation programmes will be given. An obvious starting point for this is the sun itself.

Extraterrestrial solar radiation: The sun is the center of our planetary system and contains 99.85 % of its total mass. Within the sun, hydrogen is fused to helium, which results in a mass loss of approx. $4.3 \cdot 10^6$ t/s in the form of radiative energy. Using Einstein's law it can easily be shown that the sun emits an enormous radiant flux of approx. $3.86465 \cdot 10^{26}$ W to outer space. The temperature of the sun's center is approx. 10^7 K. It decreases towards the photosphere, the approx. 200 km thick "surface" of the sun, to finally approx. 5,790 K. There, the major part of radiance is emitted. Simplified, the sun can be seen as a black body emitter. Under this assumption, its radiance can be calculated according to the Stefan-Boltzmann law with an approximated effective black body temperature of 5,777 K (Duffie and Beckman 2006, p. 3).

When viewed from earth, the opening half angle of the solar disk itself is as small as approx. 0.27°, which results in a divergence of direct sunlight of approx. 0.54° or 9.4 mrad. From satellite measurements the exact value for the intensity at the outer earth atmosphere normal to the sun direction was defined to

$$G_{sc} = 1,367 \pm 23 \ \frac{W}{m^2} \tag{2.1}$$

This value G_{sc} is called solar constant (Duffie and Beckman 2006, p. 5). The fluctuation range of this value results from the eccentricity of the earth's elliptical orbit around the sun, which causes annual variations of approx. 1.7 %. G_{sc} can be determined by Eq. 2.2.

$$G_{sc} = 1{,}367 \cdot [1 + 0.0033 \cos\left(\frac{2\pi \, i}{365}\right)] \qquad (2.2)$$

Herein, i is the day of the year (Duffie and Beckman 2006, p. 37). The equation for the instantaneous extraterrestrial irradiation on a horizontal plane G_0 (parallel to the earth's surface) as used in weather data files can be found in (Remund et al. 2007b, p. 8).

Atmospheric effects: Various processes in the atmosphere reduce the intensity of the solar radiation, and also direction and spectral distribution are changed. The extent of these effects highly depends on the atmospheric path length, which is travelled by the rays. To describe this path length relative to the shortest possible way (zenith angle $\theta_s = 0°$, cp. Figure 2.7), the value AM (*Air Mass*) was defined.

$$AM = \frac{1}{\cos\theta_s} \qquad (2.3)$$

AM 0 refers to solar irradiance intensity and spectrum at the outer edge of the earth's atmosphere. AM 1 accounts for effects to the sun rays when passing through the atmosphere perpendicularly, i.e. with shortest possible distance. Since this is only possible for beam irradiance near the equator, the spectral irradiance commonly referred to is AM 1.5. The spectra of the different irradiance types at AM 1.5 are shown in Figure 2.2.
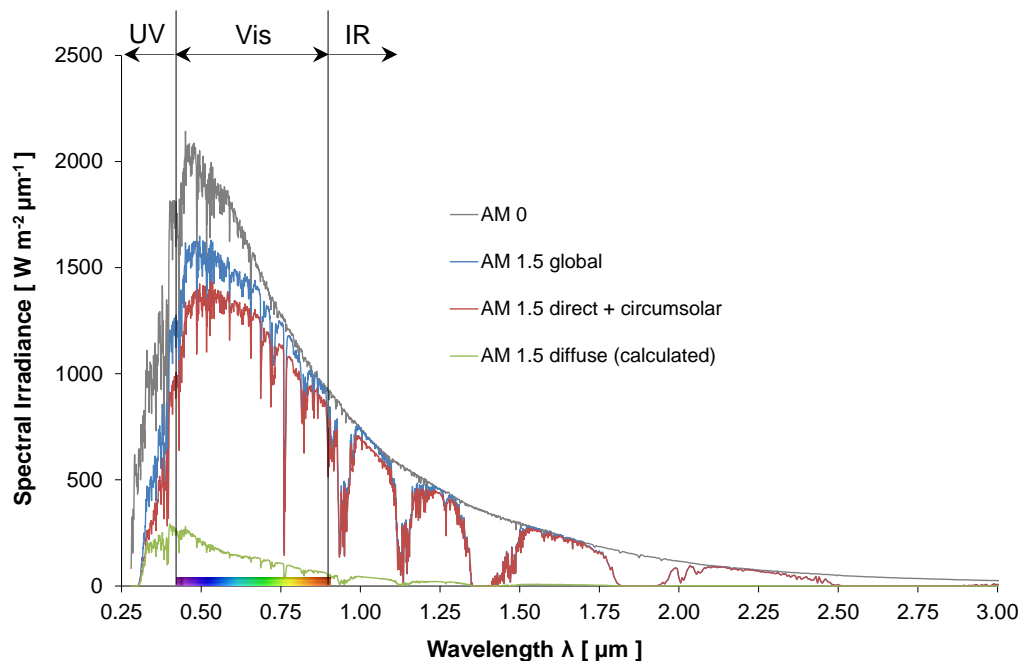

Figure 2.2: Reference spectra G173-03 of ASTM (American Society for Testing and Materials). Values provided by US National Renewable Energy Laboratory (NREL 2013). AM 1.5 defined for receiving surface tilted 37° towards the equator, surface normal pointing to sun, solar zenith angle $\theta_s = 41.81°$, albedo 0.3, turbidity 0.29 and $T_a = 20\,°C$. Spectral irradiance for "AM 1.5 diffuse" is not provided and was calculated by subtracting spectrum "AM 1.5 direct + circumsolar" (cp. section 2.1.2) from "AM 1.5 global". Iqbal (1983, p. 162) reports a very similar diffuse spectrum (for horizontal). The colored bar indicates visible light, i.e. the sensitivity of the human eye between approx. 0.38 μm and 0.78 μm). Below this is the ultra violet (UV) range, above infrared (IR).

Global (or hemispherical) irradiance is the sum of beam (i.e. direct) and diffuse. Comparing the curves of AM 0 and AM 1.5 global, the effects of atmospheric gases get visible. The different gases show individual wavelength-dependent absorptivities, which result in absorption bands. Most relevant for this effect are water vapor, oxygen, carbon dioxide and ozone. Additionally, reflections at water drops and ice particles occur, so that a part of the reflected radiation is directed back into outer space. Furthermore, the photons undergo Rayleigh and Mie scattering.

Rayleigh scattering occurs due to the interaction of light with an atmospheric gas molecule or aerosol, which has smaller dimensions than the wavelength of the light. The result is non-directional (diffuse) radiation with smaller wavelengths than beam radiation. Among others, this results in the blue sky, because the emerging radiation is primarily in the wavelengths of blue light. Rayleigh scattering occurs mostly isotropic. This is why at good weather conditions the hemisphere is evenly blue. Mie scattering is caused by larger particles like fog drops or larger aerosols. It highly increases at dusty skies. Mie scattering shows a clear overweight of forward-scattering. Its visible effect is the white circular area, which often can be observed around the solar disk. A rule of thumb is that the higher AM-value and air pollution are, the higher is also the Mie scattering. Further details on the effects of the atmosphere on solar radiation and on their modelling for solar applications can be found in Iqbal (1983) and Badescu (2008).

2.1.2 Radiation Data Measurement

It was crucial for this work to understand how radiation measurement devices work and how they distinguish between beam and diffuse. Several devices for long-term measurement of meteo data are shown in Figure 2.3.
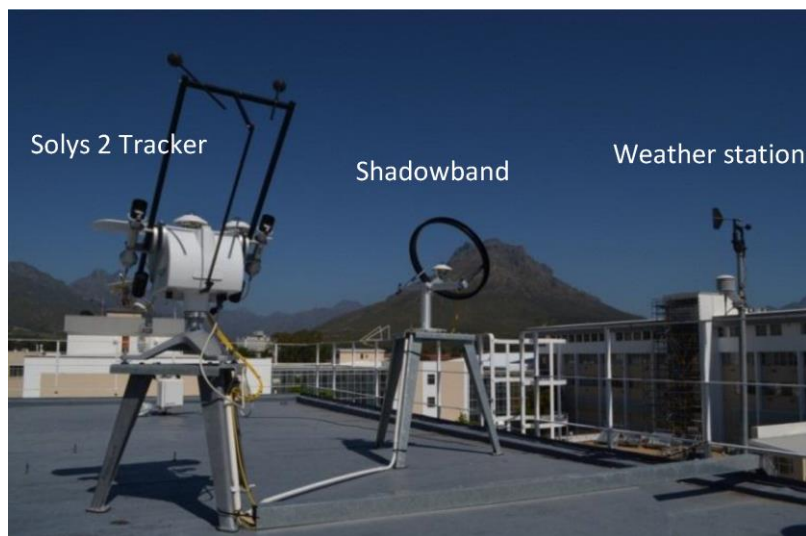

Figure 2.3: Solar tracker for irradiance measurement (left). At its edge, two pyrheliometers point to the solar disk. One measures DNI (direct normal irradiance) including circumsolar, the one shaded by the tracked ball measures only circumsolar. Two horizontal pyranometers are mounted on top; one measures GHI (global hemispherical irradiance), one is shaded from beam irradiance to only detect diffuse. Picture: (SU 2013).

The horizontal diffuse pyranometer in the back of Figure 2.3 is equipped with a shadow band, which has to be manually adjusted every few days. With a whole hemispheric segment shaded, it is less accurate and used for comparison only.

Atmospheric effects on solar radiation have been described above. In the context of focusing solar concentrator applications, the resulting brightness gradient from center of the solar disk to the circumsolar region is often referred to as "sun shape". This shape can be described by the Circumsolar Ratio (CSR), i.e. the ratio between the integrated intensity arriving from the aureole and the integrated intensity from solar disk plus aureole. The extent of this aureole depends on turbidity and zenith angle. For simulations of focusing concentrators with acceptance angles significantly below the ones of a pyrheliometer, sun shape profiles representative for certain DNI values can be approximated (Neumann et al. 2002, p. 202). Figure 2.4 shows a clear sky with horizontal brightening (left, low CSR), and a slightly covered sky (right) with higher circumsolar radiance significantly extending the acceptance of a standard-pyrheliometer.
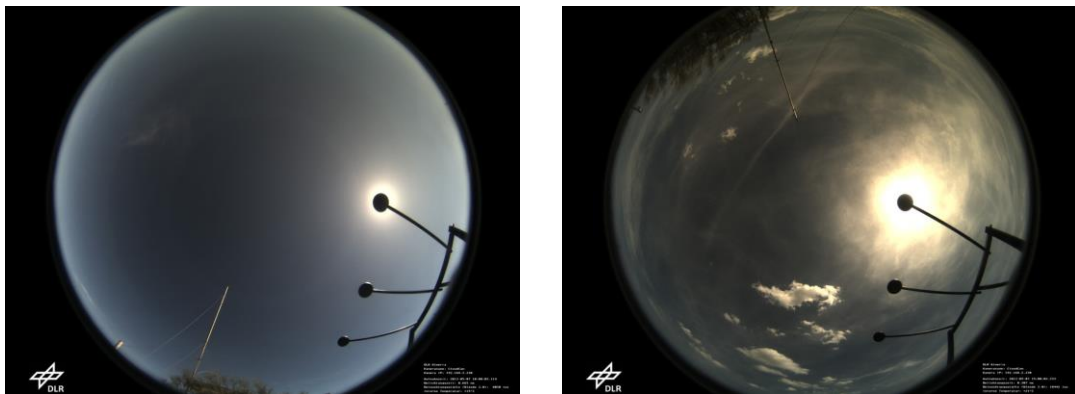

Figure 2.4: Images from "All Sky Imager" at Plataforma Solar de Almeria at 09:00 UTC (left) and 14:00 UTC (right). The sun is shaded by a tracked ball. CSR was measured with NREL SAM (Sun Aureole Measurement device) and with two Pyrheliometers with different opening angles of 1.5° and 2.5°. Left: CSR = 0. 2%, Right: CSR 18.1 % (Wilbert et al. 2012, p. 8).

Distinction between beam and diffuse: Pyranometers have a view angle of 180° and a flat absorber, thus integrating irradiance from their whole visible hemisphere and measuring with cosine-effect (cp. page 25). Pyrheliometers on the other hand are irradiance sensors equipped with a collimator. Depending on the collimator aperture width, they only detect irradiance from a small, usually circular field of view. Due to the finite extent of the sensor element itself, there is no sharp cutoff in radiation acceptance. The same partial shading of the sensor at certain incidence angles applies also when a Pyranometer is shaded with a tracked ball as in Figure 2.3. This effect with the characteristic pyrheliometer-angles "slope angle", "opening angle" and "limit angle" is discussed in (Iqbal 1983, p. 352). Effectively, pyrheliometers for DNI measurement accept radiation from a disk of 5° to 6° in diameter with the sun in its centre (Neumann et al. 2002, p. 198; Remund et al. 2007a, p. 49).

From the earth's perspective, the solar disk radius varies with the elliptical shape of the earth orbit between 4.742 mrad in January and 4.584 mrad in July (Neumann et al. 2002, p. 200). Thus, a mean solid angle of approx. 0.53° in diameter is covered by the sun disk. But Mie scattering by the earth's atmosphere causes a considerable broadening of the sun observed from earth, with an aureole around the physical solar disk. This aureole is called circumsolar region. In Figure 2.2, the spectral intensity "AM 1.5 + circumsolar" was measured with a pyrheliometer of 5° field of view (NREL 2013). Thus, the spectrum "AM 1.5 diffuse (calculated)" should represent the irradiance measured by a pyranometer with shading ball.

TMY-files: Solar thermal system simulation programs like TRNSYS, T*Sol, or Polysun, usually use standardized weather data input files. In TRNSYS, often Typical Meteorological Years (TMY-files) are used. They statistically represent a typical average year at a selected location. For their generation, either on-site long-term measurement values can be used, or the values are interpolated between meteo data measurement stations near the requested location (Remund et al. 2007a).

TMY-files contain hourly data sets for simulations. Each line includes calculated extraterrestrial direct normal irradiation, calculated extraterrestrial horizontal irradiation G_0, global horizontal irradiation (GHI) G, measured with an unshaded pyranometer, direct normal irradiation (DNI) measured with a pyrheliometer with 6° view angle, diffuse horizontal irradiation (DHI) G_d, measured by a pyranometer with tracked shading ball of 6° diameter centered at the solar disk. Diffuse irradiance in the weather data files correspondingly means GHI reduced by irradiance from solar disk and its surroundings within 6° diameter, as discussed in (Remund et al. 2007a, p. 49) and (Welford and Winston 1978, p. 125). Furthermore, the files contain illuminance data (considering only visible light), ambient temperature, wind speed and direction, relative humidity and other values (Remund et al. 2007a, p. 30).

2.1.3 Irradiance on Tilted Planes

In simulations, the irradiance components on a tilted plane are usually calculated by the software itself, based on the values for horizontal irradiation in Wh/m^2 from the weather data file. Sticking to horizontal input data allows for using one single meteo data input file, while e.g. collector slope or azimuth are varied. Within this section, basic approaches for calculation of irradiance on tilted planes are given.

Beam irradiance G_{bt} on a tilted plane can be calculated easily from the direct normal irradiance G_{bn} pyrheliometer data.

$$G_{bt} = G_{bn} \cdot \cos \theta = G_{bn} \cdot A_1/A_2 \qquad (2.4)$$

Figure 2.5 illustrates that the radiant flux density of beam irradiance decreases with $\cos \theta$ when a surface is turned away from the sun.
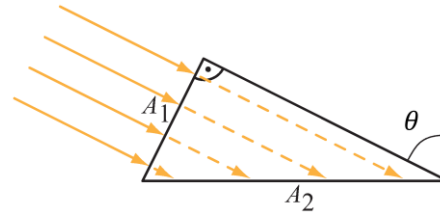
Figure 2.5: Illustration of the cosine-effect for received solar irradiance. Beam irradiance reaches the area A_2 at incidence angle θ. For the projected area A_1 perpendicular to the incidence direction, the received energy is the same, but the intensity is higher (maximal).

If only the horizontal beam irradiance G_b is available, knowledge of the solar zenith angle θ_s leads back to:

$$G_{bn} = G_b / \cos \theta_S \tag{2.5}$$

Combining Eq. 2.4 and Eq. 2.5 we obtain the calculation of G_{bt} from horizontal beam irradiance (as contained in weather data input files for simulations).

$$G_{bt} = G_b \cdot \cos \theta / \cos \theta_S \tag{2.6}$$

The radiation spectrum of beam irradiance (including CSR) is shown in Figure 2.2.

Diffuse irradiance from the sky G_{st} on a tilted plane originates from the whole sky dome except from the angle of 6° with the sun at its centre. Very simplified, it can be assumed that every sky segment has the same radiance. With this so called isotropic model, G_{st} can be calculated from the horizontal diffuse irradiance G_d by simply cutting the part of the hemisphere not visible for a surface sloped with β:

$$G_{st} = G_d \cdot 0.5 \cdot (1 + \cos \beta) \tag{2.7}$$

In reality, the diffuse sky radiance is often distributed uneven over the hemisphere, i.e. it is anisotropic. The extent of this anisotropy depends among else on instantaneous cloudiness, turbidity, and Mie and Rayleigh scattering. The two main anisotropies are the circumsolar diffuse irradiation and the brightening near the horizon (cp. blue curve in left picture of Figure 2.1). The circumsolar diffuse radiation is the brightening of the sky around the sun due to Mie scattering. The brightening near the horizon results from the much higher Air Mass in direction of the horizon and therefore the more likely scattering of solar radiation (Duffie and Beckman 2006, p. 10). Another reason for the horizontal brightening is reflections or backwards-scattering of rays due to Rayleigh scattering, which occurs in the atmosphere behind the horizon.

The radiation spectrum of the diffuse irradiance from the sky is different from beam irradiance, since parts of the scattered and reflected radiation undergoes a considerably higher path length or Air Mass. The spectrum calculated in Figure 2.2 includes due to $\beta = 37°$ both components $G_{st} + G_{rt}$. Qualitatively, the distribution corresponds well to the diffuse irradiance spectra derived by Iqbal for various conditions (Iqbal 1983, p. 159). It has its maximum intensity in the UV range.

Diffuse irradiance from the ground G_{rt}: Additionally to the diffuse irradiance from the sky also diffuse irradiance reflected by the ground reaches a sloped collector (cp. Figure 2.1). This component is usually and also within this work approximated to be isotropic. In this case, the diffuse irradiance from the ground G_{rt}, originating from reflected global horizontal irradiance G, correlates with the reflectivity of the ground ρ_{grd} and the collector slope β as follows:

$$G_{rt} = G \cdot \rho_{grd} / 2 \cdot (1 - \cos \beta) \tag{2.8}$$

The so called albedo ρ_{grd} can be measured by an albedometer. But usually, this reflectivity is not known and not constant, since a dry ground shows a different reflective behavior than a wet or snow covered surface. Therefore it is common to calculate with a constant reflectivity of $\rho_{grd} = 0.2$. In some cases meteo-files include measured or model-based albedo-values, which can be used. Values of up to 0.5 are reached for snow covers of 5 cm and higher (Remund et al. 2007b, p. 29).

Global irradiance G_t: The sum of horizontal beam irradiance G_b and horizontal diffuse irradiance G_d is referred to as global or hemispherical horizontal irradiance G:

$$G = G_b + G_d \tag{2.9}$$

The global solar irradiance G_t on a tilted plane is:

$$G_t = G_{bt} + G_{dt} + G_{rt} \tag{2.10}$$

Programs like *Meteonorm* offer detailed algorithms for such calculations based on horizontally measured meteorological data of various types and time resolutions. With validated interpolation algorithms time resolutions down to one minute for the different irradiance components on tilted planes can be generated (Remund et al. 2007b, p. 24). As stated above, it is convenient to use hourly irradiation data on the horizontal for ST system simulations. In *TRNSYS 17*, the function *"getIncidentRadiation"* combines a weather data reader and a radiation processor to provide irradiance values on tilted planes (Klein et al. 2012b, pp. 7.85-7.97). It is important to note that neither Meteonorm nor TRNSYS offer the possibility to generate a continuous distribution of diffuse sky radiance. Both only offer different models to calculate the irradiance components on a tilted plane as a summarized value (further discussed in section 4.1). In each time step, this value is then transferred to e.g. a solar thermal collector.

2.1.4 Conventions for Sun Position and Reference Planes

Aperture area: The aperture is a theoretical reference area of ST collectors, meaning the area parallel to the absorber plane, through which perpendicular irradiance can reach the absorber. For flat-plates, the aperture area is usually identical with the collector glazing; for RefleC, the projected area of the reflectors is added (cp. Figure 2.6).
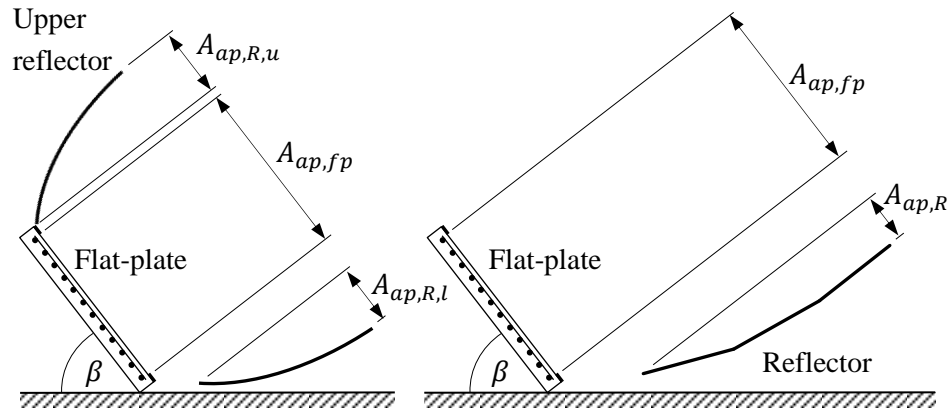
Figure 2.6: Aperture area definition for RefleC. The flat-plate aperture is the transparent part of the collector front (within the opaque front cover). Both for conventional CPC (RefleC 1 and 2, left) and one-sided CPC (RefleC 3 to 6, right) the projected reflector area parallel to the absorber plane adds to the aperture. Cp. also Figure 2.8.

Incidence angle on a horizontal plane: The sun is located by its zenith angle θ_s, which is its incidence angle onto the horizontal, and the solar azimuth angle ϕ_s from the south (see Figure 2.7). When the irradiance direction $\vec{s}_0$ is projected onto the horizontal, ϕ_s is the displacement angle between this projection and the south direction, while ϕ is referring to the transversal collector plane (cp Figure 2.8).
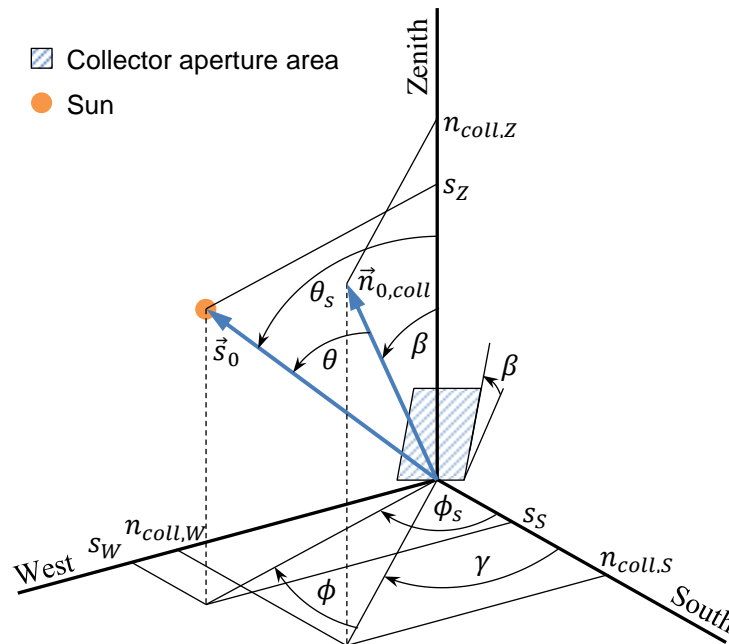
Figure 2.7: Orientation of collector plane and sun (absolute and relative). Values for sun azimuth ϕ_s and collector azimuth γ are negative for positions east of south up to -180° and positive for positions west of south until +180°.

Collector orientation and incidence angles: The collector slope β from the horizontal can also be found between zenith and collector surface normal $\vec{n}_{0,coll}$. The collector azimuth angle from the south is γ. The incidence angle θ onto the collector is clearly located by the azimuth angle $\phi = \phi_s - \gamma$.

The projection of $\vec{s}_0$ in a Cartesian coordinate system with south, west and zenith is:

$$\vec{s}_0 = \begin{pmatrix} s_S \\ s_Z \\ s_W \end{pmatrix} = \begin{pmatrix} \sin \theta_s \cdot \cos \phi_s \\ \cos \theta_s \\ \sin \theta_s \cdot \sin \phi_s \end{pmatrix} \tag{2.11}$$

Analogue to Eq. 2.11, the unit vector of the surface normal $\vec{n}_{0,coll}$ is:

$$\vec{n}_{0,coll} = \begin{pmatrix} n_{coll,S} \\ n_{coll,Z} \\ n_{coll,W} \end{pmatrix} = \begin{pmatrix} \sin \beta \cdot \cos \gamma \\ \cos \beta \\ \sin \beta \cdot \sin \gamma \end{pmatrix} \tag{2.12}$$

The angle between $\vec{s}_0$ and $\vec{n}_{0,coll}$ is the incidence angle θ on the collector plane. It is the scalar product of this two unit vectors (cp. Duffie and Beckman (2006, p. 15)):

$$\begin{aligned} \theta &= \cos^{-1}\left(\vec{s}_0 \cdot \vec{n}_{0,coll}\right) \\ &= \cos^{-1}[\cos \theta_s \cdot \cos \beta + \sin \theta_s \cdot \sin \beta \cdot \cos(\phi_s - \gamma)] \end{aligned} \tag{2.13}$$

Projection of irradiance direction into reference planes: Since many collectors show a characteristic optical behavior for rays incident parallel (longitudinal) or perpendicular (transversal) to the reflector(s), a distinction as in Figure 2.8 is needed.

The longitudinal plane is perpendicular to the aperture area. It is congruent to the main geometrical axis of the collector (cp. collector "trough" in Figure 2.1) and the surface normal of the collector aperture. For the longitudinal plane the optical conversion efficiency usually shows a smaller dependency on the incidence angle as for the transversal plane, which is positioned orthogonal to the longitudinal plane.

Different equations for calculating θ_t and θ_l for axial symmetric optical behavior are found in (Theunissen and Beckman 1985, p. 318), (Clement 2004, p. 22), and (Haller et al. 2013, p. 9). For the RefleC collector the reference planes were switched because of the above stated conditions. Also, the dependency of the optical efficiency from the incidence angle is not symmetric, so positive and negative values are to be calculated. Considering these factors, the resulting longitudinal and transversal angles of incidence are for the indicated ranges of validity:

$$\theta_t = -\tan^{-1}[\tan \theta_s \cdot \cos(\phi_s - \gamma)] - \beta \qquad \forall\, \theta_t \in\,]-90; +90[\tag{2.14}$$

$$\theta_l = \tan^{-1}\left[\frac{\sin \theta_s \cdot \sin(\phi_s - \gamma)}{\cos \theta}\right] \qquad \forall\, \theta_l \in\,]-90; +90[\tag{2.15}$$

The incidence angle θ can be calculated from its components as derived by McIntire and Reed (1983, p. 408):

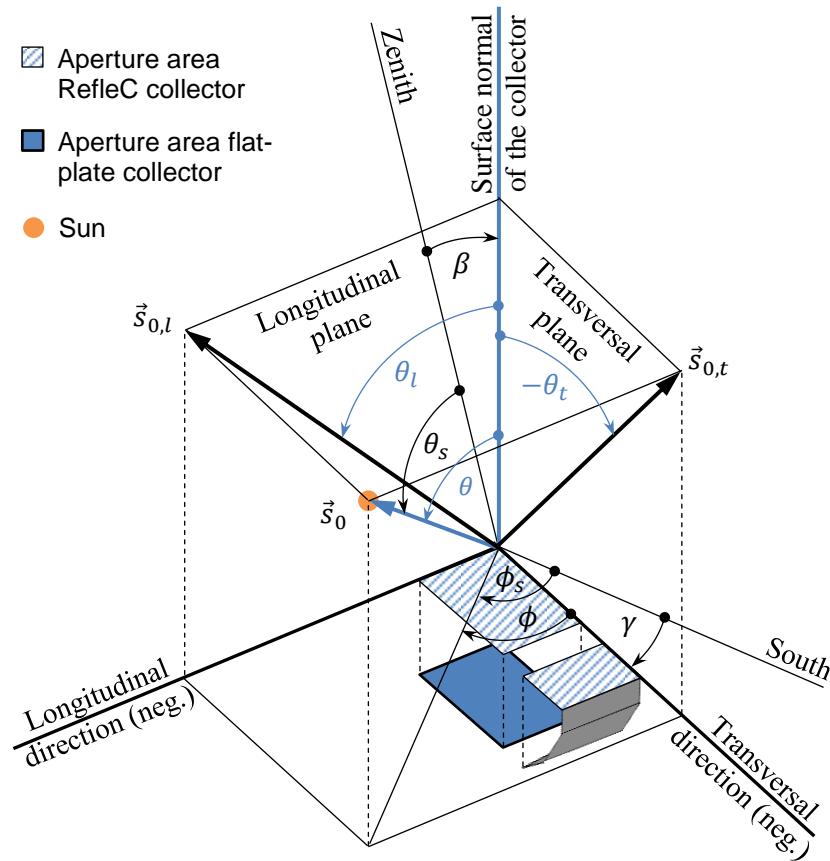$$\theta = \tan^{-1}\sqrt{\tan^2 \theta_t + \tan^2 \theta_l)} \tag{2.16}$$

Figure 2.8: Projection of the sun direction (defined by θ and ϕ) into the longitudinal and transversal collector plane. The transversal incidence angle θ_t is negative for $\phi = [-90°; +90°]$, the longitudinal angle θ_l is positive for $\phi = [0°; +180°]$.

The incidence angles' polar coordinates θ and ϕ in Figure 2.8 can be transformed into its longitudinal and transversal components by negating the equations of Theunissen and Beckman (1985, p. 318) to receive positive and negative values:

$$\theta_t = -\tan^{-1}[\tan\theta \cdot \cos\phi] \qquad \forall\, \theta_t \in\ ]-90; +90[\qquad (2.17)$$

$$\theta_l = -\tan^{-1}[\tan\theta \cdot \sin\phi] \qquad \forall\, \theta_t \in\ ]-90; +90[\qquad (2.18)$$

2.2 Raytracing

For the optimization of RefleC it was essential to know the incidence angle dependent optical losses of the measured test samples (cp. Appendix A) and of theoretically investigated variants. These losses are considered by the conversion factor η_0 (see sections 2.2.2 and 3.2.1) and the Incidence Angle Modifiers (IAM) for beam and diffuse irradiance. To determine the IAM for beam, an optical simulation model of the RefleC collector was set up and different variants were characterized by raytracing in the software OptiCAD, version 10.046 (Corporation 2009). A screenshot of the first RefleC collector concept (cp. Figure 1.2) in OptiCad is shown in Figure 2.9.
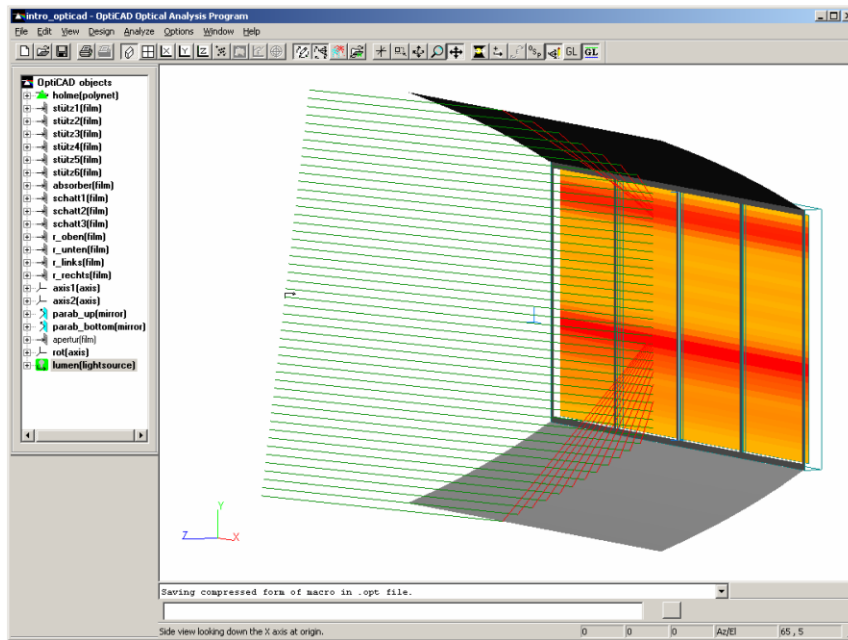
Figure 2.9: RefleC 1 in OptiCAD. For better visibility, the ray density was reduced, the glazing removed, the reflectance set ideal specular and also absorptance set ideal.

Raytracing means that energy, direction and wavelength distribution of every simulated ray are modified at interaction with configurable objects. This modification happens at every interface of the objects. At interfaces to partly transparent objects with different refractive index n, additional rays are generated according to the laws of Snell and Fresnel (cp. Figure 2.10).

On the next pages, the optical loss mechanisms of ST collectors with reflectors are briefly described, the concept of the incidence angle modifier (IAM) is introduced and the raytracing procedure is reported. Based on measurement results of the materials applied, the parameterization of the simulated objects in OptiCAD is discussed.

2.2.1 Optical Loss Mechanisms

Optical loss mechanisms cause a difference between irradiance entering the aperture of a ST collector and the energy absorbed by its absorber. The main relevant mechanisms for concentrating collectors are shown in Figure 2.10:

- Absorption and scattering[2] at the reflector
- Absorption and (multiple) reflection at the transparent cover(s)
- (Multiple) reflection at the absorber

All of these factors depend to a different extent on the incidence angle θ of radiation onto the material surface and on the wavelength λ of the light.

---

[2] Scattering (characterised by the standard deviation σ) is not always a loss-mechanism, since at RefleC for many incidence angles the scattered rays still reach the absorber (cp. Figure 2.10)
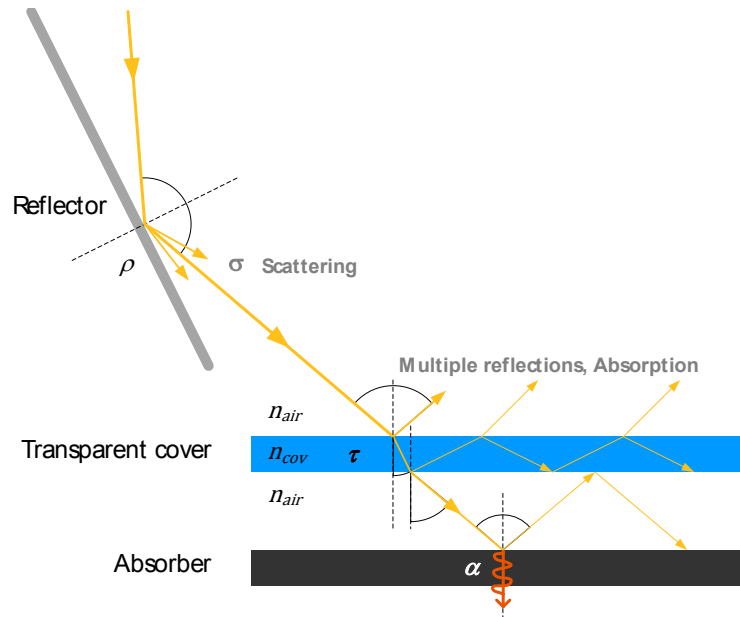
Figure 2.10: Optical loss mechanisms of a low-concentrating, single covered ST collector. An idealized theoretical path of light is shown from the first interaction with the reflector until a part of it (red) is finally being absorbed by the absorber and converted into heat. Characteristic parameters are the reflectance of the reflector $\rho(\theta, \lambda)$ and its scattering $\sigma(\theta, \lambda)$, the transmittance of the transparent cover $\tau(\theta, \lambda)$ and the absorptance of the absorber $\alpha(\theta, \lambda)$. Picture adapted from Oliva (2009, p. 18).

2.2.2 Incidence Angle Modifier for Beam Irradiance

Solar irradiance hits the aperture of stationary or one-axis tracked ST collectors from varying incidence angles. The conversion factor η_0 is the conversion efficiency for irradiance into useful heat when the mean collector fluid temperature equals ambient temperature. The incidence angle modifier (IAM) describes how physical effects change this conversion efficiency when the incidence angle onto the aperture plane changes, i.e. for $\theta \neq 0$ this correction factor *modifies* η_0. The fundamentals on the interaction between IAM and collector efficiency are discussed later within section 3.2.1.

Considered effects: Within this work, the optical losses of a ST collector at perpendicular beam irradiance are mathematically summarized by an effective reflectance-transmittance-absorptance product $(\rho\tau\alpha)_{e,\perp}$ (cp. Figure 2.10). For non-normal beam irradiance this factor is $(\rho\tau\alpha)_e(\theta_l, \theta_t)$ or $(\rho\tau\alpha)_e(\theta, \phi)$ respectively. The index e for *effective* symbolizes that this factor is not simply a product of the material parameters ρ, τ and α, but also considers all occurring optical and geometrical effects, like multiple reflections, shading and radiation reaching the flat-plate without reflection. The IAM for beam irradiance K_b can be understood as:

$$K_b(\theta_l, \theta_t) = \frac{\eta_{0,b}(\theta_l, \theta_t)}{\eta_{0,b}} = \frac{F'(\theta_l, \theta_t) \cdot (\rho\tau\alpha)_e(\theta_l, \theta_t)}{F' \cdot (\rho\tau\alpha)_{e,\perp}} \approx \frac{(\rho\tau\alpha)_e(\theta_l, \theta_t)}{(\rho\tau\alpha)_{e,\perp}} \quad (2.19)$$

Duffie and Beckman (2006, p. 297) imply that K_b only accounts for optical effects. It is true that for non-concentrating stationary ST collectors, optical mechanisms very

dominantly affect the IAM. But it is also very important to understand that for energy gain simulations the IAM also has to account for changes in the absorber heat removal factor F', which might occur e.g. at low-concentrating collectors for certain incidence angles. Since raytracing can only account for optical effects, it has to be verified by measurements if F' can be considered to be constant and raytraced curves can be used as K_b IAM files within simulation programs directly. For RefleC, this validation is done in section 3.4.3.

Types or shapes of IAM curves: The more complex the geometry of a collector, the more complex are also the changes of its IAM values with varying incidence angle. Figure 2.11 shows K_b-values of the prototype RefleC 6 GF and its receiver flat-plate.
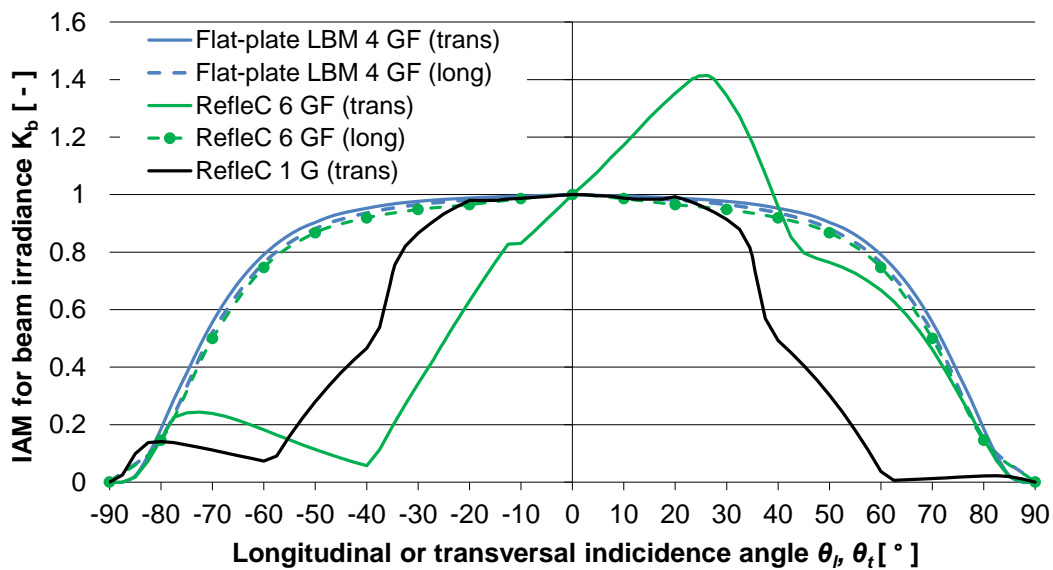
Figure 2.11: Raytraced IAM values of the RefleC prototype R6 GF (no end losses) and its receiver flat-plate compared to the first prototype R1 G. R6 GF has a biaxial-asymmetric IAM, shown for longitudinal and transversal irradiance ($K_b(\theta_l, 0)$ and $K_b(0, \theta_t)$, longitudinal values for endless trough). The flat-plate with glass-foil (GF) cover has a biaxial symmetric IAM, which can be approximated to be rotation-symmetric (cp. Figure 1.3 for a picture of the collectors). At R6 GF, reflected irradiance from $\theta_t = [-10°; +45°]$ can reach the absorber. For $\theta_t > +45°$ irradiance reaches the flat-plate directly. For $\theta_t = [-15°; -40°]$, the reflector shades the flat-plate, while for $\theta_t < -40°$ irradiance reaches the flat-plate via the gap (in reality, this would be ground reflected irradiance). For illustration of these effects, cp. Figure C.3 in Appendix C.

As stated above, the IAM for beam irradiance along the collector's optical axes $K_b(\theta_l, \theta_t)$ or from the polar coordinates $K_b(\theta, \phi)$ (cp. Figure 2.8) has the value 1 for $\theta = 0$. $K_b(\theta = 90°)$ is defined to be 0 since at parallel irradiance the aperture does not receive beam irradiance anymore. Collector data sheets based on standard collector tests only contain IAM values along the two characteristic optical axes of a collector. Thus, for collector energy gain simulations the intermediate values of $K_b(\theta_l, \theta_t)$ have to be interpolated between the existing measured values along $K_b(\theta_l, 0)$ and $K_b(0, \theta_t)$, which causes uncertainties of different extent (cp. section 3.2.2).

The shape of an IAM curve highly depends on the definition of the aperture area (cp. Figure 2.6 and Figure C.3 (b)). This reference area can in principle be chosen freely, but for correct energy output calculations, IAMs and the thermal efficiency curve must relate to the same aperture. In the following, four categories of IAMs are proposed and the motivation for this categorization is explained. As an introduction, the high-resolution raytraced spatial IAM of the first RefleC test sample R1 G is shown in Figure 2.12.
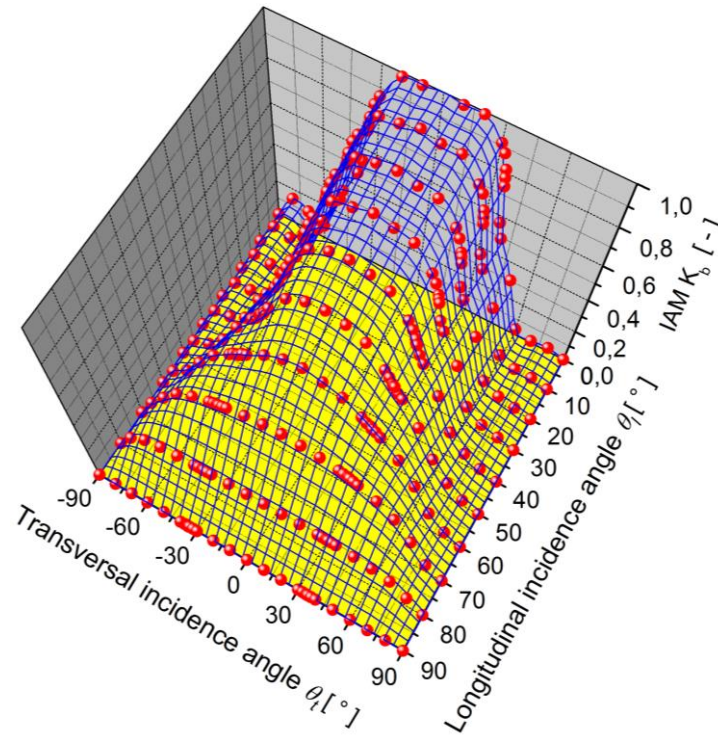
Figure 2.12: Raytraced 3D-IAM of the first test sample RefleC 1 G (no end losses, lower reflector gap 150mm, $\rho = 0.82$, $\sigma = 1°$). Every red dot is a raytraced value for K_b (θ_l, θ_t). R1 G shows a mirror-inverted optical behavior along its longitudinal axis; therefore only positive longitudinal values are displayed (i.e. the IAM for irradiance from half of the collector hemisphere is shown). In the transversal plane, K_b of RefleC 1 is asymmetric because of the lower reflector gap (cp. $K_b(0; \pm80°)$). The raytracing-resolution was increased near the acceptance half-angle $\theta_a = 35°$ of the collector.

For flat-plate collectors because of their geometry the incidence angle dependent optical behavior is approximately **rotation-symmetric** (i.e. approximately independent of ϕ, cp. Figure 2.8). This simplifies the simulation, since only one single curve $K_b(\theta)$ from $[0; +90]$ has to be given. In Figure 2.11, the slight difference between the curves of LBM 4 GF results exclusively from shading of the absorber by the collector frame. The share of shaded absorber surface is smaller at incidence from longitudinal direction, so the values of $K_b(0, \theta_l)$ are slightly higher there.

In contrast, e.g. vacuum tube collectors show a highly incidence angle dependent optical behavior. If this different optical behavior (the IAM) along the two main axes of a collector is mirror-inverted within the 180° of one axis, the IAM of this collector can be called **biaxial-symmetric**. For these biaxial IAMs, two curves, one for θ_t and one for θ_l, both from $[0;+90°]$, are sufficient to describe the optical behavior.

Collectors like RefleC or horizontal evacuated tubes with sloped east-west fin-absorbers show an acceptance behavior which is only mirror-inverted along the longitudinal axis. The two reflectors of RefleC 1 and 2 are not exactly symmetric, because the lower reflector shows a gap. The other RefleC samples only have one reflector. Thus, in contrast to biaxial-symmetric collectors, the transversal IAM has to be displayed for a range from -90° to +90° (cp. Figure 2.11). Within this work, such IAMs will be called **biaxial-asymmetric** IAMs.

When the optical IAM is determined for all combinations of θ [0; 90°] and ϕ [$-180°; +180°$], or θ_t [$-90°; +90°$] and θ_l [$-90°; +90°$] respectively, the optical behaviour of a ST collector is fully and exactly described. Within this work, such information is called **3D-IAM** (three-dimensional Incidence Angle Modifier, cp. Figure 2.12). This term was proposed by Häberle (1999), who raytraced and tested the AoSol CPC-collector (cp. Figure 1.14) for intermediate incidence angles.

2.2.3 Raytracing Procedure and Parameters

In the following sections within this chapter it will be explained how the raytracing simulations to get IAM curves were performed and how the simulated variants were parameterized. To simulate IAM beam values of various collector variants, an Excel-Tool for use in combination with OptiCAD was developed (Figure 2.13).
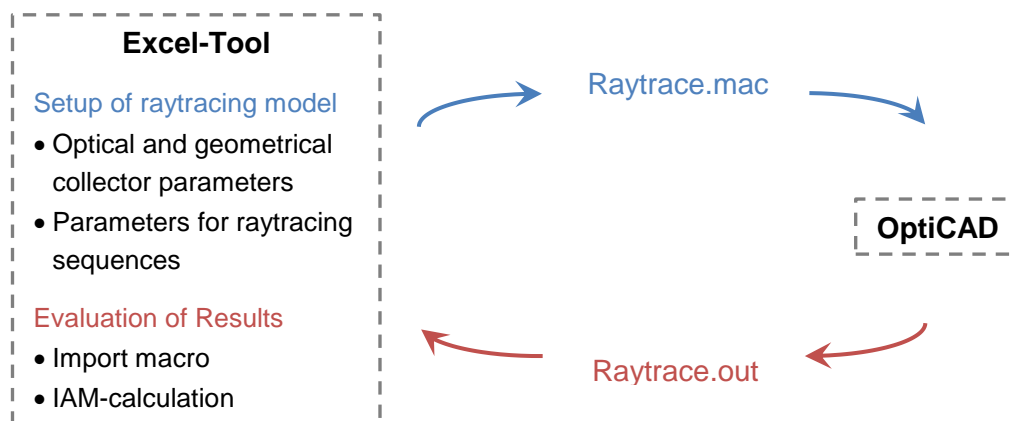

Figure 2.13: Partly automated procedure for IAM simulation with OptiCAD using a self-developed Excel-Tool.

In the input worksheet of the Excel-tool, the optical and geometrical collector parameters are entered and components to be included in the simulation can be chosen (number of transparent collector covers, number and type of reflectors, etc.). Construction data of the reflector are calculated (based on inputs for reflector type, acceptance half-angle and arc length of reflector material) and displayed in another worksheet (e.g. for test sample construction). Parameters for the raytracing itself can be set (type and power of lightsource, lightsource geometry, number of rays, rotation center and angular step with, rotation along longitudinal and transversal axes or 3D-IAM, name of output file, etc.). Another worksheet contains OptiCAD-code, where all potential collector and reflector

types with their parameters and also the specifications on the raytracing itself are included. This worksheet is modified according to the information from the input-sheet, where also the reflector geommetry is calculated. If for example no second transparent cover and no upper reflector are to be simulated, the respective passages of the code are commented out. The modified code is then manually exported as a macro, named e.g. *Raytrace.mac*. This macro then runs in OptiCAD. Results for absorbed energy are stored in one single output text file, e.g. *Raytrace.out*. This file can be imported into the Excel-tool again, where IAM values for the simulated setup are calculated by comparing the energy onto the aperture and that absorbed at all investigated incidence angles. Due to this procedure it was ensured that RefleC parameters, construction data, raytracing-macro, simulation results and calculated IAM values were always consistent and documented in one folder.

The geometrical dimensions of the collector variants were simulated 1:1 in OptiCAD. The lightsource used in the simulation consisted of ideal parallel rays. The ray density of the lightsource was usually $1/mm$ at perpendicular irradiance onto the aperture area. The lightsource was then rotated to simulate different incidence angles on the aperture. The IAM of stationary collectors must not account for cosine-losses[3], so the ray density was increased by $\cos\theta$ already in the input macro. Its absolute power and number of rays was not changed. This way, the IAM for beam irradiance can be calculated directly from the raytracing results by dividing the absorbed power at a certain incidence angle by the absorbed power at perpendicular irradiance. To determine the transversal IAMs of an investigated variant, it was enough to simulate one row of ideal parallel rays as shown in Figure 2.9. For IAM simulations with a longitudinal component (and thus for all 3D-IAM) a rectangular lightsource was used to accurately account for end losses and optical effects that only a part of the rays undergo.

The main reasons for the application of raytracing in this work are:

- <u>Complexity of optical effects</u>
  Scattering by reflectors, various incidence angles onto a receiver after reflection, transmission of scattered rays through multiple covers and the polarization of light are very difficult to determine analytically.
- <u>IAM for pure beam irradiance</u>
  The IAM for pure beam irradiance can be determined, which is not possible by measurements, since in reality always a part of irradiance is diffuse.
- <u>High resolution</u>
  IAM values for a higher number of incidence angles than via measurements can be generated, which improves the accuracy (cp. high resolution 3D-IAM).

---

[3] This effect is a decrease of ray density incident on a receiver surface by $\cos\theta$, cp. Figure 2.5. It must not be included in the IAM, because the measured irradiance G_t already accounts for it.

- Parameter variations

   Automated parameter variations can be performed to investigate a high variety of concentrator and receiver collector concepts in short time.

Optical parameters used: A realistic optical behavior of all collector components in the raytracing was ensured by measuring their characteristic optical parameters. The meaning of these parameters, their determination and the validation of their accurate representation in OptiCAD are reported in the following sections. A summary of the raytracing parameters used based on these measurements is given in Table 2.2.

Table 2.2: Parameters used to model the different RefleC variants (R1 to R6, cp. Appendix A) in OptiCAD. Meaning and determination of the parameters are discussed in the next sections.

	R1	R2	R3	R4	R5	R6
Reflector (anodized aluminium)						
ρ	0.820 (data sheet)				0.866 (measured, cp. Figure 2.15)	
$\rho(\theta)$	constant (measured but not applied, cp. comment on Figure 2.17)					
σ	1° or 0,0175 rad (measured by manufacturer, cp. Figure 2.18)					
Collector glazing (white AR, 4 mm)						
τ	0.948 (measured, cp. Table 2.3)					
$\tau(\theta)$	n = 1.330; K = 5 (adapted to fit measured curve in Figure 2.21)					
ETFE-foil $(25\,\mu m)$						
τ	0.938 (measured for ETFE, cp. Table 2.3) (value of ETFE 50 μm foil was used)					
$\tau(\theta)$	n = 1.409; K = 120 (measured for FEP, cp. Figure 2.21) (curve of FEP 25 μm was used)					
Absorber (selective)						
α	0.950 (data sheet)					
$\alpha(\theta)$	Fit curve in Figure 2.26, cp. Eq. 2.24					

2.3 Material Properties

In the following, material investigations in the course of the RefleC development are reported. The simulations were performed wavelength independent, so all parameters were determined for the AM 1.5 spectrum ASTM E891 of global irradiance. This reference spectrum was replaced by ASTM G173-03 (cp. Figure 2.2), but since only integrated values are used in this work, differences in the spectra should be neglectable.

2.3.1 Reflectors

Requirements: Important criteria for solar reflectors are a high reflectance for solar radiation, low scattering of the reflected radiation, high reflector shape accuracy, and good resistance against environmental impacts. This means low degradation (loss of reflectance over time), UV-resistance, good self-cleaning behavior, and hail resistance.

As described above, aluminum (Alu) CPC reflectors for evacuated tube collectors (cp. Figure 1.12) are widely used for mid-temperature applications. These reflectors are usually made of an anodized metal sheet with a PVD[4]-layer of pure Alu and a transparent protective layer on top to prevent corrosion. The solar reflectance of such commonly used Alu reflectors ranges from 0.82 to 0.90 (new). Silver offers a significantly higher solar reflectance than Alu. Metal-based outdoor reflectors with silver layers are under development, but the problem of corrosion protection has not been solved yet. Polymeric reflector films with silver layers for outdoor use are on the market and show reflectivities of 0.94 to 0.96 (new). But they always need an additional back structure ensuring shape accuracy and mechanical stability.

Reflectance and scattering: Besides the total (hemispherical) reflectance ρ of a reflector, also the spatial distribution of the reflected rays is important for solar concentrators. Ideal and real reflection characteristics are symbolized in Figure 2.14. Real reflectors cause a combination of the idealized cases specular and Lambertian. The higher the quality of a reflector, the higher is the reflected intensity around the specular direction. To assess the optical reflector quality, the hemispherical reflectance can be devided into specular and diffuse reflected fractions (Eq. 2.20).

$$\rho = 1 - \alpha = \rho_{spec} + \rho_{diff} \tag{2.20}$$

The hemispherical reflectance ρ and the diffuse reflectance ρ_{diff} are usually measured with an integrating sphere (*Ulbricht sphere*). Specular reflectance ρ_{spec} and absorptance α of a reflector sample can then be calculated.

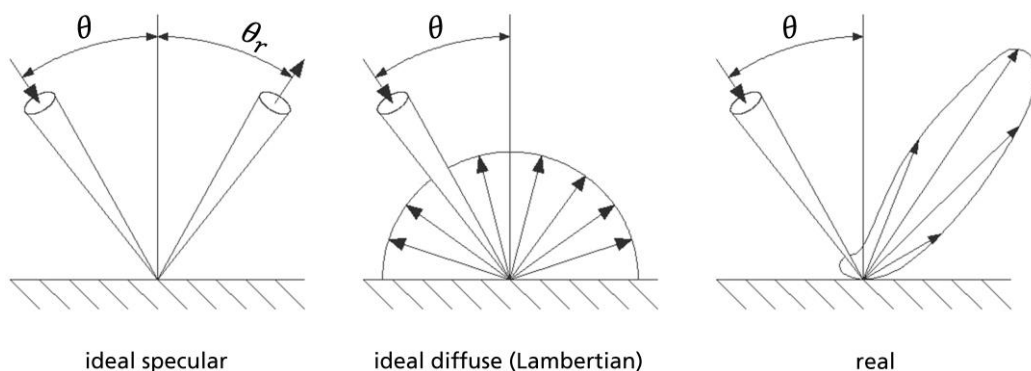ideal specular   ideal diffuse (Lambertian)   real

Figure 2.14: Comparison of surfaces with ideal and real reflectance characteristics for nonparallel sunlight. Redrawn from Duffie and Beckman (2006, p. 179).

---

[4] Physical Vapour Deposition

Figure 2.15 and Figure 2.16 show the results of reflectance measurements of reflector samples investigated for RefleC. The **Silver polymer foil** has not been further used for the project. The **Alu sheet** has been used for the test samples R1 and 2 and the theoretical investigations of R3 and R4. The **Alu composite** material has been used for test sample R5 and the prototype R6 (cp. overview of test samples in Appendix A).
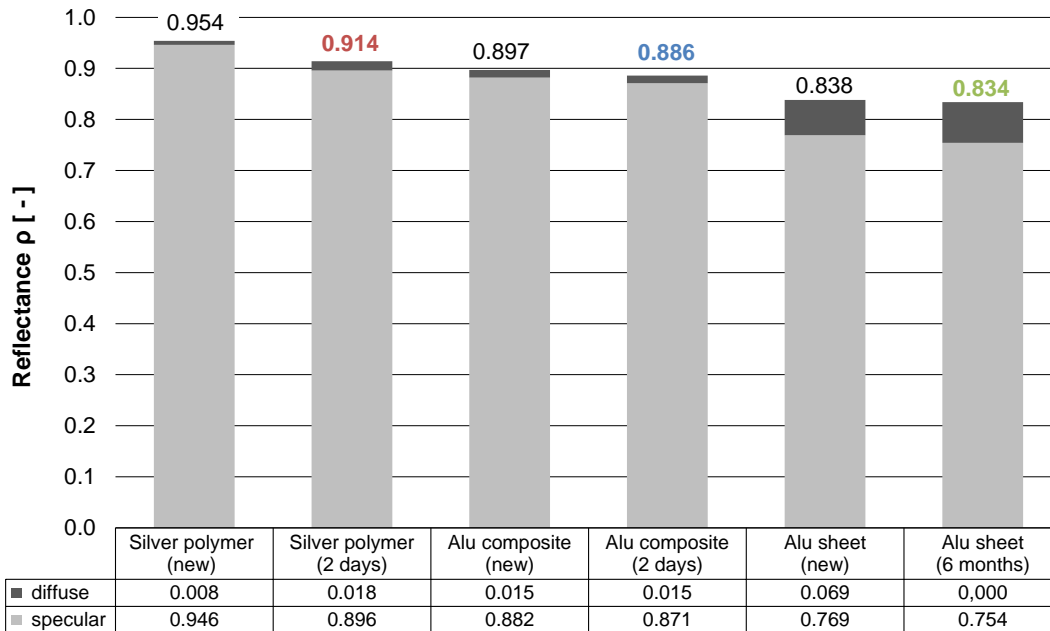
	Silver polymer (new)	Silver polymer (2 days)	Alu composite (new)	Alu composite (2 days)	Alu sheet (new)	Alu sheet (6 months)
■ diffuse	0.008	0.018	0.015	0.015	0.069	0,000
▫ specular	0.946	0.896	0.882	0.871	0.769	0.754

Figure 2.15: Reflectance (hemispherical) of new and exposed (aged) reflector samples. Total hemispherical reflectance above the bars, specular and diffuse fractions below. Aged samples have not been cleaned. Measurements performed according to DIN 5036-3 with an integrating sphere of 22 cm diameter and specular exit aperture of $\pm$ 6.79°. Values determined for AM 1.5, spectrum global ASTM E891.

To measure ρ_{diff}, a small, circular segment was removed from the integrating sphere, so that the rays reflected specular left this exit port without being detected. The diameter of this segment was 5 cm and its center was perpendicular to the direction of ideal specular reflectance. The distance between sample and circular segment was 21 cm. Thus, all rays reflected within this opening solid angle of $\pm$ 6.79° around the direction of ideal specular reflection were considered as reflected specular (assumption of ideal parallel, point light source). Looking at the real reflectance characteristic in Figure 2.14 reveals that this solid angle highly influences the measured fractions.

The silver polymer foil showed a very high and specular reflectance, but ρ decreased significantly after 2 days of sun exposure. Alu composite showed a comparably high and specular reflectance for an Alu reflector. The reflectance was slightly dropping after short exposure, but ρ_{diff} did not increase. The Alu sheet reflector has a lower overall reflectance and a comparably high ρ_{diff}, but did not show any degradation after six months of weathering and light exposure. A similar behavior can be expected for Alu composite, since the reflective surfaces of Alu sheet and Alu composite are very similar.
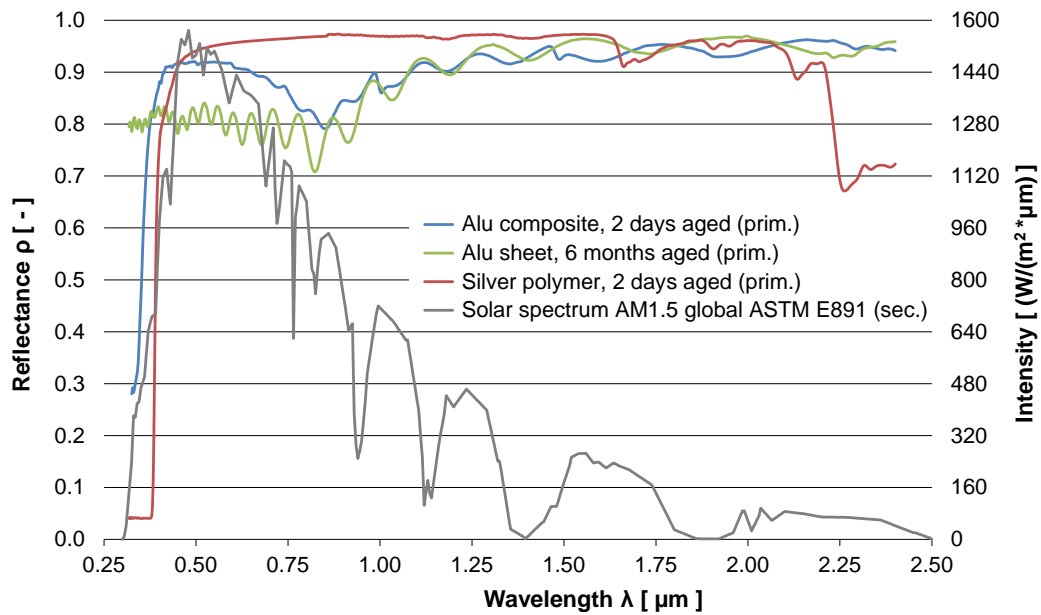
Figure 2.16: Reflectance (hemispherical) of exposed (aged) reflector samples for global solar irradiance. Measurements performed as described for Figure 2.15.

Figure 2.17 shows the variation of ρ for varying incidence angles θ. For small incidence angles, ρ is slightly decreasing; for $\theta > 50°$ the reflectance gets higher than the perpendicular value. This dependency was not implemented in the raytracing simulations; it was assumed that $\rho(\theta) = const$ (as it is common practice in raytracing). Reasons for this decision were the uncertainties of the measured values, expected changes in the angular reflectance characteristic over time (ageing) and uncertainty about the angular reflectance of the other reflector types simulated.

For realistic simulation of reflected radiation, the measured values of ρ_{spec} and ρ_{diff} are not appropriate. On one hand, the share ρ_{spec} can not be assumed to be reflected in the ideal specular direction (cp. integrating sphere measurement explanation above). On the other hand, receivers of low-concentrating collectors can absorb also a large share of diffuse reflected rays, since the absorber covers a wide view angle
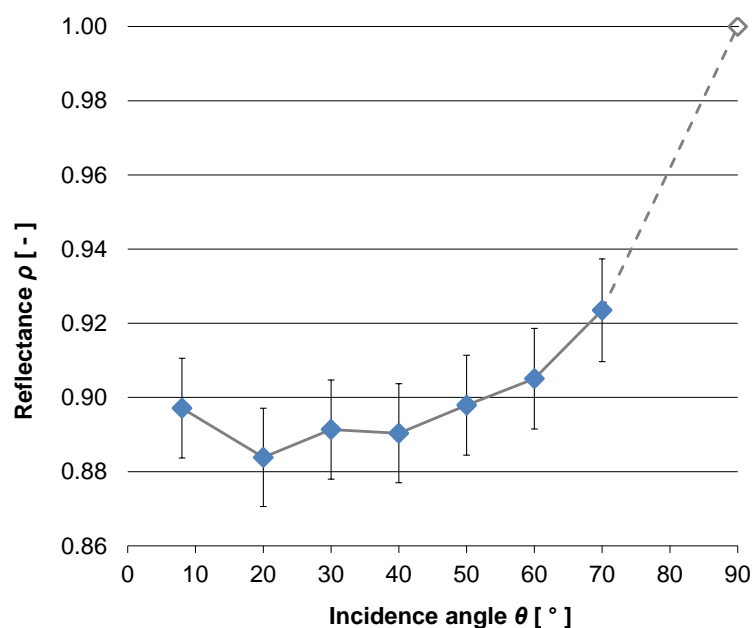
Figure 2.17: Reflectance (hemispherical) of the Alu composite material (new) for varying incidence angles. Measured values (blue) determined for spectrum ASTM G173, uncertainty of ± 1.5 % of the measured value

39

observed from a point on the reflector. To account for the reflector surface properties accurately, the spatial distribution of the reflected intensity had to be measured with a high resolution Goniometer. Figure 2.18 shows such measurement results of the reflector sheet used for the Alu composite material. The spatial distribution of the reflected intensity is determined for three different incidence angles θ onto the reflector (cp. Figure 2.14). The red curves show an approximation of this characteristic by a Gaussian probability density function. The values show that almost the whole reflected intensity is within a solid angle of 4°.
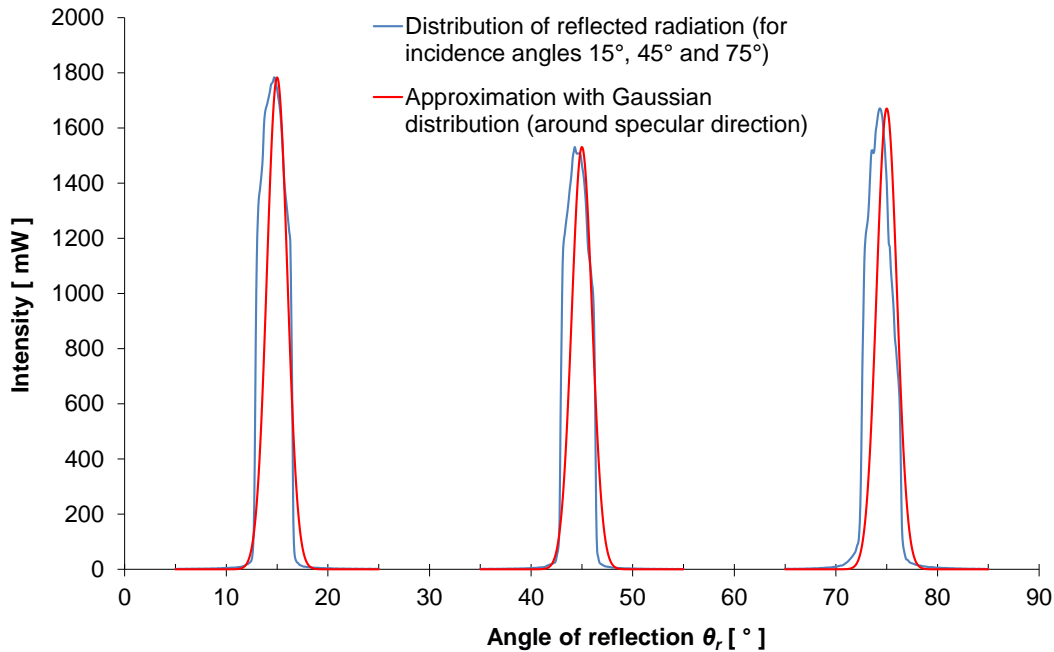
Figure 2.18: Measured distribution of reflected radiation intensities of the reflector used for the **Alu composite** material. One-axis scanning in steps of 0.1°, Goniometer-measurement combined with integrating sphere, measurement plane perpendicular to rolling direction of metal sheet, standard deviation of Gaussian probability distribution $\sigma_{refl} = 1° = 17.45\ mrad$, distribution scaled to maximal reflected intensity. The raw data for the graph were provided by the reflector manufacturer.

Alu sheets are rolled during production, which causes small "grooves" in the reflector surface. Measurements were performed perpendicular to these grooves, where the highest scattering can be expected (Brogren et al. 2004b, p. 511). The scattering width does not increase significantly for higher angles and can therefore be considered to be constant. For higher incidence angles, the angle of reflection tends a bit towards the surface normal of the reflector (cp. curve at $\theta_r = 75°$, i.e. the reflected intensity is not distributed equally around specular direction.

It can be seen from Figure 2.18 that the Gaussian distribution does not perfectly fit the shape of the reflected intensity curves. Nevertheless, it can easily be implemented in OptiCAD, consuming far less computing capacity than implementing real distributions. The main criterion for selecting an appropriate standard deviation of the Gaussian distribution (i.e. for fitting it to the measured values) was, that a similar share of the

reflected radiation is within the solid angle of 4° than for the real reflector. Integrating the measured intensities within 4° (2° radius from maximum) shows, that at $\theta_r = 15°$, about 97,29 % of the reflected energy is within this range. The Gauss curve shows for the selected standard deviation of $\sigma_{refl} = 1°$ per definition 95.45 % of the reflected intensity is within 2 $\sigma_{refl} = 4°$. The drawback of the good representation in this respect is that the intensity distribution within the 4° is more dense than in reality, slightly distorting the shape of the IAM curve around the acceptance half angle. Furthermore, σ_{refl} is expected to increase due to ageing and/or soiling (Brogren et al. 2004b).

Scattering of the reflected rays does not only occur due to microscopic reflector surface errors, which are accounted by σ_{refl}, but additionally due to surface displacement or shape errors σ_{ori}, and due to the non-parallel light reflected (sunshape-distribution σ_{sun}). Assuming a Gaussian distribution of these errors, they can be superpositioned to get the standard deviation for overall ray scattering σ:

$$\sigma = \sqrt{\sigma_{refl}^2 + \sigma_{ori}^2 + \sigma_{sun}^2} \qquad (2.21)$$

The overall scattering parameter σ is highly influenced by the highest of the contributing scattering errors. For the raytracing simulations, surface orientation errors were neglected, because the raytracing values should represent an ideal shaped reflector. The sunshape distribution can only poorly be approximated by a gaussian distribution, but the vast majority of beam irradiance originates from a solid angle within 4.65 mrad (Badescu 2008). A representative standard deviation would then be about a factor 6 smaller than σ_{refl}, almost not influencing σ. Thus, only the microscopic scattering of the reflector was considered and it was simulated with $\sigma = \sigma_{refl} = 1°$. Detailed measurements on optical properties and durability of reflectors for low-concentrating collectors have been reported by Nostell et al. (1998), Brogren et al. (2004b) and Brogren et al. (2004a). Lindseth et al. (1999) and Nilsson et al. (2007) evaluated uncertainties of Al-reflector characterization with integrating spheres.

Hail impact tests: The reflectors of RefleC are quite large. They fulfill a static function and are the most eye catching part of the collector. Thus, ensuring the mechanical stability and resistance against environmental impacts at affordable costs was crucial for the concept. Pre-fabricated and self-fabricated sandwich reflector constructions were tested. Figure 2.19 shows hail resistance test results. All in all, twelve reflector constructions were tested systematically according to the standard (EN 12975-2:2006), method two, with ice balls. The main boundary conditions for the ice ball are a diameter of 25 mm ($-$ 5 %), a mass of 7.53 g ($-$ 5 %), and a velocity of 23 m/s ($\pm$ 5 %).

After a reflector was tested under standard-conditions, the impulse energies of the ice balls were either increased or decreased to assess a constructions potential for further development. Sample 1 showed deep indentations even at low impulses and was there-

fore excluded for RefleC. Different variants of Al-sheets or polymer films bonded or glued to hail-resistant substrates were tested, but hail resistance could only be achieved at high effort. The polymer film used for Sample 2 is hail resistant if applied to a stiff substrate, but for all gluing methods the resulting planarity was unsatisfactory.
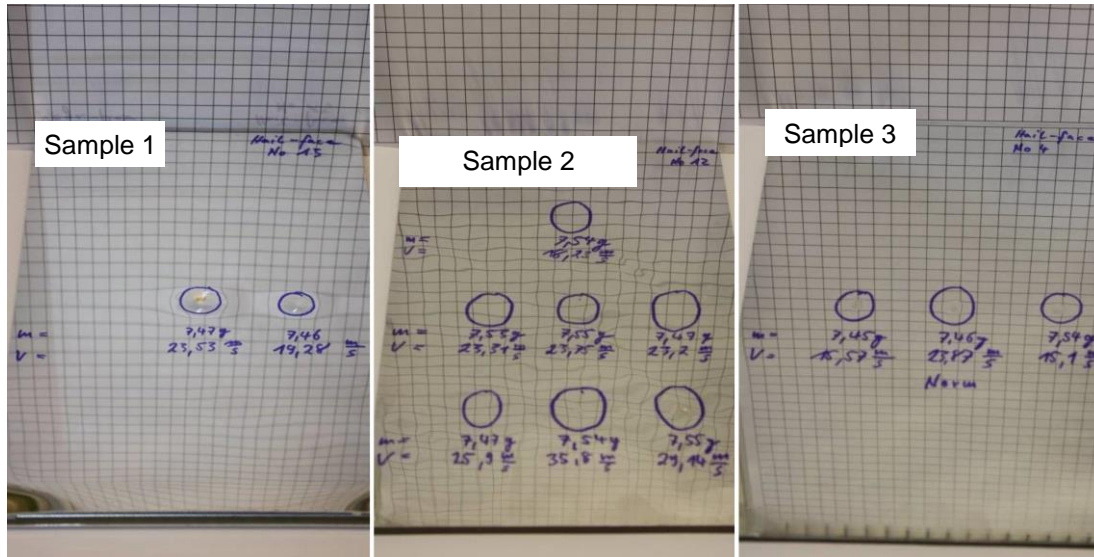

Figure 2.19: Selected reflector samples after hail impact. The measured mass and velocity of every ice ball is noted below the impact point. Sample 1: Full-Alu-sheet sandwich, consisting of two Alu sheets (one reflective) and a trapezoidal bended sheet glued in between (pre-fabricated); Sample 2: Polymer film with reflective silver layer, glued to epoxy paper laminate (self-built); Sample 3: Alu sheet composite with PE core (pre-fabricated). Reflection of a grid by the samples allows assessment of deformations.

Comparing the hail resistance test, reflectivity, durability, and price of the reflector constructions, finally a pre-fabricated Alu sandwich very similar to Sample 3 in Figure 2.19 was used for RefleC. The mechanical stability of Sample 3 was sufficient, but in the hail resistance test it showed small deformations already at comparably low impulses of the hailstones. So, fiber-additives were applied to the polymer-core of the reflector and the modified construction did not show any deformations at standard hail impact test parameters. The reflecting sheet remained the same; its optical characteristics were shown in Figure 2.15, Figure 2.16, Figure 2.17, and Figure 2.18.

2.3.2 Transparent Covers

Requirements: At single glazed collectors with backside insulation, ca. 85 % of the thermal losses occur via the front side (cp. Figure 1.11). A second transparent cover can effectively reduce heat losses, but of course increases the optical losses. This applies to RefleC in particular, since the reflected rays often reach the transparent cover(s) with flat incidence angles. As for the reflector materials, also for the cover materials certain criteria apply. They should have a high transmittance τ for sunlight (low refractive index, low absorptance), sufficient thermal stability, and low thermal expansion. Furthermore, they should show a low degradation over time (loss of transmittance), high UV-resistance, good self-cleaning behavior, and hail resistance (if applied as front cover).

Solar glass and polymer foils: Standard window panes ($\tau \approx 83\,\%$) absorb too much of the solar spectrum because of its iron compounds. For solar collectors, white glass with very low iron content is applied ($\tau \approx 91\,\%$). In high performance collectors, white anti-reflective glass (AR glass) is used (τ up to $96\,\%$). One method to create an AR coating is to etch the glass surface, which locally decreases the refractive index. The durability of such AR-coatings has been proved by long-term tests (Sunarc n.a.). Detailed results of a cover material research and of own tests can be found in Table 2.3.

Table 2.3: Properties of cover materials (mostly from data sheets, exceptions indicated)

Properties	PTFE 50 µm	ETFE 50 µm	FEP 50 µm	PFA 50 µm	White glass 4 mm	White AR glass 4 mm
Optical						
Solar transmittance * [%]	95.3	93.8	95.7	96.0	90.5	94.8
Refractive index [-]	1.38	1.40	1.34	1.35	1.52	1.33
Thermal						
Upper service temperature [°C]						
long term	260	150	205	260	250	
short-term	300	200	250	-	300	
Crystallite melting temperature [°C]	327	270	290	305	> 500	
Lin. expansion coefficient [10^{-5}/K]	12-25	7-10	8-12	10-12	0.8 – 0.9	
Shrinkage [%] ** (30 min., 150°C)	-	M.D. 0 T.D. 5	M.D. 0 T.D. 2	M.D. 1 T.D. 1	-	
Thermal conductivity [W/(m*K)]	0.2				0.8	
Other						
Density [g/cm³]	2.15				2.5	
Tension elastic modulus [MPa]	400-750	800-1100	400-700	600-700	0.07	
Tensile strength [MPa]	20-40	40-50	15-25	20-35	-	
Material degradation [%-points] ***	-	8 – 16	0	-	1 – 2.5	-

* Values determined from transmittance measurement results for global solar radiation spectrum AM 1.5, ASTM E891 (cp. Figure 2.20)

** Shrinkage in Machine Direction (M.D.) and in Transverse Direction (T.D.)

*** Average transmittance reduction (absolute) of measured samples after 20 years outdoor weathering in Davos and Rapperswil (Ruesch and Brunold 2008, p. 26). Samples: 8 low-iron float glasses, 3 ETFE samples of 60 µm, 80 µm and 120 µm and 2 FEP samples of 25 µm and 50 µm. Samples were expositioned below glass panes, but with free air exchange. Cleaning with ethanol before measurements. Sample description in (Frei et al. 1998, page 7).
High uncertainty in degradation assessment for ETFE, since a large share of the transmittance reduction was caused by irremovable, adhering layer of dirt (Ruesch and Brunold 2008, pp. 44-47), which might occur to a lesser extent in real ST collectors due to less contact with ambient air

Polymer foils can show an even higher solar transmittance than solar glass. Compared to other polymers, Fluor polymers are very UV stable, which is precondition for outdoor durability. Temperature stability and thermal expansion can be critical at these materials

and have to be investigated in detail. ETFE foils show the lowest thermal expansion and are comparably cheap. The prices of polymer foils usually correlate with the polymer mass itself, which leads to high price reductions for reduced foil thickness.

Transmittance measurement results for some of the investigated cover materials are shown in Figure 2.20. For white (i.e. low iron content) glass it can be observed that AR coating or etching results in a high transmittance increase at wavelengths where the intensity of solar irradiance is high. Polymeric foils show a high transmittance for the whole solar spectrum, except for very short wavelengths. The transmittance of ETFE is significantly lower than that of the other foils shown.
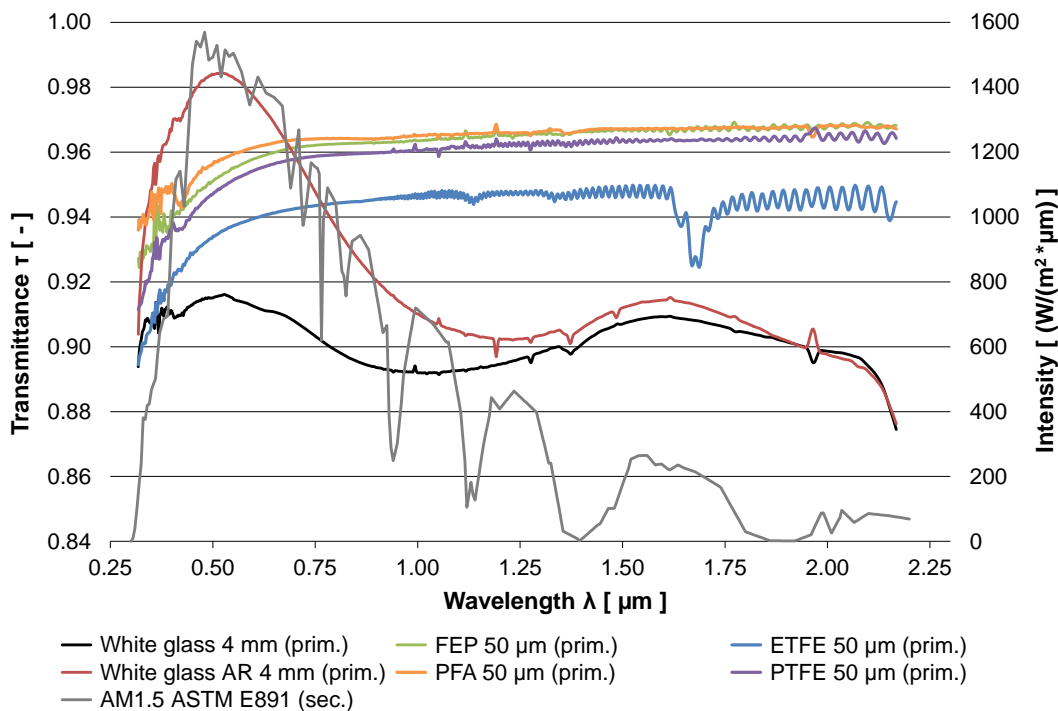
Figure 2.20: Transmittance of transparent cover materials for the wavelengths of global solar irradiance. Measurements performed with an integrating sphere of 22 cm diameter.

At RefleC, the basis for correctly raytraced IAM values was to determine the incident angle dependent solar transmittance of investigated cover materials as accurately as possible. Figure 2.21 shows measurement results for this. Glass-glass and glass-foil covers both identically reduce a collector's convective heat losses. Regarding the radiative heat losses, they behave slightly different (cp. Figure 2.22). As for all optical devices, also for transparent cover materials the equation applies:

$$\tau(\lambda) = 1 - \rho(\lambda) - \alpha(\lambda) \tag{2.22}$$

From the data from Figure 2.22 it can be expected that collectors with a glass-glass cover have slightly lower heat losses than with glass-foil combinations, because the lower glass pane does almost not transmit infrared to the front cover below temperatures of 200 °C. On the other hand, for glass-foil-covers the front glazing reflects a small share of infrared transmitted through the foil backwards towards the absorber.
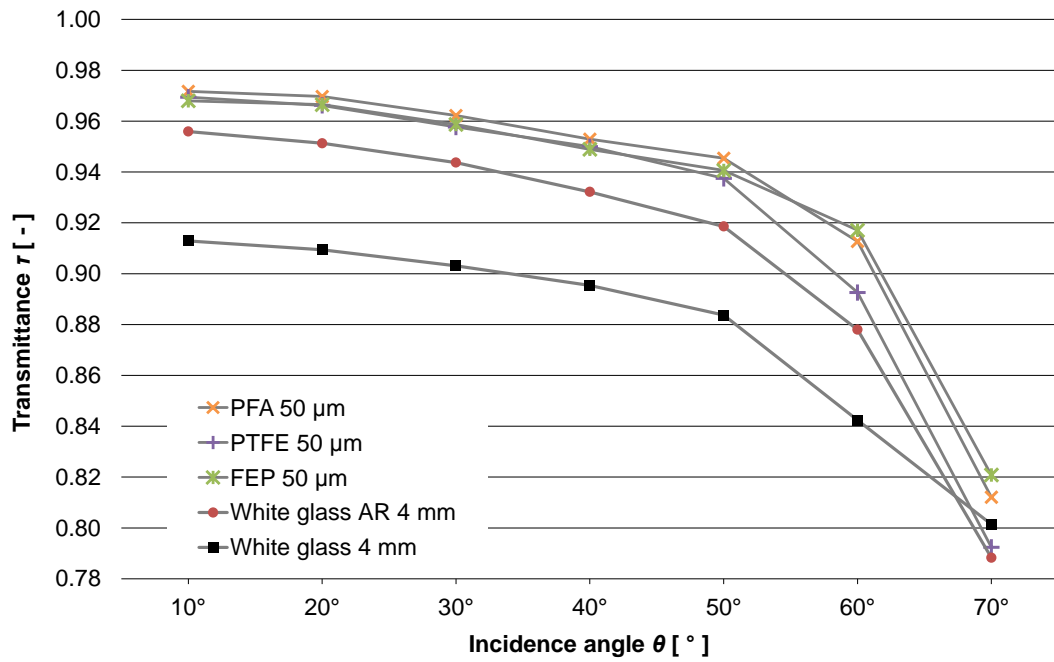
Figure 2.21: Transmittance of transparent cover materials at varying incidence angles. Measurements performed with an integrating sphere of 22 cm diameter. Values determined for AM 1.5, spectrum global ASTM E891.
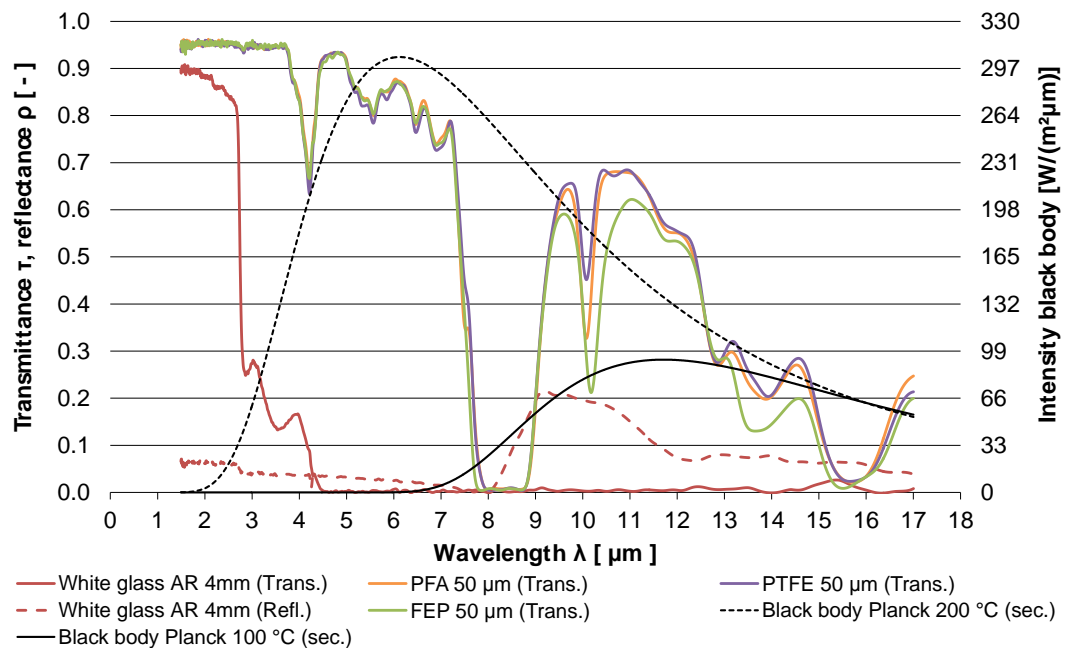
Figure 2.22: Transmittance of transparent cover materials for infrared radiation (Planck black bodies of 100 °C and 200 °C). Measurements performed with an integrating sphere of 22 cm diameter. Polymer foils show significant transmittance for infrared, while glass is almost opaque for these wavelengths (up to 200 °C radiation temperature). Both for glass and polymer covers, the vast majority of the radiant energy not transmitted is being absorbed (not shown). Reflectance of glass for infrared is also indicated.

Modelling in OptiCAD: Important effects to consider for realistic transmittance-simulation of double collector covers are multiple reflections (cp. Figure 2.23) and light polarization.
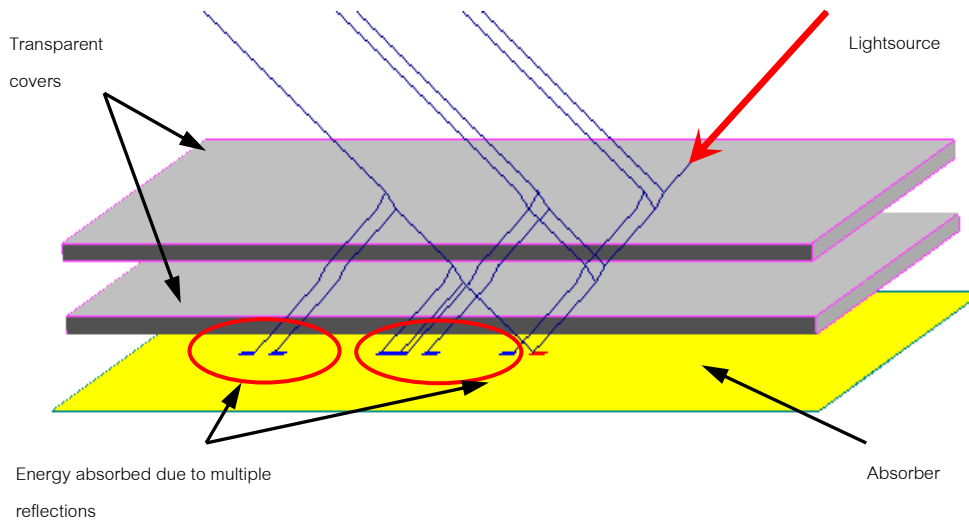
Figure 2.23: Screenshot from OptiCad with setup to validate the simulation of multiple reflections and polarization effects at the collector front. Multiple reflections are visible between the two front covers, absorber, and second cover. The red circles show the resulting additional absorption.

Solar irradiance can be considered to be unpolarized, but depending on the incidence angle, the light gets polarized by the front glass cover, resulting in a modified transmittance through the second cover (Duffie and Beckman 2006, pp. 204-208). So the transmittance of the simulated second cover materials for perpendicular (s) and parallel (p) polarized light had to be measured and modeled accurately (cp. Figure 2.24).
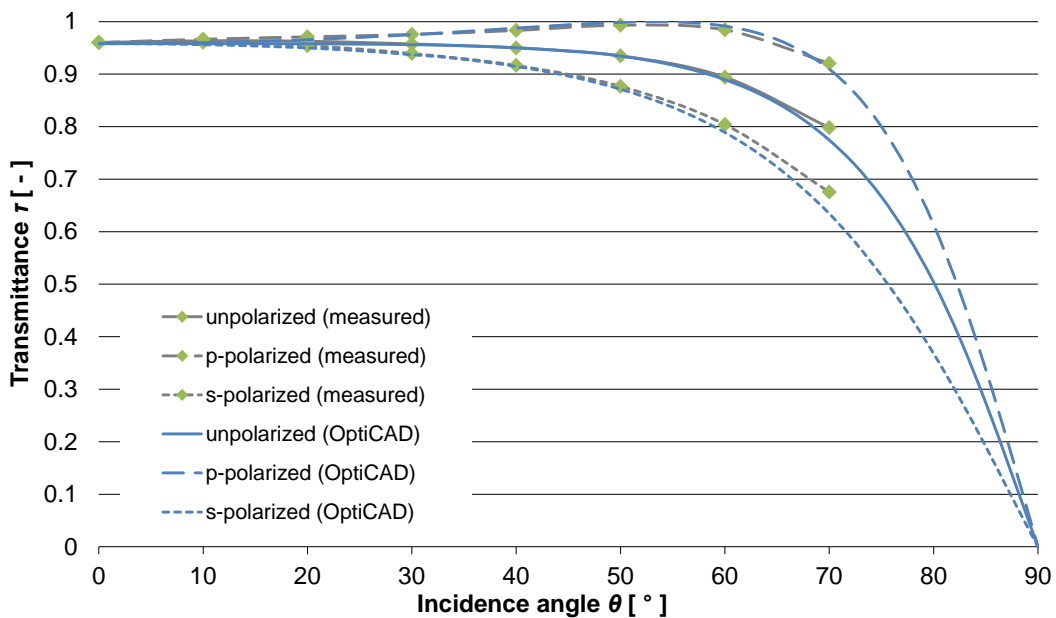
Figure 2.24: Measured transmittance of a 25 μm FEP foil for purely parallel (p) and perpendicular (s) polarized light compared to OptiCAD results, cp. parameters in Table 2.2.

For the comparison in Figure 2.24, the transmittance of a FEP-foil was measured with nonpolarized, s- and p-polarized light. In OptiCAD, a cover material is simulated as a volumetric body (polynet) with specified refractive index and absorption factor (cp. Table 2.2). In the simulation, the material parameters were varied until the simulation

results fitted the measurements. After validating the measured angular transmittance of foil and glass for purely polarized light, double glass-glass and glass-foil covers were simulated to validate partial polarization and multiple reflections for incidence angles up to 87.5°. Multiple reflections between double-covers result in slightly higher transmittance detection as expected from multiplying the $\tau(\theta)$-values of both covers.

2.3.3 Absorber

Absorptance and selectivity: As absorbing material, usually sputtered[5] selective coatings are applied. The selective behavior can be understood by means of Figure 2.25.
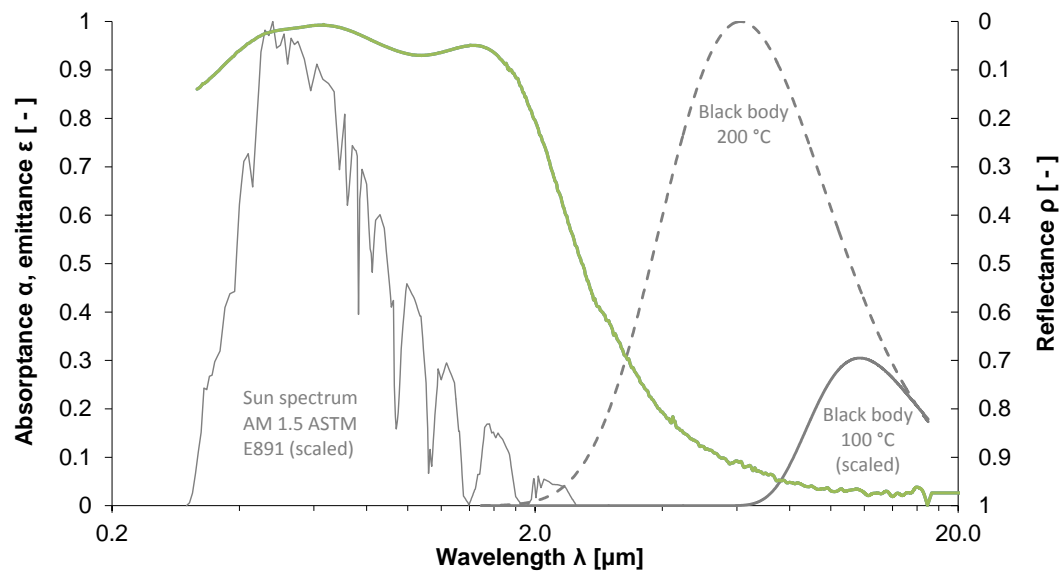
Figure 2.25: Spectral absorptance of a sputtered selective coating as used for the RefleC collector with solar spectrum and emittance of black bodies at $100\,°C$ and $200\,°C$ (wavelength in logarithmic scale). The emittance ε of the absorber surface is temperature-dependent and increases for increasing temperatures, because the wavelengths of infrared radiance decrease.

For a certain wavelength, the absorptance α of every opaque physical material has to equal its emittance ε. All energy not absorbed is reflected. Selective absorbers show a high absorptance for solar irradiance ($\alpha \sim 0.95$) and at the same time also a low emittance of infrared radiation ($\varepsilon \sim 0.05$ at $100\,°C$). This is possible because the optical properties of the coating rapidly change above approx. 2 µm (cp. Figure 2.25).

Modelling in OptiCAD: Wagner & Co. use absorbers from different manufacturers, so small variations in α and ε are possible. The incidence angle dependent behavior of these highly absorbing surfaces is also very difficult to measure. Thus, a curve for $\alpha(\theta)$ was fitted to values calculated by coating experts at Fraunhofer ISE (cp. Figure 2.26).

---

[5] In different evacuated chambers ionised particles are struck out of a cathode by high voltage. The particles are deposited on a metal surface. Selectivity is usually achieved by sputtering three different layers – an IR-reflective, an absorptive, and finally an anti-reflective layer.
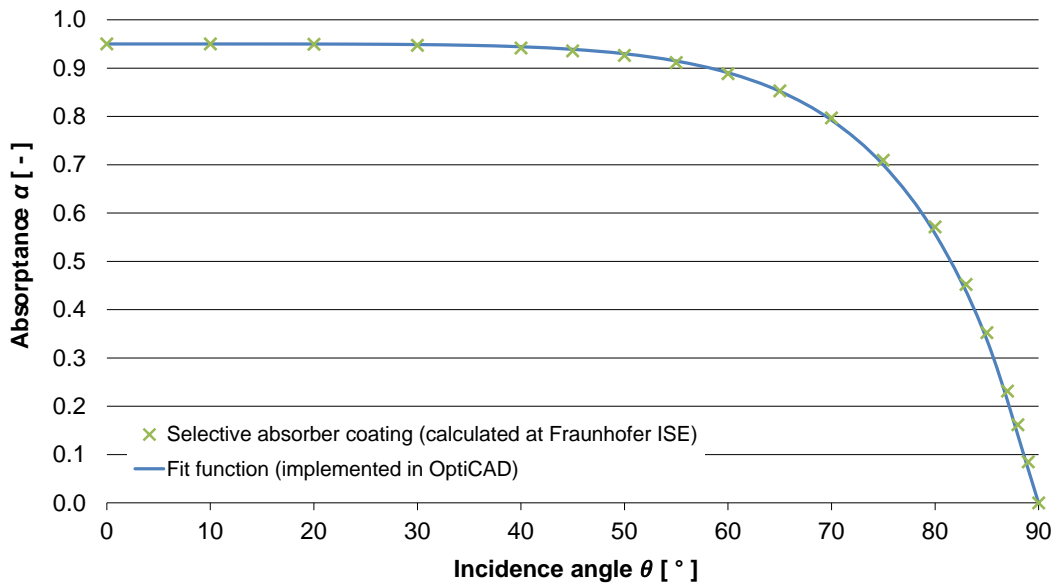
Figure 2.26: Angular absorptance of a selective solar absorber coating as implemented in OptiCAD (cp. reflectance function in Eq. 2.24 and Figure 2.27). The function was fitted to absorptance values for a selective Cermet-coating with gradient of Al and Al_2O_3 with sputtered cover layer of Al_2O_3 and n = 1.5, simulated at Fraunhofer ISE in program *Simulay* for AM 1.5, spectrum global ASTM E891 (Georg 2007). Similar values also for other types of selective coatings can be found in (Tesfamichael and Wäckelgård 2000).

The following function was fitted to the green values in Figure 2.26:

$$\alpha(\theta) = 0.95 - \tan\left(\frac{\theta}{2.0129}\right)^{\frac{1}{0.1975}} \tag{2.23}$$

To simulate the multiple reflections between absorber and transparent cover(s) correctly, a functional film as shown in Figure 2.27 was used.
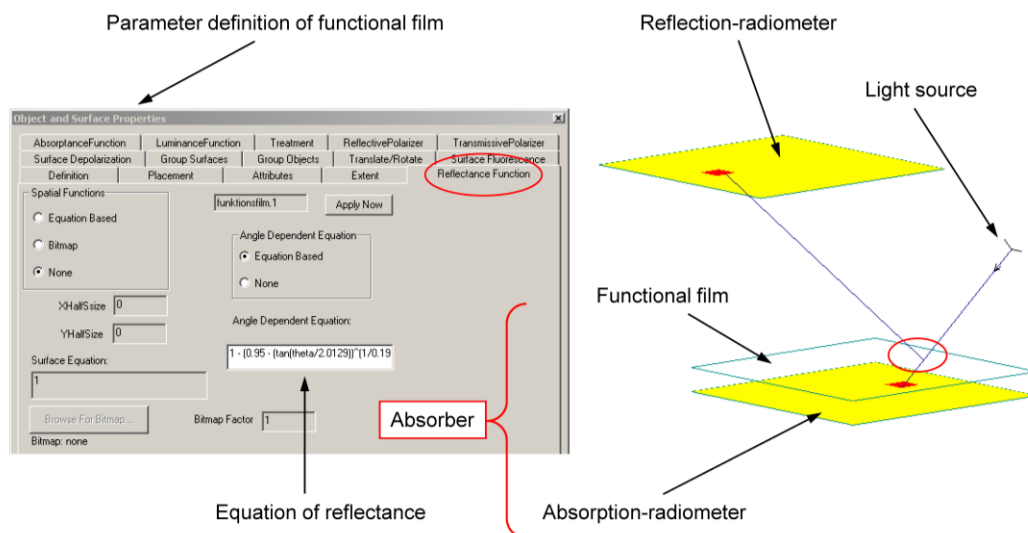
Figure 2.27: Simulation model to validate the correct implementation of angular absorptance in OptiCAD (parameter window of the functional film on the left hand side).

In OptiCAD, so called radiometers have to be applied to be able to count energy at optical surfaces. In the simulation model, the absorber consists of two components. The first

one is a radiometer with $\alpha = 1$ to count the absorbed energy. A semi-transparent functional film is applied $1 \cdot 10^{-3}$ mm above this radiometer. It reflects radiation which shall not be absorbed (cp. Eq. 2.24) and ensures multiple reflections.

$$\rho(\theta) = 1 - \alpha(\theta) = 1 - \left(0.95 - \tan\left(\frac{\theta}{2.0129}\right)^{\frac{1}{0.1975}} \right) \tag{2.24}$$

2.4 Concentrator Design

2.4.1 Concentration of Solar Radiation

Solar irradiance has a relatively low power density, which can be increased by applying solar concentrators. For RefleC, concentrators are applied for the following reasons:

- Reduction of specific heat losses (per aperture area). Thermal losses occur at the smaller absorber area within the receiving flat-plate collector box. Concentration allows higher collector efficiencies and higher working temperatures.
- Lower specific collector costs (per aperture area), if the aperture area gained by the reflectors is cheaper than flat-plate aperture area.
- Better utilization of roof area. A distance between standard collector rows is always necessary to avoid shading. At the final RefleC concept, the lower reflector fills this distance and increases the summer-gains (cp. Figure 1.13).

In the following, the characteristic parameters and principles of solar concentrators are discussed and applied to the RefleC concept.

Concentration Ratio: The principles of the concentration of sunlight are explained based on Figure 2.28. Herein r_S is the radius of the sun and r_{SE} is the median orbital radius of the earth's path around the sun.
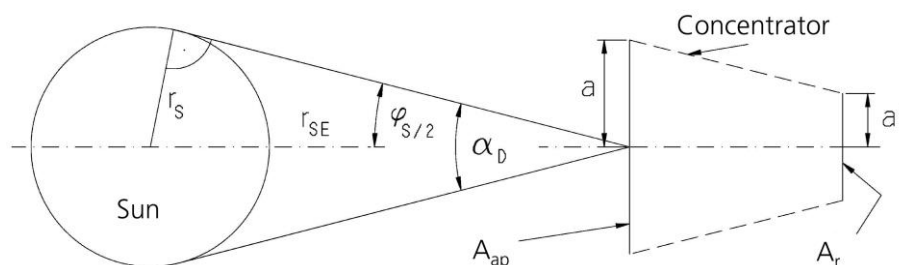
Figure 2.28: Geometric relations between sun and solar concentrator (shape not defined). Adapted from (Rabl 1976a, p. 95).

When viewed from the earth, the solar disk has an opening half angle $\varphi_{S/2} \approx 0.2°$. Since radiation originates from everywhere on the sun's surface, beam irradiance reaches the earth with a divergence angle $\alpha_D \approx 0.53°$ (simplified, cp. section 2.1.2). The inci-

dent light passes the entrance aperture A_{ap} of the concentrator. The concentrator bundles the rays (i.e. it enhances the radiant flux density) until they reach the exit aperture A_r, which is usually the position of the receiver. The flux density can be increased one-dimensional or two-dimensional. In case of imaging (i.e. focusing) concentrators, one-dimensional systems generate a focal line, two-dimensional systems a focal point. The most important parameter of a concentrator is its concentration ratio C_{geo}. It is usually expressed as ratio of areas (Eq. 2.25), but indexing is helpful since also the ratio of intensities is important (Eq. 2.26).

$$C_{geo} = \frac{A_{ap}}{A_r} = \frac{a}{a'} \qquad (2.25)$$

$$C_{rad} = \frac{I_{ap}}{I_r} \qquad (2.26)$$

The geometric concentration ratio C_{geo} is not influenced by the material properties of the reflector. For one-dimensional, symmetric concentrators it is the ratio of the aperture half-widths a and a' of entrance and exit aperture. The radiation concentration ratio C_{rad} additionally accounts for the optical losses of the reflector. It is the ratio of the radiant fluxes I at the entrance and exit apertures of the concentrator.

Ideal parallel light could be concentrated endlessly. Due to the divergent sunlight (cp. Figure 2.28), the maximal geometric concentration for ideal one-dimensional concentrators is $C_{geo} \approx 212$, for ideal two-dimensional concentrators $C_{geo} \approx 45,030$ (Welford and Winston 1978). Spirkl et al. (1998) give equations to optimize concentration ratio and annual collection efficiency of different stationary ST collectors with concentrators.

Acceptance half-angle: A characteristic and very important parameter of every concentrator is its acceptance half-angle θ_a. This angle is explained in Figure 2.29.
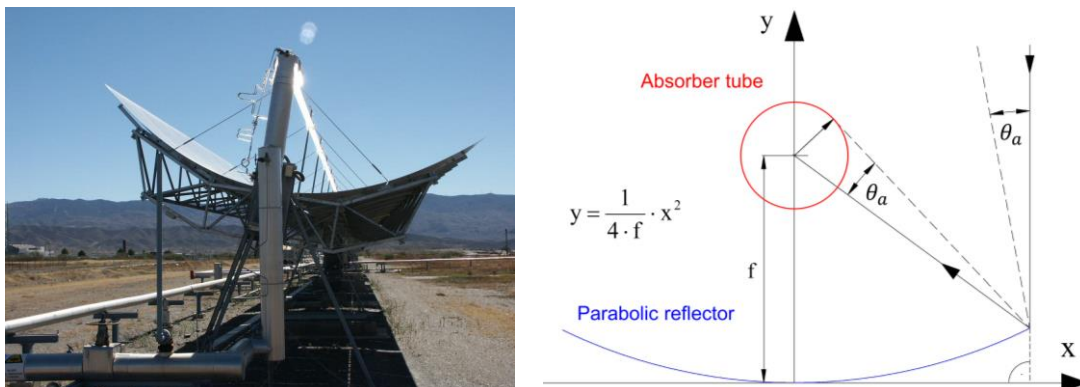

Figure 2.29: Illustration of the acceptance half-angle θ_a. Left: parabolic trough collector at the Plataforma Solar de Alméria (Quaschning 2007). Right: cross-section of a parabolic trough, adapted from Rabl (1976a). If the trough would have an ideal specular reflector (cp. Figure 2.14), all incident rays within $\pm\,\theta_a$ would hit the absorber; they would be *accepted*. All rays with $\theta > \pm\,\theta_a$ miss the absorber.

The angle θ_a defines the maximum deviation of the solar incidence angle θ from the surface normal of the aperture until that all irradiance is directed to the exit aperture of a concentrator. For one-dimensional concentrators (like parabolic trough and RefleC), the term acceptance half-angle always refers to the transversal direction.

The trough of Figure 2.29 is focusing, that means that the transversal angle between the axis of the parabola and the centre of the sun is zero for ideal tracking. A perfect parabolic trough could be built in a way that the radius r of the absorber tube would be barely wide enough to absorb all irradiance arriving from the divergence angle of the sun α_D. In this case θ_a would equal the opening half-angle of the sun $\varphi_{S/2}$. In reality, parabolic troughs must have larger acceptance half-angles to account for sunshape, parabolic shape accuracy, scattering, positioning errors of the absorber tube, and tracking errors. This increases θ_a but decreases C_{geo}, which results in increased thermal losses.

2.4.2 Compound Parabolic Concentrator

The RefleC collector is a stationary concentrating collector not tracking the sun. Thus, its concentrator must be shaped in a way that it offers a sufficient concentration ratio C_{rad} and acceptance half-angle θ_a at the same time. Therefore, it must be of the non-focusing type, i.e. non-imaging concentrators must be used.

The early publications on non-imaging optics originate from the 1970s, cp. (Winston 1974), (Rabl 1976b), (Rabl 1976a), (Welford and Winston 1978), and (Rabl et al. 1980). Rabl (1985) extensively discusses non-imaging concentrators for ST applications. Winston et al. (2005) and Chaves (2008) report the current state of the art.

An ideal concentrator offers the highest possible C_{geo} for a given θ_a. It can be demonstrated that for an ideal, one-dimensional operating concentrator, C_{geo} and θ_a are linked by the following equation (Welford and Winston 1978):

$$C_{geo} = \frac{A_{ap}}{A_r} = \frac{a}{a'} = \frac{1}{\sin \theta_a} \tag{2.27}$$

Only some concentrator types are ideal, e.g. the full compound parabolic concentrator (CPC) (cp. Figure 2.30). Parabolic troughs are no ideal concentrators. The CPC was developed 1966 in the USA by Hinterberger and Winston (Winston 1974) and in parallel in the USSR by Baranov and Melnikov (Duffie and Beckman 2006, p. 340).

The construction principle of a CPC for flat receivers is shown in Figure 2.30. The surface normal of the flat receiver is the center line of the CPC. The two curved parabolic segments belong to two different, but identically shaped parabolas. The opening width of the parabolas is exclusively determined by their focal length f. Parallel rays reaching the aperture from incidence angles $\pm \theta_t < \theta_a$ are all transferred to the receiver (cp. Figure 2.31).
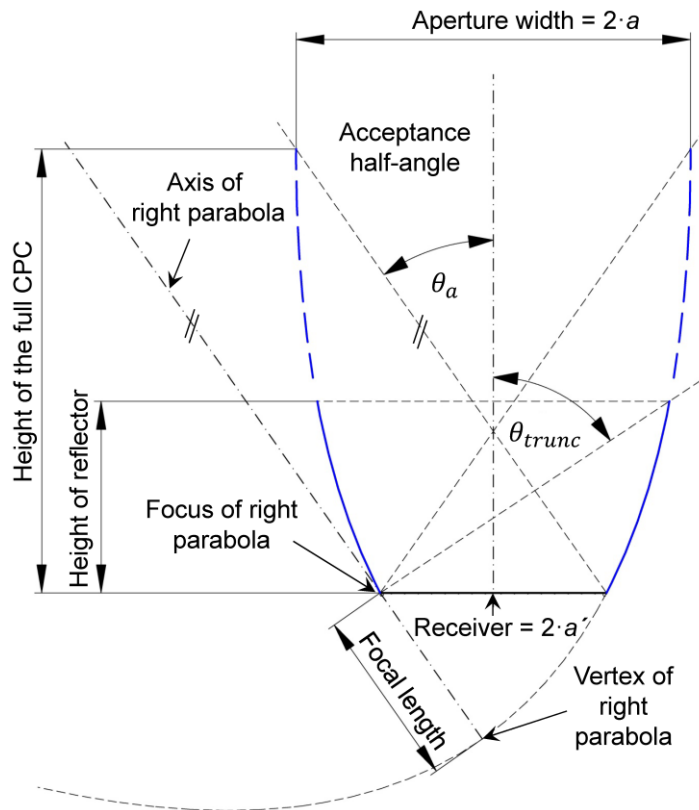
Figure 2.30: Schematic drawing of a symmetric CPC with $\theta_a = 35°$. The continuous blue line is the reflector after truncation. The reflector of a full CPC would extend to the upper end of the dashed blue line. Adapted from (Duffie and Beckman 2006 p. 341).

The relation between f, θ_a and a' is (Duffie and Beckman 2006, p. 344):

$$f = a' \cdot (1 + \sin \theta_a) \tag{2.28}$$

The placement of the parabolas is defined by meeting three conditions:

- Their focal points are the endpoints of the receiver.
- Their centre lines are sloped by θ_a (in this case 35°) towards the receiver.
- The parabolas intersect the endpoints of the receiver.

The left parabola is a mirror image of the right one. The reflector height of an ideal (full) CPC is reached when the tangents of the parabolic branches are parallel to the center axis of the CPC, so that the aperture width cannot increase further. In practice a CPC is usually truncated (cp. truncation angle θ_{trunc} in Figure 2.30), so that the reflector height is usually not as large as for a full-CPC. Drawback of a truncation is a reduced C_{geo} for the same θ_a, so the conditions of an ideal concentrator are not met anymore. On the other hand the upper part of the full-CPC reflector contributes much less to C_{geo} than the lower part and an application of a full-CPC would result in extreme reflector-heights and costs.

To illustrate the radiation acceptance behavior of the CPC in Figure 2.30, Figure 2.31 shows simplified raytracing. A schematic acceptance curve is given in Figure 2.32.

a) Direct normal irradiance

b) Irradiance at $\theta_t = 25°$

c) Irradiance at $\theta_t = 35°$

d) Irradiance at $\theta_t = 45°$
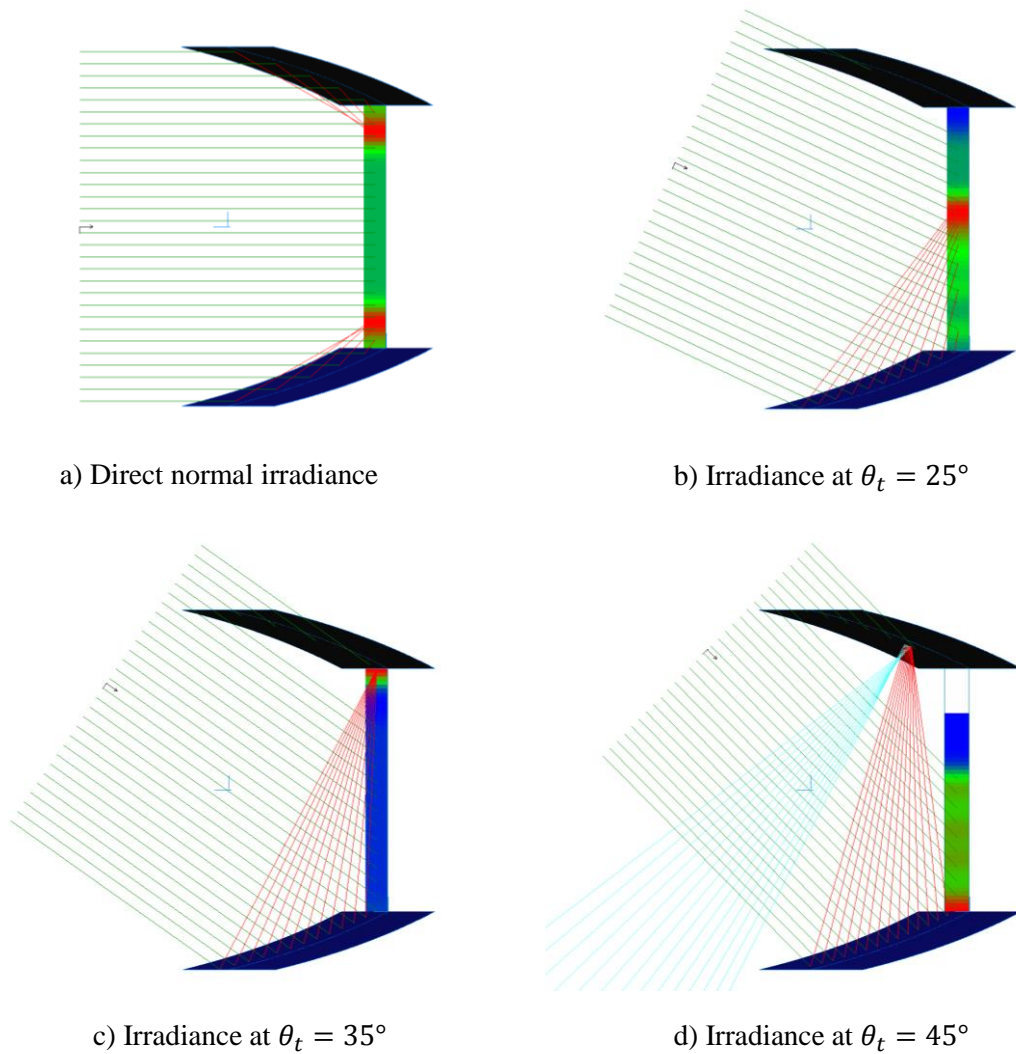
Figure 2.31: Raytracing analysis of the truncated CPC in Figure 2.30. The acceptance half-angle is $\theta_a = 35°$ and the reflector arc length[6] is 1145 mm (Hess 2007, p. 46).
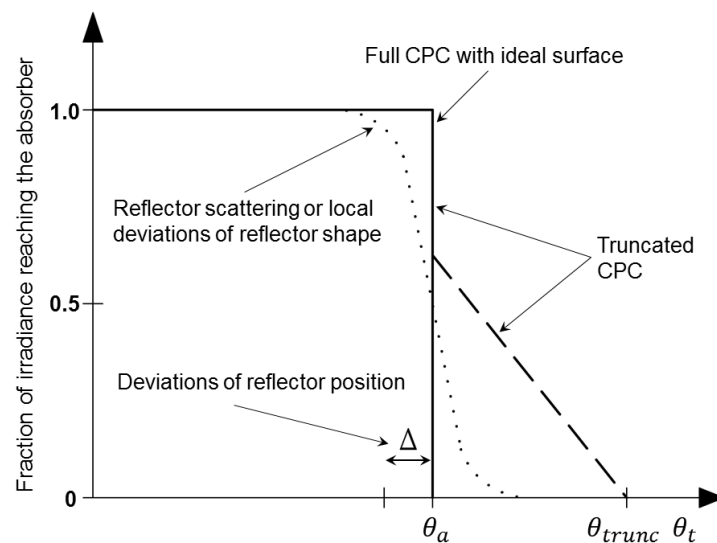

Figure 2.32: Acceptance function of a CPC for characteristic transversal incidence angles θ_t onto the aperture, cp. Figure 2.30 and Figure 2.31. Based on (Rabl 1976a, p. 99).

---

[6] line integral from the lower until the upper end of the curved reflector (parabolic segment)

At a full CPC, no rays can pass the concentrator after θ_a is exceeded. When the CPC is truncated, due to the lower C_{geo} less irradiance reaches the aperture, but a part of the rays can directly reach the receiver between θ_a and θ_{trunc} (cp. Figure 2.31(d)). The result of diffuse reflector scattering is symbolized by the dotted cumulative curve (indicated for a full CPC). For $\theta_t = \theta_a$, full and truncated ideal CPC reflectors would focus all irradiance to the edge of the receiver (cp. Figure 2.31 (c)). Reflector displacements result in a reduction of the acceptance half-angle θ_a, symbolized by Δ.

The important interrelation between θ_a and C_{geo} can be understood from Figure 2.30 and is reflected by Eq. 2.27 and Eq. 2.28. For a constant receiver width and reflector length, an increase of C_{geo} is only possible when θ_a is decreased and vice versa. When θ_a shall be enlarged, the focal length increases. To still meet the positioning conditions above, the right parabola has to be sloped to the left, and C_{geo} decreases.

2.4.3 Annual Acceptance of Irradiance

For a first estimation of a reasonable θ_a for high annual energy collection, the incidence angles of beam irradiance have to be considered. Figure 2.33 shows the virtual path of the sun on the sky dome for Würzburg, Germany.
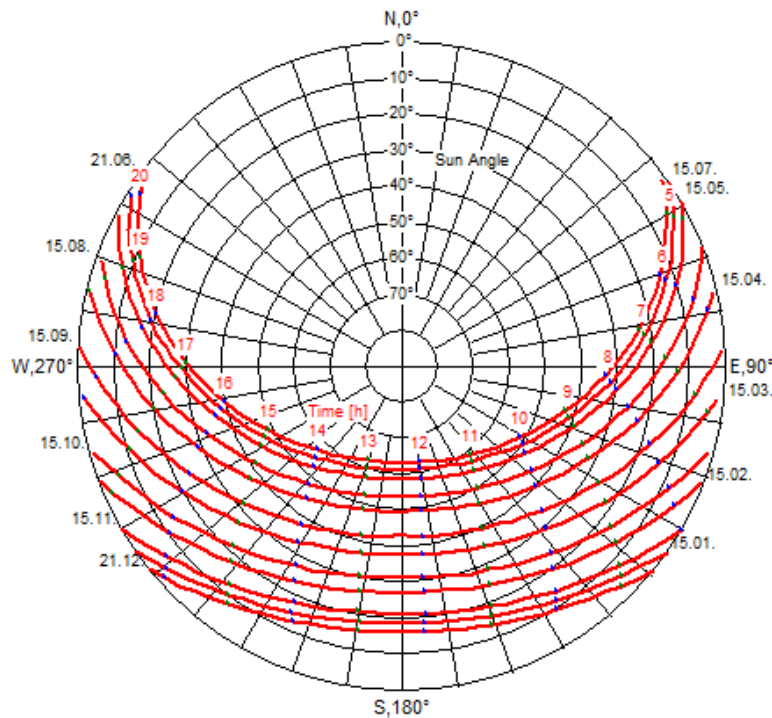
Figure 2.33: Ecliptic of the sun on the sky dome for the twelve months of a year in Würzburg, Germany (latitude 49.48° N, longitude 9.56° E). The maximum solar altitude of 63.65° (corresponding to minimal zenith angle $\theta_s = 26.35°$) is observed on summer solstice (21.06.) at solar noon (12:22 pm UTC+1, sun at south position). Here, the sun is above the horizon from sunrise in the north-east (4:12 a.m. UTC+1) to sunset in the north west (ca. 8:32 p.m. UTC+1). The coordinated universal time UTC is the standard time, Würzburg is located in the time zone UTC+1 (central European time; for Germany in winter legal time UTC+1, in summer legal time UTC+2). Contrary to UTC, Local Solar Time is defined as 12:00 at solar noon, i.e. for highest sun position.

Since the radiation acceptance of a CPC trough is determined by its acceptance in transversal direction, it is helpful to project the sun positions shown in Figure 2.33 into the north-south-plane as shown in Figure 2.34.

If a stationary, south orientated CPC collector is sloped by the local latitude, θ_t varies at solar noon by about $\pm\ 23.5°$ in the course of the year (extremes at summer and winter solstice). As a rule of thumb, Rabl (1985) suggests an acceptance half-angle $\theta_a = 35°$ for maximal annual solar gains. A full CPC of $\theta_c = 35°$ would have $C_{geo} = 1.74$ and would at summer and winter solstice be able to concentrate beam irradiance onto the absorber between ca. 08:30 a.m. and ca. 3:30 p.m., i.e. for ca. 7 hours. For all other times of the year, this time is considerably longer.
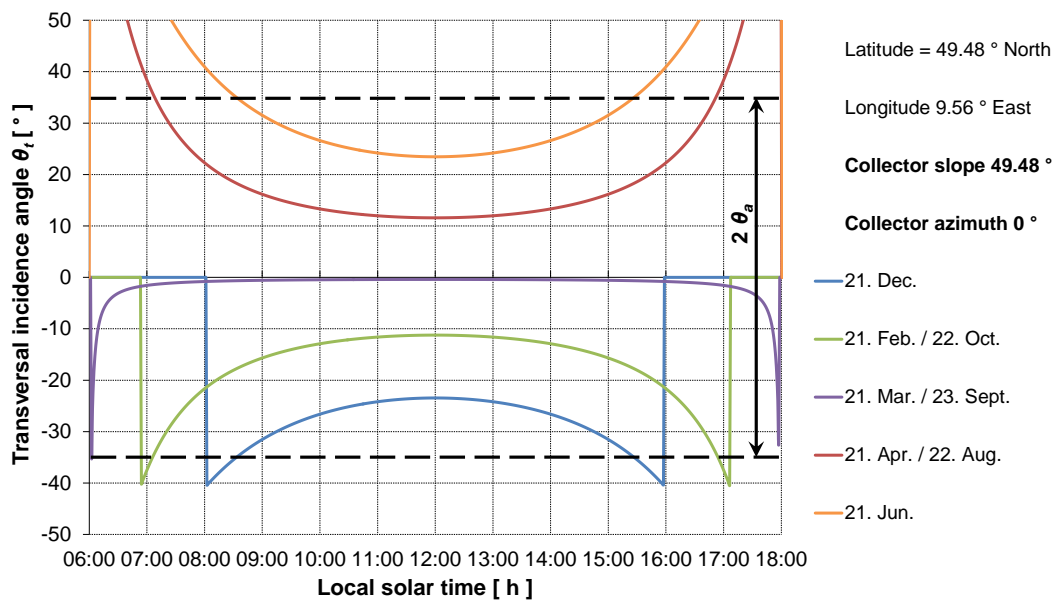
Figure 2.34: Sun positions projected into the north-south plane of a south facing aperture sloped by $\beta = 49.48°$ in Würzburg, Germany (latitude 49.48° N, longitude 9.56° E) for summer and winter solstice, equinox and four days in between, calculated based on (Duffie and Beckman 2006, pp. 9-20.). A full CPC of $\theta_a = 35°$ is able to concentrate irradiance whenever θ_t is between the two dashed lines, i.e. within its acceptance angle $2\ \theta_a$.

For $\theta_a = 35°$, an ideal full CPC as shown in Figure 2.30 would have had a reflector arc length of 3.26 m. The supplier produced a reflector coil width of 1165 mm at this time, and 20 mm of the reflector were bent to make it stiffer. Thus, the first RefleC test sample had a reflector arc length of 1145 mm (cp. full blue line in Figure 2.30). Also lower wind loads and the possibility of direct irradiance collection from $\theta_t > \theta_a$ (cp. Figure 2.31(d) and Figure 3.8) are strong arguments for a truncated CPC.

All the considerations above show that the optimum combination of θ_a, C_{geo}, truncation angle and heat losses of the flat-plate receiver collector can only be determined iteratively. In the RefleC project, a combination of raytracing, thermal efficiency tests and annual energy output simulations was performed for the different collector variants.

2.4.4 Flat Reflectors (V-Trough) Compared to a CPC

There were three main reasons for an investigation of flat reflectors for RefleC:

- They are cheaper, since they can be constructed and positioned more simply.
- They do not cause as flat incidence angles onto the receiver as CPCs, so the optical losses, especially for irradiance close to θ_a, are lower (cp. Figure 2.36).
- The absorber is irradiated more homogenously, because the rays are reflected parallel. Thermal losses due to a poor heat removal (cp. Eq. 3.5) because of high local concentrations on the absorber can be avoided.

Figure 2.35 shows a V-trough with its characteristic angles, which can be derived by the *Edge-Ray Principle*. The V-Trough shows an opening half angle of ψ, which is in Figure 2.35 determined by start and endpoints of the truncated CPC. Ray S_1 with $\theta_t = \theta_{a,V}$ reaches the receiver edge after reflection, so this is the acceptance half-angle $\theta_{a,V}$ of the V-trough. As for the truncated CPC, S_2 from direction $\theta_t = \theta_{trunc}$ is the last ray that reaches the receiver.

Figure 2.36 reveals the very small reflector shape deviation between CPC and V-trough, but also makes a big difference in their angular acceptance behavior visible. The CPC with $\theta_a = 35°$ directs all rays up to $\theta_t = 35°$ to its absorber; for $\theta_t > \theta_a$ all reflected rays are rejected (cp. Figure 2.31). The V-trough is constructed with the same reflector start- and endpoints as the CPC (i.e. same C_{geo}). When θ_t exceeds its acceptance half-angle $\theta_{a,V}$, the rays reflected by the upper end of the reflectors miss the receiver, while the rays reflected from lower parts still reach it. Thus, the acceptance of a V-trough is linear decreasing for increasing incidence angles $\theta_t > \theta_{a,V}$. This is a very important difference to the CPC, where the acceptance of reflected rays stops abruptly at θ_a.
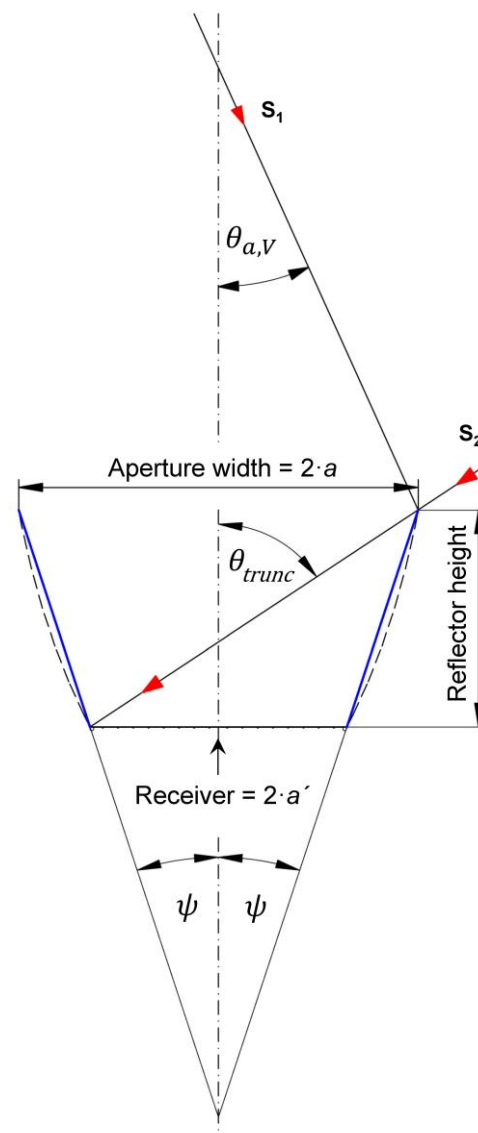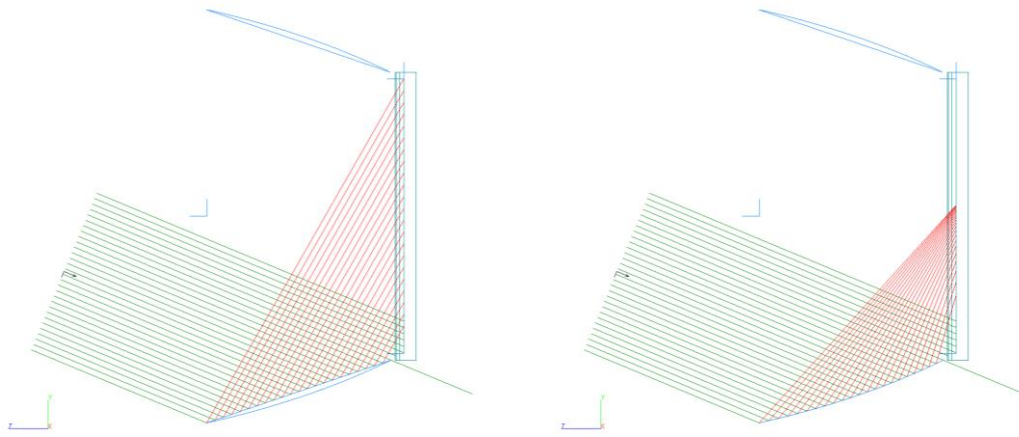

Figure 2.35: Parameters of a V-trough with edge rays S_1 and S_2 and with CPC-shape indicated for comparison. Adapted from (Rabl 1976a, p. 107)

(a) Reflections of a flat reflector (V-trough)   (b) Reflections of a parabolic segment (CPC)

Figure 2.36: Radiation acceptance comparison between a truncated CPC and a V-trough. The acceptance half-angle of the CPC is $\theta_a = 35°$, of the V-trough it is $\theta_{a,V} = 22.62°$ (resulting from constructing the V-Trough between the edge points of the truncated CPC). The pictures are screenshots from OptiCAD at $\theta_t = 22.62°$ for ideal reflectors and without consideration of optical effects of the flat-plate (Hess 2007, p. 73).

The raytracing simulation setup shown in Figure 2.36 was used to compare the absorbed energy of the receiver flat-plate collector LBM 67 AR of RefleC 1 for both reflector variants (Figure 2.37).
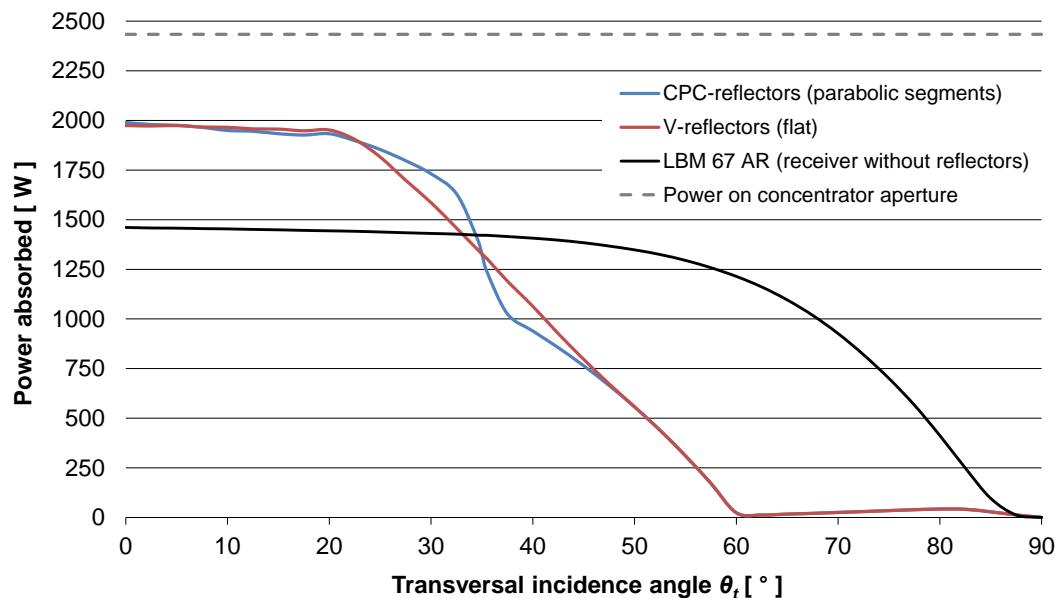
Figure 2.37: Comparison of absorbed irradiance of a single-covered flat-plate, a truncated CPC (RefleC 1) and a V-trough. For acceptance-angles, cp. caption of Figure 2.36. Parameters: $\rho = 0.82$, $\sigma = 1°$, power of lightsource 2434 W per concentrator aperture (constant at all incidence angles), ray density at perpendicular irradiance 1/mm, width of lightsource 50 concentrator apertures, reduced by $\cos \theta_t$ to maintain constant power (dashed grey line). Above $\theta_t \approx 45°$, the blue curve is identical to the red.

The parabolic reflectors were constructed in such a way, that the absorber of the receiving flat-plate is also the receiver of the CPC, so the foci of the CPC are located at the

edges of the absorber. Because of the flat-plate collector casing, the reflectors physically start at the point where a plane, coincident with the side surfaces of the flat-plate casing, intersects the theoretical contour of the CPC. Thus, a small gap between flat-plate and CPC remained (cp. Figure 2.36). From this starting point, the reflectors were extended until they reached an arc length of 1145 mm. This resulted in a truncation angle of θ_{trunc} = 60.19° (same for V-trough and CPC) and an opening half-angle of the V-trough of ψ = 18.79°. The resulting aperture width is 2434 mm (absorber width of LBM 67 is 1618 mm). Since the V-Trough is adapted to the start and end points of the CPC, its flat reflectors show a slightly reduced length of 1142 mm.

The raytracing results in Figure 2.37 allow for assessment of the increase in absorbed power due to the reflectors. IAM curves would have the same shape, but start at 1, since K_b = 1 for θ_t = 0°. The flat-plate shows a typical IAM curve caused by its optical losses $(\tau\alpha)_{eff}$ (cp. $\tau(\theta)$ in Figure 2.21 and $\alpha(\theta)$ Figure 2.26). It reaches zero before θ_t = 90° because of geometrical effects (distance between absorber and glass pane). For the CPC, close to θ_a the effects of reflector scattering are clearly visible (s-shape instead of vertical line, cp. Figure 2.32). Furthermore, the decrease in absorbed energy starts well before θ_a, which is caused by the low IAM (i.e. high reflection losses) of the receiver flat-plate at flat incidence of reflected radiation (Figure 2.31c). This effect is significantly lower for the V-trough, which shows the expected linear drop in absorbed power between $\theta_{a,V}$ and θ_{trunc}. Above θ_{trunc}, the flat-plate is shaded by the reflectors. The very small amount of absorbed power (maximum around θ_t = 80°) in the simulations with reflectors originates from irradiance reaching the absorber via the gaps between flat-plate casing and start of the reflector.

Two important conclusions can be drawn from this section:

- When <u>used as external reflectors for ST collectors, the optical advantages of CPCs compared to V-troughs are smaller</u> than expected.

For the example of RefleC 1, a CPC still shows significant advantages. But because of the receiver flat-plate's increased optical losses at flat incidence angles, these advantages are smaller than expected from comparing the angular acceptance functions of the two concentrator types (cp. (Rabl 1976a, p. 107) for acceptance function of V-trough). The higher θ_a and the lower the reflector height, the smaller is the difference between CPC and V-trough acceptance.

- <u>A V-trough</u> adapted to the end-points of a CPC <u>can direct irradiance onto an absorber from a significantly higher angular range</u> than this CPC.

For incidence from θ_a > 35°, the CPC reflectors do not work anymore. In contrast, the V-trough directs irradiance up to θ_t ≈ 45° to the absorber. For this angular range the V-trough is more profitable.

2.5 Raytracing Results

Results for endless troughs and pilot plant: The IAM curve for beam irradiance $K_b(\theta_l, \theta_t)$ of RefleC 6 GF without end losses and the curve of its receiver flat-plate LBM 4 GF have been given in Figure 2.11 above. In Figure 2.38 and Figure 2.39 below, the longitudinal and transversal raytracing results of the other test samples are given.
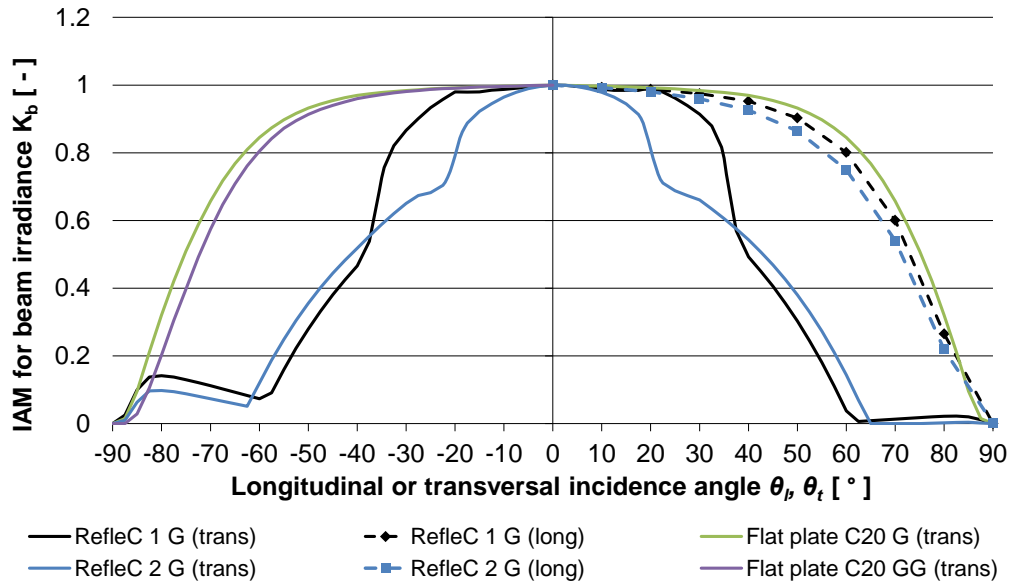
Figure 2.38: Raytraced IAM curves of R1 G, R2 G and the receiver flat-plates C20 AR G and C20 AR GG without end-losses. The longitudinal IAM curves of R1 G, R2 G and C20 AR GG are symmetric within the longitudinal plane of $\theta_l = [-90°; +90°]$. To improve the graph's clarity, they were displayed for positive longitudinal incidence angles only. The transversal plane of RefleC is identical to that of the flat-plates (cp. Figure 2.8).
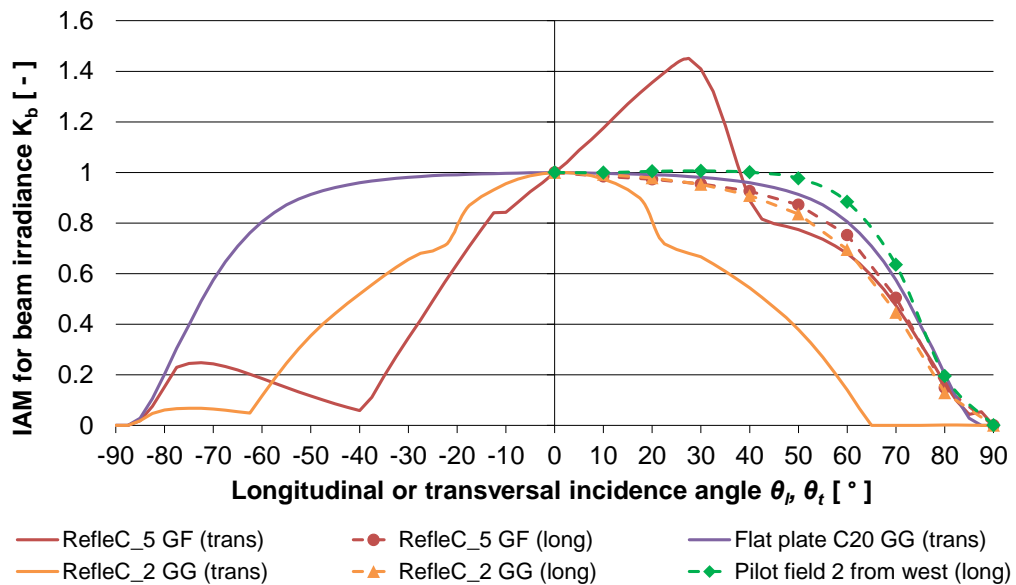
Figure 2.39: Raytraced IAM curves of R2 GG, R5 GF, receiver flat-plate C20 AR GG and the RefleC pilot plant without end losses. The longitudinal curves of R2 GG and R5 GF are symmetric, but only displayed either for positive or negative incidence to improve the clarity. The transversal plane of RefleC is identical to that of the flat-plates (cp. Figure 2.8). The longitudinal IAM of the pilot plant was only determined for positive angles.

59

In Figure 2.38, the effect of a second glass cover on the IAM can be observed when comparing C20 G (trans) to C20 GG (trans). This effect is very similar for a glass-foil covered collector. At RefleC 1 G and RefleC 2 G the drops of the IAM at their acceptance half-angle θ_a are clearly visible. It is also shown that their radiation acceptance is significantly reduced compared to a flat-plate.

In Figure 2.39, the longitudinal IAM of the RefleC subfield 2 of the pilot plant remains close to 1 until $\theta_l = 50°$. This is due to the trough closure reflectors (cp. Figure 5.4 and Figure 5.5).

Results for test samples: The results for the test sample modules accounting for their end-losses are given in Appendix C. The transversal IAMs of the test-samples are not influenced by the trough length. But for the longitudinal IAMs, the exact assessment of the influence of reflected longitudinal irradiance missing the flat-plates laterally was important, e.g. for the calculation of the test sample's IAM for isotropic diffuse irradiance.

3 RefleC Collector Testing

Initially, the development history of RefleC is briefly described. For ray-tracing validation, the influence of diffuse irradiance on measured conversion efficiencies and the effect of local concentration on F´ are assessed. The applicability of standard output equations for RefleC is proved, and raytracing-based efficiency curve calculation is shown.

3.1 Stages of Development

Six different RefleC generations have been developed. Four of them were built and tested. Their parameters and the test results are summarized in Appendix A.

RefleC 1 (test sample): The first test sample is shown in Figure 3.1 below.
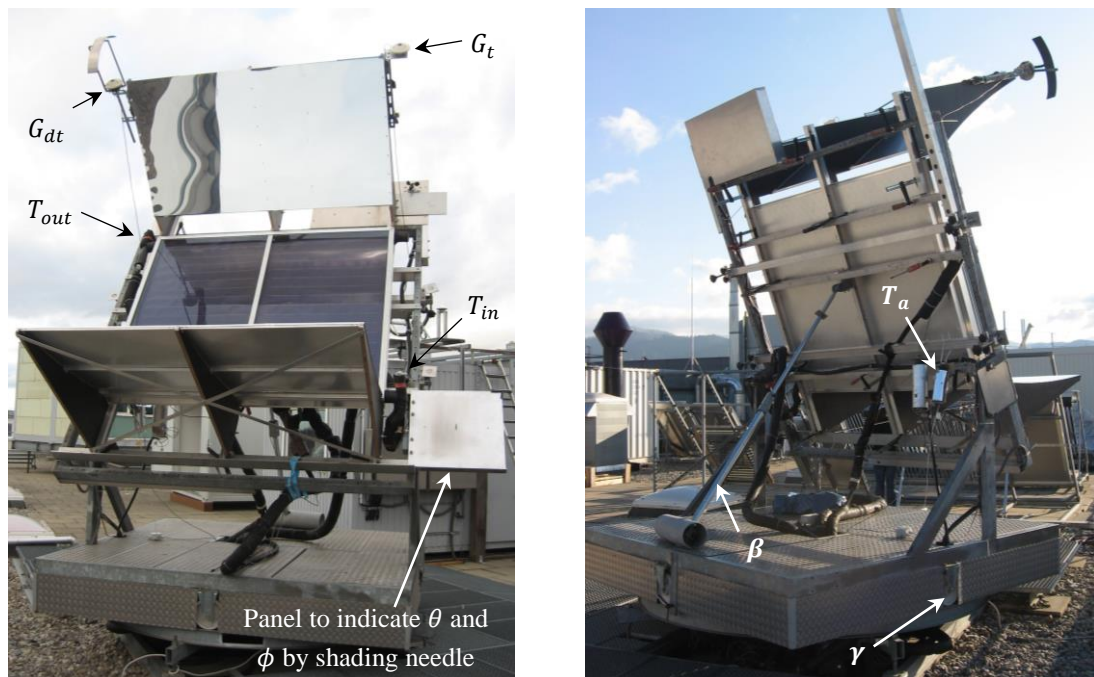
(a) Irradiance sensors for global G_t and diffuse G_{dt}; temperatures at inlet T_{in} and outlet T_{out}.

(b) Tracking devices for slope β and azimuth γ; shaded sensor for ambient temperature T_a.

Figure 3.1: RefleC 1 during outdoor IAM determination (rotated 180°). Tracking of collector slope β and azimuth γ maintained a constant solar incidence angle θ and sun azimuth ϕ (cp. Figure 2.7 and Figure 2.8) for stationary measurements. The indicator panel was parallel to the aperture and allowed a visual check of these two values. The container in the back of picture (a) contains a process thermostat, maintaining a constant water inlet temperature T_{in}, and also a MID volumetric flow sensor to calculate the mass flow $\dot{m}$.

The first RefleC test sample was built from available components right at the start of the project. Its purpose was a proof of principle, not construction for series production. Thus, RefleC 1 was tested to:

- validate the raytracing simulations; especially the simulated IAM curves
- assess the increase in thermal efficiency due to concentration.

The flat-plate LBM 67 AR was used as receiver. This is a large-area collector of Wagner & Co. with serpentine absorber and one anti-reflective glass pane. The reflectors were made from reflective Aluminum sheet (cp. reflectance measurements in Figure 2.15) and shaped to a CPC of $\theta_a = 35°$. The exit aperture of the CPC was the absorber of the receiver flat-plate. The arc lengths of the upper and lower reflector sheets along the parabolic contour were both 1145 mm (cp. section 2.4.2). The reflectors were not symmetric, since the upper reflector started at the casing of the flat-plate, while the lower reflector showed a gap of 150 mm to allow for rain water run-off and leaves and snow to slip away out of the trough. From the construction described above results a geometrical concentration ratio of $C_{geo} = 1.435$. Figure 2.6 shows the definitions of the RefleC apertures. In Figure 3.1 the collector is rotated 180°, so that the gap in the lower reflector is visible at the top. This allowed for IAM measurements from θ_t [0; 90].

RefleC 2 (test sample): The second test sample is shown in Figure 3.2. Building upon the successful proof of principle by RefleC 1, the purposes of RefleC 2 were to:

- further reduce aperture-area-specific heat losses by increased concentration
- separately test the efficiency curves of RefleC and receiver flat-plates

(a) RefleC 2 with the first variant of a mounting system with trapezoidal sheets

(b) RefleC 2 rotated by 90° to allow defined forced convection at the glazing (2 to 4 m/s).

Figure 3.2: Second test sample RefleC 2. Left: First version of a support structure of the collector. Right: R2 during outdoor measurement of thermal efficiency curve.

As the receiver, the high performance flat-plate EURO C20 AR of Wagner & Co. was used. Three variants were available: the standard single AR-glazed, a double AR-glazed variant with argon filling and a provisional double covered glass-foil-collector (cp. Table A.2 in Appendix A).

It was intended to allow for a rough assessment of the influence of increased concentration (or reduced θ_a respectively) on the efficiency. Since the flat-plate receiver of RefleC 1 and 2 had different aperture widths, the geometry of RefleC 2 had to be adapted. Thus, the reflectors of R2 were first calculated for θ_a and C_{geo} of R1. This resulted in a reflector arc length of 1435 mm and a gap of 190 mm. Increasing the concentration by reducing the irradiance acceptance to $\theta_a = 20°$ resulted in the final $C_{geo} = 1.625$ of R2.

RefleC 3 (theoretical investigations): The experiences and test results of RefleC 1 and 2 indicated that substantial improvements in annual energy gain per unit ground area would be possible when changing the RefleC concept from a truncated CPC to a booster reflector concept. The booster was approximated to one side of a CPC and the ratio of reflector area to absorber area was the same as for R1 and R2. At this stage of the project, comprehensive simulations with a wide range of acceptance angles and collector slopes were performed to optimize the reflector geometry.

The generation RefleC 3 was based on the double-glazed EURO C20 AR GG. Different booster variants were designed and raytraced in OptiCAD. Their annual energy gain was simulated in TRNSYS based on calculated efficiency curves. Its purpose was to:

- compare the annual gain of RefleC with CPC to RefleC with different boosters
- optimize the booster reflector shape (parabolic or flat, optimal θ_a).

RefleC 3 showed a significant increase in performance compared to R1 and R2. The main advantages of only the lower reflector are:

- reduced wind loads leading to cheaper mounting system
- reduced row distance leading to more effective use of roof area
- avoided glare in the ambience from reflections by the upper reflector
- steeper incidence of reflected irradiance on the flat plate improving transmission
- higher utilization of diffuse irradiance
- higher additional gain per unit reflector area and per unit roof area

Results of the simulations comparing R1 and R2 to R3 are given in (Raucher 2009).

RefleC 4 (theoretical investigations): In parallel to the theoretical reflector optimization, the development of a glass-foil receiver flat-plate for RefleC at Wagner & Co. was in progress. RefleC 4 is the adaption of the RefleC 3 concept to the new receiver flat-plate LBM 22 AR GF, a glass-foil collector with a 50 μm ETFE-foil, which had been especially designed for RefleC. The resulting concept is shown in Figure 3.3.
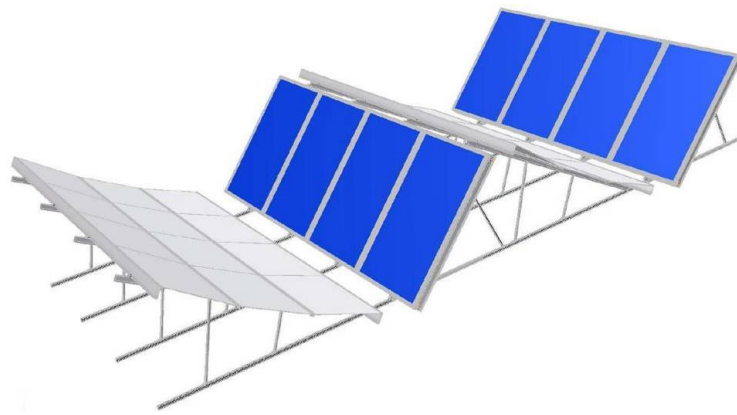
Figure 3.3: CAD impression of RefleC 4 on a flat roof. Its theoretical optimization result-ed in three flat segments of 900 mm approximated to the shape of a one-sided CPC with $\theta_c = 35°$ with a trough slope of $\beta = 55°$. The reflectors fill the necessary distance be-tween the flat-plates and support the collector row in their front.

RefleC 5 (test sample): The optimal reflector concept resulting from the investigations of RefleC 3 and 4 was built ($C_{geo} = 1.257$). As final reflector material the aluminum sheet composite was selected (cp. section 2.3.1). The sandwich-construction with PE-core is technically optimal, but it significantly increased the reflector costs. The receiver flat-plate LBM 22 AR GF has anti-reflective glazing and was tested with ETFE-foils of 50 μm and 25 μm. Wires below the foil allowed measurement of the sagging of the foil at increasing temperatures and avoided contact between foil and absorber at this early stage of development. Finally, RefleC 5 V2 with 25 μm ETFE was characterized.
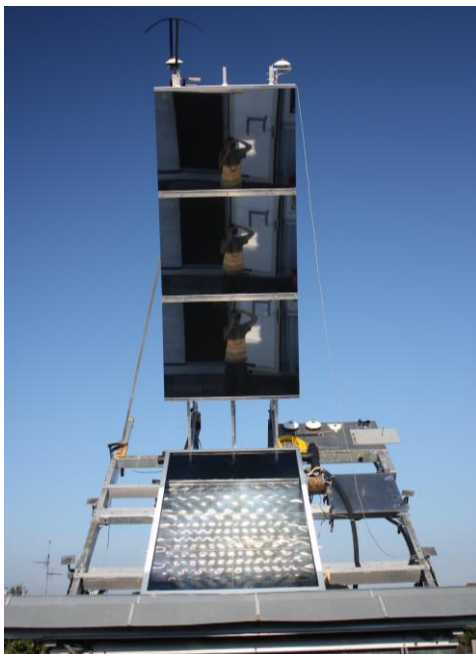
(a) RefleC 5 V2 at irradiance from $\theta_t = 35°$
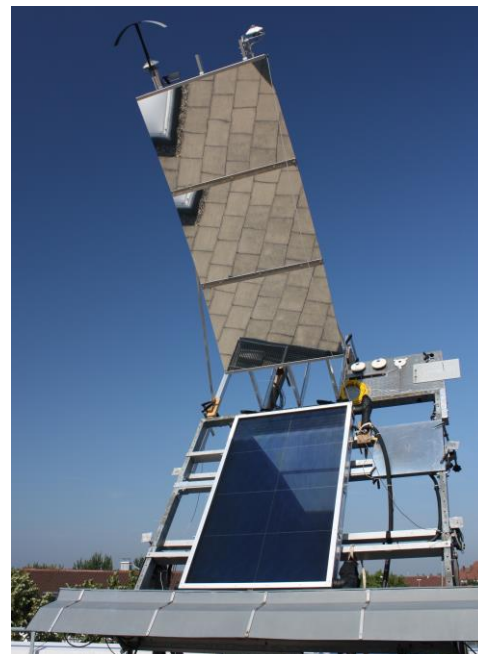
(b) RefleC 5 V2 with ground reflected in the mirror and LBM 22 AR GF with wires

Figure 3.4: RefleC 5 during outdoor test. The reflections in picture (a) show homogenous absorber illumination, implying good heat removal. A good planarity of the aluminum composite reflector can be deduced from the undistorted ground image in picture (b).

RefleC 6 (test sample): The last test sample was the prototype of RefleC (Figure 3.5). Receiver flat-plate and reflector are identical to those at the pilot plant.
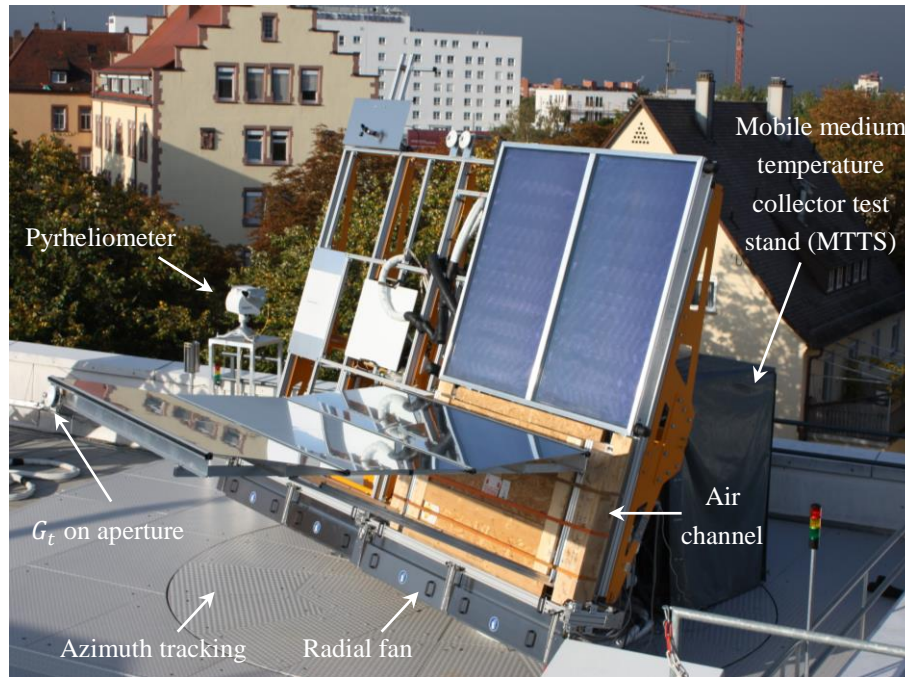

Figure 3.5: RefleC 6 during efficiency curve and IAM measurement at the TestLab Solar Thermal Systems of Fraunhofer ISE. The pyrheliometer allowed for accurate determination of diffuse irradiance. The wooden air channel was constructed to direct the air from the radial fan to the flat plate, ensuring defined convection during characterization.

Due to the air channel and the new tracker, the position of the collector on the tracker had not to be changed between efficiency-curve and IAM measurement. Measuring the collector with the reflector covering a large share of the ground assured realistic acceptance of diffuse irradiance during the tests and a good comparability to the pilot plant results.

RefleC 6 was improved in some details compared to RefleC 5. At R6, the final glass-foil receiver flat-plate LBM 4 AR GF was applied. Its reference areas are $A_{ap} = 4.04$ m^2 and $A_{gr} = 4.55$ m^2. Its backside insulation was identical to LBM 22 AR GF and consisted of a rigid foam panel for backside support and of mineral wool, together estimated to result in a heat transition coefficient of 100 mm mineral wool equivalent. Additionally, the middle support profile of the glass panes was insulated with 20 mm mineral wool on both sides. A cross-section of LBM 4 AR GF is shown in Figure 3.6.

An optimal distance between absorber, plastic foil and glass pane is difficult to determine theoretically. The convective, conductive and radiative heat losses of a certain combination depend on ambient- and absorber temperature, on the optical parameters emittance $\varepsilon(\lambda)$, absorptance $\alpha(\lambda)$, reflectance $\rho(\lambda)$ and transmittance $\tau(\lambda)$ of the components, as well as on the collector slope. In reality, temperature-dependent thermal expansion of the foil during operation (sagging), and potentially also of the absorber, can lead to different gap widths from the edge of the collector to the middle.
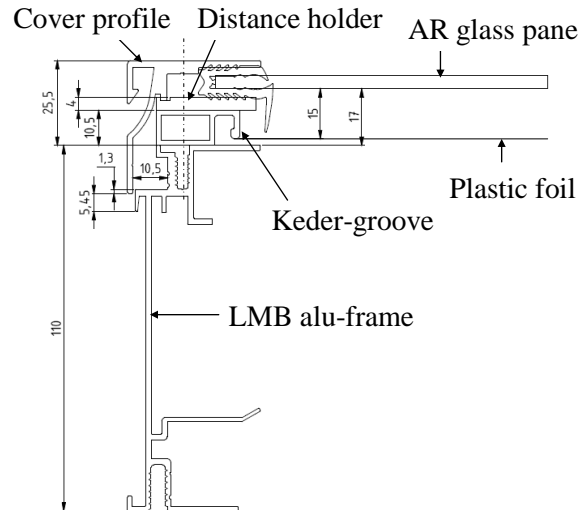
65

Figure 3.6: Cross section of LBM 4 AR GF, receiver flat-plate of RefleC 6 and also applied at the pilot plant (as large-area collector with four glass-panes). The separate foil-frame has a Keder-groove, where the edges of the 25 μm ETFE-foil are laid in. Then, the foil is mechanically pre-tensioned, fixed with a Keder-string and thermally tensioned.

Duffie and Beckman (2006, p. 248) show calculations of the top heat loss coefficient of double glass-covered collectors with identical space between absorber and the two glass covers. In the course of the RefleC project, similar calculations were performed by Rose (2008) for LBM with glass-foil cover and different spacing between absorber and covers, using the measured material parameters shown in Figure 2.20 and Figure 2.22.

3.2 Fundamentals of Collector Performance

3.2.1 Efficiency, IAM and Power

The working principle of SPH collectors has been described in section 1.3. The heating power output $\dot{q}_{use}$ of a ST collector per unit aperture area is for stationary conditions:

$$\dot{q}_{use} = \eta \cdot G_t = \dot{m} \cdot \int_{T_{in}}^{T_{out}} c_{p,fl}(T_f)\, dT \approx \dot{m} \cdot \bar{c}_{p,fl} \cdot (T_{out} - T_{in}) \qquad (\,3.1\,)$$

Herein, η is the collector's efficiency for conversion of global irradiance G_t reaching its aperture plane into useful heat. The specific mass flow $\dot{m}$ of the collector fluid experiences dependent on its heat capacity $c_{p,fl}(T_f)$ a useful temperature lift from inlet temperature T_{in} to outlet temperature T_{out}. Following the illustration of Figure 1.11, the main thermal loss mechanisms are:

- Natural, free convection between absorber and transparent cover(s) as well as natural and forced convection between collector (front) and ambience.
- Heat conduction between absorber, rear panel and the sides of the collector as well as heat conduction to and between the transparent cover(s)
- Infrared radiation between absorber, transparent cover(s) and ambience.

From the energy balance of a ST flat-plate at stationary conditions, the aperture-specific useful power $\dot{q}_{gain}$ can be calculated. It is given by the difference between radiative gains $\dot{q}_{rad}$ of the collector and its thermal losses to the ambient air $\dot{q}_{loss}$, both per m^2 aperture area (Duffie and Beckman 2006, p. 239):

$$\dot{q}_{gain} = \dot{q}_{rad} - \dot{q}_{loss} = \dot{q}_{rad} - U_{loss} \cdot (T_p - T_a) \tag{3.2}$$

The thermal losses depend on the difference between mean absorber plate temperature T_p and ambient temperature T_a as well as on the heat loss coefficient from absorber to ambient U_{loss}. This coefficient includes all convective, conductive and radiative losses and is therefore temperature dependent. To characterize the performance of a ST collector, it is not practicable to calculate these complex physical mechanisms analytically. Following the international collector testing standard (ISO 9806:2013), the temperature dependence of η can be determined from measurements under perpendicular irradiance onto the aperture. The stationary collector efficiency curve is approximated by a polynomial fit of second order. In Europe, the common expression for stationary conditions is obtained from a regression analysis of measured values:

$$\eta_\perp = \eta_0 - c_1 \cdot \frac{T_f - T_a}{G_t} - c_2 \cdot G_t \cdot \left(\frac{T_f - T_a}{G_t}\right)^2 \tag{3.3}$$

The coefficients c_1 and c_2 are heat loss coefficients of first and second order. They are related to the mean fluid temperature T_f:

$$T_f = \frac{T_{in} + T_{out}}{2} \tag{3.4}$$

This temperature can be determined easier than the absorber plate temperature T_p, which also varies locally over the absorber. Thus, the conversion factor η_0 at perpendicular irradiance is the efficiency when T_f equals the ambient temperature T_a. It is important to note that c_1 and c_2 are not physical parameters and that the efficiency curve is only valid within the measured temperature range. Figure 3.7 shows the measured efficiency curves of RefleC 6 and its receiver collector.

When relating η to T_f, the very important collector efficiency factor F' has to be considered. It accounts for the quality of the heat transfer from the absorber plate to the fluid. The ratio between the produced useful power within the heat carrier fluid and the power of a collector with equal fluid and mean absorber plate temperature is:

$$F' = \frac{\dot{q}_{rad} - U_{loss} \cdot (T_p - T_a)}{\dot{q}_{rad} - U_{loss} \cdot (T_f - T_a)} \tag{3.5}$$

For flat-plates, the influence of absorber fin thickness, absorber pipe distance and welding type on F' has been investigated by (Frey et al. 1997) and (Eisenmann et al. 2004).
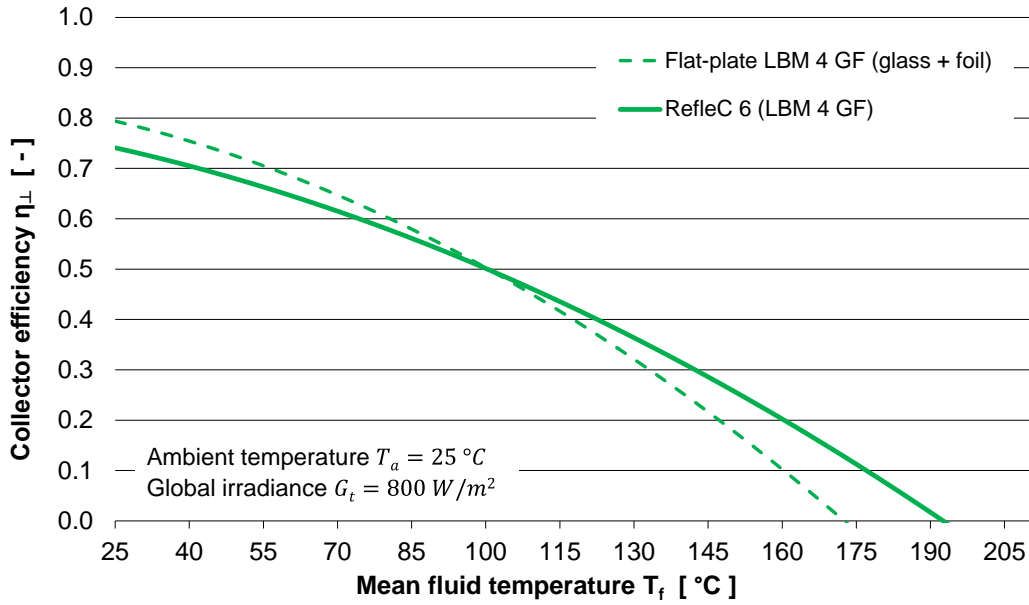
Figure 3.7: Measured efficiency curves of RefleC 6 and its flat-plate receiver collector LBM 4 GF (cp. values in Table B.1 and Table B.2). The conversion factor η_0 is found at intersection with the ordinate. R6 GF shows a lower value of η_0 because of the reflector's absorptance losses. The aperture area related thermal losses of R6 GF are lower than of LBM 4 GF, since R6 GF has a higher A_{ap} but the flat-plate, where the thermal losses occur, is the same LBM 4 GF (concentration ratio of $C_{geo} = 1.26$, cp. Table A.1)

The conversion factor η_0 has to account for this influence of the changed temperature basis. Therefore, η_0 results from a multiplication of F' and the effective reflectance-transmittance-absorptance product at a certain incidence angle $(\rho\tau\alpha)_e(\theta_l, \theta_t)$.

$$\eta_0(\theta_l, \theta_t) = F' \cdot (\rho\tau\alpha)_e(\theta_l, \theta_t) = F' \cdot (\rho\tau\alpha)_{e,\perp} \cdot K_h \quad (3.6)$$

It is further considered that K_h, the IAM for hemispheric irradiance, shows for the different types of irradiance different values and angular dependencies. This is expressed as follows:

$$\eta_0(\theta_l, \theta_t) = F' \cdot (\rho\tau\alpha)_{e,\perp} \cdot \left[K_b(\theta_l, \theta_t) \cdot \frac{G_{bt}}{G_t} + K_s \cdot \frac{G_{st}}{G_t} + K_r \cdot \frac{G_{rt}}{G_t}\right] \quad (3.7)$$

Herein K_b represents the IAM for beam irradiance at incidence angle θ_l, θ_t, K_s the IAM for diffuse irradiance from the sky dome and K_r the IAM for diffuse irradiance reflected by the ground. These shares of the irradiance were explained in detail in section 2.1.3. From Eq. 3.3 and 3.7 the efficiency curve for stationary conditions results:

$$\eta = F' \cdot (\rho\tau\alpha)_{e,\perp} \cdot \left[K_b(\theta_l, \theta_t) \cdot \frac{G_{bt}}{G_t} + K_s \cdot \frac{G_{st}}{G_t} + K_r \cdot \frac{G_{rt}}{G_t}\right]$$
$$- c_1 \cdot \frac{T_f - T_a}{G_t} - c_2 \cdot \frac{(T_f - T_a)^2}{G_t} \quad (3.8)$$

The specific power output $\dot{q}_{gain}$ per aperture area is determined according to eq. 3.9.

$$\dot{q}_{gain} = \eta_0 \cdot [K_b(\theta_l, \theta_t) \cdot G_{bt} + K_s \cdot G_{st} + K_r \cdot G_{rt}]$$
$$- c_1 \cdot (T_f - T_a) - c_2 \cdot (T_f - T_a)^2 \tag{3.9}$$

The output results from specific radiative gains $\dot{q}_{rad}$ and thermal losses $\dot{q}_{loss}$:

$$\dot{q}_{rad} = \eta_0 \cdot [K_b(\theta_l, \theta_t) \cdot G_{bt} + K_s \cdot G_{st} + K_r \cdot G_{rt}] \tag{3.10}$$

$$\dot{q}_{loss} = c_1 \cdot (T_f - T_a) + c_2 \cdot (T_f - T_a)^2 \tag{3.11}$$

Besides the very detailed modeled optical behavior, the following dynamic simulations take also the effective thermal capacity c_{eff} of the collector into account (i.e. the capacity of all components and fluid content of the collector). This is especially necessary because of the high working temperatures of more than $100\,°\mathrm{C}$ and due to rapidly changing irradiance conditions at locations in Central Europe. For the dynamic, aperture area related specific useful power $\dot{q}_{use}$ then it can be written:

$$\dot{q}_{use} = \dot{q}_{gain} - c_{eff} \cdot \frac{dT_f}{dt} = \dot{q}_{rad} - \dot{q}_{loss} - c_{eff} \cdot \frac{dT_f}{dt} \tag{3.12}$$

Thermally, Eq. 3.12 with input from Eq. 3.10 and 3.11 follows the standard expression of full instantaneous steady-state efficiency test results as described in the current standard (ISO 9806:2013, p. 105).

When testing according to the steady-state method, the IAM K_d is not identified from the measurements, but determined from the K_b test results afterwards. This is done under the simplifying assumption of isotropic irradiance from the overall collector hemisphere (180°, cp. Figure 2.1, left). The dynamic test method also assumes isotropic irradiance from the collector hemisphere, but the important difference is that K_d is determined from the test results directly. This way, the real sky anisotropy during the test affects K_d, so that for the same collector often higher K_d values are determined. But in both methods as well as in state-of-the-art collector simulation models, G_{st} and G_{rt} are summarized and one single IAM K_d for diffuse irradiance accounts for their utilization (cp. e.g. (Haller et al. 2013, p. 6)). K_d is always constant and independent of β. It is provided in collector test reports and not varied within a simulation. In Eq. 3.10 and in the model developed within this work, G_{st} and G_{rt} are treated separately to allow for separate K_s and K_r.

The three IAMs of the irradiance components introduced above account for all optical, geometrical and thermal effects occurring when incidence of irradiance is not perpendicular to the aperture. The IAM leads to a decrease or increase of η_0, resulting in a parallel translation of the collector efficiency curve. It is therefore notable that the relative influence of the IAM on the collector output increases with increasing thermal losses (i.e. at low-efficiency operation as in some process heat applications, for further explanation cp. section 3.4.4).

This work primarily assesses the effect of anisotropic irradiance modeling on the collector output. Therefore, the expression in Eq. 3.12 was considered to be sufficient. State-of-the-art dynamic collector characterization determines four other factors: zero heat loss coefficient dependency on wind speed, the thermal loss coefficients dependency on wind speed, radiative gains dependency on infrared ("sky-temperature"), and a coefficient for condensation gains (when the collector is below T_a). These factors are included in dynamic collector models (ISO 9806:2013), (Haller et al. 2013), (Fischer et al. 2004), but are mainly relevant for uncovered collectors. For steady-state tested, covered ST collectors these parameters are not determined separately and therefore they are not included in the model developed.

Test reports with performance parameters (efficiency curve and IAM) of certified ST collectors can be obtained from the online databases of the *CEN* (Comité Européen de Normalisation), *Solar Keymark Scheme* (Solarkeymark 2014), and the US *SRCC* (Solar Rating and Certification Corporation) (SRCC 2014). Solar Keymark reports also include calculated values of monthly collector output at constant mean collector fluid temperatures T_f of $25\,°C, 50\,°C$ and $75\,°C$ for Stockholm, Athens, Davos and Würzburg. They are calculated with the publicly available Excel-based tool *SCEnOCalc* (Solar Collector Energy Output Calculator) (SCEnOCalc 2014).

3.2.2 IAM Values for Beam Irradiance

In section 2.2.2, the IAM for beam irradiance has been introduced and different categories have been proposed.

Interpolations for rotation symmetric IAMs: When testing flat-plate collectors with rotation symmetric IAM, often only one single value $K_b(\theta = 50°)$ is determined. Since the shape of the IAM curve mainly depends on the optical losses caused by collector cover and absorber, Souka and Safwat suggest the use of a cosine-function with the collector-specific parameter b_0 to describe the shape of such an IAM curve (Souka and Safwat 1966, p. 171). Such IAM reach the value of zero well before $\theta = 90°$, which accounts for shading effects at high incidence angles. The function of the often so called "b_0-method" is usually written as:

$$K_b(\theta) = 1 - b_0\left(\frac{1}{\cos\theta} - 1\right) \qquad \text{solved for} \qquad b_0 = \frac{1 - K_b(\theta)}{\frac{1}{\cos\theta} - 1} \tag{3.13}$$

Solving the equation for b_0 allows for approximating all $K_b(\theta)$ from one known value. Ambrosetti and Keller (1985, p. 19) suggest to use a tangent function instead, which results in the effect that for all parameters r the IAM reaches a value of zero at $\theta = 90°$. This can be more accurate for small distances between absorber and glazing.

$$K_b(\theta) = 1 - \left(\tan\frac{\theta}{2}\right)^{\frac{1}{r}} \qquad \text{solved for} \qquad r = \frac{\ln\left(\tan\frac{\theta}{2}\right)}{\ln(1 - K_b(\theta))} \tag{3.14}$$

A good overview on these and other interpolation methods is given by (Fischer 2011, pp. 45-50). If, as in case of evacuated tube collectors, IAM values at $\theta = 20°, 40°$ and $60°$ have been determined, Fischer recommends a linear interpolation ending at $K_b(\theta = 90°) = 0$ (Fischer 2011, p. 49).

Interpolations for biaxial IAMs: When the shapes of the longitudinal and transversal IAM curve differ significantly (as for evacuated tubes and RefleC), values of $K_b(\theta_l, \theta_t)$ have to be calculated for intermediate angles (usually no 3D-IAM is available). The state-of-the-art approach is the approximation of McIntire (1982, p. 315):

$$K_b(\theta_l, \theta_t) \equiv K_b(\theta_l, 0) \cdot K_b(0, \theta_t) \tag{3.15}$$

This so called *multiplication approach* shows the highest relative errors in K_b for high incidence angles θ and from directions, where $K_b(\theta_l, 0)$ and $K_b(0, \theta_t)$ differ much from each other (cp. 3D-IAM of RefleC in Figure 2.12).

Rönnelid et al. classified beam irradiance data of Stockholm (only above 200 W/m^2 and from March to October) into 10°-intervals of θ_t and θ_l. Accurate raytracing-values of $K_b(\theta_l, \theta_t)$ of a symmetric CPC-collector were available (flat absorber, $C_{geo} = 1.56$, $\theta_a = 35°$, truncation 0.4). The absorbed energy using the exact raytraced values was lower than for the approximated values determined by eq. 3.15. In comparison to the measured output of the collector ($\beta = 40°$, $T_m \approx 70\,°C$) the authors conclude that a simulation with the approximation of Eq. 3.15 would have overestimated the annual collector output by approx. 4 to 5 % in this specific case (Rönnelid et al. 1997, p. 285).

The factorized calculation method of McIntire is used in nearly all established computer programs for solar thermal simulations and is therefore a factor of uncertainty for calculations of annual energy gains. For specific collector designs, specific modifications of the approach of McIntire have been proposed, e.g. by Helgesson (2004, p. 114), who introduced a multiplication approach where the influence of the glazing and the reflector were accounted separately for a flat-plate variant of the MaReCo (cp. Figure 1.15).

3.2.3 IAM Values for Isotropic Diffuse Irradiance

The nature of diffuse irradiance from sky and ground has been discussed in detail within section 2.1. Particularly in central Europe with latitudes between 40° and 60° N the contribution of diffuse to the overall annual irradiation is in the range of 40 % to 60 % (Badescu 2008, page 427).

Concentrator acceptance: Before the IAM for diffuse irradiance is discussed, the radiation acceptance of R1 is used to illustrate some basic considerations. In Figure 3.8, the collector is exposed to an ideal isotropic sky. The dashed parabolic segments show a full CPC. It accepts all diffuse irradiance from $\theta_t < \theta_a$, because it directs all irradiance from within its acceptance angle towards the absorber (green arrows).
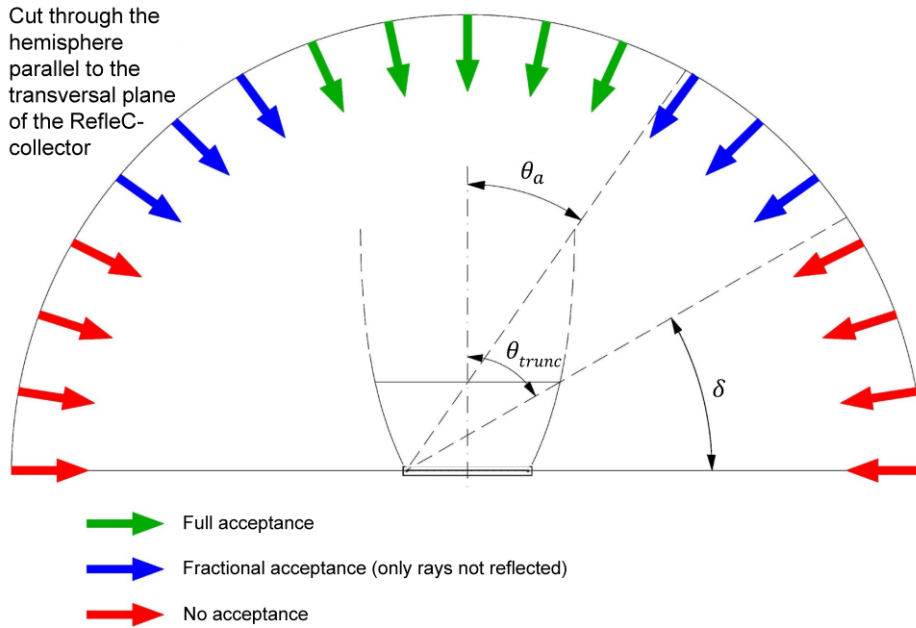
Figure 3.8: Acceptance of RefleC 1 for isotropic diffuse irradiance from lune-shaped segments of the sky (along its longitudinal axis), adapted from (Hess 2007, p. 38)

No rays from $\theta_t > \theta_a$ are accepted; the absorber is shaded from these rays by the reflector. When the CPC is truncated, θ_a does not change. Diffuse irradiance reaching the reflectors from $\theta_t = [\theta_a; \theta_{trunc}]$ can therefore not be reflected towards the absorber. However, such rays may reach the absorber directly without reflection (blue arrows). Diffuse irradiance from $\theta_t > \theta_{trunc}$ cannot reach the absorber. If the collector would be sloped to the right, the angle $\delta = 90° - \theta_{trunc}$ would decrease and the collector's field of view would turn to the right. For isotropic irradiance, the acceptance does not change until collector slope $\beta > 90° - \theta_{trunc}$ or $\delta = 0°$ respectively. Thus, for collector slopes $\beta > \delta$, diffuse irradiance from the ground can reach the absorber.

To approximately calculate the fraction of isotropic diffuse irradiance transferred from a concentrator aperture to its absorber, Winston (1974, p. 89) postulates a very simple correlation between the acceptance factor $f_{acc,iso}$ and the concentration ratio C_{geo}:

$$f_{acc,iso} = 1/C_{geo} \tag{3.16}$$

Rabl (1985, p. 131) derives the same equation from basic radiative heat transfer correlations. Applying this to the non-truncated R1 collector with $\theta_a = 35°$ and $C_{geo} = 1/\sin 35° = 1.743$ results in $f_{acc,iso} = 0.57$, i.e. the absorber of the non-truncated R1 in Figure 3.8 "sees" this share of the hemisphere (green arrows). For the real, truncated R1, $f_{acc,iso} = 0.70$ ($C_{geo} = 1.435$, cp. Table A.1). The factor $f_{acc,iso}$ differs from the isotropic $K_{d,iso}$ in the important aspect that it does neither consider optical effects of concentrator or receiver, nor the in reality finite trough length.

IAM for isotropic diffuse irradiance: For an isotropic collector hemisphere, Brandemuehl and Beckman (1980, p. 511) used an integration approach with spherical

coordinates to express the transmittance of sky and ground reflected diffuse via flat-plate collector covers and CPCs. Their transmittance function can be applied analogue to the IAM. Using the coordinates of the collector hemisphere (cp. Figure 2.8) the general expression for an isotropic hemisphere is Eq. 3.17.

$$K_{d,iso} = \frac{\int_0^{2\pi} \int_0^{\pi/2} K_b(\theta, \phi) \cdot \cos\theta \cdot \sin\theta \; d\theta \; d\phi}{\int_0^{2\pi} \int_0^{\pi/2} 1 \cdot \cos\theta \cdot \sin\theta \; d\theta \; d\phi} \tag{3.17}$$

In the denominator of Eq. 3.17, the irradiance from a unit sphere is integrated. Herein, the cosine accounts for the cosine-losses of the irradiance onto the flat aperture (cp. Figure 2.5); the sinus accounts for the increase of radiating area when finite surface elements of the sphere are considered in equidistant angular steps of θ and ϕ. This approach assumes an isotropic collector hemisphere, i.e. sky and ground have the same radiance and $K_{d,iso}$ is independent of the collector slope β. By weighting the irradiance with $K_b(\theta, \phi)$, optical losses of the collector are considered, so the result is a collector incidence angle modifier for isotropic, hemispheric diffuse irradiance $K_{d,iso}$. For R1, $K_{d,iso} = 0.62$ for an endless trough (calculated by Eq. 3.17 and using the R1 K_b-values of Figure 2.38), and $K_{d,iso} = 0.59$ for the test sample with end losses (Eq. 3.17 and K_b-values of Figure C.1), while the concentrator's acceptance for isotropic irradiance calculated above was $f_{acc,iso} = 0.70$.

Determination for rotation symmetric IAMs: In this case eq. 3.17 can be simplified to (Fischer 2011, p. 58):

$$K_{d,iso} = 2 \int_0^{\pi/2} K_b(\theta) \cdot \cos\theta \cdot \sin\theta \; d\theta \tag{3.18}$$

Bosanac and Nielsen (1997, p. 141) give an analytic solution in case only the Ambrosetti IAM parameter is known; Uecker (2000, p. 123) gives a solution for Souka/Safwat.

Determination from biaxial IAMs: Eq. 3.17 can also be expressed in terms of θ_l and θ_t, so that $K_{d,iso}$ can be calculated when longitudinal and transversal values of K_b are available (Fischer 2011, p. 59). But of course the numerical integration can also be performed along θ and ϕ when values of $K_b(\theta, \phi)$ are calculated from values of $K_b(\theta_l, \theta_t)$ by the separation approach according to McIntire (cp. Eq. 3.15).

The investigations in chapter 4 will show that an isotropic collector hemisphere is a very rough simplification, not only because isotropic sky radiance is usually not the case. Since ST collectors are usually sloped, the IAM for reflected irradiance K_r will usually vary significantly from the IAM for sky irradiance K_s. Carvalho et al. (2007, p. 611) separate between irradiance from sky and ground, so that isotropic values of $K_{s,iso}$ and $K_{r,iso}$ can be calculated. They give tabular values of the integration limits in longitudinal and transversal direction depending on the collector slope β, its acceptance half-

angle θ_a and its truncation angle θ_{trunc}. In their table, integration limits for rotation symmetric and biaxial symmetric collectors are given. Because the IAM of RefleC is biaxial asymmetric and anisotropic diffuse irradiance cannot be directly included, this approach is not applied within this work.

3.3 Collector Efficiency Testing

The RefleC test samples and their receiver flat-plate collectors were characterized at the Test Lab Solar Thermal Systems of Fraunhofer ISE, which runs an indoor sun simulator and an outdoor testing laboratory with two trackers. The indoor simulator and both tracker sites each have independent testing equipment, but their thermostats for conditioning of the collector fluid have a maximum working temperature of 95 °C. Some of the other testing equipment is shown in Figure 3.1 and Figure 3.5. To measure the efficiency of RefleC up to its application temperature, the mobile Medium Temperature Collector Test Stand (MTTS) of Fraunhofer ISE was used. It allows testing with pressurized water up to 200 °C and 20 bar. Among other components, the test stand consists of a thermostat (electrical heater and air/water water/water cooler), a PC with multiplexer, a pump with valve, and all necessary sensors. A Coriolis sensor allows for direct mass flow measurement and avoids uncertainties due to temperature dependence of the fluid density. A detailed description of the test stand can be found in (Rommel 2008). Fraunhofer ISE is a certified body able to perform standard ST collector and system tests, e.g. according to the requirements of the European quality label *Solar Keymark*. The efficiency curves of the RefleC collector test samples and partially also their IAM values were determined as close as possible to the steady-state method described in the European testing standard (EN 12975-2:2006), which has recently been substituted by (ISO 9806:2013). The laboratory meets the accuracy requirements of these standards.

Appendix A contains a detailed description of all RefleC test samples (Table A.1) and their receiver flat-plates (Table A.2). Appendix B contains the test results of RefleC (Table B.1) and the flat-plates (Table B.2).

3.3.1 Efficiency Curve Determination

Figure 3.9 shows the efficiency curve (cp. Eq. 3.3) of RefleC 6. Contrary to Figure 3.7, here the efficiency is plotted over the reduced temperature difference:

$$\frac{\Delta T}{G} = \frac{(T_f - T_a)}{G_t} = \frac{(\frac{T_{out} + T_{in}}{2} - T_a)}{G_t} \tag{3.19}$$

Use of the reduced temperature difference allows for an assessment of the measured values and their distribution independent of the individual G_t or T_a of each value. The operational points for which the curve has been determined are given in Table 3.1.
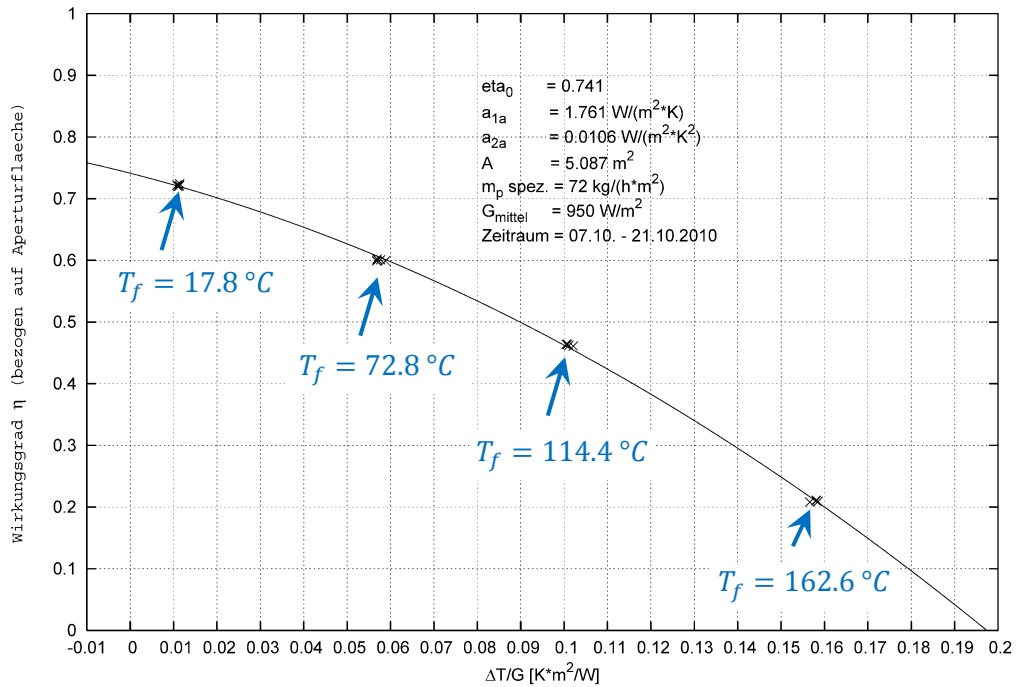
Figure 3.9: Efficiency test results (outdoor, MTTS) of RefleC 6 GF at $\dot{m} = 72 \text{ kg}/(\text{m}^2\text{h})$ for four averaged fluid inlet temperatures with fitted collector efficiency curve

Table 3.1: Stationary test data of RefleC 6 GF used to fit the curve in Figure 3.9

Date	Time (UTC)	G_t [W/m²]	G_{dt}/G_t [−]	$\dot{m}$ [kg]	T_a [°C]	T_{in} [°C]	T_{out} [°C]	T_f [°C]	η [−]
08.10.2010	14:11:15	945	19.5	373	19.2	69.6	76.3	72.9	0.602
08.10.2010	14:52:45	927	19.8	373	20.2	69.5	76.0	72.8	0.599
08.10.2010	15:02:45	921	20.9	373	19.5	69.5	76.0	72.7	0.601
08.10.2010	15:12:45	891	21.8	372	20.2	69.4	75.7	72.6	0.599
11.10.2010	12:38:00	988	12.5	370	13.5	111.7	117.0	114.3	0.461
11.10.2010	12:48:00	992	12.3	371	14.1	111.7	117.0	114.4	0.462
11.10.2010	12:58:00	993	12.1	371	14.3	111.7	117.1	114.4	0.464
11.10.2010	13:08:00	991	12.4	372	14.8	111.7	117.0	114.4	0.464
12.10.2010	12:28:15	952	17.4	364	13.6	161.4	163.7	162.6	0.208
12.10.2010	12:38:15	959	16.8	364	11.0	161.4	163.8	162.6	0.210
12.10.2010	12:48:15	956	16.9	364	11.5	161.4	163.8	162.6	0.211
12.10.2010	12:58:30	952	17.1	363	11.7	161.4	163.8	162.6	0.209
21.10.2010	11:20:15	982	12.0	371	6.5	13.4	21.7	17.6	0.721
21.10.2010	11:30:15	990	13.1	372	6.4	13.4	21.8	17.6	0.724
21.10.2010	11:40:15	1012	14.9	372	6.9	13.5	22.1	17.8	0.722
21.10.2010	11:51:15	1018	13.7	372	6.8	13.7	22.3	18.0	0.720

Preparation: In the following, the procedure for determination of a collector's efficiency curve is explained briefly for the example of RefleC 6 and its receiver flat-plate. First, the collector was conditioned, i.e. it was exposed without fluid to $G_t >$ 700 W/m² for more than five hours. This ensured that the collector was dry and that all initial thermal outgassing or initial component degradation occurred before testing. The collector was mounted with its aperture parallel to the tracking plain and orientated as in reality with reflector downside. This ensured realistic diffuse irradiance and convection within the flat-plate casing. The collector remained in this position for all efficiency curve and IAM tests, since the tracker is able to adjust to the necessary positions. It was

ensured that the global tilted irradiance pyranometer was within the aperture plane beside the collector and that the pyrheliometer was placed nearby. A wind channel ensured an even distribution of the forced convection over the cover of the receiver (cp. Figure 3.5). The hydraulic circuit consisted of thermostat, pump, mass flow sensor and adjustment valve, expansion vessel, deaerator, and the collector with the Pt 100 sensors T_{in} and T_{out}. The circuit was fully insulated and free of leakage or air. Inlet and outlet temperature sensors were positioned directly beside the collector and had been calibrated absolutely and then relative to each other. They were mounted in such a way that the fluid flow was parallel towards the tips of the centred temperature lance of the sensors.

Testing: To account for the particular characteristics of RefleC, special attention was paid to the accurate determination of incidence angle (visual verification) and fraction of diffuse irradiance. The collector efficiency tests were performed under clear sky conditions. The collector efficiency was determined for at least four different temperature levels T_f. These temperature levels were evenly distributed over the operation range of the collector. For each of the four temperature levels, at least four independent stationary test data points (mean value of 10 min interval) were determined (cp. Table 3.1), i.e. a minimum of 16 valid data points was determined to generate one efficiency curve. The (stability) criteria for these data points are given in Table 3.2. Before a valid stationary phase of 10 min can start, a pre-conditioning phase of 15 min with a stable inlet temperature (i.e. with deviation according to Table 3.2) is mandatory. The values of all sensors were logged by the multiplexer in a 15 s interval and stored in daily files.

Table 3.2: Criteria for valid outdoor steady-state efficiency test points according to (EN 12975-2:2006) with own comment on test of RefleC 6 and LBM 4 GF (n. s. = not specified). The criteria are identical to these in the current standard (ISO 9806:2013).

Parameter	Requirement	Permitted deviation*	Comment
G_t	> 700 W/m^2	± 50 W/m^2	Pyranometer in A_{ap}
G_{dt}/G_{bt}	< 0.3	n. s.	G_{dt} calculated from pyrheliometer-DNI
T_a	n.s.	± 1.5 K	Shaded and vented
T_{in}	One temperature level $T_f > 80\,°C$	± 0.1 K	Recommended: One level at $\Delta T/G > 0.09$, one at $T_f = T_a \pm 3$ K
T_{out}	$T_{out} > T_{in} + 1$ K	n.s	Avoiding high errors
$\dot{m}$	0.02 kg/(m^{2}s) ** if not specified	± 0.1 %	i.e. 72 kg/(m^{2}h)
Air speed	3 m/s	± 1 m/s	at flat-plate aperture

* of 30s average value from mean value within one 10 min data point test interval
** the selected $\dot{m}$ must not vary above 10 % for all data points of an efficiency curve

Efficiency curve determination: The test data were filtered for valid test data points by a script with adjustable conditioning phase and deviation ranges. The final selection of valid data points for one temperature level was done manually, taking high resolution curve-plots of all sensor values into account. The collector efficiency of one test interval

was calculated according to Eq. 3.1. Then, the efficiency curve was fitted to the valid efficiencies at the four temperature levels by a quadratic function (second degree polynomial). Therefore, the regression method of least squares was used. The resulting fit then has the form of Eq. 3.3 with the characteristic values η_0, c_1 and c_2. (ISO 9806:2013) recommends that the highest T_f is at $\Delta T/G > 0.09$, and the lowest at $T_f = T_a \pm 3$ K (to ensure accurate determination of η_0). The latter was not met for RefleC 6 and LBM 4 GF, because the MTTS was cooled by ambient air only. Thus, the uncertainty of the η_0-values is expected to be slightly higher than necessary. The following Figure 3.10 and Table 3.3 give the testing details of LBM 4 GF.
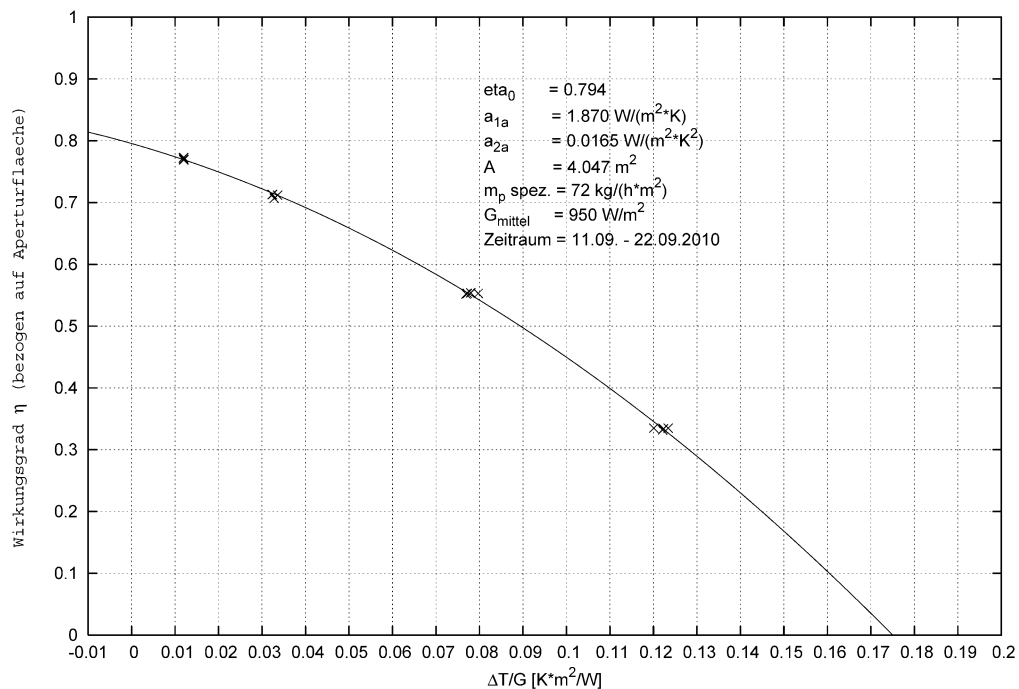
Figure 3.10: Efficiency test results (outdoor, MTTS) of LBM 4 GF (receiver flat-plate of RefleC 6) at $\dot{m} = 72$ kg/(m^{2}h) with fitted collector efficiency curve

Table 3.3: Stationary test data of LBM 4 GF used to fit the efficiency curve (cp. Figure 3.10)

Date	Time (UTC)	G_t [W/m^2]	G_{dt}/G_t [−]	$\dot{m}$ [kg]	T_a [°C]	T_{in} [°C]	T_{out} [°C]	T_f [°C]	η [−]
11.09.2010	12:14:45	1006	13.5	303	20.0	27.7	36.6	32.1	0.769
11.09.2010	12:24:45	1012	13.2	303	20.1	27.8	36.7	32.3	0.770
11.09.2010	12:34:45	1013	12.9	303	20.2	27.8	36.8	32.3	0.772
11.09.2010	12:44:45	1010	13.0	303	20.2	27.8	36.8	32.3	0.773
11.09.2010	14:09:15	997	14.2	311	22.6	51.4	59.3	55.3	0.707
11.09.2010	14:19:15	976	15.3	311	22.6	51.4	59.2	55.3	0.712
11.09.2010	14:53:45	996	14.4	311	23.3	51.5	59.5	55.5	0.713
11.09.2010	15:03:45	990	13.7	311	23.4	51.5	59.4	55.5	0.713
12.09.2010	15:16:00	985	16.0	309	24.0	96.7	102.8	99.7	0.552
12.09.2010	15:26:00	975	17.3	309	24.3	96.6	102.7	99.7	0.553
12.09.2010	15:36:00	960	17.9	309	24.7	96.6	102.6	99.6	0.554
12.09.2010	15:46:00	948	18.7	309	24.0	96.6	102.4	99.5	0.553
22.09.2010	15:13:15	955	15.1	316	23.4	136.3	139.8	138.0	0.335
22.09.2010	15:23:15	938	15.4	316	23.3	136.3	139.6	138.0	0.332
22.09.2010	15:33:15	936	15.5	316	23.6	136.3	139.7	138.0	0.334
22.09.2010	15:43:15	925	14.9	316	23.9	136.3	139.6	138.0	0.335

3.3.2 Importance of High Temperature Testing

Figure 3.11 shows the measured efficiency test data of RefleC 6 and its receiver flat-plate LBM 4 GF again. For each collector, the four testing temperatures can be distinguished. To illustrate how the fitted efficiency curves would deviate if only the three lower temperature levels would have been set, the data points at $T_f = 139.7\,°\text{C}$ (LBM 4 GF) and $T_f = 162.6\,°\text{C}$ (RefleC 6 GF) were excluded from the dashed line fits. Similar comparisons for other collectors had shown that extrapolation of efficiency curves to values of $\Delta T / G_t$ higher than tested causes high uncertainties (Kramer 2006, pp. 47-49).
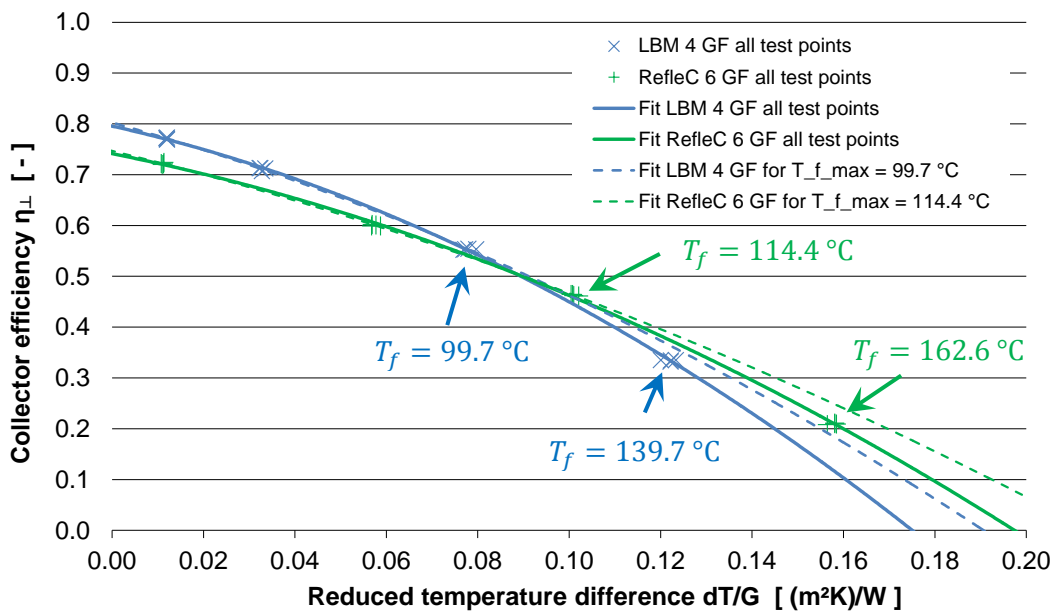
Figure 3.11: Efficiency curves of RefleC 6 GF and LBM 4 GF as shown in Figure 3.9 and Figure 3.10 fitted from the data points of all four temperature levels (solid lines) and without the highest temperature level (dashed lines).

Figure 3.11 reveals that the efficiency of both collectors would be overestimated for operation at values of $\Delta T / G_t$ outside of the tested range. This would for example be the case when using the efficiency curve of RefleC 5 V2, where the MTTS was not available for the test, for the prediction of low-efficiency operation (cp. Figure B.4).

Inclusion of the high temperature test results leads to a higher curvature of the fitted efficiency curve. This is expected to be a systematic effect occurring at all ST collectors, because the radiative heat losses of the absorber increase with the square of the absorber temperature. At the current example of RefleC 6 and LBM GF, potential sagging of the foil with increased temperature (resulting in increased heat losses due to suboptimal distance between absorber, foil and glazing) might have further added to the increased curvature.

It is important to note that missing data points at low efficiency operation do not only cause an overestimation at high temperature differences ΔT between ambient T_a and fluid T_f, but would also overestimate the collector performance at low irradiance.

If for example LBM 4 GF was operated at a comparably high temperature of $\Delta T = 80\,°C$ and $G_t = 500\,W/m^2$ (resulting in $\Delta T/G = 0.16$), the efficiency at perpendicular irradiance is $\eta_\perp = 10\,\%$. A test without the MTTS (i.e. without $T_f = 139.7\,°C$) would have predicted $\eta_\perp = 17\,\%$. In process heat applications, such high values of $\Delta T/G$ frequently occur also at high irradiance. To give an example, in the morning or the afternoon of a clear day RefleC 6 GF may e.g. be operated at $T_a = 20\,°C$, $T_f = 95\,°C$, $G_t \approx 750\,W/m^2$ and projected incidence angles of $\theta_t \approx 0°$ and $\theta_l = 70°$. When neglecting the diffuse-IAM to simplify the example, the irradiance would be multiplied by the IAM of $K_b \approx 0.5$, resulting in an operational parameter of $\Delta T/G \approx 0.2$. Figure 3.11 shows that the collector does not have positive gains at this point anymore. Testing the collector only up to $T_f = 114.4\,°C$ would have resulted in a positive efficiency of $7\,\%$ and gains of approx. $50\,W/m^2$, which would be a significant error. It is concluded that:

- <u>Extrapolation of a collector efficiency curve</u> to higher values of $\Delta T/G$ than tested <u>overestimates the collector efficiency</u>.
- At medium temperature process heating, high values of $\Delta T/G$ occur not only at low, but also at high irradiance. Thus, collector efficiency curves determined from test results below $100\,°C$ are expected to cause higher absolute simulation errors for process heating than for domestic applications.
- If possible, SPH collectors should therefore be tested up to mean fluid temperatures resulting in efficiencies of $\eta_\perp \approx 20\,\%$ or below.

The recommendation of (ISO 9806:2013) to test "the whole operating temperature range" is not sufficiently explicit, since irradiance below test conditions ($G_t > 700\,W/m^2$) will lead to higher values of $\Delta T/G$ for the same operation temperatures.

3.4 Test Results

3.4.1 Mass Flow Influence on Efficiency

Depending on the absorber piping design, some ST collectors might show a transition from turbulent to laminar flow within their mass flow operation range. This can affect the collector efficiency factor F', which is influenced by the heat transfer coefficient from absorber to fluid. For efficiency-curve determination, usually a standard mass flow of $\dot{m} = 0.02\,kg/(m^2 s) = 72\,kg/(m^2 h)$ is used. This equalizes heat capacity effects quickly, so at stationary conditions T_{out} stabilizes quickly and valid stationary test sequences can be found fast. On the other hand, the measurement accuracy can decrease at low efficiency (operation at high T_f) due to a low difference $T_{out} - T_{in}$.

At the RefleC pilot plant, the mass flow was initially about $25\,kg/(m^2 h)$, so it was questioned if the measured efficiency curve was still valid in this case. Figure 3.12

shows test results at standard and reduced mass flow. For the receiver flat-plate it indicates a slight decrease in F', which results in a parallel, slightly lower efficiency curve. RefleC 6 GF shows no decrease, but $\dot{m}$ through the LBM is a factor of C_{geo} higher, since it is related to aperture. The high temperature results of RefleC 6 at $\dot{m} = 35$ kg/(m^{2}h) have a high uncertainty, since $T_{out} - T_{in}$ is very low in this case.
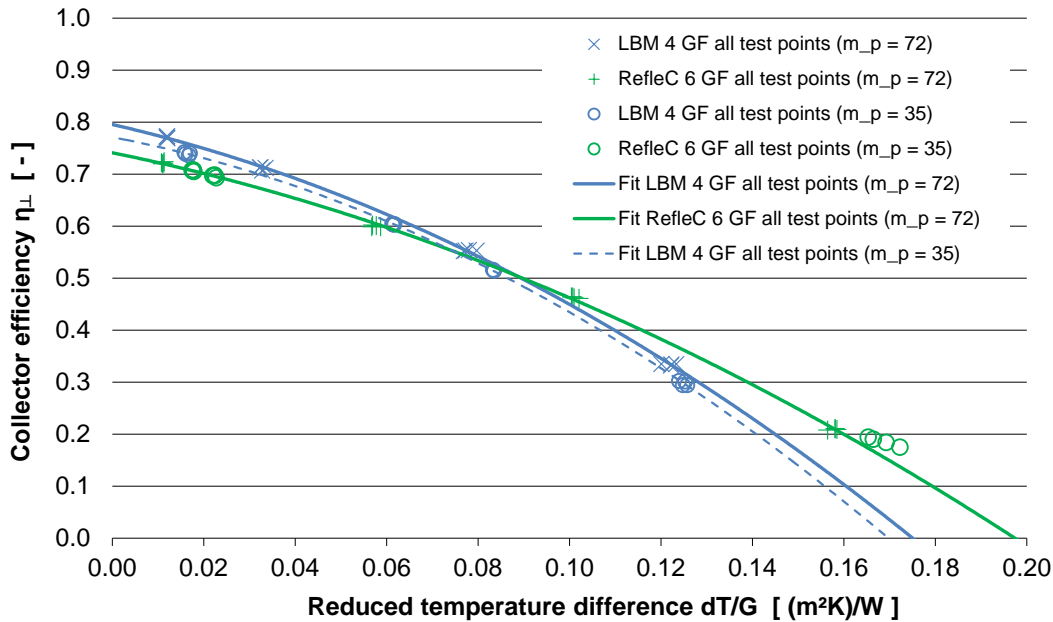
Figure 3.12: Comparison of MTTS-measured collector efficiencies of RefleC 6 GF and LBM 4 GF at mass flow rates 72 kg/(m^{2}h) and 35 kg/(m^{2}h), cp. Figure 3.10 to Figure B.10 and Figure 3.9 to Figure B.6 for original test results. No fit curve is provided for RefleC 6 GF at 35 kg/(m^{2}h) because only two temperatures could be tested.

The receiver of RefleC 5 V2 has the same LBM absorber as RefleC 6. It was tested at $\dot{m} = 72$ kg/(m^{2}h) and $\dot{m} = 26$ kg/(m^{2}h) (not shown in Figure 3.12, cp. Figure B.4 and Figure B.5). Since standard equipment was used (limitation to $T_{out} = 95\,°C$), a comparison of the efficiency curves does not make much sense in this case; no efficiencies below 55 % were determined. But due to the process thermostat, η_0 was measured very accurately and is as at RefleC 6 GF not affected by the smaller mass flow.

3.4.2 Absorber Temperatures and Local Concentration

On their receivers, CPC concentrators cause regions with higher intensity. Raytracing shows that this is maximal at transversal irradiance from $\theta_t = \theta_a$, where all irradiance reaching a reflector is focused onto the edge of the absorber. In this case, a concentration line is created (cp. Figure 2.31 c and Figure 3.13). The highest local concentrations are to be expected for RefleC 2, since it has the highest C_{geo}. To investigate effects of this, a combination of thermographic imaging and absorber temperature measurement with direct contact sensors was used. The tests were carried out with a single glass cover because the transmittance of the glazing for infrared radiance from the absorber is poor (cp. Figure 2.22). Figure 3.14 and Figure 3.15 show the results.
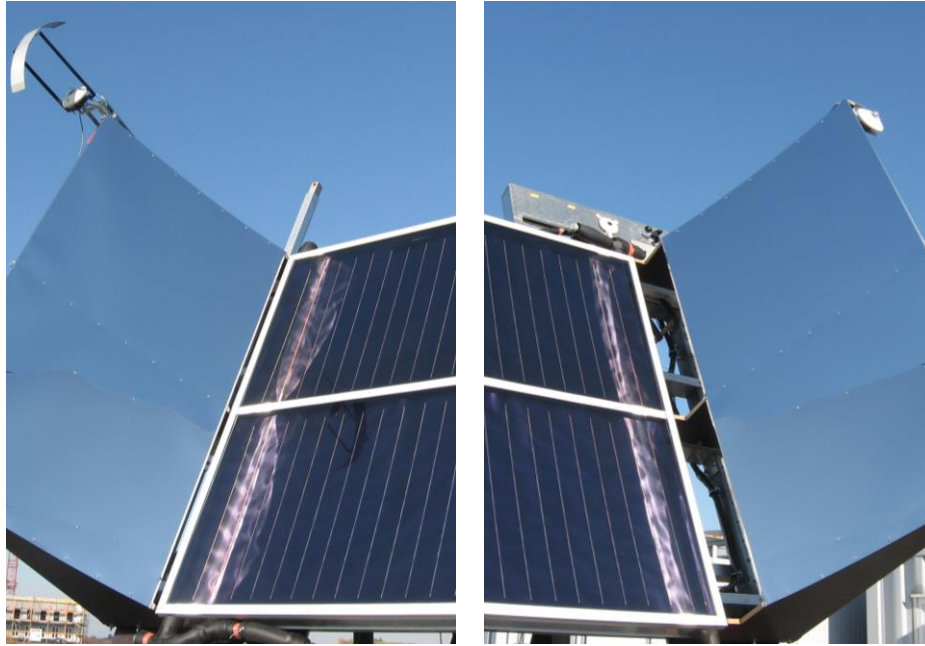
Figure 3.13: Local concentration onto the absorber of RefleC 1 at perpendicular irradiance (photographs taken from lateral positions). The shape accuracy of the right reflector (in reality the lower reflector) is better, since the reflected lines are more parallel.
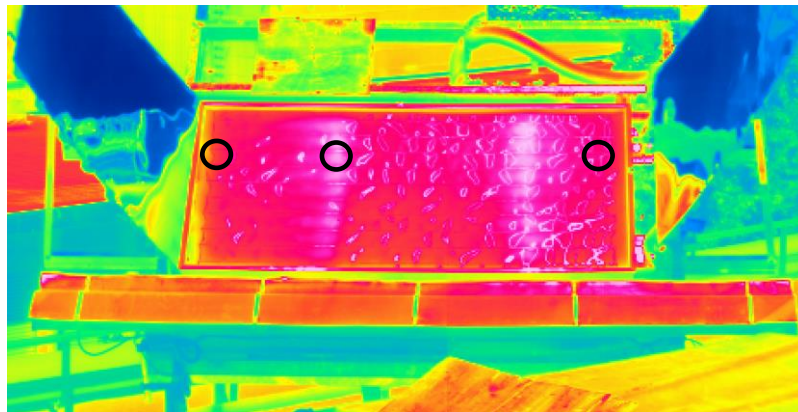
Figure 3.14: Thermographic image of RefleC 2 G on the tracker (single-glazed, no mass flow, $G_t = 995$ W/m², $G_{dt}/G_t = 0.1$, $T_a = 28$ °C, $\theta_t = 0$°, $\beta = 35$°. Below the collector, the radial fan is visible (cp. Figure 3.2 b)). The absorber temperature was measured by three Pt100 temperature sensors riveted to the absorber. These sensors were placed in a height of two thirds from the collector bottom (indicated by black circles). The collector glazing (almost IR-opaque) only allows for a qualitative assessment (cp. Figure 2.22).

These and following investigations show clear drawbacks of the application of a standard truncated CPC geometry for the collector:

- External CPCs for flat-plates cause a transversal absorber temperature gradient
- In stagnation, the gradient can be very high and might create local thermal sagging of a plastic foil and temporal deformation of the absorber.
- With a CPC, locally a significantly higher gradient between T_p and T_f than without reflector can be expected. This results in an increased F', since for $T_f = T_a$ (η_0-situation) higher heat losses occur (cp. calculations in section 3.4.5).

$$\theta_t = 0° \qquad \theta_t = \theta_a = 20°$$

$T_p = 192 °C$

$T_p = 260 °C$

$T_p = 193 °C$

$T_p = 262 °C$

$T_p = 210 °C$

$T_p = 179 °C$
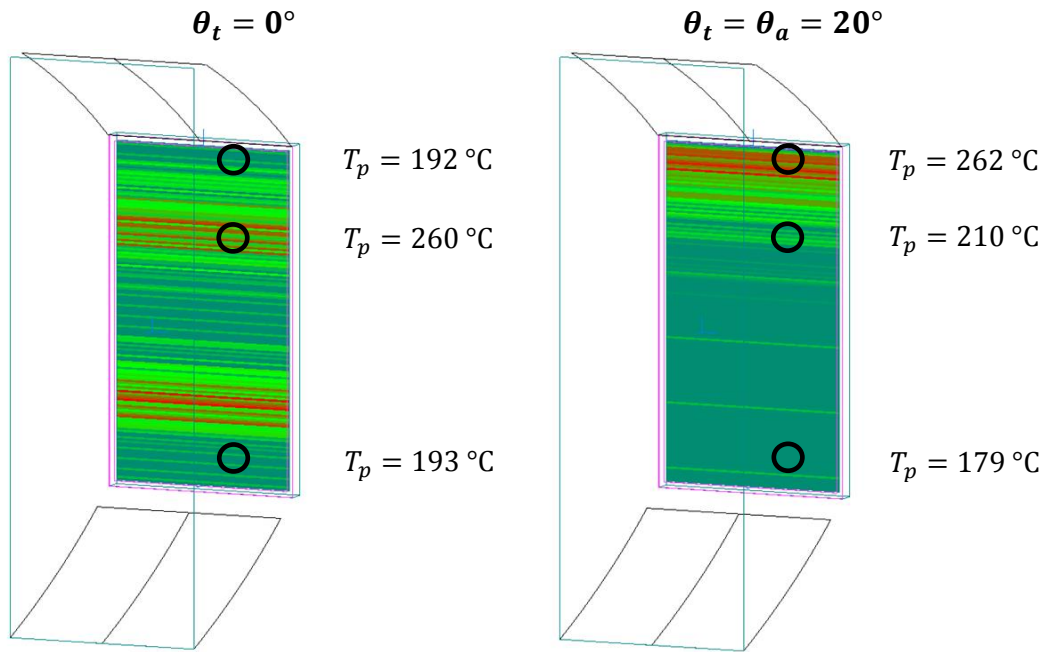
Figure 3.15: Local stagnation absorber plate temperatures T_p of RefleC 2 at perpendicular irradiance (cp. Figure 3.14) and at $\theta_t = 20°$ (conditions approx. as in Figure 3.14). The temperature sensor positions are indicated by black circles. Test results without mass flow or forced convection. The irradiance concentration on the absorber is qualitatively shown by raytracing.

3.4.3 Validation of Raytracing

In this work, the annual energy gain simulations and the calculations of the IAMs for diffuse irradiance are based on raytraced values. Thus, it was very important to ensure that the raytraced K_b-values are sufficiently close to reality. This validation was done by outdoor measurements of RefleC 1 G (cp. Figure 3.16) and RefleC 6 GF.
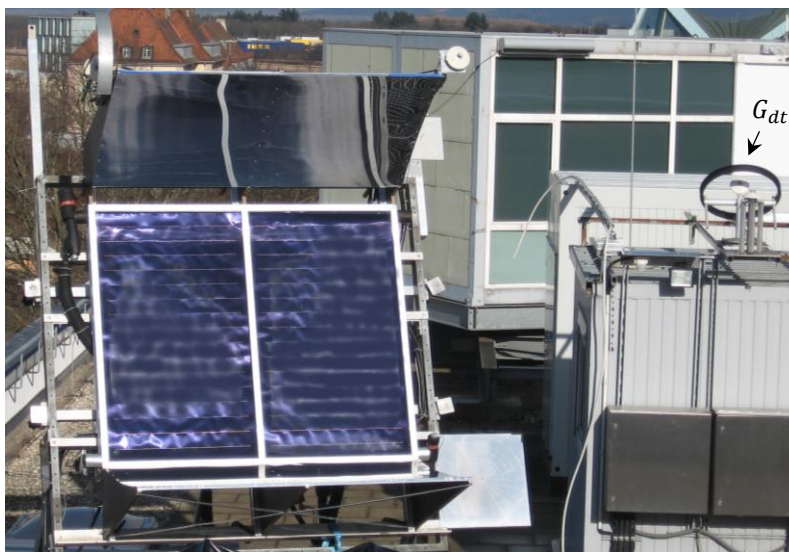
Figure 3.16: RefleC 1 G at test of the hemispheric IAM $K_h(\theta_l, \theta_t)$. To allow for tests at longitudinal and high transversal angles, the indicated diffuse-pyranometer with fixed orientation of $\beta = 45°$ and $\gamma = 0°$ had to be used. A pyrheliometer was not available.

Eq. 3.20 gives the definition of K_b for a certain incidence angle (θ_l, θ_t). For stationary collectors, usually a constant F' independent of the incidence angle is assumed. If F' changed with the incidence angle, the IAM would also account for thermal effects and could therefore not be determined by the pure optical raytracing. For RefleC, this was questioned, since the investigations in sections 3.4.2 and 3.4.5 show that CPC-reflectors decrease the conversion efficiency $F'_\perp$ at perpendicular irradiance. K_b is only then expressed sufficiently by raytracing, if the thermal effects are constant for all θ_t and θ_l.

$$K_b = \frac{\eta_{0,b}}{\eta_{0,b,\perp}} = \frac{F' \cdot (\rho\tau\alpha)_e}{F'_\perp \cdot (\rho\tau\alpha)_{e,\perp}} \approx \frac{(\rho\tau\alpha)_e}{(\rho\tau\alpha)_{e,\perp}} \tag{3.20}$$

Outdoor IAM tests allow measuring the influence of potential angular thermal effects. The drawback of IAM calculations from outdoor-tested efficiencies is that all test points result from a superposition of beam and diffuse, and that the influence of both irradiance components can vary over time and varies with θ.

The state of the art approach to calculate the IAM for hemispherical irradiance $K_h(\theta_l, \theta_t)$ from measured efficiency values is given in Eq. 3.21 (ISO 9806:2013, p. 69):

$$K_h = \frac{\eta_{0,h}}{\eta_{0,h,\perp}} = \frac{\eta_h + c_1 \cdot \dfrac{\Delta T}{G_t} + c_2 \cdot G_t \cdot \left(\dfrac{\Delta T}{G_t}\right)^2}{\eta_{0,h,\perp}} \tag{3.21}$$

To calculate K_h from measurements, first a standard efficiency curve at $\theta = 0°$ was determined. It gave the conversion factor $\eta_{0,h,\perp}$ for perpendicular hemispherical irradiance and the heat loss coefficients c_1 and c_2. Then, the efficiencies $\eta_h(\theta_l, \theta_t)$ for irradiance from certain incidence angles were measured. Eq. 3.21 allows these efficiencies to be affected by thermal losses, which simplifies the process (i.e. one constant inlet temperature can be used for all incidence angles). For the single glazed RefleC 1, K_h-values determined from tests at six incidence angles are shown in Figure 3.17 as green dots.

For energy gain simulations, it is state of the art to use measured IAM values for hemispherical irradiance $K_h(\theta_l, \theta_t)$ as IAM for beam irradiance $K_b(\theta_l, \theta_t)$. In the following, the influence of diffuse irradiance on the measured IAM values of RefleC is assessed by calculating a pure $K_b(\theta_l, \theta_t)$ from the $K_h(\theta_l, \theta_t)$-values. The results are shown in Figure 3.17. To explain the methods used and results found, Table 3.4 gives the transversal raytracing values, test results, and calculated values as shown in Figure 3.17. For the longitudinal direction, the results can be found in Figure 3.18 and Table 3.5.

Correction equations: Some equations have been developed, on which the following investigations are based. A measured conversion efficiency value is influenced by the IAM as follows (cp. Eq. 3.7):

$$\eta_{0,h} = \eta_{0,b,\perp} \cdot K_h = \eta_{0,b,\perp} \cdot (K_b \cdot f_b + K_d \cdot f_d) \tag{3.22}$$

This efficiency for hemispherical irradiance $\eta_{0,h}$ is the conversion factor $\eta_{0,b,\perp}$ for pure and perpendicular beam irradiance, modified or influenced by the IAM for hemispheric irradiance K_h. It consists of the IAM for beam K_b and diffuse K_d, weighted by the fractions of diffuse $f_d = G_{dt}/G_t$ and beam $f_b = 1 - f_d$ during the test. With the definition $K_b(\theta = 0°) = 1$, Eq. 3.22 allows a correction of the influence of diffuse on the measured conversion factor, if $K_{d,\perp}$ and $f_{d,\perp}$ are known:

$$\eta_{0,b,\perp} = \frac{\eta_{0,h,\perp}}{(1 \cdot f_{b,\perp} + K_{d,\perp} \cdot f_{d,\perp})} \tag{3.23}$$

With Eq. 3.20 and 3.22 the conversion efficiency for beam irradiance from a certain incidence angle can generally be expressed as:

$$\eta_{0,b} = \frac{\eta_{0,h} \cdot K_b}{(K_b \cdot f_b + K_d \cdot f_d)} \tag{3.24}$$

With Eq. 3.23 and Eq. 3.24, K_b can be expressed and solved for K_d.

$$K_b = \frac{\eta_{0,b}}{\eta_{0,b,\perp}} = \frac{\eta_{0,h} \cdot (f_{b,\perp} + K_{d,\perp} \cdot f_{d,\perp}) - \eta_{0,h,\perp} \cdot K_d \cdot f_d}{\eta_{0,h,\perp} \cdot f_b} \tag{3.25}$$

$$K_d = \frac{\eta_{0,h} \cdot (f_{b,\perp} + K_{d,\perp} \cdot f_{d,\perp}) - \eta_{0,h,\perp} \cdot K_b \cdot f_b}{\eta_{0,h,\perp} \cdot f_d} \tag{3.26}$$

With these two equations, test results and raytracing can be compared.
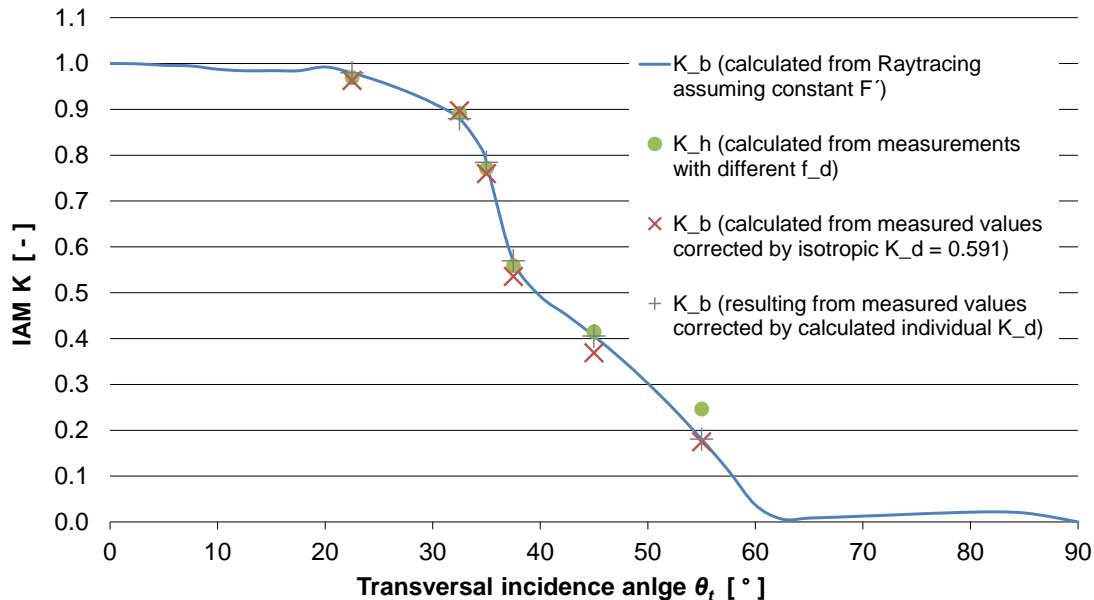
Figure 3.17: Raytraced beam-IAM K_b of RefleC 1 (blue), compared to the hemispherical IAM K_h calculated from tested efficiencies (green) and to K_b-values calculated from a correction of the tested efficiencies by the influence of diffuse. The red crossed values result from correction of each test value by a constant isotropic $K_d = 0.591$, determined by Eq. 3.17 from the raytraced K_b of R1 (cp. Figure C.1). The grey values result when K_d is determined for the assumption of a correctly raytraced K_b-curve (see details in Table 3.4).

Table 3.4: Raytracing results ($(\rho\tau\alpha)_e$ and K_b) vs. test results and corrected test results of the transversal IAM of RefleC 1 G (cp. Figure 3.17).

θ_t [°]	0 ($\perp$)	22.5	32.5	35	37.5	45	55	Comment
$(\rho\tau\alpha)_e$ [−]	0.838	0.820	0.737	0.657	0.477	0.340	0.151	Raytraced values
$\eta_{0,h}$ [−]	0.727	0.705	0.649	0.561	0.406	0.302	0.179	Measured efficiency for hemispherical irradiance
Valid test data points	7	5	5	3	3	6	8	Number of valid 10 min stationary test intervals for $\eta_{0,h}$
f_d [−]	0.093	0.078	0.135	0.102	0.110	0.184	0.156	Mean fraction of diffuse irrad. during valid test intervals
K_b [−]	1	0.98	0.88	0.78	0.57	0.41	**0.18**	Calc. by $(\rho\tau\alpha)_e$ from raytr. for constant F´(Eq. 3.20)
K_h [−]	1	0.97	0.89	0.77	0.56	0.42	**0.25**	Calc. from measured $\eta_{0,h}$ **without correction** (Eq.3.21)
K_b [−]	1	0.96	0.90	0.76	0.53	0.36	**0.17**	Calc. from measured $\eta_{0,h}$ **assuming constant isotropic** $\boldsymbol{K_{d,iso} = 0.591}$ (Eq. 3.25)
K_d [−]	0.591	0.39	0.71	0.35	0.29	0.37	0.54	K_d calc. from $\eta_{0,h}$ by Eq. 3.26 **assuming raytr. K_b is correct** (isotropic $\boldsymbol{K_{d,\perp} = 0.591}$)
K_d [−]	*0.80*	*0.63*	*0.85*	*0.50*	*0.38*	*0.42*	*0.57*	K_d calc. from $\eta_{0,h}$ by Eq. 3.26 **assuming raytr. K_b is correct** (exemplary for $\boldsymbol{K_{d,\perp} = 0.8}$)

For the IAM measurements, the collector position on the tracker was changed from reflectors left and right (efficiency tests) to reflectors up and down (no forced convection, because T_f was close to T_a at all test points). To avoid errors due to new setup of the hydraulic loop, the conversion efficiency $\eta_{0,h}$ was tested in IAM mode also. This is why the value in Table 3.4 and Table 3.5 slightly differs from the one given in App. B.1.
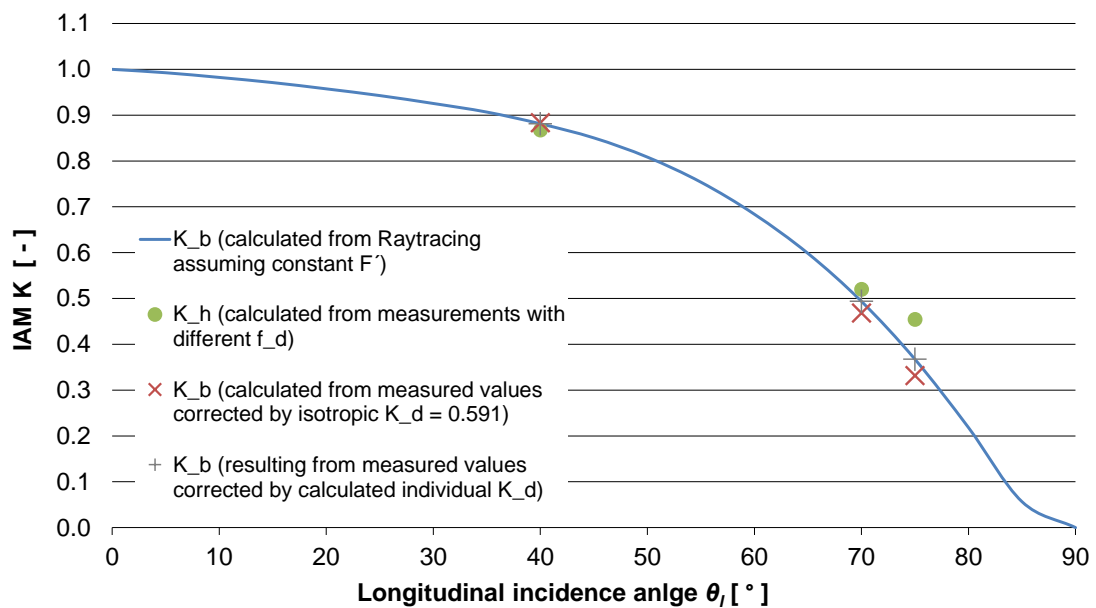
Figure 3.18: Raytraced longitudinal IAM of RefleC 1 G compared to the hemispheric IAM calculated directly from the test results (green). The red crossed values result from "correction" of each measured value by a constant isotropic $K_d = 0.591$ (Eq. 3.17) to get "pure" beam efficiency to calculate $K_b(\theta_l, 0)$. The grey values result when K_d of each measured value is determined assuming a correct K_b-curve (for details cp. Table 3.5).

Table 3.5: Raytracing results of RefleC 1 G vs. test results and „correction" calculations of longitudinal IAM $K_b(\theta_l, 0)$ (cp. Figure 3.18).

θ_l [°]	0 (⊥)	40	70	75	Comment
$(\rho\tau\alpha)_e$ [−]	0.838	0.738	0.413	0.308	Raytraced values
$\eta_{0,h}$ [−]	0.727	0.631	0.378	0.330	Measured efficiency for hemispherical irradiance
Valid test data points	7	5	5	1	Number of valid 10 min stationary test intervals for $\eta_{0,h}$
f_d [−]	0.093	0.168	**0.347**	**0.521**	Mean fraction of diffuse irrad. during valid test intervals
K_b [−]	1	0.88	0.49	0.37	Calc. by $(\rho\tau\alpha)_e$ from raytr. for constant F´(Eq. 3.20)
K_h [−]	1	0.87	0.52	0.45	Calc. from measured $\eta_{0,h}$ **without correction** (Eq.3.21)
K_b [−]	1	0.88	0.47	0.33	Calc. from measured $\eta_{0,h}$ **assuming constant isotropic $K_{d,iso} = 0.591$** (Eq. 3.25)
K_d [−]	0.591	0.60	0.52	0.50	K_d calc. from $\eta_{0,h}$ by Eq. 3.26 **assuming raytr. K_b is correct** (isotropic $K_{d,\perp} = 0.591$)
K_d [−]	*0.80*	*0.70*	*0.54*	*0.52*	K_d calc. from $\eta_{0,h}$ by Eq. 3.26 **assuming raytr. K_b is correct** (exemplary for $K_{d,\perp} = 0.8$)

General considerations: Looking at Eq. 3.22, a significant effect of diffuse irradiance on a measured efficiency value $\eta_{0,h}$ is expected, when K_d differs significantly from K_b **and** a significant share of diffuse irradiance f_d is present during the test. This is why the standard states that for the quasi-stationary case ST collectors shall generally be tested at $f_d < 0.3$ (ISO 9806:2013, p. 49). At perpendicular irradiance (efficiency curve determination), this condition can be easily fulfilled. At high incidence angles (IAM curve determination), fulfillment is difficult, since G_{bt} on the aperture decreases by $cos\theta$, while G_{dt} does not decrease at the same rate.

In principle, the task of comparing measured collector efficiencies is not trivial. It was mentioned above that $F´$ is usually unknown for a tested collector and might change with the incidence angle. A highly relevant uncertainty is the distribution of diffuse irradiance over the collector hemisphere (sky diffuse and ground reflected). This distribution is usually not known and therefore the real $K_{d,\perp}$ and K_d are not known. Assuming an isotropic distribution of diffuse (i.e. $K_{d,iso}$ from Eq. 3.17, when the K_b-values are considered to be correct) is only a "first guess", as isotropy is usually not the case at quasi-stationary collector tests ($f_d < 0.3$ requires a certain sky clearness). A large share of diffuse is the brightening around the sun, so for clear sky and perpendicular irradiance it can be expected that $K_d > K_{d,iso}$.

The other test principle, quasi-dynamic testing, considers different sky conditions, but still has the drawback that one constant collector parameter K_d is determined, which is not reflecting the dynamic reality. This is why in this work it is also tried to assess based on the quasi-stationary data, how K_d varies with the incidence angle for the different RefleC collectors.

Influence of diffuse irradiance on the conversion factor: When the isotropic $K_{d,\perp} = 0.591$ of the RefleC 1 test sample is used, $\eta_{0,b,\perp} \approx 0.756$ results (calculated by Eq. 3.23 with values of Table 3.4). When a freely chosen but tendentially more realistic value of $K_{d,\perp} = 0.8$ is assumed (last line of Table 3.4), then $\eta_{0,b,\perp} \approx 0.741$. If $K_{d,\perp}$ should indeed have been in the range between 0.6 and 0.8 during measurement of the conversion efficiency, then the underestimation of $\eta_{0,b,\perp}$ by using the measured value of $\eta_{0,h,\perp}$ would be in the range of 2 to 4 % for the f_d present at the test. For a higher f_d, of course the influence of diffuse would be higher.

Influence of diffuse irradiance, K_d and F' on K_h: First, we have to consider that the IAM is determined from a division of measured conversion factors. This means, that if two conversion factors with identical f_d, K_d and F' would be divided to calculate an IAM, we would receive a "pure" K_b-value and the influence of diffuse and F' on the IAM would be zero. So their influence is only significant when one or several of the factors f_d, K_d and F' vary between the tests at perpendicular and angular irradiance.

Looking at Figure 3.17, simply dividing the hemispheric conversion factors to receive a hemispheric IAM K_h (green dots) shows a good correlation with the raytraced curve of K_b, except for $\theta_t = 55°$. This is also observed at $\theta_l = 75°$ in Figure 3.18. At such high incidence angles, contrary to $\theta_t = 0°$, K_d is higher than K_b, and thus diffuse is affecting the collector output significantly more. This is proven by the red crossed values of K_b, resulting from the "isotropically corrected" measured efficiency values. Finally, the grey values of K_d in Table 3.4 and Table 3.5 show how the IAM for diffuse irradiance K_d would have been during test of $\eta_{0,h}$, when $K_{d,\perp}$ of 0.591 or 0.8 and correct raytracing values of K_b (with constant F') are assumed. For the longitudinal results, very realistic values are found for $K_{d,\perp} = 0.8$. In the transversal direction, a variation of F' cannot be excluded but is also not clearly indicated by the results. Such variations might be caused by varying distances between concentration lines and absorber tube weldings (cp. Figure 3.13) or by the fact that at $\theta_t = 55°$ a large share of the absorber is shaded from beam due to the opposite reflector. Finally, it has to be stressed that there is a high uncertainty in the values of $G_{d,t}$ (and thus f_d), since they were not measured in the collector aperture plane and the shading of a large part of the hemisphere by the shadow band leads to high errors.

All in all, having the above considerations and measurement uncertainties in mind, the IAM test results show a good correlation with the raytracing results; the calculated values of K_d are in a comparably reasonable range. From the investigations above for RefleC 1 it cannot clearly be answered if $F'(\theta_t) = const$.

To conclude, the raytracing simulations of the single-covered RefleC 1 collector with CPC are considered to represent the collector's IAM for beam irradiance sufficiently.

IAM test of RefleC 6 GF: Determining K_h and K_b of R6 GF was important, since this collector was used for the energy gain simulations and applied in the pilot plant. Optically, the main difference of R6 GF compared to R1 G is the second transparent cover (polarization) and that local concentration onto the absorber is avoided (cp. Figure C.3).

At testing R6 GF, a Pyrheliometer was used, so diffuse irradiance in the aperture plane was calculated with a significantly increased accuracy compared to the test of R1 G reported above. Furthermore, the collector was tested in the same position as applied at the pilot plant and forced convection was also ensured for IAM measurements. Figure 3.19 shows the IAM test result for maximum efficiency operation.
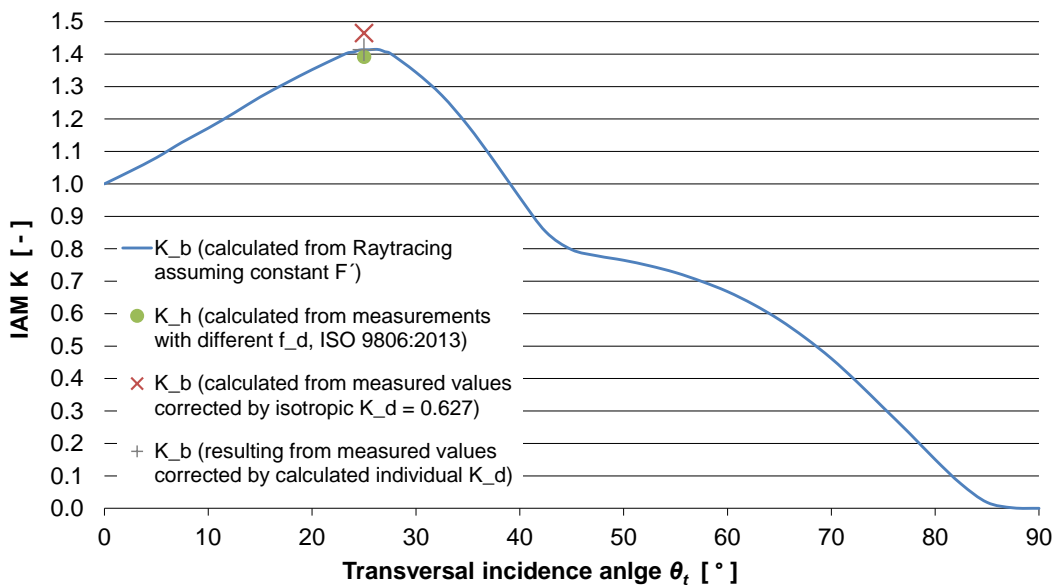
Figure 3.19: Raytraced transversal beam-IAM of RefleC 6 GF compared to its hemispheric IAM calculated from the test results (green). The red crossed values result from "correction" of each measured value by a constant isotropic $K_d = 0.627$ (Eq. 3.17) to get "pure" beam efficiency to calculate $K_b(0, \theta_t)$. The grey values result when K_d of each measured value is determined assuming a correct K_b-curve (for details cp. Table 3.6).

For RefleC 6, K_b reaches values above 1.4, since the IAM relates to the aperture and at $\theta_t \approx 25°$ the effect of the reflector is maximal. The position of the red cross shows an overestimation of K_b, when a isotropic K_d is assumed. The values of K_d calculated for assuming correct raytracing (grey cross) are significantly above the value at perpendicular irradiance. $K_d(\theta_t = 25°) = 1.07$ means that the conversion efficiency for diffuse irradiance at beam irradiance from $\theta_t = 25°$ is higher than the conversion efficiency for beam at perpendicular irradiance. This is plausible, since sky diffuse represents a major share of hemispheric diffuse and in case of relatively clear sky the brightening around the sun experiences the same high IAM values as beam irradiance. When the isotropic $K_d = 0.627$ of the RefleC 6 test sample is used, it results $\eta_{0,b,\perp} \approx 0.780$ (cp. Eq. 3.23 and Table 3.4). When as for RefleC 1 G a value of $K_{d,\perp} = 0.8$ is assumed, then $\eta_{0,b,\perp} \approx 0.761$, so the underestimation of $\eta_{0,b,\perp}$ by using the measured $\eta_{0,h,\perp}$ should be in the range of 2 to 5.5 % for the f_d present at the test.

Table 3.6: Raytracing results of RefleC 6 GF vs. test results and „correction" calculations of transversal IAM $K_b(0, \theta_t)$ (cp. Figure 3.17).

θ_t [°]	0 (⊥)	25	Comment
$(\rho\tau\alpha)_e$ [−]	0.806	1.138	Raytraced values
$\eta_{0,h}$ [−]	0.741	1.031	Measured efficiency for hemispherical irradiance
Valid test data points	4	2	Number of valid 10 min stationary test intervals for $\eta_{0,h}$
f_d [−]	0.134	0.170	Mean fraction of diffuse irrad. during valid test intervals
K_b [−]	1	1.41	Calc. by $(\rho\tau\alpha)_e$ from raytr. for constant F´(Eq. 3.20)
K_h [−]	1	1.39	Calc. from measured $\eta_{0,h}$ **without correction** (Eq.3.21)
K_b [−]	1	1.46	Calc. from measured $\eta_{0,h}$ **assuming constant isotropic** $K_{d,iso} = \mathbf{0.627}$ (Eq. 3.25)
K_d [−]	0.627	0.88	K_d calc. from $\eta_{0,h}$ by Eq. 3.26 **assuming raytr. K_b is correct** (isotropic $K_{d,\perp} = \mathbf{0.627}$)
K_d [−]	0.80	1.07	K_d calc. from $\eta_{0,h}$ by Eq. 3.26 **assuming raytr. K_b is correct** (exemplary for $K_{d,\perp} = \mathbf{0.8}$)

To conclude, a "validation" of the raytraced K_b in the strict sense could not be performed by the measurements, since the angular distribution of diffuse irradiance could not be measured and the effects of $F´$ and varying conversion efficiency for diffuse cannot be separated in the calculations. But the following was shown:

- The IAM values of R1 G and R6 GF calculated from test results correspond very well to the raytracing results.
- The IAM for diffuse irradiance $K_d(\theta)$ of a collector is not constant
- For RefleC 6 GF, $F´(\theta)$ can be assumed to be constant, since already at the potentially higher sensitive RefleC 1 a variation was not distinctly visible.

3.4.4 IAM Effect on Thermal Efficiency Curve

For non-perpendicular irradiance of beam or diffuse, the aperture-based collector efficiency curve experiences a vertical translation by K_h. To generate the following Figure 3.20, a standard efficiency curve of R6 GF was measured at $\theta_t = 0°$. This curve is compared to measured efficiencies at $\theta_t = 25°$. Purpose of this comparison is to confirm, that the power output of RefleC is correctly represented by the standard approach of Eq. 3.9 for different fluid temperatures, mass flows and incidence angles.

The measured curve was multiplied by the raytraced $K_b = 1.41$, corresponding to $\theta_t = 25°$. This value was used instead of the measured $K_h = 1.39$ (cp. Figure 3.19 and Table 3.6) to allow for independent comparison. Besides, the investigations above had shown that for small incidence angles and similar f_d, K_h is very similar to the raytraced K_b. The theoretical, dashed green curve is plotted for the same irradiance as at the high temperature tests to allow for a comparison of all measured values in one graph.
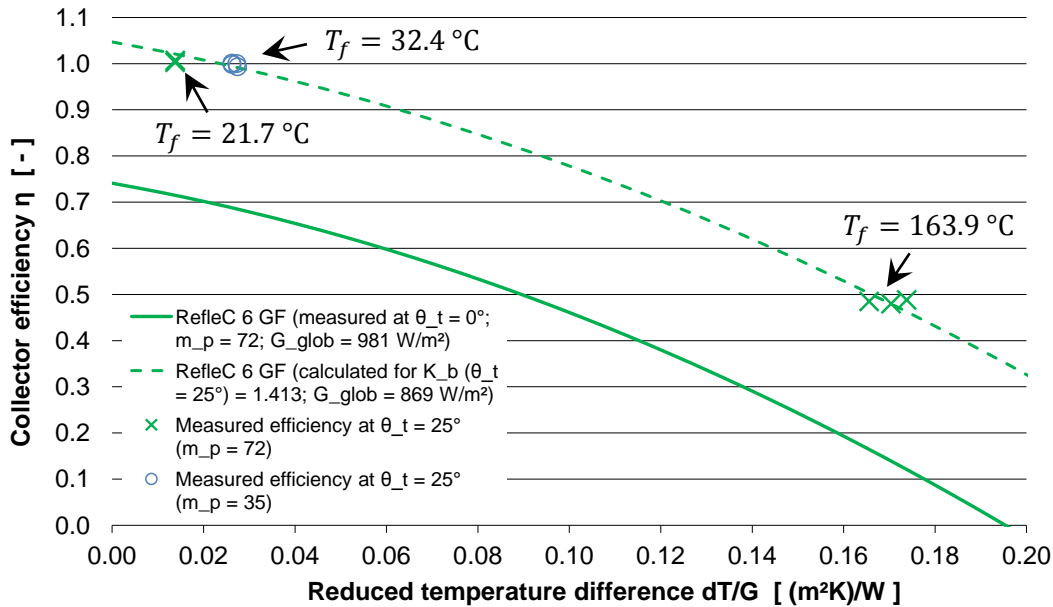
Figure 3.20: Efficiency test results (outdoor, MTTS) of RefleC 6 GF for perpendicular irradiance (solid green) and for irradiance from $\theta_t = 25°$ at two different T_f and $\dot{m}$ (values cp. Table 3.7). The aperture-related theoretical curve for $K_b = 1.41$ is dashed green.

Besides confirming the validity of Eq. 3.9 for RefleC, this representation shows the increasing contribution of K_h to the collector output at increasing thermal losses (right hand side of diagram). An error in the IAM-value would cause a constant absolute error in collector output along the whole efficiency curve, but the influence of this IAM-error in percentage terms would highly increase at lower efficiencies.

Table 3.7: Stationary test data points of RefleC 6 GF at $\theta_t = 25°$ (cp. Figure 3.20)

Date	Time (UTC)	G_t [W/m²]	G_{dt}/G_t [−]	$\dot{m}$ [kg]	T_a [°C]	T_{in} [°C]	T_{out} [°C]	T_f [°C]	η [−]
12.10.2010	13:46:45	869	18.0	363.01	12.9	161.47	166.4	163.9	0.488
12.10.2010	13:56:45	861	18.1	362.72	21.3	161.42	166.28	163.9	0.485
12.10.2010	14:06:45	855	18.6	362.86	18.2	161.47	166.25	163.9	0.480
21.10.2010	12:53:00	967	16.3	367.21	8.3	15.80	27.36	21.6	1.003
21.10.2010	13:03:00	964	17.8	367.12	8.4	15.89	27.46	21.7	1.007
26.10.2010	12:49:45	912	14.3	183.37	7.4	21.59	43.22	32.4	0.993
26.10.2010	12:59:45	910	13.9	183.38	7.6	21.59	43.32	32.5	1.000
26.10.2010	13:09:45	901	13.8	183.32	8.0	21.61	43.16	32.4	1.002
26.10.2010	13:19:45	916	14.3	183.42	8.2	21.58	43.3	32.4	0.993

3.4.5 Test Sample Performance with two CPC Reflectors

In this and the following section, the tested efficiency parameters of all RefleC test samples and of their receiver flat-plate collectors are compared and further investigated. The efficiency-curves of the early-stage collectors with upper and lower reflectors are shown in Figure 3.21. The flat-plate LBM 67 (1 x AR), receiver of RefleC 1, was not tested at Fraunhofer ISE. Thus, for this comparison efficiency curve parameters reported by Wagner & Co. Solartechnik are used. The values result from standard efficiency tests according to (EN 12975-2:2006), but the exact conditions for determining these parameters are not known (i.e. indoor- or outdoor, f_d, $T_{f,max}$ are not known).
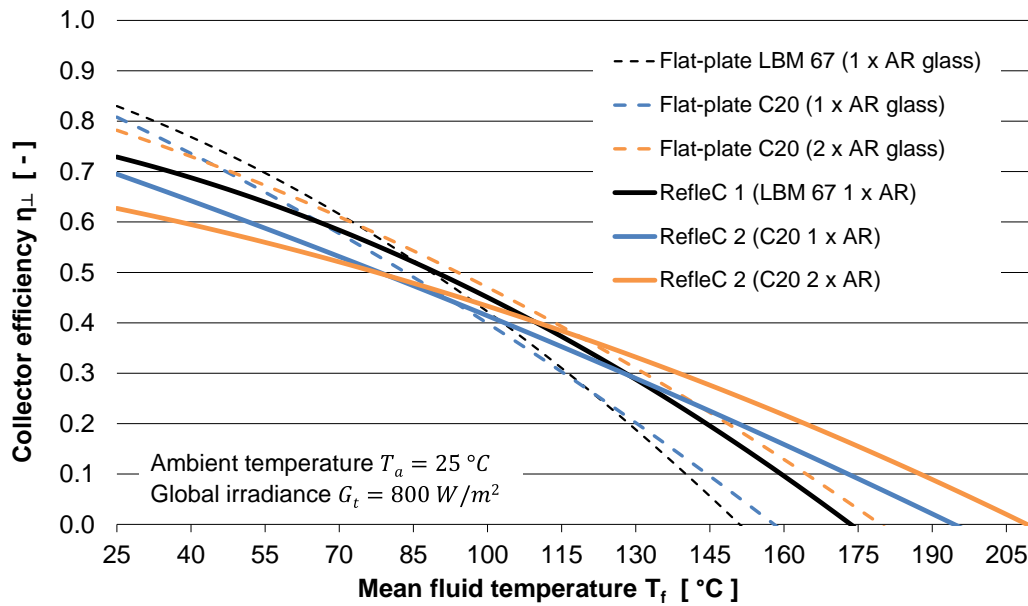
Figure 3.21: Comparison of measured efficiency curves of RefleC 1 and 2 (two reflectors) and their flat-plate receiver collectors. The respective values are given in Table 3.8.

Thermal loss coefficients: The reflectors increase the aperture area and thus at $\theta = 0°$ the irradiance onto the flat-plate. Thermal losses still occur only at the thermally insulated flat-plate, so that the concentration is expected to reduce the aperture area specific thermal losses. This was verified by testing RefleC 1 (lower slope of curve than LBM 67) and further confirmed testing the other RefleC samples and receiver collectors. Precisely, it is shown in section 3.4.7 that the heat loss coefficients c_1 and c_2 of RefleC can be calculated from the ones of its flat-plate receiver by relation of the apertures.

Conversion factors: Figure 3.21 reveals that physically every reduction of thermal losses due to concentration results in the drawback of lower conversion factors $\eta_{0,h}$. This results from increased optical losses (cp. section 2.2.1), decreased acceptance of diffuse irradiance and depending on absorber type and concentrator shape, also from decreased collector efficiency factors due to local concentration. RefleC with two CPC reflectors shows a high decrease in conversion efficiency per aperture. For R1 G it is approx. 12 %, for R2 G approx. 14 % and for R2 GG even 20 % (cp. Table 3.8).

Qualitative assessment of RefleC with two CPC-reflectors: Having in mind the aim to significantly increase efficiency and annual energy gain of a standard flat-plate at working temperatures T_f between 80 and 150 °C, the results of Figure 3.21 are not satisfying. The performance of the double glazed collector without reflectors is encouraging. Comparing C20 GG to C20 G shows a high increase of efficiency within the working temperature range and below. K_b (and thus K_d) is only marginally lower than of C 20 G. But of course the overall efficiencies are still low, so that a further increase of efficiency as desired by the reflectors seems necessary for economic SPH systems.

Table 3.8: Overview of measured RefleC and flat-plate receiver collector efficiency parameters complemented by raytracing results and calculated values. Here and in the following, $(\rho\tau\alpha)_{e,\perp}$ is used for RefleC and the flat-plate receiver (though this one has no reflector).

Test sample	Raytraced [a]			Measured [b]				Calculated [c]			
	C_{geo} [−]	$(\rho\tau\alpha)_{e,\perp}$ [−]	$K_{d,iso}$ [−]	$\eta_{0,h,\perp}$ [−]	c_1 $\left[\frac{W}{m^2K}\right]$	c_2 $\left[\frac{W}{m^2K^2}\right]$	$f_{d,\perp}$ [−]	$\eta_{0,h,\perp}$ [−]	c_1 $\left[\frac{W}{m^2K}\right]$	c_2 $\left[\frac{W}{m^2K^2}\right]$	$F'_\perp$ [−]
Flat-plate **LBM 67** (1 x AR glass)	-	0.894	-	0.83	3	0.018	-	-	-	-	-
RefleC 1 (LBM 67 1 x AR)	1.435	0.838	0.591	0.729	1.996	0.013	0.093		2.091	0.013	0.905
Flat-plate **C20** (**1 x AR** glass)	-	0.894	0.869	0.808	3.716	0.009	0.2	-	-	-	0.928
Flat-plate **C20** (**2 x AR** glass)	-	0.842	0.843	0.782	2.642	0.009	0.2	-	-	-	0.959
RefleC 2 (C20 **1 x AR**)	1.625	0.806	0.486	0.695	2.773	0.003	0.063	0.670	2.287	0.005	0.892
RefleC 2 (C20 **2 x AR**)	1.625	0.750	0.485	0.627	1.618	0.006	0.188	0.602	1.626	0.006	0.926
RefleC 5 (LBM 22 GF)	1.257	0.793	0.614	0.723	1.79	0.005	0.123	-	-	-	0.958
Flat-plate **LBM 4 GF** (glass + foil)	-	0.841	0.819	0.794	1.87	0.017	0.132	-	-	-	0.967
RefleC 6 (LBM 4 GF)	1.257	0.806	0.627	0.741	1.761	0.011	0.134	0.740	1.488	0.013	0.968

[a] $K_{d,iso}$ calculated from K_b of the test samles (cp. Figure C.1 and Figure C.2) by Eq. 3.26.

[b] Efficiency parameters of LBM 67 reported by Wagner & Co. Solartechnik, not tested at Fraunhofer ISE. C 20 was tested at the indoor sun simulator, where $f_{d,\perp}$ is not measured. A constant fraction of 20 % is assumed.

[c] F' calculated by Eq. 3.27 with K_d representing K_r and K_s (they can not be assessed because only the sum of $G_{dt} = G_{st} + G_{rt}$ is measured); $\eta_{0,h,\perp}$ is calculated by Eq. 3.28, c_1 and c_2 are calculated by Eq. 3.29 and 3.30.

Unfortunately, the efficiency of R1 G (single glazing) is at all working temperatures below that of the double glazed flat-plate C20 GG. R2 GG, where double glazing as well as CPC concentrator is applied, shows significantly reduced thermal losses. But the efficiency within the application temperature range is well below 50 % and only at elevated temperatures marginally above C20 GG. Generally, for two CPC-reflectors, the reduced thermal losses are almost compensated by the reduced conversion efficiency.

After these first tests it was important to reflect on the RefleC concept in general, especially on the low conversion efficiency. Can the three conversion loss effects mentioned above be quantified? Can one or several of these effects be reduced and if yes, at which increase of thermal loss coefficients? And not to forget, how does the shape of the K_b-curve (and the IAM K_d for diffuse) affect the collector's annual gain? Complementing the collector development by accurate output simulations was crucial, since finally the annual gain, and not the efficiency curve, is the decisive performance criterion.

Effective optical losses: Contrary to irradiance onto a flat-plate aperture, irradiance onto the RefleC aperture experiences absorption losses at the share of the aperture covered by reflectors (i.e. $1/C_{geo}$). Furthermore, the non-perpendicular incidence of the reflected rays onto the receiver cover results in lower transmittance of these rays than at

perpendicular incidence. Both factors reduce $(\rho\tau\alpha)_{e,\perp}$. Comparing RefleC 2 to its receiver collectors C20 G and C 20 GG in Table 3.8 reveals that for both the decrease in optical efficiency is very high. The raytracing values show for R1 G a reduction in optical efficiency of ca. 6 % compared to LBM 67 G. This further decreases for R2 G (ca. 10 % compared to C20 G) and R2 GG (ca. 11 % compared to C20 GG).

IAM for diffuse: The diffuse-IAM $K_{d,iso}$ of the single-covered flat-plates is maximal and slightly decreasing for a double cover. The K_b-shape of each RefleC test sample determines $K_{d,iso}$. Due to the reduced acceptance angle, R1 G shows a decrease of ca. 30 % in diffuse utilization, while R2 G and GG show an even higher decrease of above 40 % compared to their receiver flat plates.

Calculated collector efficiency factors: From the investigations in section 3.4.3 it is expected that setting $K_{d,\perp} = K_{d,iso}$ does not reflect reality. But possible errors of this approach can be expected to be similar for one RefleC geommetry. For the purpose to finally separate the effects of optical losses, reduced diffuse acceptance and reduced F', it can be calculated following Eq. 3.7:

$$F'_{\perp} = \frac{\eta_{0,h,\perp}}{(\rho\tau\alpha)_{e,\perp}\cdot[(1-f_d)+f_d\cdot K_{d,\perp}]} \qquad \text{with} \quad f_d = \frac{G_{dt}}{G_t} = 1 - f_b \qquad (3.27)$$

The results of this calculation are remarkable already for the flat-plate. The optical efficiency $(\rho\tau\alpha)_{e,\perp}$ of C20 GG is approx. 6 % below that of C20 G, while the difference in $\eta_{0,h}$ is only approx. 3 %. Application of Eq. 3.27 reveals that this is due to an approx. 3 % increase of F', when the second cover is applied (cp. right column of Table 3.8).

This is plausible, since F' depends on the front heat losses, which are reduced by the second cover. Both collector variants were tested at a solar simulator, for which a diffuse fraction of $f_{d,\perp} = 0.2$ is assumed (not measured). For RefleC, the F'-calculation is also very enlightening. A comparison of R2 with its respective receivers indeed shows an decrease of F' due to the CPC-concentration of about 4 %, both in the case of single and double glazing. Since the flat-plate LBM 67 was not tested at ISE, F' cannot be calculated here due to missing information. But R2 G and R1 G show a very similar calculated F', so that the effect can be assumed for all flat-plates with CPC reflectors.

Sensitivity of the decreased hemispheric conversion efficiency: The high absolute reduction of $(\rho\tau\alpha)_{e,\perp}$ by the reflectors and its direct effect on $\eta_{0,h}$ due to multiplication (cp. Eq. 3.7) reveal that the major share of the observed reduction of the conversion efficiencies is caused by the increased optical losses. The efficiency factor F' is also directly multiplied, so a decrease here causes the same decrease of $\eta_{0,h}$. The effect of $K_{d,iso}$ on $\eta_{0,h}$ depends on f_d during the test. In case of R2 G the effect of reduced $K_{d,iso}$ is smaller than of the reduced F'; in case of R2 GG the reduced $K_{d,iso}$ overweighs because of the relatively high $f_d = 0.188$ during this test.

3.4.6 Test Sample Performance with One Reflector

The detailed analysis of the test results of RefleC with two CPC reflectors revealed many opportunities to further improve the RefleC concept. Due to lower costs, higher roof-area efficiency and higher annual gains per reflector area it was decided to apply only one lower reflector. Comparative simulation results for RefleC with one and two reflectors can be found in (Raucher 2009).

Systematic improvement: The optical losses were reduced by increasing the reflectors reflectivity. Local concentration on the absorber was reduced to $C_{max} = 4$ by applying a reflector with three flat-segments approximating the one-sided CPC-shape, which for the optimal $\theta_a = 35°$ additionally results in significantly lower incidence angles of the reflected rays onto the flat-plate than at RefleC 1 and 2. Furthermore, the backside insulation of LBM 4 GF was improved compared to C20 GG. In Figure 3.22, the efficiency test results for the original and the improved concept are shown.
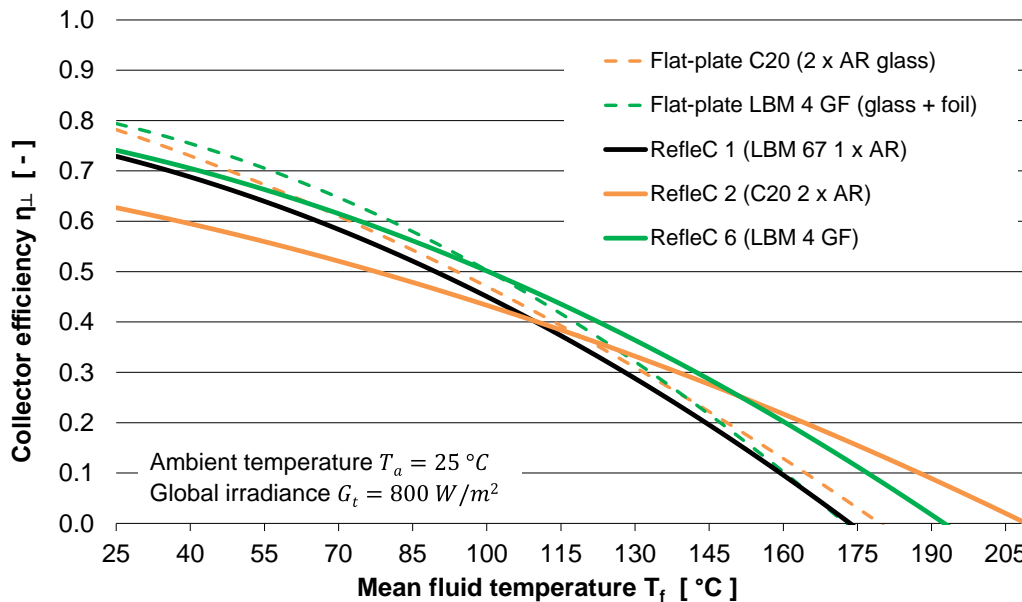
Figure 3.22: Comparison of measured efficiency curves of RefleC 1 and 2 (two reflectors) to RefleC 6 (one segmented lower reflector) and their flat-plate receiver collectors. The respective values are given in Table 3.8. Results for RefleC 5 are not shown since they are not valid for the whole temperature range.

Results of improvements: Comparing the flat-plates, the slightly higher transmittance of the foil compared to a second glazing results in a slightly higher $\eta_{0,h}$. The efficiency decrease with temperature is higher with glass-foil cover than for double glazing. This is due to higher IR-transmittance of the foil and speculatively due to sagging of the foil at higher temperatures, resulting in suboptimal distance between glazing, foil and absorber. Improved backside insulation as expected reduces losses at high temperatures.

At higher irradiance levels, the aperture-area specific efficiency of R6 GF is above that of R1 G and R2 GG. The thermal loss coefficients are higher due to the lower concentration, but the conversion efficiency is more than 10 percentage points above R2 GG,

which compensates the higher specific losses. But, of course it has to be remembered that differences in the efficiency curves here do not result in the same differences in annual energy gain, since RefleC 6 has a significantly better transversal K_b-behavior than RefleC 1 and 2. Summarizing the advantages of RefleC with one lower, segmented reflector compared to the concept with two reflectors, as they result from the measurements reported above, leads to the following conclusions:

- The reflector does not increase in F' anymore. This results in a parallel upward translation of the efficiency curve of four percentage points compared to R2.
- Because the beam-IAM reaches values above 1.4, significant additional gains (in summer) are to be expected. This parallel translation of the curve due to $K_b > 1$ (cp. Figure 3.20) does not occur for RefleC 1 and 2, where $K_b < 1$ for all θ.
- Significantly more diffuse irradiance can be utilized.

3.4.7 Efficiency Curve Calculation for RefleC

If the thermal efficiency curve of a receiver collector is known, one may want to assess the efficiency curve of a RefleC collector variant theoretically based on the test results of its flat-plate receiver collector. This can have the following purposes:

- Generation of theoretical efficiency curves of RefleC variants for optimization simulations. Not all variants (e.g. with varying θ_a) can be built and tested.
- Predicting the efficiency of a RefleC test sample to evenly distribute test collector inlet temperatures T_{in} over the whole range of $\Delta T/G_t$ for measuring a high quality efficiency curve.
- Plausibility check of collector efficiency curves determined from test results.

Conversion factor: Relating the conversion efficiency of a receiver (here called flat-plate $\eta_{0,\perp,fp}$) to that of RefleC $\eta_{0,\perp,R}$ results in:

$$\eta_{0,\perp,R} = \eta_{0,\perp,fp} \cdot \frac{F'_{\perp,R} \cdot (\rho\tau\alpha)_{e,\perp,R} \cdot [(1 - f_{d,R}) + f_{d,R} \cdot K_{d,R}]}{F'_{\perp,fp} \cdot (\tau\alpha)_{e,\perp,fp} \cdot [(1 - f_{d,fp}) + f_{d,fp} \cdot K_{d,fp}]} \tag{3.28}$$

The factors $(\rho\tau\alpha)_{e,\perp}$ and $K_{d,iso}$ of flat-plate and RefleC can be determined by raytracing. Regarding the factor F' it has to be assessed if it can change when the reflector is applied. If the calculated curve shall e.g. be valid for the same irradiance conditions as during test of the flat-plate, f_d can be set identical. To evaluate the plausibility of measured curves, the measured f_d and F' calculated from the test results can be used.

Heat loss coefficients: They can be calculated by Eq. 3.29 and Eq. 3.30.

$$c_{1,R} = c_{1,fp} \cdot \frac{A_{ap,fp}}{A_{ap,R}} = c_{1,fp} \cdot \frac{1}{C_{geo,R}} \tag{3.29}$$

$$c_{2,R} = c_{2,fp} \cdot \frac{A_{ap,fp}}{A_{ap,R}} = c_{2,fp} \cdot \frac{1}{C_{geo,R}} \tag{3.30}$$

This is because the heat loss coefficients (not the absolute heat losses!) are independent of the optical collector properties and proportional to $1/C_{geo}$, when the flat-plate remains the same and both parameter sets refer to the aperture area. For the flat-plate receivers tested, the following Figure 3.23 shows the calculated corresponding RefleC efficiency curves.

Result: The calculated efficiency parameters of RefleC 2 show a small deviation from the measured ones. This is because of a higher uncertainty since values determined indoor at the simulator are compared to outdoor test results. Furthermore, the high mass flow of $\dot{m} = 300 \text{ kg/(m}^2\text{h)}$ leads to higher uncertainties because of a low ΔT, and air extraction out of the test loop was difficult because of a double-harp absorber. The calculated efficiencies of R6 GF correspond very well to the test results. It can be concluded that at least for this variant the theoretical calculation of efficiency parameters for other θ_a to use them for optimization simulations is permissible.
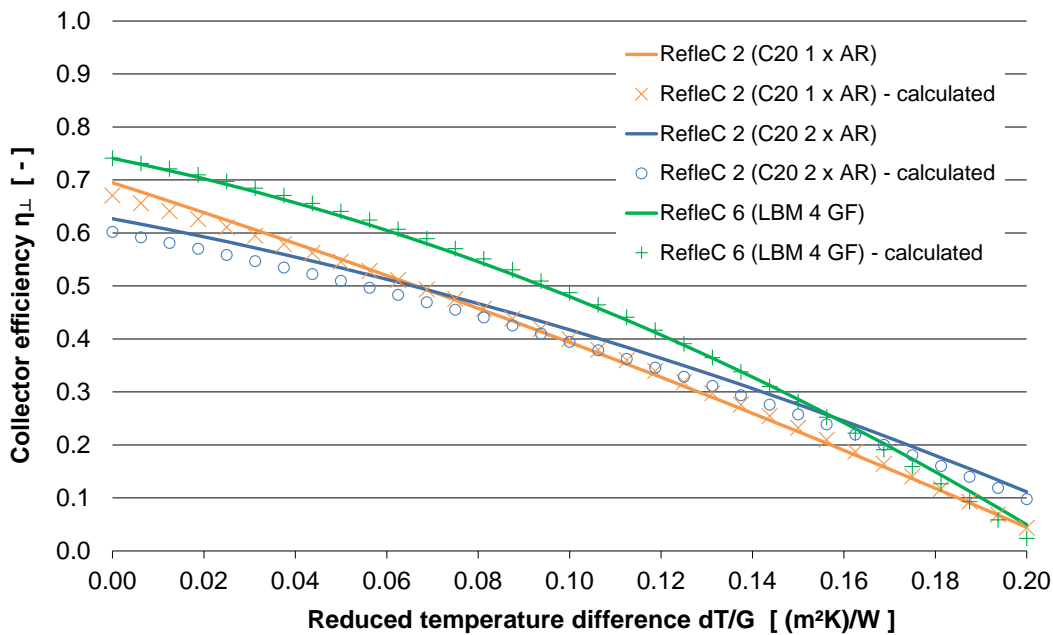
Figure 3.23: Comparison of the measured thermal efficiency curves of RefleC 2 G/GG and RefleC 6 GF to efficiency curves calculated based on raytracing and test results of their flat-plate receiver collectors. For the calculations, the values from Table 3.8 were used.

4 Energy Gain Simulations

A new collector simulation model is discussed. It considers the influence of the varying anisotropy of sky diffuse irradiance on a collector's IAM and energy gain. This influence is determined for RefleC and its flat-plate receiver collector. Initially, the chapter gives fundamental information on the different solar irradiance components and their consideration in state of the art simulations. The findings from the new modeling approach are analyzed in detail and reflected against the state of the art.

In the course of the RefleC collector development, the energy gain of certain collector variants had to be assessed and compared to other variants or collector types. Raytracing results revealed a very distinct radiation acceptance of the collector. In conjunction with the collector efficiency tests reported in the last chapter they indicated that the anisotropy of diffuse irradiance may be of significant relevance for accurate assessment of the annual collector yield. To investigate this, a new simulation approach was developed. Figure 4.1 illustrates the input values and parameters needed:
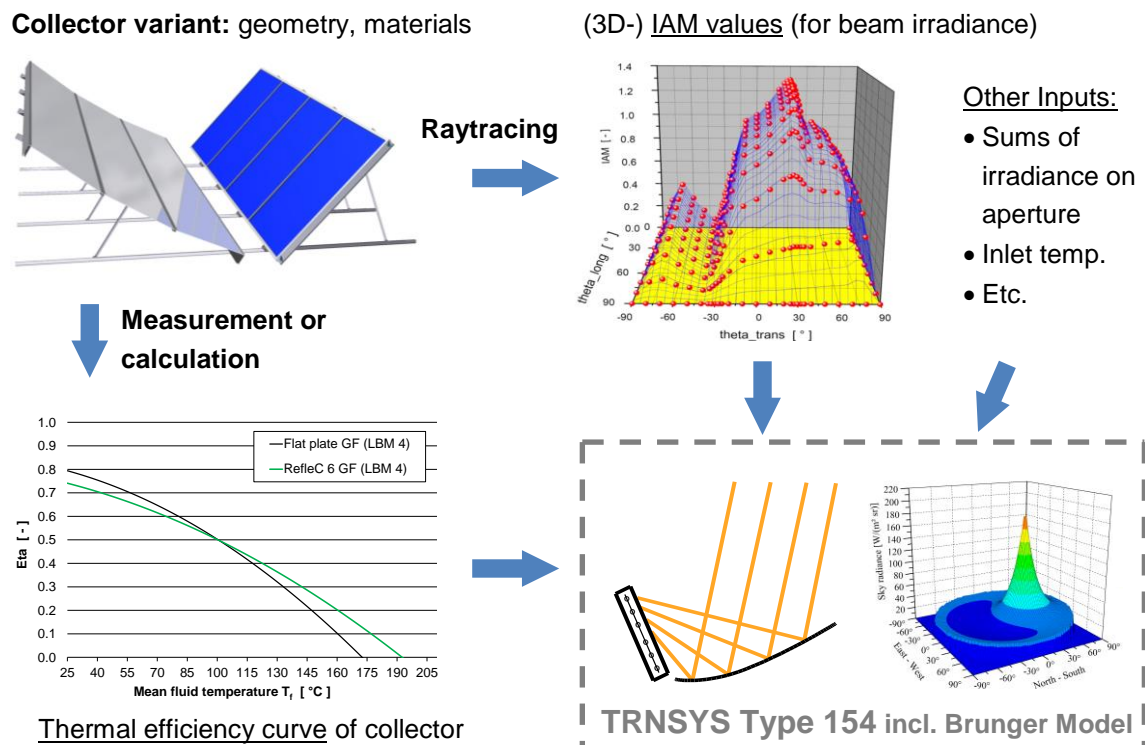
Figure 4.1: Values needed for new collector model "Type 154" to calculate the annual energy gain of a certain collector variant based on its thermal and optical properties.

4.1 Modeling Anisotropic Diffuse Irradiance

Low-concentrating ST collectors show a high but very incidence-angle selective acceptance of diffuse irradiance. In reality this irradiance is to different extents anisotropic (cp. section 2.1.3) and the varying circumsolar radiance is at times with high collector gains often within θ_a of the collector. Therefore, the angular distribution of incident diffuse irradiance is expected to have significant influence on the collector energy gain.

From the discussions in section 3.2.3, we realize that diffuse irradiance can be understood as beam irradiance originating from the whole collector hemisphere (sky dome and ground). This leads to the fundamental approach of this work, which is that accurate instantaneous diffuse-IAM values for sky and ground irradiance (K_s and K_r) can be calculated by weighting the irradiance from hemispheric sky and ground segments visible for the collector aperture by the individual beam-IAM values of these segments. Eq. 3.17 already follows this thought, but assumes isotropic radiance.

To evaluate the different RefleC concepts and to accurately calculate the additional gains by the reflectors, a time-dependent anisotropic modelling of diffuse irradiance and the corresponding K_s was realized. In this case, K_s is not a constant collector parameter anymore, but changes with varying diffuse irradiance distribution.

This distribution is not available from weather data files or the radiation processors used in state-of-the-art solar thermal simulation programs (cp. sections 2.1.2 and 4.2.1). Thus, it had to be modelled within the developed collector Type 154 to allow for considering it when determining K_s. As a first step, an appropriate model for the anisotropic distribution of diffuse radiance across the sky dome had to be selected.

4.1.1 Review of Available Models

To account for anisotropic sky radiance incident on sloped surfaces, different models have been developed. The most common are the Hay-Davies-Model (Hay 1979), the Reindl-Model (Reindl et al. 1990) and the Perez-Models (Perez et al. 1986 ; Perez et al. 1987 ; Perez et al. 1990). A comparison between these and some other models can be found e.g. in (Reindl et al. 1990), (Evseev and Kudish 2009), or (Gueymard 2009). All of the named models have in common that they provide the sum of incident diffuse irradiance from a non-uniform sky on a tilted plane, but they do not give a continuous anisotropic distribution of diffuse sky radiance.

To achieve a high accuracy at calculating K_s, only more detailed models, providing a continuous sky radiance distribution over the hemisphere, were considered. The models of Igawa et al. (2004), the *Perez All-Weather-Model* (Perez et al. 1993), the *Brunger Model* (Brunger and Hooper 1993), and the models of Harrison (1991) and Kittler (1985) fall into this category.

Igawa et al. (2004) compared different sky radiance distribution models for a high variety of weather conditions. Among others, they compared their highly elaborated All-Sky-Model-R to the Brunger model and the Perez All-Weather-Model. The model quality was assessed by determining *MBE (Mean Bias Error)* and *RMSE (Root Mean Square Error)* of the models. The MBE is the average of all relative deviations from real sky radiance and therefore identifies the overall over- or underestimation of a model compared to the measured data base. The RMSE, on the other hand, is a measure for the distribution range of the modeled values around the measured ones (Badescu 2008, pp. 136-138). The calculation of both values is given by Eq. 4.1 and 4.2. Therein, y_{ci} is the calculated value, y_{mi} the measured, and n the number of comparison values.

$$MBE = \frac{1}{n}\sum_{1}^{n}\frac{y_{ci} - y_{mi}}{y_{mi}} \tag{4.1}$$

$$RMSE = \sqrt{\frac{1}{n}\sum_{1}^{n}\left(\frac{y_{ci} - y_{mi}}{y_{mi}}\right)^2} \tag{4.2}$$

A further explanation of these values together with an exemplary assessment of solar diffuse radiance models can be found in (Iqbal 1983, pp. 383-386).

The validation results of the three most precise models identified by Igawa et al. (2004) are summarized in Figure 4.2 for different categories of instantaneous cloudiness.
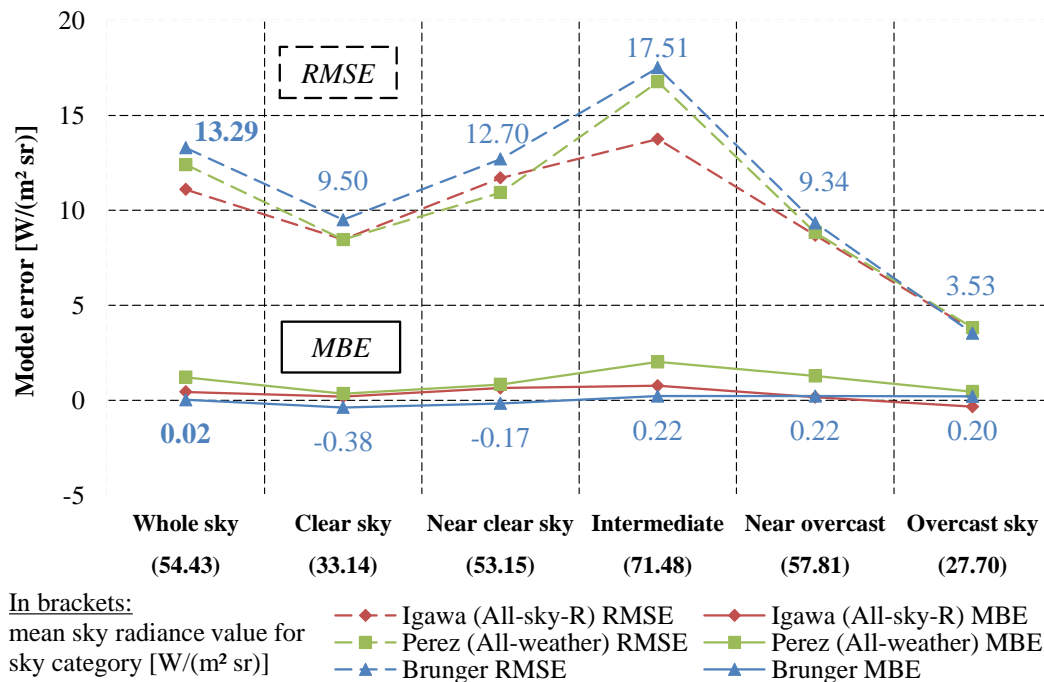
Figure 4.2: Sky radiance modeling errors of the continuous models of Igawa et al. (2004), Perez et al. (1993) and Brunger and Hooper (1993), when compared to real skies. Results of Igawa et al. (2004, p. 152), graphic adapted from Raucher (2009, p. 13).

The irradiance data used for this validation were measured with a sky-scanner of acceptance half-angle 11°. The data were collected from March 1992 to September 1993 in Tokyo and from January to December 1994 in Fukuoka, Japan. These values at the same time also provide the database for the development of the Igawa-Model. Therefore, it is important to note that the validation of this model was not done independently.

The Brunger model shows the lowest MBE of the three models when all sky conditions are considered (cp. $0.02\,W/(m^2sr)$ for *whole sky*), so for annual simulations the generated distributions should be a good representation of the distributions occurring in reality. In comparison to the model of Igawa, the models of Perez (All-Weather) and Brunger show significantly higher RMSE values for intermediate skies. The RSME of Brunger is the highest of all three models but still only approx. $2\,W/(m^2sr)$ higher than Igawa, when all sky conditions are considered. Brunger and Hooper state that their model covers 83 % of the deterministic variation in instantaneous sky radiance and they recommend their model to calculate irradiance incident on CPC collectors with complex or biangular incidence angle modifiers (Brunger and Hooper 1993, p. 53). Only the All Sky Model-R of Igawa and the Brunger Model were explicitly designed for solar sky radiance distribution. The All Sky Model-L of Igawa, the Perez All-weather-, Harrison- and Kittler-Model were originally developed for sky brightness distribution. Badescu (2008, p. 428) states that brightness is in direct correlation with radiance since it is only weighted with the sensitivity of the human eye, so the relative distribution of brightness and radiance should be approximately identical. Figure 4.2 indeed does not show an apparent systematic error of the brightness models in predicting sky radiance. But Figure 2.16, Figure 2.20 and Figure 2.25 clearly show the wavelength-dependence of the optical ST collector properties, also outside the spectrum of visible light. A significant share of diffuse spectral irradiance is in the UV range (cp. Figure 2.2). Thus, selecting a brightness distribution model for the current task might have involved additional uncertainties for ST collector output calculation.

Finally, the selection of a model to apply in collector energy gain simulations could not only be based on the maximal accurate representation of irradiance from real skies. The formulation of the model also had to be not too complex, because programming errors and long simulation times had to be avoided. The Igawa model has a significantly higher complexity than the Brunger model. Considering and weighing all the factors above, it was decided to use the Brunger model for inclusion in Type 154.

4.1.2 Brunger Model

Within collector Type 154 described in the next section, the model of Brunger and Hooper (1993) is applied to generate a realistic distribution of sky diffuse radiance over the sky dome in every simulation time step. This is used to calculate the irradiance from finite sky elements onto the sloped collector. This irradiance is weighted with the re-

spective raytraced K_b-value of each sky element. <u>Integration results in a new collector IAM K_s for diffuse</u> sky irradiance, <u>whenever the</u> radiance <u>distribution changes.</u>

The meteorological data set used to develop the Brunger Model was measured from February 1983 to February 1984 at the University of Toronto, Canada (latitude 43° 40´ N) (Brunger and Hooper 1993, p. 53). This set contains irradiance measurements from a 5° acceptance half-angle pyroelectric radiometer, measuring 10° hemispherical intervals and being blocked from beam by a shadow ball (Siala and Hooper 1990, p. 293).

Mathematical Description: The Brunger Model describes the distribution of diffuse sky radiance $L(\theta_h; \phi_h)$ in any direction, defined by zenith angle θ_h and azimuth gle ϕ_h of each sky element (cp. Figure 4.3). This distribution is continuous (cp. Figure 4.4 to Figure 4.7) and an integration over the solid angles results in the horizontal diffuse irradiance G_d or for sloped collectors in G_{st}.
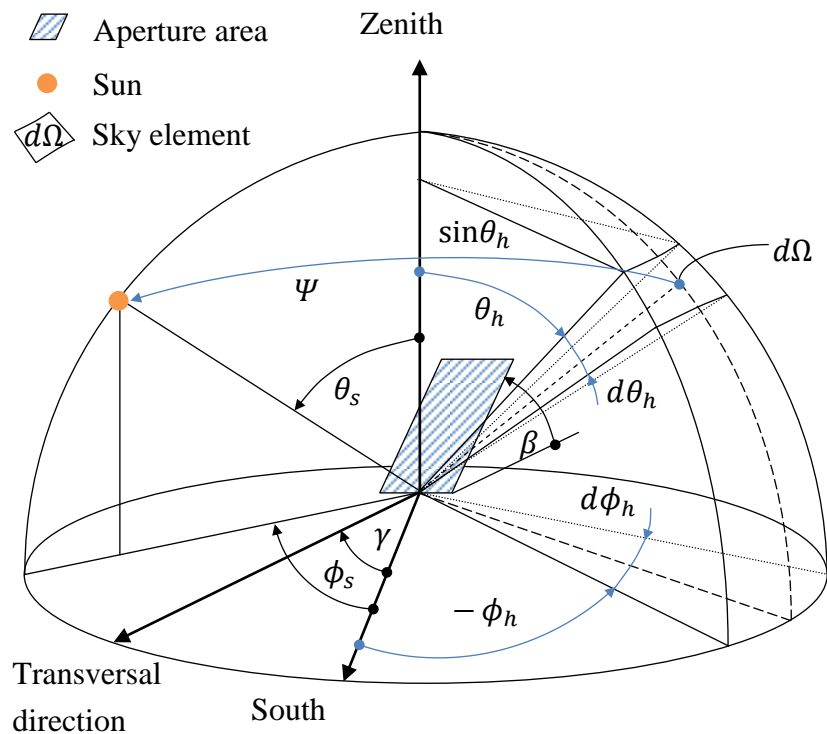
Figure 4.3: Horizontal plane with positions of sun and diffuse radiating sky element $d\Omega$. The collector is positioned by its azimuth γ and slope β. The sun is located by sun azimuth ϕ_s and solar zenith angle θ_s. The azimuth of the center of a considered sky element is ϕ_h, its zenith angle is θ_h. The angle between sun and sky element is Ψ.

For this work, some variable names of the Brunger Model have been modified to avoid duplications with common variable names in the solar thermal field. The standardized function of the Brunger distribution is:

$$\frac{L(\theta_h, \phi_h)}{G_d} = \frac{a_0 + a_1 \cos\theta_h + a_2 \exp(-a_3 \cdot \Psi)}{\pi(a_0 + 2a_1/3) + 2a_2 I(\theta_s, a_3)} \quad (4.3)$$

Input to the distribution from the weather data is provided by the correct determination of the Brunger coefficients a_0 to a_3. In Eq. 4.3, the three main fractions of sky radiance are considered: The coefficient a_0 accounts for the isotropic background; the horizontal brightening is modeled by a cosine-function, and the circumsolar radiance by an exponential function. In addition to the sun position, only the two factors k, the fraction of diffuse irradiance on the horizontal, and k_t, the atmospheric clearness index are needed from the weather data to set up the sky radiance distribution. The clearness-index is the quotient of the global irradiance G and the horizontal extraterrestrial irradiance G_0:

$$k_t = \frac{G}{G_0} \tag{4.4}$$

The fraction of diffuse is calculated from the horizontal diffuse irradiance G_d and G:

$$k = \frac{G_d}{G} \tag{4.5}$$

Brunger and Hooper identified 49 tabulated sets of the coefficients a_0, a_1, a_2 and a_3. Thus, the model gives 49 different sky radiance distributions. Each set is valid for a certain combination of k and k_t, with k and k_t both separated into nine classes with intervals of 0.1. These sets are given in Table 4.1. The angle Ψ is the angle between the investigated hemispherical segment and the sun. It is needed to generate the distribution by Eq. 4.3 and is calculated by:

$$\Psi = \arccos[\sin\theta_h \sin\theta_s \cos(\phi_h - \phi_s) + \cos\theta_h \cos\theta_s] \tag{4.6}$$

Furthermore, the distribution includes a function, which depends on the solar zenith angle θ_s and on the factor a_3. This *Brunger function* is written as[7]:

$$I(\theta_s, a_3) = \frac{1 + \exp(-a_3\pi/2)}{a_3{}^2 + 4}$$
$$\cdot \left\{\pi - \left[1 - \frac{2[1-\exp(-a_3\pi)]}{\pi a_3[1+\exp(-a_3\pi/2)]}\right] \cdot [2\theta_s \sin\theta_s - 0{,}02\pi \sin(2\theta_s)]\right\} \tag{4.7}$$

Note that within this work, zenith angle ϕ and azimuth angle θ of a sky element as defined in (Brunger and Hooper 1993) were substituted by ϕ_h and θ_h to allow for a clear distinction between beam and diffuse incidence angles.

Visualization: According to the meteorological factors cloudiness and air pollution, the distribution of radiation density over the hemisphere is very diverse. Table 4.1 includes the most frequent combinations of k and k_t. The span reaches from a heavily overcast sky in the upper left corner up to a very clear sky in the lower right corner.

---

[7] There is an error in the original source of Eq. 4.7. In Brunger, A. P. and Hooper, F. C. (1993). "Anisotropic sky radiance model based on narrow field of view measurements of shortwave radiance." Solar Energy 51(1): 53-64. the first dividend is written as $1 + \exp(-a_3\pi/3)$, but must be $1 + \exp(-a_3\pi/2)$ (cp. Solar Energy 51/6, 1993, Erratum p. 523).

Further situations can be described as follows: If one moves e.g. along the first row at $k = 0.95$ towards higher clearness indexes, the sky stays covered, but the global irradiance increases due to a thinner layer of clouds. In the mid of the table (e.g. at $k = 0.55$ and $k_t = 0.55$), a partly cloudy sky is found. The model was visualized in a resolution of 2,5° to show circumsolar radiance and horizontal brightening (cp. Figure 4.7).

Table 4.1: The coefficients a_0 to a_3 of the Brunger Model dependent on the clearness-index k_t and the fraction of diffuse irradiance k (Brunger and Hooper 1993, page 57). The **bold printed values are illustrated** in Figure 4.4 to Figure 4.8.

$k_t \rightarrow$ k $\downarrow$	0.05	0.15	0.25	0.35	0.45	0.55	0.65	0.75	0.85
0,95	**0,1864**	0,2002	0,138	**0,1508**	0,1718	0,2060			
	0,1979	0,1772	0,093	**0,5472**	0,0566	-0,0294			
	0,0000	0,0000	0,289	**0,6659**	0,8734	2,9511			
	1,0000	1,0000	0,9667	**1,6755**	2,4129	3,7221			
0,85	0,1431		0,3477	0,2664	0,2139	0,1520	0,1151		
	0,142		-0,2153	-0,1559	0,0307	0,1497	0,1805		
	2,636		5,3170	1,7758	1,6099	1,8315	2,2284		
	5,525		4,4211	2,8590	3,726	4,6125	4,1553		
0,75			0,3687	0,2684	0,2019	0,1870	0,1842	0,1566	
			-0,2927	0,1615	-0,1275	-0,0632	0,0253	0,3003	
			2,6268	4,5224	1,4096	1,2819	1,3080	1,8486	
			2,8413	4,0842	2,2453	2,5932	3,1127	14,744	
0,65			0,3851	0,2843	0,2713	0,1597	0,2088	0,1273	
			-0,2726	-0,1645	-0,1837	-0,1715	-0,0520	-0,0500	
			4,1962	5,2960	2,822	1,2964	1,3225	1,5961	
			5,259	4,3678	3,486	1,9183	2,8364	2,0993	
0,55			0,6079	0,2892	0,2816	**0,2465**	0,2070	0,2477	
			-0,4838	-0,1953	-0,1945	**-0,1245**	-0,0927	-0,0711	
			11,078	2,1346	3,8606	**2,9163**	1,1098	1,5836	
			4,588	3,7268	3,7447	**4,0760**	2,5586	3,450	
0,45				0,2337	0,2822	0,2916	0,2583	0,2457	0,2315
				-0,1015	-0,1842	-0,2065	-0,1654	-0,1398	-0,2028
				11,792	6,0300	2,7327	1,9525	1,512	1,5803
				5,3698	4,5241	3,7624	3,3769	2,964	2,3229
0,35		$a_0 \leftrightarrow$			0,3162	0,3006	0,2871	0,2491	0,2510
		$a_1 \leftrightarrow$			-0,2039	-0,2172	-0,2184	-0,2224	-0,0907
		$a_2 \leftrightarrow$			6,2226	4,5443	2,6467	1,5992	0,9733
		$a_3 \leftrightarrow$			5,8975	4,2660	3,594	2,6404	2,6775
0,25						0,3417	0,3153	**0,3071**	0,2971
						-0,2574	-0,2338	**-0,2576**	-0,3126
						4,1918	3,8860	**2,3127**	1,3594
						4,3268	4,3920	**3,5189**	2,397
0,15							0,3360	0,3243	0,3061
							-0,2600	-0,3003	-0,4531
							4,2481	1,9157	1,612
							4,3727	3,2680	2,319

(a) Three-dimensional diagram   (b) Polar diagram
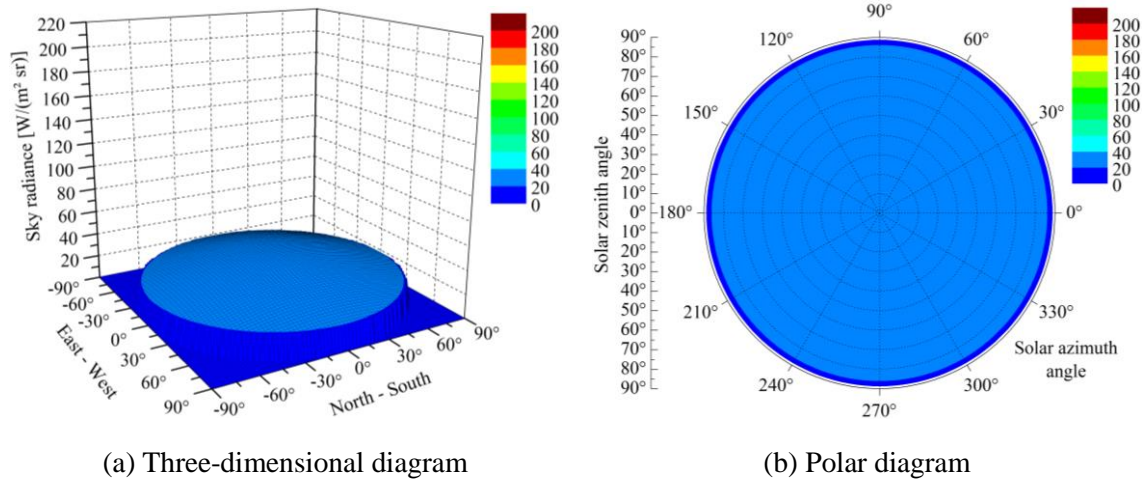
Figure 4.4: Diffuse sky radiance distribution according to the Brunger Model for a heavi-ly overcast sky ($k_t = 0.05$; $k = 0.95$; $\theta_s = 30°$; $\phi_s = 0°$; $G_d = 100\,\text{W/m}^2$). Visualization based on Brunger and Hooper (1993, p. 58).

(a) Three-dimensional diagram   (b) Polar diagram
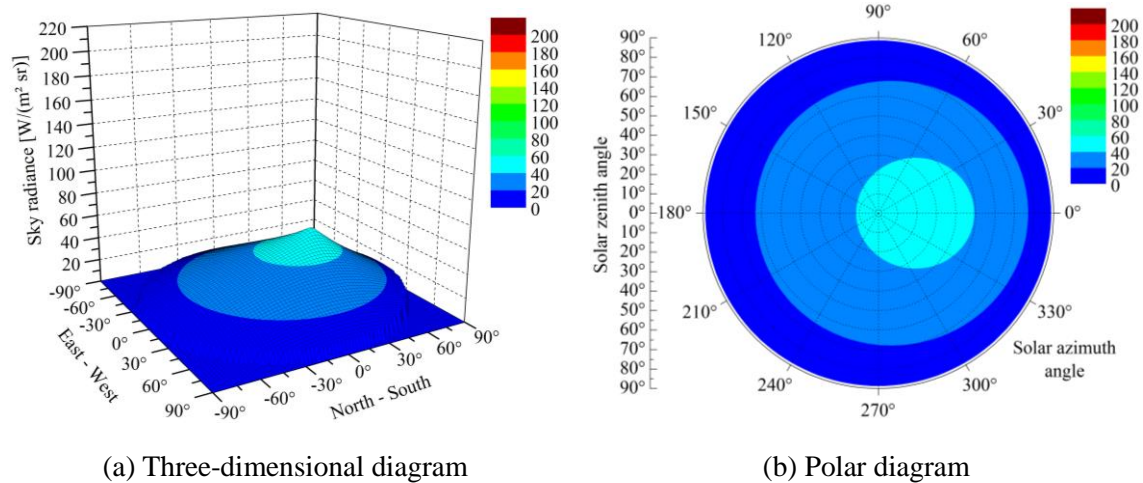
Figure 4.5: Diffuse sky radiance distribution according to the Brunger Model for a lightly overcast sky ($k_t = 0.35$; $k = 0.95$; $\theta_s = 30°$; $\phi_s = 0°$; $G_d = 100\,\text{W/m}^2$). Visualization based on Brunger and Hooper (1993, p. 59).

(a) Three-dimensional diagram   (b) Polar diagram
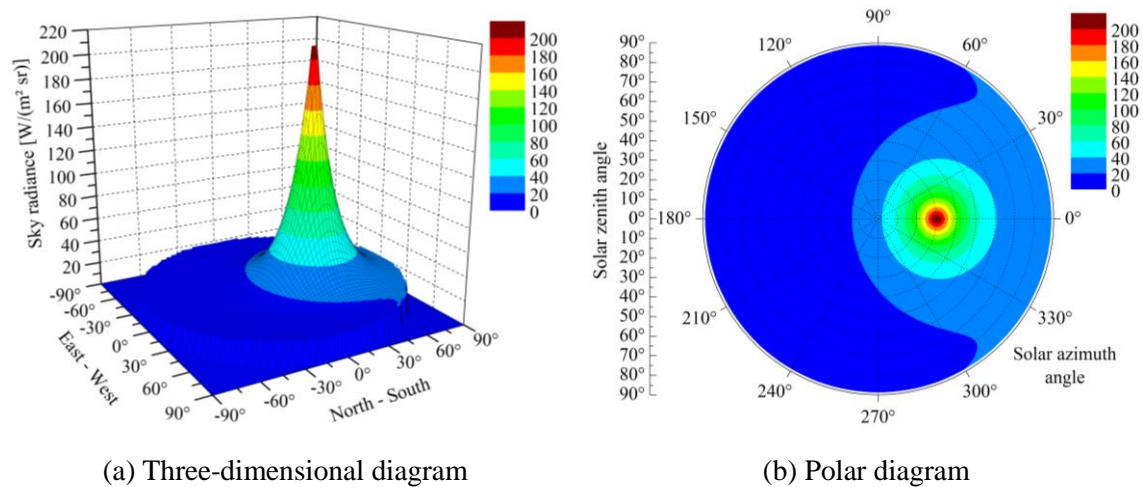
Figure 4.6: Diffuse sky radiance distribution according to the Brunger Model for a partly cloudy sky ($k_t = 0.55$; $k = 0.55$; $\theta_s = 30°$; $\phi_s = 0°$; $G_d = 100\,\text{W/m}^2$). Visualization based on Brunger and Hooper (1993, p. 59).

(a) Three-dimensional diagram   (b) Polar diagram
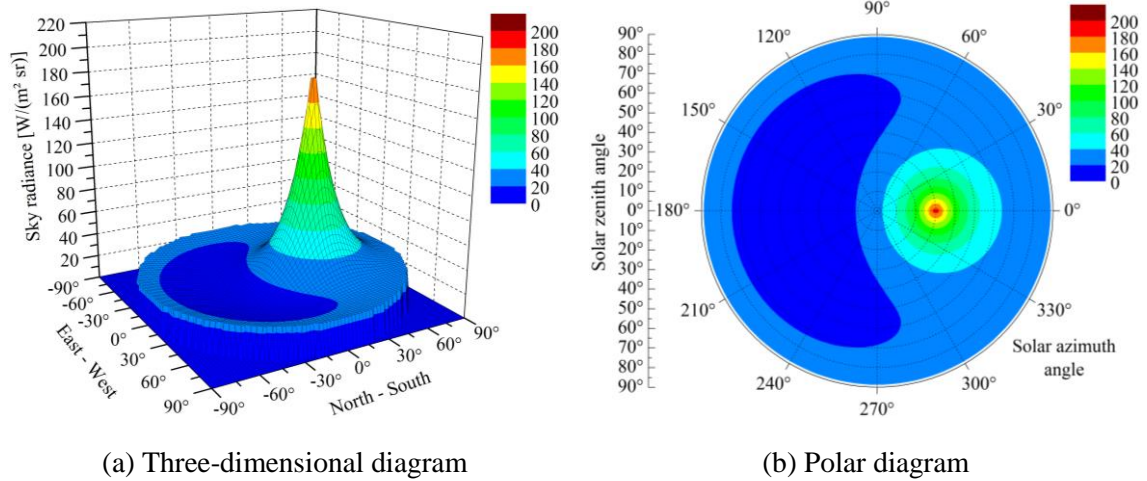
Figure 4.7: Diffuse sky radiance distribution according to the Brunger Model for a relatively clear sky ($k_t = 0.75$; $k = 0.25$; $\theta_s = 30°$; $\phi_s = 0°$; $G_d = 100 \text{ W/m}^2$).
Visualization based on Brunger and Hooper (1993, p. 58).

(a) heavily overcast   (b) lightly overcast

(c) partly cloudy   (d) relatively clear
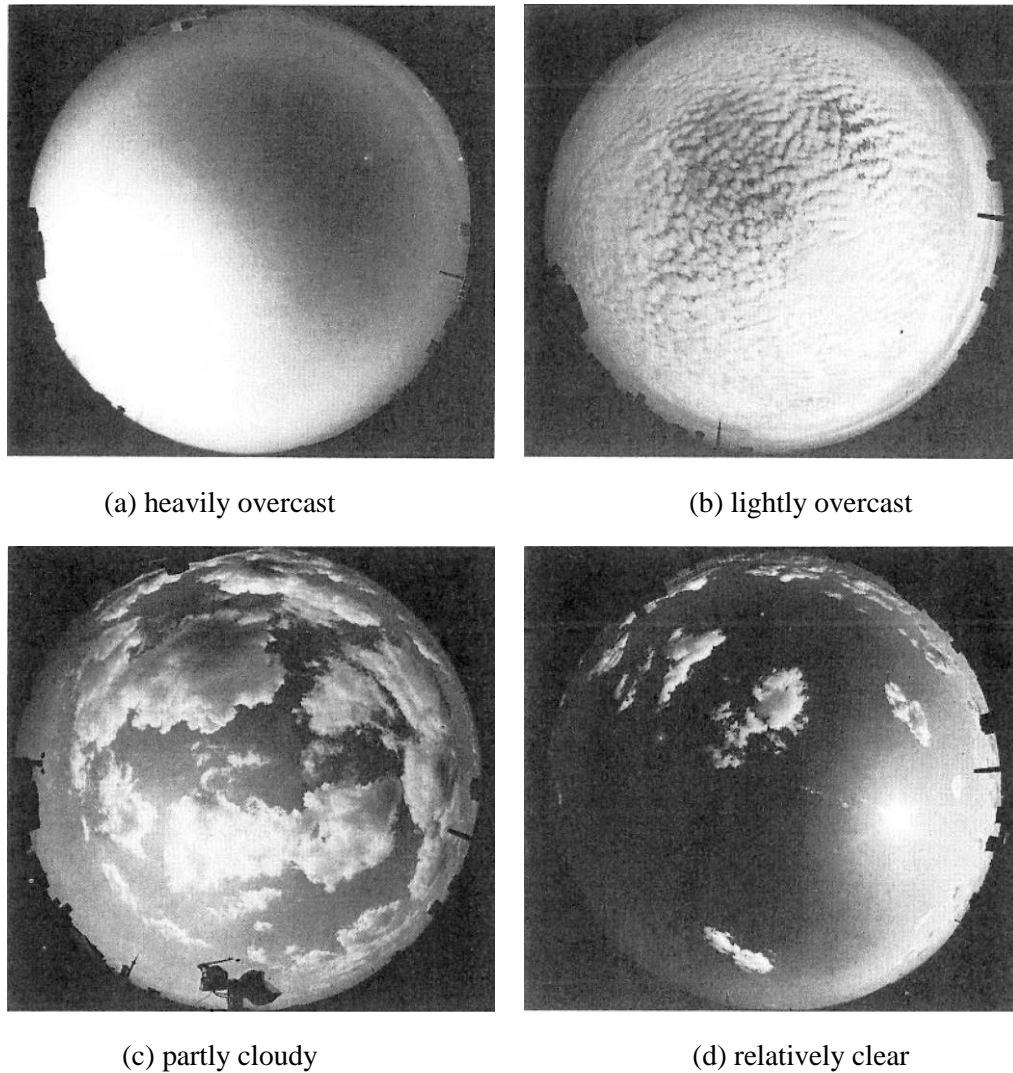
Figure 4.8: Wide-angle 180° photographs of the sky dome at the measurement site for generation of the Brunger model parameters, showing the high variety of real sky conditions. Photographs from Brunger and Hooper (1993, p. 55).

4.2 Collector Simulation Model

The current version (Type 154) of the collector simulation model was already described in Hess and Hanby (2014). Therein, primarily the optical part of the model and its implications for RefleC were discussed. The work in hand contains in section 4.2.2 a summary of the functionalities of Type 154. This is complemented by Appendix D, where a detailed documentation on the optical and thermal modelling as well as on the programming structure of the model is given.
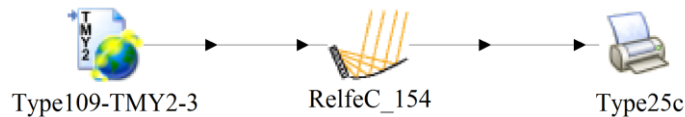
Figure 4.9: Type 154 within TRNSYS Simulation Studio. Weather data (TMY 2) are read e.g. by Type 109, also containing the radiation processor. Irradiance values and directions are transferred to Type 154, where with other model parameters the energy output is calculated (cp. Figure 4.1). The results are plotted and stored in a data file.

4.2.1 State of the Art

Influence of anisotropic diffuse on energy gain: Siala and Hooper reported on the influence of the anisotropic nature of sky radiance on the irradiance accepted by an ideal CPC concentrator. They had developed a semi-empirical model for anisotropic sky radiance using the same SKYSCAN 1983/84 data set of Toronto, Canada as Brunger and Hooper (1993). They state an *MBE* of their model of -5.2 % and an *RMSE* of 39.5 %, both based on the normalized observed average radiance (Siala and Hooper 1990, p. 294). This model was not considered for the RefleC collector simulation type since its errors are significantly above those of the other models compared in Figure 4.2.

To study the effect of sky radiance anisotropy on a CPC, Siala and Hooper used the acceptance function (cp. Figure 2.32) of an east-west aligned full-CPC of $\theta_a = 36°$. Their study was pure geometrical, and no optical or thermal collector losses were considered. Compared to the isotropic distribution model, the fraction of accepted diffuse was up to 10 % higher for the anisotropic case, when the sun was within θ_a of the collector sloped at β = latitude 43.7°. For $\beta = 0°$ and with the sun outside θ_a, the fraction of accepted diffuse was up to 15 % below that of the isotropic approach (Siala and Hooper 1990, p. 295).

Bollentin and Wilk (1995) modelled the effect of planar booster reflectors on the irradiation availability of flat-plate collectors. Isotropically modelled contributions of G_{bt}, G_{st} and G_{rt} were used to optimize reflector and collector tilt. The authors conclude that anisotropic modelling of diffuse irradiance could be used to further increase the accuracy of their model.

To conclude, there has been one assessment of the influence of anisotropic irradiance on the radiation acceptance of a theoretical CPC collector. Until now, the influence of anisotropic irradiance on the IAM for diffuse irradiance or on a collector's annual energy has not been investigated.

IAM in State of the Art Simulations: This section discusses how different publicly available simulation programs currently account for the acceptance of ST collectors for diffuse irradiance. In all programs, representative weather data files (typical meteorological years TMY) with horizontal irradiation data are used. The irradiance on the tilted plane is calculated for every time step and the irradiance values are used to calculate the efficiency.

TRNSYS: The TRaNsient SYstem Simulation program is a common platform for scientific use. In TRNSYS 16 (Klein et al. 2006), within the *Weather Data Processor* the simplified Perez diffuse irradiance model for sloped surfaces (Perez et al. 1988) is the most advanced option to determine G_{st} (Mode 4). This model considers the three radiation components isotropic background, circumsolar radiance and horizontal brightening, but does not give a continuous sky radiance distribution, cp. also Perez et al. (1987). In TRNSYS 17, the internal TRNSYS function *getIncidentRadiation* calculates the sum of irradiance on a tilted plane from horizontal weather data. Compared to TRNSYS 16, here tilted radiation Mode 5 was added. It uses more accurate fit coefficients from the year 1999, but is still the identical model of Perez et al. (1988), cp. Klein et al. (2012b, p. 7-95). So, both in TRNSYS 16 and 17, the angular distribution of the sky radiance is not available to the user.

In the TRNSYS standard library there are different collector models (so called *Types*) available. An overview is given in (Klein et al. 2012c, pp. 3-74 to 3-79); a mathematical reference in (Klein et al. 2012a, pp. 4-315 to 4-350). The flat-plate collector *Type 1* offers five different optical modes. In the most advanced one, effective incidence angles for sky and ground irradiance are calculated based on rotation symmetric input values of $K_b(\theta)$ to determine values for $K_{s,iso}$ and $K_{r,iso}$ (Klein et al. 2012a, p. 4-321). The functions for these effective incidence angles have been determined by Brandemuehl and Beckman (1980, p. 511) and are only valid for flat plates.

The vacuum-tube collector *Type 71* performs an isotropic calculation of $K_{d,iso}$, which is applied to all diffuse irradiance (no distinction between sky and ground). Since only biaxial symmetric inputs for $K_b(\theta_l, \theta_t)$ are allowed, the integration of Eq. 3.17 can be performed for only a quarter of the collector hemisphere (Klein et al. 2012a, p. 4-331).

The non-standard Type 832 v5.01, the *Dynamic Collector Model by Bengt Perers,* is thermally the most advanced collector model in TRNSYS, since additionally to the stationary collector curve it considers wind-speed dependency of thermal losses, infrared heat losses as well condensation gains and collector capacity (Haller et al. 2013, p. 6).

As in Type 71, no distinction between sky and ground diffuse is made. Different from Type 71, $K_{d,iso}$ here is an input parameter which the user has to take from test lab reports or calculate with Eq. 3.17.

T*SOL, Polysun: T*Sol Pro v5.5 (Valentin 2014) and Polysun v5.10 (Velasolaris 2013) are common commercial solar thermal system simulation programs used by planners. Extensive collector bibliotheca are available containing biaxial symmetric $K_b(\theta_l, \theta_t)$-values and $K_{d,iso}$ as input parameter from test lab measurements. These values can also be entered for a self-defined collector.

SCEnOCalc: The Solar Collector ENergy Output CALCulator v4.06 is a MS Excel-based tool to calculate the thermal output of *Solar Keymark* tested collectors for the four locations Athens, Davos, Stockholm and Würzburg for the three constant collector mean temperatures 25 °C, 50 °C and 75 °C (SCEnOCalc 2014). When quasi-dynamic test results are used, also biaxial asymmetric $K_b(\theta_l, \theta_t)$-values can be entered. As in TRNSYS *Type 71*, $K_{d,iso}$ is an input parameter and no distinction between diffuse from sky and ground is made.

To conclude, state of the art simulation programs / collector models:

- do not have the angular distribution of diffuse sky radiance available
- consider IAM values K_d (or K_s and K_r) as constant collector parameters only.

Only RefleC_154 and TRNSYS Type 71 do work with 3D K_b-values from an external file. The other types use two-dimensional IAM curves (e.g. flat-plate IAM approach of Souka/Safwat for longitudinal direction and measured transversal IAM values). The beam-IAMs for intermediate angles are calculated within the collector types itself by the separation approach of McIntire.

4.2.2 Model Description

Modelling the IAM for anisotropic diffuse irradiance: The collector simulation model introduced here was programed in Fortran and is applied in TRNSYS 16 as user-defined Type 154. Its unique difference compared to existing models is that the IAM for diffuse irradiance from the sky K_s is re-calculated in every time step based on realistically distributed anisotropic diffuse sky radiance. The change of the optical efficiency with varying skies allows for investigating to which extent the sky radiance anisotropy influences the collector output. For this purpose, Type 154 distributes the sum of horizontal sky diffuse irradiance (input from weather data reader) over the hemisphere according to the model of Brunger and Hooper (1993), cp. section 4.1.2 for a description. Ground reflected diffuse is treated isotropic. The model calculates the collector's IAMs K_b, K_s and K_r separately and for arbitrarily shaped K_b-curves provided in an input text file. Figure 4.10 illustrates schematically the functions of Type 154.
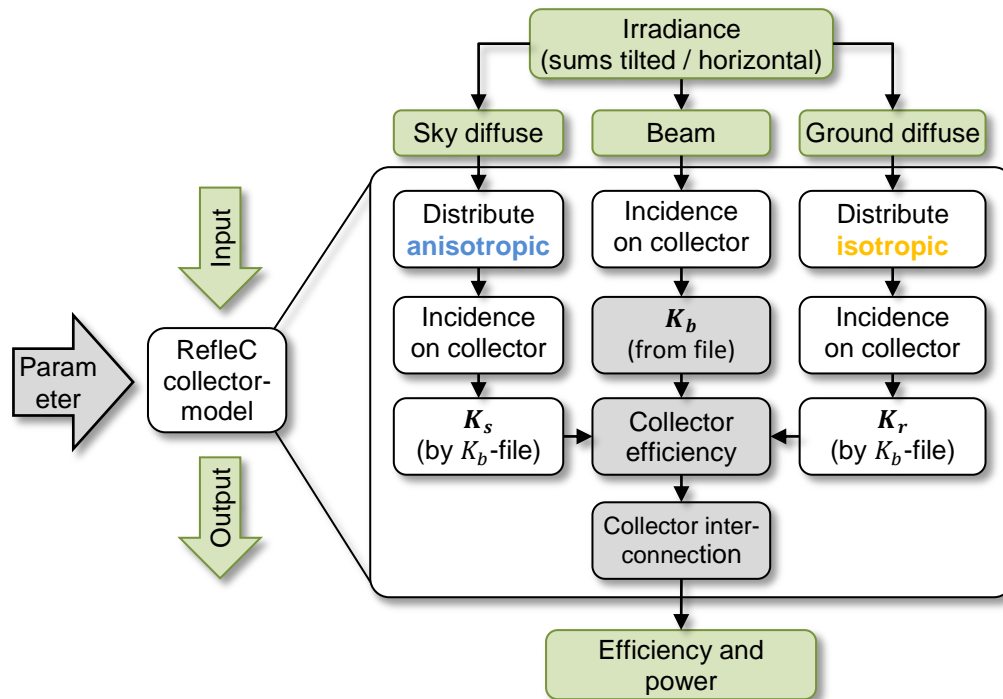
Figure 4.10: Simplified illustration of the functions of Type 154

Both in TRNSYS 16 and 17 the angular distribution of the sky radiance is not available to the user. This is the reason why the input sum of sky irradiance on the horizontal has to be anisotropically distributed over the hemisphere within Type 154. This distribution is exclusively used to get a realistic value of K_s. The integral value of G_{st} used for energy output calculation is still taken from the weather data processor, not from the Brunger model. This allows an independent comparison of Type 154 to other models.

The approach for calculating K_s is explained based on Figure 4.3. The diffuse sky irradiance $L(\theta_h, \phi_h)$ is treated as beam irradiance of infinitesimal sky elements $d\Omega(\theta_h, \phi_h)$. The incidence angle of one element onto the collector aperture is calculated and its radiance of $d\Omega(\theta_t, \theta_l)$ is multiplied with its individual IAM $K_b(\theta_t, \theta_l)$ and cosine losses $\cos\theta(\theta_t, \theta_l)$. Division of the sum of all IAM weighted sky irradiance by the sum of sky irradiance onto the aperture (not weighted with IAM) gives a collector's K_s for the considered distribution of diffuse sky radiance.

Type 154 has **three optical modes** for the calculation of the IAM for diffuse irradiance (cp. Figure 2.1):

- **Mode 1**: <u>**anisotropic**</u> calculation of the IAM from the **sky** K_s <u>with Brunger distribution,</u> isotropic calculation of K_r
- **Mode 2:** **isotropic** calculation of <u>separate</u> IAMs for **sky** K_s **and ground** K_r
- **Mode 3:** <u>manual input</u> of the IAM for isotropic diffuse irradiance K_d <u>for the whole collector hemisphere</u> (no separation into K_s and K_r).

In **Mode 1**, K_s is calculated new for every time step, since K_s depends on the current sky radiance distribution. K_r is calculated once per simulation for isotropic ground radiance. Both K_s and K_r depend on the collector's IAM for beam irradiance K_b and therefore also on the collector slope β.

In **Mode 2**, K_s and K_r are calculated once per simulation for isotropic sky and ground. They depend on the collector´s IAM for beam irradiance K_b and therefore also on the collector slope β.

Mode 3 does not distinguish between sky and ground diffuse irradiance. In this most simple case, the sum of diffuse irradiance is considered to originate from a 180° collector hemisphere of isotropic radiance. Only for this simplification, the IAM for diffuse irradiance (sky and ground) K_d is a constant collector parameter, which only depends on the IAM for beam irradiance K_b. It is independent of β and of the current values of G_{st} and G_{bt}. For $\beta = 0$, K_d equals K_s from Mode 2. All collector simulation models described in section 4.2.1 calculate according to this approach, which is a very rough simplification and source of uncertainty for most collector types, as will be shown in the next sections.

The values of $K_b(\theta_t, \theta_l)$ are provided by the user in an external text file and can originate from measurements or raytracing. Thus, the errors by applying the separation approach of (McIntire 1982) are not made within Type 154 and it depends on the external IAM file how exactly $K_b(\theta_t, \theta_l)$ is accounted for. Type 154 is the only collector model allowing for biaxial, asymmetric 3D-IAM input.

Type 154 offers the following functions:

- Three optical modes to calculate the IAM for diffuse irradiance are provided.
- Input of biaxial, asymmetric 3D-IAM values is possible.
- The effective thermal collector capacity c_{eff} is considered.
- Up to ten collectors can be connected serially, an unlimited number in parallel. The outlet temperatures of all serially connected collectors $T_{out,i}$ are provided
- When there is no mass flow, the stagnation temperature is calculated.

The modelling of Type 154 is described in detail in Appendix D. In Appendix D.1, an overview on the modelling structure is given. Appendix D.2 contains all Inputs, Parameters and Outputs of the model. Therein, "inputs" are variables provided from links to other TRNSYS types, "parameters" are constant user-input values and "outputs" are variables calculated by Type 154 based on the inputs and parameters. The appendices D.3 to D.7 give detailed information on the optical and thermal modelling.

In the following, simulation results of Type 154 for RefleC and the flat-plate are given. Their implications on the simulation of stationary solar thermal collectors are discussed.

4.3 Simulation Results

4.3.1 Irradiation Distribution Diagrams

In section 2.4.3, it has been discussed from which sun positions beam irradiance can be accepted by a stationary CPC concentrator (cp. Figure 2.34). The considerations related to Figure 3.8 illustrated in principle the acceptance of a CPC for diffuse irradiance. Rönnelid and Karlsson (1997) introduced *irradiation distribution diagrams* to optimize stationary concentrators by projecting the sums of hourly beam irradiance from annual weather data files into the north-south plane. They used the south projection angle $\theta_{p,NS}$, which would be located within the transversal plane of an east-west orientated CPC trough (Rönnelid and Karlsson 1997, p. 193).

The new simulation model introduced additionally offers the exciting possibility to also analyze the directional distribution of annual diffuse irradiation (isotropic and anisotropic) onto a receiving plane. Figure 4.11 shows a diagram of this type. It was generated with TRNSYS Type 154 without thermal or optical losses. Type 154 was exclusively used to generate Brunger distributions for every time step. Contrary to (Rönnelid and Karlsson 1997), cosine-effects for diffuse irradiance were considered.
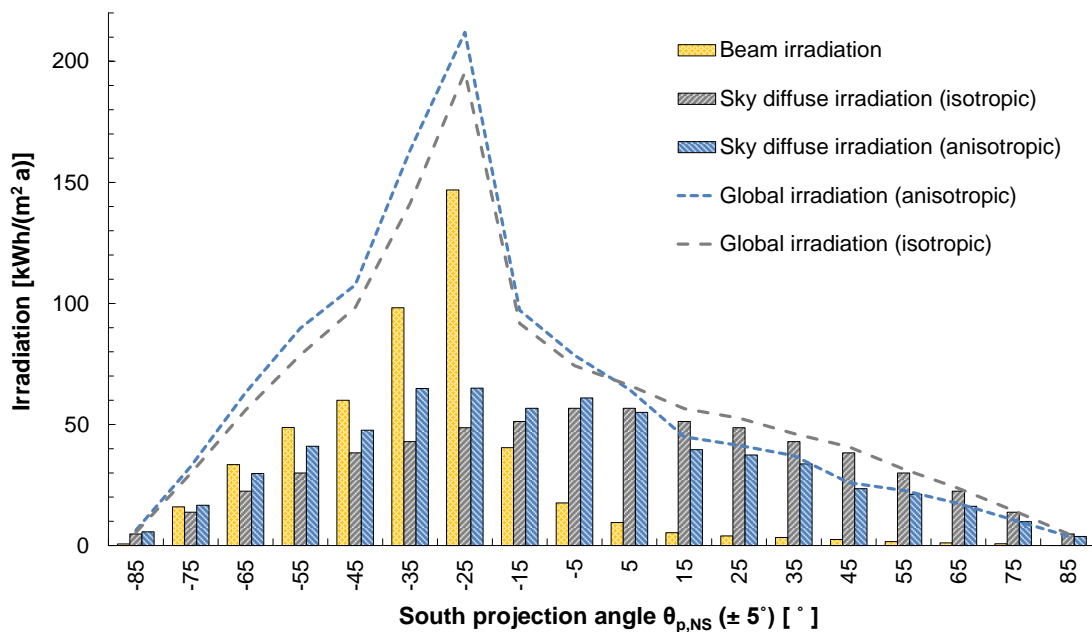
Figure 4.11: Annual horizontal irradiation distribution diagram for Würzburg, Germany (latitude 49.48° N), showing the difference between isotropic and anisotropic modeling of diffuse irradiance. In TRNSYS 16, for every simulation time step of 0.25 h, irradiation from a TMY-2 file (annually $G = 1091$ kWh/a, $G_s = 606$ kWh/a, $k = 0.55$) has been distributed over the hemisphere by Type 154 and classified into lune-shaped segments ("bins") of 10° south projection angle. Results were added up for a whole year. The sum of diffuse is the same for isotropic and anisotropic modelling. The south projection angle as used in this work is identical to the transversal incidence angle θ_t of a collector with azimuth $\gamma = 0°$ and slope $\beta = 0°$ in Figure 2.8.

The distribution of beam can be understood from Figure 2.33 and Figure 2.34 and corresponds very well to the results of Rönnelid and Karlsson (1997). It is not affected by the diffuse irradiance model used. When looking at the distribution of diffuse, in case of isotropic distribution only the cosine effect is visible, since in Mode 2, Type 154 distributes the sky radiance evenly over the hemisphere. The sums of isotropic irradiation are mirror-symmetric between the northern and southern hemisphere. When distributing it according to Brunger by Mode 1, the result is considerably different. Particularly from directions with regular beam irradiance, a significant increase of diffuse irradiance can be observed. This is expected to be caused by broad circumsolar diffuse irradiance. For the simplified assumption of an isotropic sky, 70 % of the annual global irradiance originates from the southern hemisphere. This value increases to 77 % for more realistic anisotropic modelling. It is found that for Würzburg, isotropic modelling underestimates the diffuse irradiance from the southern hemisphere by 20 %.

But how does this affect the irradiance onto the sloped RefleC collector? Figure 4.12 shows the same investigation as in Figure 4.11, but for the aperture plane of RefleC 6 GF sloped by $\beta = 55°$, and with a simplified transversal K_b-curve indicated. To understand Figure 4.12, it is again important that the annual sum G_{st} is the same in the isotropic and the anisotropic case, since Type 154 was only used to classify the directions of irradiance into transversal intervals, not to calculate the irradiation itself. As in Figure 4.11, the anisotropic distribution causes significantly higher sky diffuse irradiation from the segments with high beam irradiation. Correspondingly, less irradiance originates from the north. Comparing Figure 4.12 to Figure 4.11 shows that for the isotropic case the incident sky diffuse irradiance is as expected still mirror-symmetric to the surface normal, when we consider that $\theta_t = -35°$ represents a sky segment of only half the width than its opposite segment $\theta_t = +35°$. This is because of the fact that for $\beta = 55°$ the horizon is within the interval $\theta_t = -35° = [-40°; -30°]$, dividing it into two equal lune shaped segments, of which the lower one already belongs to the ground.

The ground reflected diffuse irradiation is one order of magnitude smaller than diffuse from the sky. There is also some ground reflected diffuse from $\theta_t < -35°$, since ground irradiance from east or west has smaller projected transversal incidence angles (cp. Figure 2.8). Comparing the distributions of ground and sky diffuse irradiance gives clear indication that the isotropic distribution of $G_{dt} = G_{st} + G_{rt}$ over the collector hemisphere, as it is practice in standard simulation programs and possible with Mode 3 of Type 154, is a very rough simplification expected to cause significant errors in simulated annual energy gain. This is relevant for all stationary collectors, we considered only the irradiance on the tilted plane, and not yet the irradiation utilization by RefleC.

Figure 4.12 shows a clear maximum of beam irradiance from $\theta_t = [20; 30]$. For RefleC sloped $\beta = 55°$, this is also the maximum of K_b. So Figure 4.12 indicates that this slope can be expected to be around the optimum for maximal annual gains.
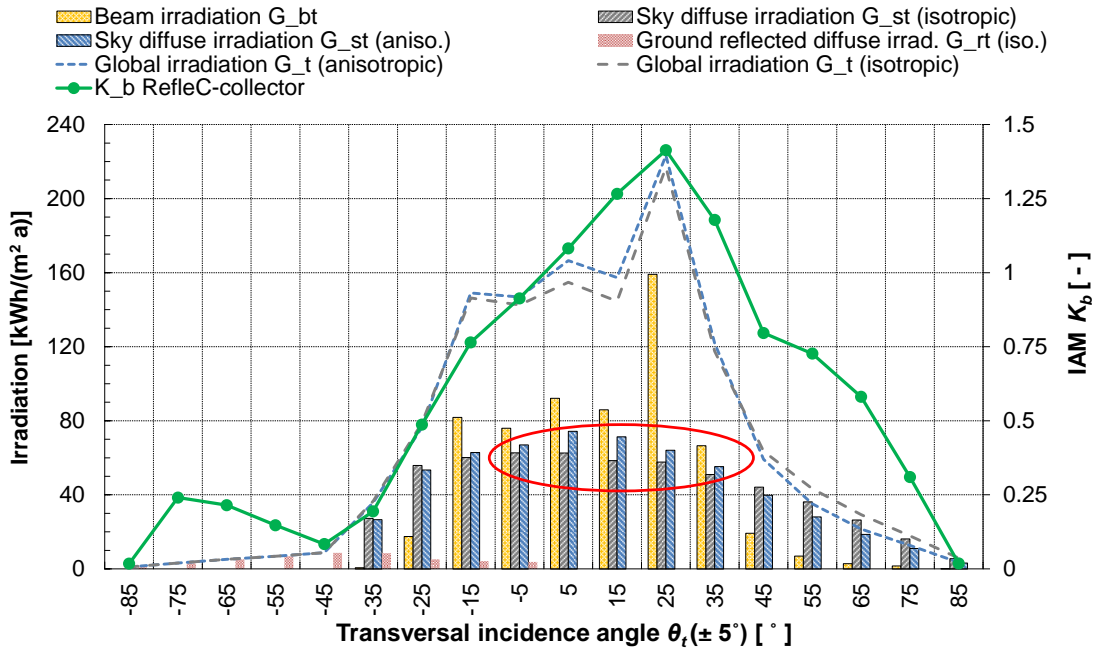
Figure 4.12: Annual irradiation distribution diagram for a sloped surface of $\beta = 55°$ and $\gamma = 0°$ in Würzburg. In TRNSYS 16 within every simulation time step of 0.25 h, horizontal irradiation from a TMY-2 file has been calculated for the sloped surface by weather data reader type 109 using the model of Perez et al. (1988) and ground albedo $\rho_{grd} = 0.2$, resulting in $G_t = 1213$ kWh/a, $G_{st} = 560$ kWh/a, $G_{rt} = 47$ kWh/a and $k = 0.50$ (annually). This irradiance has been distributed over the hemisphere by Type 154 and classified into lune-shaped segments of 10° south projection angle. Mean IAM values $K_b(0, \theta_t)$ of RefleC are indicated for each interval (cp. collector picture in Figure 2.1 and raytraced K_b-curve in Figure 2.11) (Hess and Hanby 2014, p. 95).

When distributed anisotropic, a significant increase of diffuse irradiation is observed in the range of $\theta_t = [-10°; 40°]$. For these incidence angles, the highest IAM values $K_b(0, \theta_t)$ occur, so that a significant influence of the directional modelling of diffuse on the annual gain is to be expected for RefleC. Before this, first the effect of anisotropic sky radiance on the instantaneous IAM for sky and ground diffuse irradiance is shown.

4.3.2 Anisotropy-Effect on the IAM

In the next Figure 4.13, the new simulation model Type 154 is applied to the low-concentrating, stationary RefleC 6 GF collector. The working principles and effects of the model's three optical modes (cp. detailed model description in Appendix D) are illustrated by a detailed look into the IAM simulation results for three very different days.

To calculate K_s, the raytraced K_b-values of RefleC 6 GF given in Figure 2.11 were used. From these biaxial raytracing results, an input-file containing $K_b(\theta_l, \theta_t)$ was generated, by calculating the values for intermediate angles with the separation approach of McIntire. In the isotropic Mode 2, $K_{s,iso}$ and K_r are calculated once within the first time step and the values remain constant. The isotropic IAM K_d of the whole collector hemisphere (for manual input Mode 3) was determined by calculating $K_{s,iso}$ in Mode 2 with $\beta = 0°$. For $\beta = 0°$, Type 154 can be used to perform the integration in Eq. 3.17.
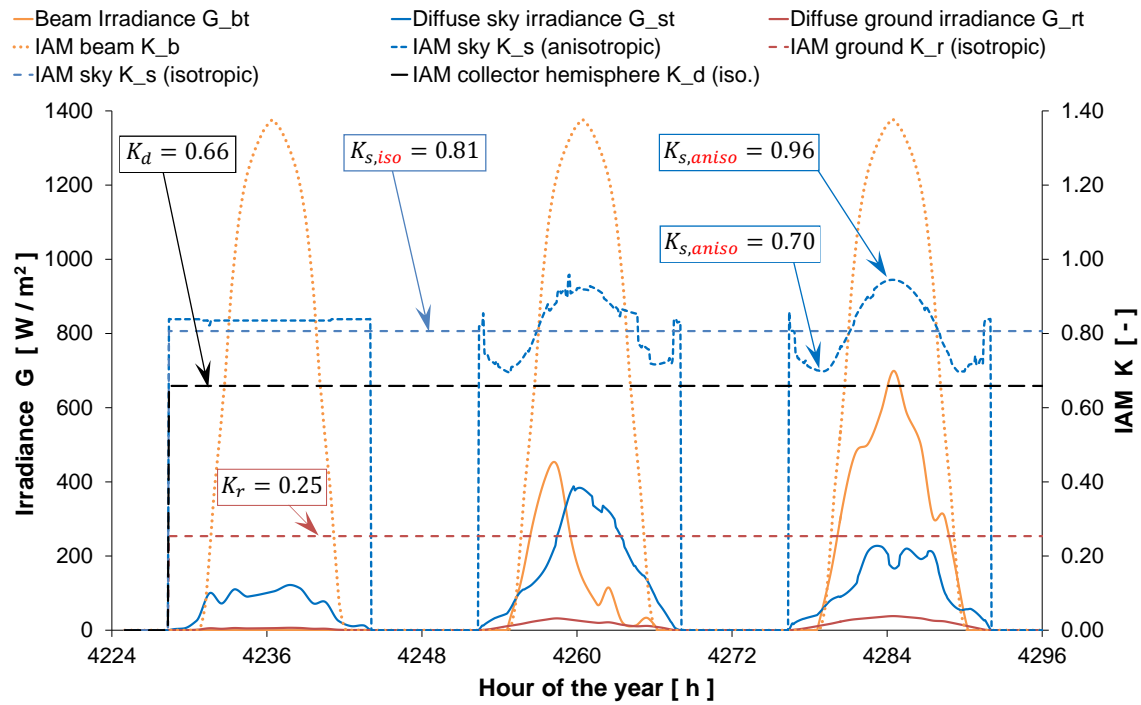
Figure 4.13: IAM values of Type 154 for beam, sky diffuse and ground reflected diffuse onto a RefleC 6 GF collector ($\beta = 55°$, $\gamma = 0°$) in Würzburg for three days with highly different irradiance (27 to 29 June in the TMY). If Mode 3 (manual input) is selected, the sum $G_{dt} = G_{st} + G_{rt}$ is weighted with a diffuse IAM for the collector hemisphere $K_d = 0.66$. In Mode 2, separate and β-dependent but still constant isotropic IAMs $K_{s,iso} = 0.81$ and $K_r = 0.25$ are calculated by the model. Only the values of $K_{s,aniso}$ calculated by Mode 1 respond to the actual instantaneous irradiance conditions (time step = 5 min, $\Delta\theta_{diff} = 2.5°$ for Mode 1 and 2) (Hess and Hanby 2014, p. 94).

The integration results for $K_{s,iso}$ and K_r are highly differing from K_d, because of the very incidence angle selective behavior of RefleC in the transversal direction (cp. Figure 4.12). At solar noon, K_b reaches values close to 1.4, since around summer solstice angles of $\theta_t \approx +30°$ are reached for $\beta = 55°$ (cp. max. solar altitude in Figure 2.33).

For the first day shown, the TMY weather data file does not contain any beam irradiance at all. A maximum diffuse fraction $k = 1$ and a very low clearness index of $k_t = 0.05$ are observed, corresponding to a heavily overcast sky (cp. Figure 4.4). This distribution is the one most close to isotropic offered by the Brunger model. In the course of the day, k_t increases to $k_t = 0.15$, but $k = 1$ remains - the sky is still overcast. Thus, $K_{s,aniso}$ does not significantly change during the day. Why is it above $K_{s,iso}$? A close look into the Brunger distribution for heavily overcast sky reveals that it is not ideally isotropic. The sky radiance around the zenith is about 50 % above that near the horizon, which leads to a slightly higher value of $K_{s,aniso}$ also in this case.

By contrast, the third day is very sunny with a partly cloudy sky (cp. Figure 4.6) in the morning and in the evening and relatively clear sky (cp. Figure 4.7) during the day. These conditions cause a high anisotropy of the diffuse irradiance. In the morning after sunrise, solar disk and thus circumsolar radiance are behind the collector (i.e. $\theta > 90°$).

Since a share of the brightening around the sun is diffuse, in the morning of a clear day the majority of sky radiance is in the northern hemisphere. At this time, for the RefleC aperture, $K_{s,aniso}$ is smaller than for the isotropic assumption. With progressing sun movement in the course of the day this changes, and around noon the solar brightening is incident from $\theta_t \approx +30°$, where K_b of RefleC is maximal. Due to these effects, variations of $K_{s,aniso}$ by up to ca. 25 %-points during one day are possible. Analyzing Figure 4.13, we can conclude for RefleC that constant, isotropic treatment of diffuse irradiance from the collector hemisphere (i.e. K_d in Mode 3):

- significantly overestimates the contribution of ground reflected diffuse, and
- highly underestimates the contribution of sky diffuse irradiance.

For RefleC, the impact of these errors is very high. K_b reflects the character of the reflector: It shades the absorber for ground irradiance and increases the absorbed irradiance from the sky. So another conclusion, proved by Figure 4.13, is:

- For RefleC, the calculation of a separate, but isotropic diffuse IAM for the sky (Mode 2) still underestimates the contribution of sky diffuse irradiance.

This is because relevant collector gains occur when sun and diffuse circumsolar have small incidence angles onto the collector at high K_b-values. During these times, usually $K_{s,aniso} > K_{s,iso}$ is observed (cp. Figure 4.13, days two and three). Qualitatively very similar daily variations of $K_{s,aniso}$ are predicted by Siala and Hooper (1990, p. 295).

4.3.3 Anisotropy-Effect on Collector Output

The results of annual energy output simulations of RefleC and its flat-plate receiver are given in Table 4.2. Differences between the three optical modes of Type 154 are shown. In terms of radiation acceptance, RefleC 6 GF and LBM 4 GF form two extremes: The concentrating RefleC has a very incidence angle selective acceptance, while its non-concentrating flat-plate shows a very good acceptance also for high incidence angles.

The main market of Wagner & Co. Solartechnik is in Europe. To determine the effect of different annual fractions of beam and diffuse irradiance on the gain of RefleC, the locations Würzburg and Seville were selected for comparison. Würzburg has moderate irradiance and a high diffuse fraction, while Seville has high irradiance and a small fraction of diffuse. For Table 4.2, the irradiance was calculated by Type 109 from a TMY-2 Meteonorm file with the model of Perez et al. (1988). In Würzburg (49.48° N) at $\beta = 55°$ it is 1213 kWh/(m^2 a) with diffuse fraction $k = 50$ % (sky: 46 %, ground 4 %), in Seville (37.25 N) at $\beta = 45°$ it is 1955 kWh/(m^2 a) with $k = 36$ % (sky: 33 %, ground 3 %).

Annual collector output: Assessing the relevance of anisotropic sky modelling for RefleC, the most important result of Table 4.2 is that the use of an isotropic K_d (Mode 3), as it is state of the art, would underestimate the annual output of RefleC in Würzburg

by approx. 14 % at its desired operation with $T_{in} = 120\,°C$. Separating diffuse into isotropic sky and isotropic ground (Mode 2) would reduce undervaluation to about 6.5 %.

The <u>undervaluation by isotropic modeling</u> depends on the operation temperature. It <u>increases with increasing operation temperatures.</u> This was expected, since the same errors in IAM have a higher effect at low efficiency operation (i.e. at high temperatures, cp. Figure 3.20). For high inlet temperatures, positive energy gain occurs only at times with high irradiance and high values of K_b. At these times, the sky anisotropy and thus the error of K_d is high (cp. Figure 4.13). As expected, the flat plate shows less sensitivity to how the IAM for diffuse irradiance is calculated. But the effect is still significant, since operation temperatures up to 90 °C frequently occur, also in standard applications. It also has to be considered that a glass-foil collector was simulated – for a standard flat plate the effect is expected to be higher due to lower efficiency at high temperatures.

Table 4.2: Annual gain of RefleC 6 GF and its flat-plate receiver LBM 4 GF at constant inlet temperatures with every positive temperature lift counted (cp. K_b-values in Figure 2.11). RefleC gains are related to 1 m² flat-plate aperture to illustrate the additional gain by the reflectors. Efficiency curves determined at Test Lab Solar Thermal Systems at Fraunhofer ISE for mean fluid temperatures up to $T_f = 163\,°C$ (RefleC) and $T_f = 138\,°C$ (flat-plate); c_{eff} taken from Solar Keymark test report of LBM 4. Simulation parameters in TRNSYS 16: Type 154 with $\Delta\theta_{diff} = 5°$ for Mode 1, constant mass flow of 25 l/m_{Ap}^2, ground albedo $\rho_{grd} = 0.2$, time step = 15 min. Results for optimized tilt β.

Collector type and T_{in}	Würzburg (RefleC: $\beta = 55°$; flat-plate: $\beta = 37.5°$)			Seville (RefleC: $\beta = 45°$; flat-plate: $\beta = 32.5°$)		
	Collector gain Mode 1 [a) (kWh $m_{fp}^{-2}a^{-1}$)	Mode 2 [a) underv. [b)	Mode 3 [a) underv. [b)	Collector gain Mode 1 [a) (kWh m_{fp}^{-2} a^{-1})	Mode 2 [a) underv. [b)	Mode 3 [a) underv. [b)
RefleC 6						
40 °C	771	-2.8 %	- 9.3 %	1397	- 1.6 %	- 3.8 %
120 °C	271	**-6.5 %**	**- 13.7 %**	638	- 3.8 %	- 6.4 %
Flat-plate[c)						
40 °C	645	-1.6 %	**- 3.3 %**	1195	- 0.9 %	- 1.7 %
120 °C	145	-5 %	- 7.5 %	415	- 2.7 %	- 3.9 %
Increase[d)						
40 °C	19.6 %	18.1 %	12.2 %	17.0 %	16.2 %	14.5 %
120 °C	**87.0 %**	84.0 %	74.4 %	53.7 %	51.9 %	49.7 %

[a) <u>Mode 1</u>: anisotropic sky, isotropic ground; <u>Mode 2</u>: isotropic sky, isotropic ground; <u>Mode 3:</u> isotropic collector hemisphere (1 IAM for diffuse irradiance from sky and ground as in state of the art simulations)

[b) **Undervaluation** of collector gain compared to Mode 1

[c) Receiver flat-plate collector of RefleC with glass-foil double cover and without reflector

[d) Increase of annual output due to the reflector per m² aperture of flat-plate receiver collector

For Seville, qualitatively the same results as for Würzburg are observed. The relevance of anisotropic modelling is lower here, since the diffuse fraction is lower and due to higher ambient temperature and higher overall irradiance the collectors operate at higher efficiencies. Also the lower latitude plays a role here, because it leads to a lower collector slope and thus to a larger share of the sky being within the collector's field of view.

Effect of the reflectors at different Modes: The increase in annual collector output due to the reflectors in percentage terms highly depends on the operation temperature, as indicated in Figure 4.14. Seeing the RefleC collector as one unit, this effect can be explained as follows: The conversion factor of RefleC is lower than that of its receiver flat-plate but also its thermal losses are lower, i.e. it has a flatter efficiency curve. Because the IAM influence increases at low-efficiency operation, the effect of the increased IAM by the booster is much higher at $T_{in} = 120\,°\mathrm{C}$.
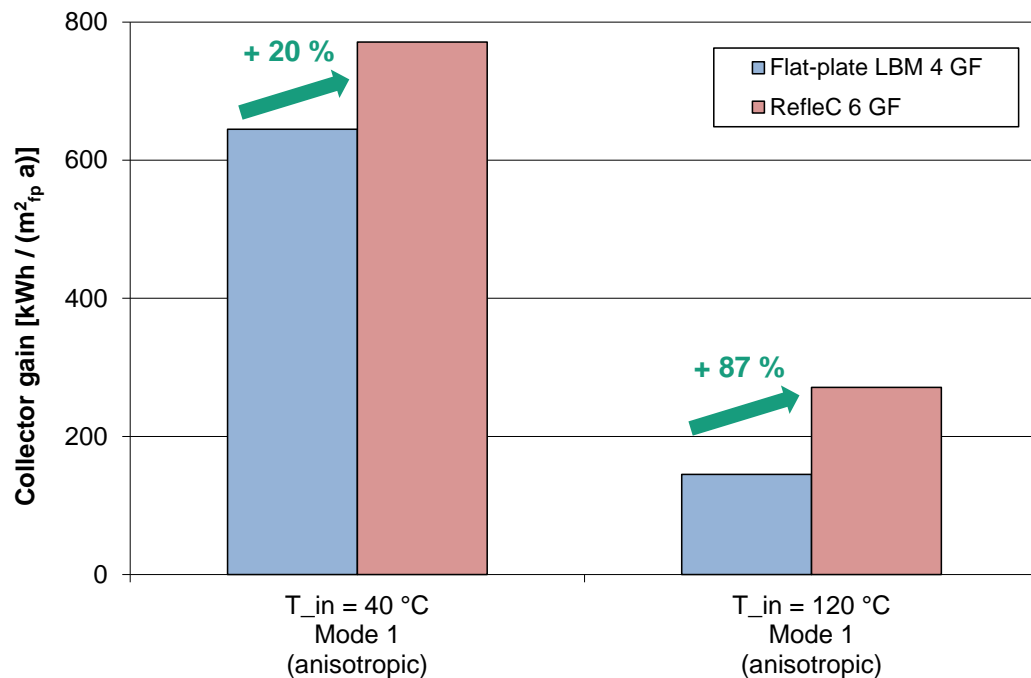
Figure 4.14: Increase in annual collector output by the boosters in Würzburg, calculated with Type 154 for anisotropic sky (Mode 1, cp. Table 4.2). The annual output of the receiver flat-plate LBM 4 GF is blue, that of RefleC 6 GF (receiver with booster) red.

Comparing both investigated locations shows a high difference in the additional energy gain by the reflectors. On the first view, as indicated in the table, the increase in percentage of flat-plate gain is much higher in Würzburg than in Seville. This can again be explained by the considerations on low-efficiency operation. But comparing the absolute gains reveals that the reflector increases the annual output at 120 °C in Würzburg by 126 kWh and in Seville by 223 kWh (+ 77 %). Figure 4.12 illustrates that the reflector is very well directing beam irradiance onto the absorber (high beam irradiance at high K_b-values). In Seville, beam has a higher contribution to the additional gain.

Furthermore, it is interesting to note that in Würzburg and Seville the absolute additional gains by the booster reflector are almost the same for both inlet temperatures, i.e. the

<u>absolute additional gains by the reflectors are largely independent of the fluid-temperature</u>. This confirms the observation of Perers and Karlsson (1993, p. 336).

Comparison of the results from the different Modes shows, that consideration of the sky anisotropy is essential to predict the reflector-gains accurately (cp. Figure 4.15). At $T_{in} = 40\,°C$ the simulated additional gain caused by the reflector increases by 66 %, when instead of an isotropic collector hemisphere (Mode 3) an anisotropic sky IAM K_s is simulated. At 120 °C the difference is reduced but still significant. For Seville, the deviations are again smaller since the contribution of diffuse is smaller here.
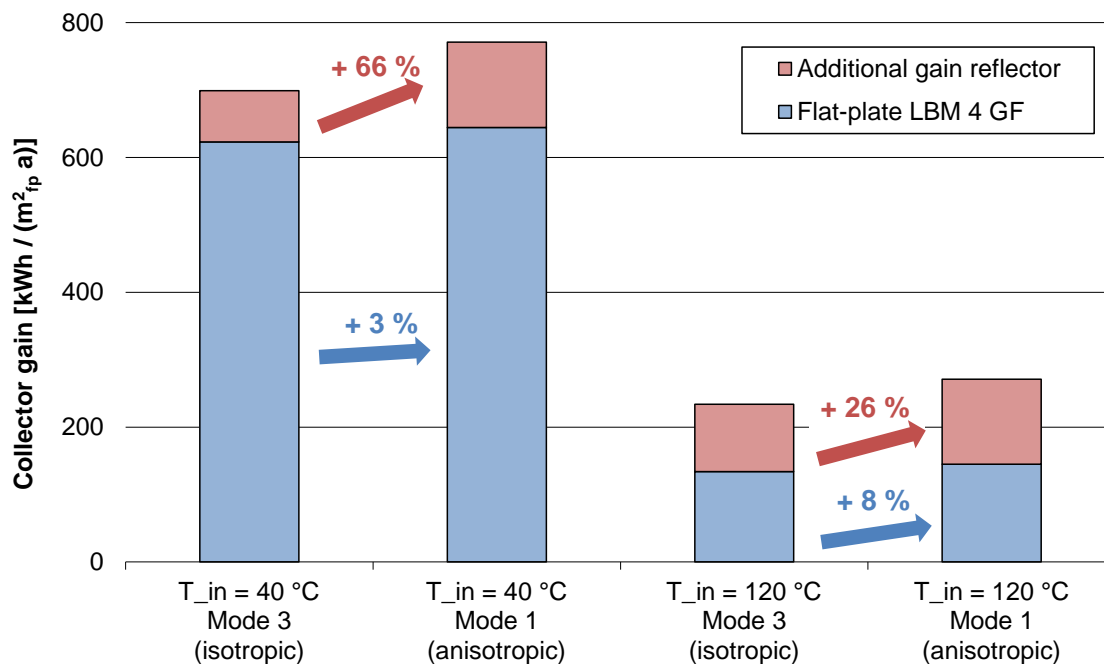
Figure 4.15: Annual output of RefleC 6 GF (blue plus red) and its receiver LBM 4 GF (blue) in Würzburg. The arrows separately indicate the increase in collector output by both RefleC components (flat-plate and reflector) when simulated with anisotropic Mode 1 (new model) instead of isotropic Mode 3 (state of the art). Overall RefleC increase using Mode 1 instead of 3 is 10 % at $T_{in} = 40\,°C$ and 16 % at $T_{in} = 120\,°C$, cp. Table 4.2.

Seasonal analysis: Figure 4.16 and Figure 4.17 show the monthly RefleC collector gains, on which the annual values of Table 4.2 are based, for $T_{in} = 120\,°C$. In Würzburg, from November to January there is almost no collector gain – neither from the double covered flat-plate ($\beta = 37.5°$) nor from RefleC ($\beta = 55°$). At the low overall irradiation level and the low ambient temperatures, almost no positive collector efficiencies are reached for this constantly high inlet temperature. A closer look into Figure 2.11 reveals that the reflectors are not active during these months of the year, since most of the day it is $\theta_t < -10°$, so in the morning and in the afternoon the flat-plate is also shaded by the reflectors[8]. In February and October, the sun takes a glimpse above the reflector, so at noon there is relevant contribution by the reflectors.

---

[8] For ground or flat roof installations with several rows, the „shading" of the flat-plate by the reflector is no drawback, because in a collector field the flat-plates would shade each other.
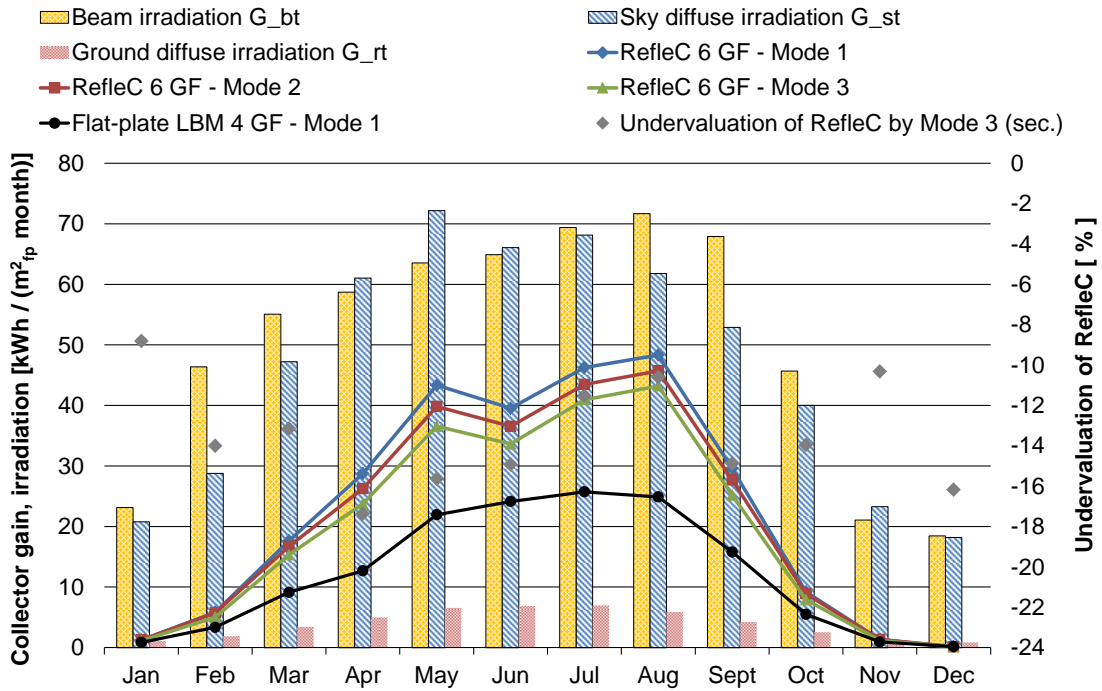
Figure 4.16: Monthly gains of LBM 4 GF and RefleC 6 GF in <u>Würzburg</u> at $T_{in} = 120\,°\mathrm{C}$. RefleC results given for the three modelling variants (Modes 1 to 3) of K_s and the undervaluation when simulated by Mode 3 is indicated (comparison base is Mode 1). Irradiance is valid for RefleC aperture. For simulation parameters cp. Table 4.2.
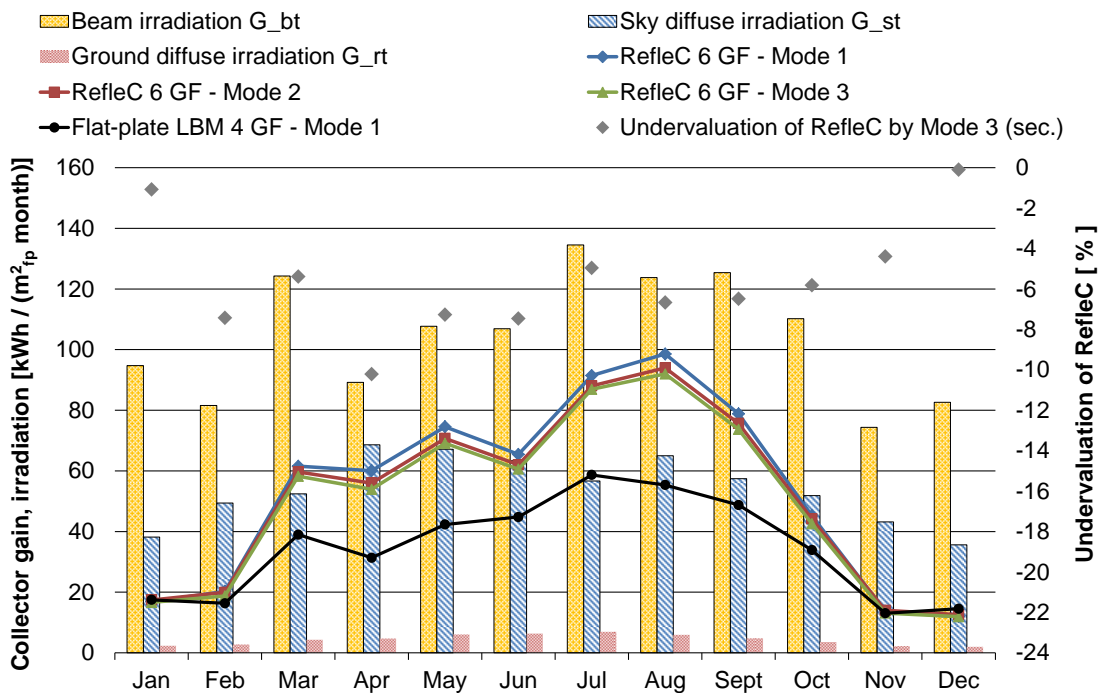
Figure 4.17: Monthly gains of LBM 4 GF and RefleC 6 GF in <u>Seville</u> at $T_{in} = 120\,°\mathrm{C}$. RefleC results given for the three modelling variants (Modes 1 to 3) of K_s and the undervaluation when simulated by Mode 3 is indicated (comparison base is Mode 1). Irradiance is valid for RefleC aperture. For simulation parameters cp. Table 4.2.

From March to May and from July to September, very high K_b-values are reached, since θ_t is in its optimum range – often during the whole day. In June the additional gain by

the reflectors decreases, since the sun's path is within the northern hemisphere of the aperture at $\theta_t > 30°$. Incidence angles around this value are only reached at noon and highly increase in the morning and the afternoon. Thus, around summer solstice the optimal value of $K_b \approx 1.4$ is not reached anymore. Figure 2.11 shows that K_b is sharply decreasing for $\theta_t > 30°$, which results in reduced additional gain. From March to September, the months with significant gain, the undervaluation of the RefleC output by Mode 3 is in Würzburg between 10 and 18 %.

In Seville, also significant collector gains are observed from November to February, because of higher overall irradiance and ambient temperatures. Because of the lower latitude and better weather conditions, the irradiance is also distributed more homogenously over the year. The undervaluation of the RefleC collector output by Mode 3 is between 0 and 10 %, which is significantly smaller than in Würzburg.

The undervaluation by isotropic modelling of diffuse does not directly correlate with the amount of diffuse irradiation per month. This is because instantaneous beam irradiance and sun position (i.e. the instantaneous K_b-values) primarily determine, if any positive gain can be achieved at $T_{in} = 120\ °C$. Figure 4.18 and Figure 4.19 show the same comparison for Würzburg and Seville, but for $T_{in} = 40\ °C$. There, also in Würzburg some gains in winter are observed. Because gains occur also at low irradiance, the undervaluation of RefleC by Mode 3 is more constant over the year; in Würzburg it is between 7 and 11 %, in Seville between 0 and 7 %.
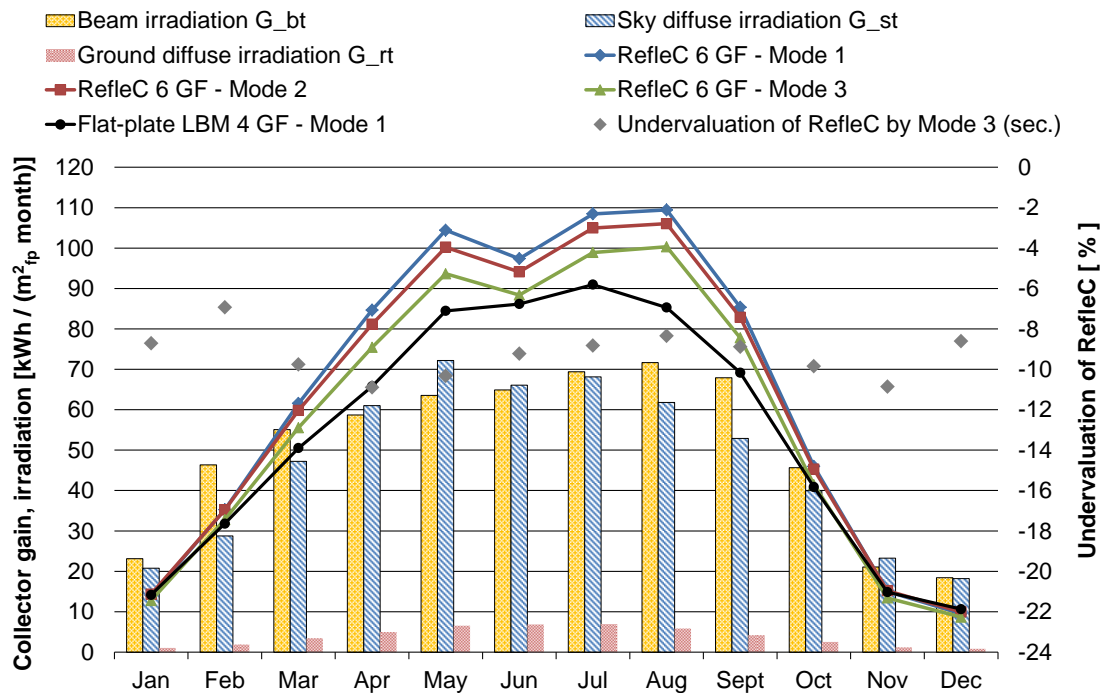
Figure 4.18: Monthly gains of LBM 4 GF and RefleC 6 GF in Würzburg at $T_{in} = \mathbf{40\ °C}$. RefleC results given for the three modelling variants (Modes 1 to 3) of K_s and the undervaluation when simulated by Mode 3 is indicated (comparison base is Mode 1). Irradiance is valid for RefleC aperture. For simulation parameters cp. Table 4.2.
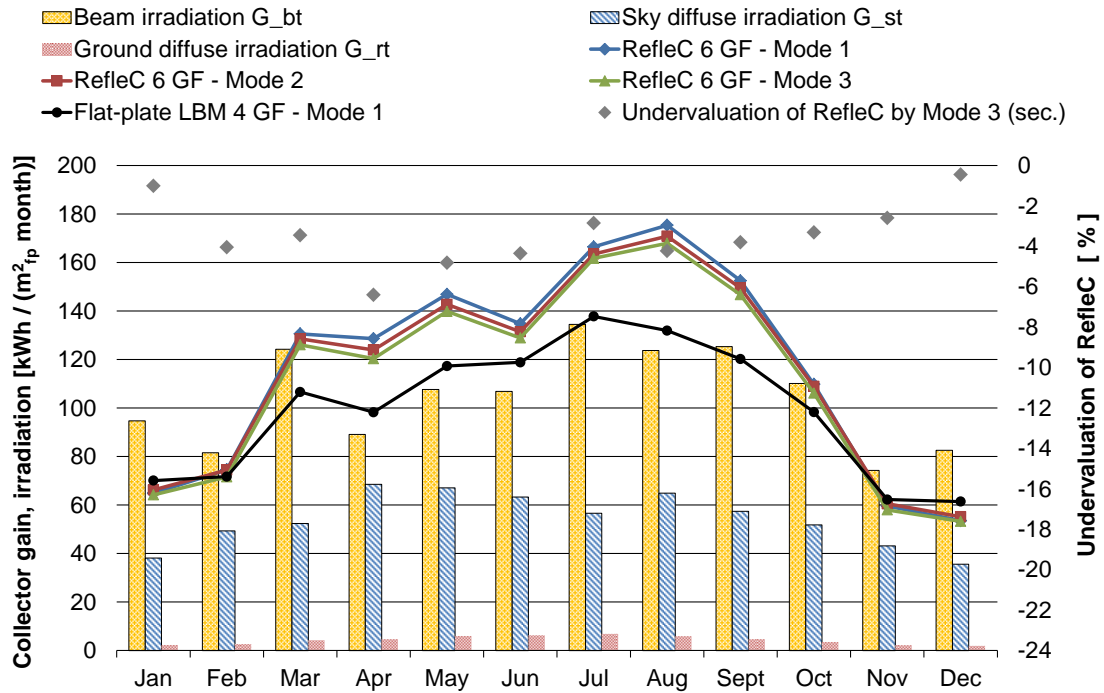
Figure 4.19: Monthly gains of LBM 4 GF and RefleC 6 GF in <u>Seville</u> at $T_{in} = \mathbf{40\,°C}$. RefleC results given for the three modelling variants (Modes 1 to 3) of K_s and the undervaluation when simulated by Mode 3 is indicated (comparison base is Mode 1). Irradiance is valid for RefleC aperture. For simulation parameters cp. Table 4.2.

Optimal collector slope: Figure 4.20 shows a variation of the collector slope β to determine the optimal collector position of RefleC and its flat-plate receiver for maximal annual energy output. The <u>gain of RefleC is</u> much <u>more sensitive for collector slope</u> variations than that of the flat-plate. Therefore, RefleC has to be positioned accurately. This is because of its very distinctive radiation acceptance.
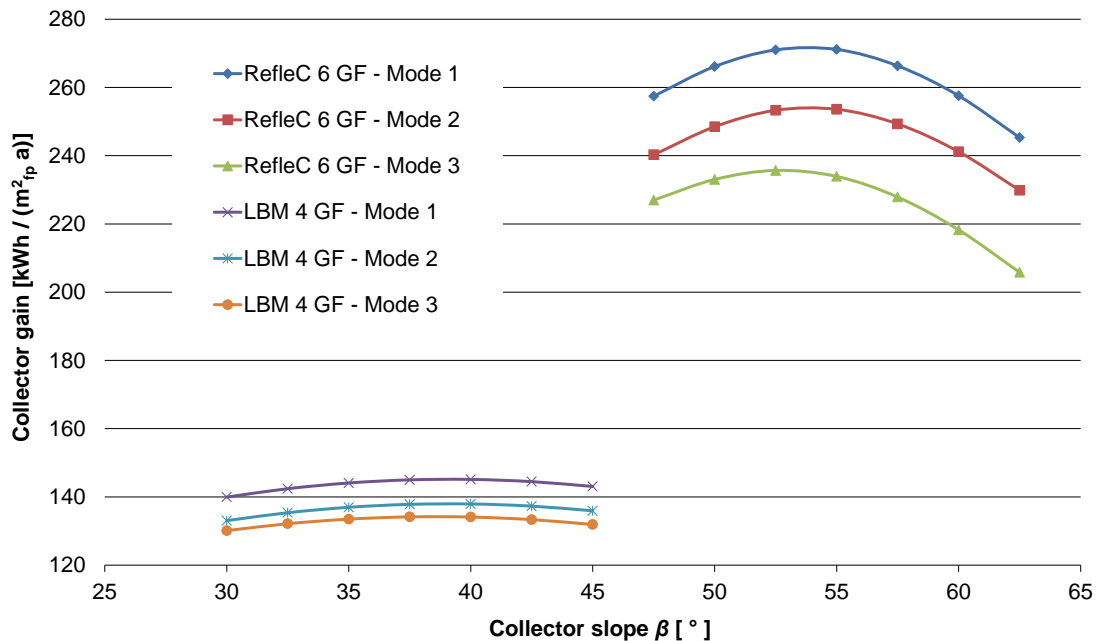
Figure 4.20: Annual collector gain of RefleC and its receiver flat-plate collector in Würzburg for different collector slopes modes for the IAM of diffuse irradiance at $T_{in} = 120\,°C$. For simulation parameters cp. Table 4.2.

From comparing the curves generated by the three different simulation modes it can be concluded that for both collectors the correct determination of the optimal β is almost not affected by the method of determining the IAM for diffuse irradiance. This is because the incidence angles of beam irradiance during the year are the dominating effect that changes the annual energy gain with varying collector slope β. Qualitatively the same curves are observed for Seville. They are flatter, since beam irradiance is distributed more homogenous over the year. For $T_{in} = 40\,°\text{C}$, the identical optimal collector slopes as for $120\,°\text{C}$ were found. They were as well not affected by the diffuse IAM Mode.

It can be concluded that simplified, isotropic hemispherical modelling of a collector's diffuse-IAM (Mode 3) does not lead to a wrong optimal collector slope. Furthermore, the optimal slope is independent of the operation temperature.

The other important results of this chapter can be summarized as follows:

- It is expected that isotropic hemispherical modelling of a collector's diffuse-IAM significantly undervalues the diffuse utilization of all non-focusing collectors, when this diffuse-IAM is determined from K_b-values out of raytracing simulations or steady-state collector tests.
- This undervaluation can be significantly reduced by simply generating separate isotropic diffuse-IAMs for sky and ground irradiance. These IAMs only depend on the collector slope β and are constant during the simulation. Their determination at the start of the simulation would not notably increase the simulation time.
- Simulation with a dynamic diffuse-IAM for anisotropic sky radiance (Mode 1) especially increases the accuracy in instantaneous power output prediction of ST collectors.
- Furthermore, it is expected to be essential for accurate prediction of the additional gains by booster reflectors.

5 Pilot Plant

The final RefleC collector is demonstrated in an innovative solar thermal process heat system. By monitoring of this installation, characteristic annual system performance figures are determined and RefleC is compared to its receiver flat-plate collector during real system operation. Finally, the operational collector performance is assessed against the theoretical expectations, also in regard to the IAM for diffuse irradiance.

5.1 Pilot Plant Description

5.1.1 Laundry Laguna

Laguna is a medium-sized laundry situated in Marburg an der Lahn, Central Germany. About 12 regular staff members and approx. 30 disabled part-time employees treat approx. three tons of laundry per working day (mix of hospital, hotel and private laundry as well as cleaning mops). Working hours are from 7:30 a.m. to 15:30 p.m. The laundry is closed during weekends and short public holidays, but there are no company holidays.

Figure 5.1: Laundry Laguna with production and service building (front), boiler house (left) and solar thermal installation. Picture: Wagner & Co. Solartechnik

The laundry is either cleaned in one of the three drum washing machines or in an auto-mated batch tunnel washer (cp. Figure 5.2). After washing, flat linen is finished in a mangle, while shirts and outerwear are further treated in finishers and/or presses. The other types of laundry are treated by dryers.

Figure 5.2: Unclean side with three industrial washing machines (left: 50 kg charging weight; central background: two machines à 25 kg) and the batch tunnel washer (right background) with its charging conveyor belt (front). All these devices are heated by steam injection. Their outlet is on the clean side, where the laundry is dried and finished.

These heat consumers are all supplied by a steam network, which is fed centrally by initially two gas-fired steam boilers (burner max. 1750 kW each). The boiler room is shown in Figure 5.3.

The boilers can each produce up to 1250 kg/h saturated steam at 14 bar and 195 °C. The steam is used indirectly (via heat internal exchangers) to heat the mangle, the air for the dryers, as well as the finishers and the presses. But a share of the steam is also used di-rectly (without heat exchanger). It is injected into the washing machines and into the batch tunnel washer. Thus, the condensate return mass flow is only about 50 % of the mass of produced steam. In a feed-water tank, the condensate is collected. Here, also the necessary 50 % boiler make-up water is added and thermally degassed. The feed water is then pumped through the economizers (heat recovery from boiler exhaust gas) and back into the steam boilers.

Details on the water- and heat distribution network can be found in the final RefleC project report (Eisenmann et al. 2011).

Figure 5.3: Boiler room with one of the initially two steam boilers on the left hand side, its gas burner (red, foreground), and the boiler control board (right). In the central background, a plate heat exchanger for solar pre-heating of the boiler feed-water is visible (black insulated). Below is the changeover valve for solar pre-heating of the discharge loop before the heat exchanger is flown through (red with red LED). A ladder (left) leads to an intermediate story above, where the boiler feed-water tank is located.

5.1.2 Solar Thermal Installation

A quick impression of the system is given in Figure 5.6, where a simplified hydraulic scheme includes the most important system parameters. A detailed scheme, also including all monitoring sensor types and positions, can be found in the Appendix, Figure E.5.

RefleC Prototype and collector field: The collector field with an overall aperture ea $A_{ap} = 56.6 \text{ m}^2$ is shown in Figure 5.4. The only difference between the prototype and the test sample R6 GF is that the prototype has twice the length of the test sample. Thus, the receiver flat-plates have four glass panes instead of two. The field consists of six such LBM 8 glass-foil collectors with $A_{ap} = 8.08 \text{ m}^2$ each. In each collector, four meander absorbers are connected parallel by integrated header tubes. The field has two rows, the first row consisting of two LBM 8 GF without reflectors, and the second of four LBM 8 GF with reflectors (cp. Figure 5.5). Both rows are identically sloped by $\beta = 55°$ and orientated 21° towards east out of the south direction. The two rows form three hydraulically parallel sub-fields with a mass flow of ca. $\dot{m} = 35 \text{ kg/(m}^2\text{h)}$ in the whole field. Due to the risk of glare and radiation concentration in the surrounding, the ends of the RefleC trough were closed with vertical reflector metal sheets. To conclude, the field is constructed in such a way that the RefleC trough can be compared to its glass-foil receiver collectors directly during operation. Due to the identical slope of the flat-plates, the effects of the reflectors can directly be measured.

Figure 5.4: Collector field of the pilot plant from east direction. On the right, the eastern of the two vertical RefleC trough closure reflectors (with revision opening) is visible. Three pyranometers are located centrally in the field beside the front row. One of the MIDs (magnetic inductive flow meters) can be recognized in the right field inlet pipe (light blue cover). The vertical stakes belong to the lightning protection concept.
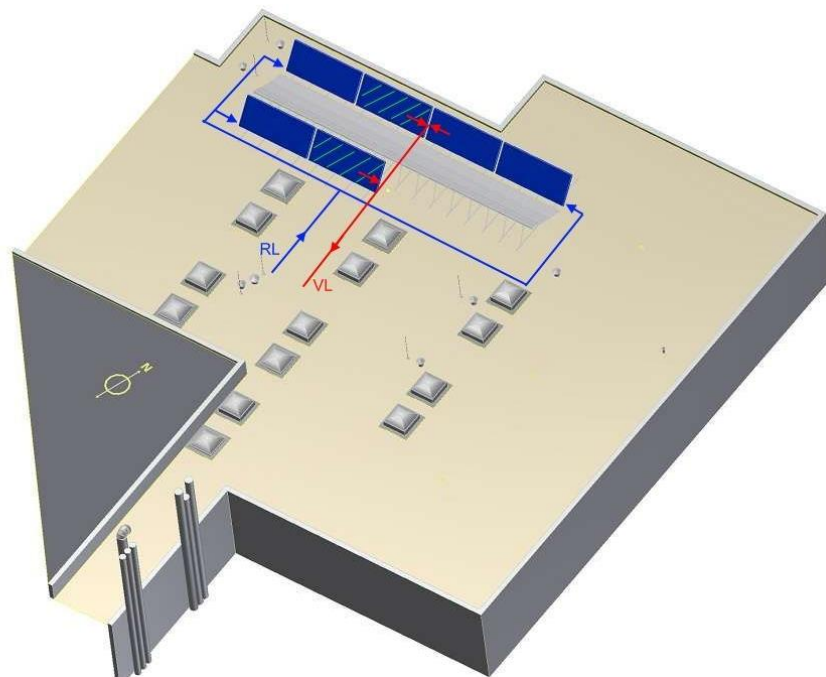
Figure 5.5: Computer graphic of the collector field on the laundry roof. The field is orientated parallel to the edge of the roof and therefore turned 21° east from the south. The colder return flow (RL) enters the three sub-fields on their outside; the hot supply flow (VL) is collected centrally and leads back to the charging heat exchanger. The left (western) field of the RefleC trough is subfield 1, the right (eastern) one is subfield 2. In front is the flat-plate subfield (cp. Figure E.5). Graphic: Wagner & Co.

Processes: When potential solar heat integration points were analyzed by Wagner & Co. Solartechnik, their thermal load profile, technical integration effort, potential interference with existing processes, and of course their potential solar gains were assessed. But also the objectives of the RefleC project played a role. So on the one hand, a process with comparably high integration temperature had to be found to demonstrate the RefleC concept as well as to optimize the operation strategies of the system for process

heat generation at temperatures between 80 and 130 °C. On the other hand, the system had to be commercially feasible, so also a low-temperature process ensuring high and long-term solar gains had to be connected. The following Table 5.1 describes the three heat integration points that were finally selected to discharge the solar plant.

Table 5.1: Thermal loads at the solar heat integration points calculated on the basis of measured temperature levels and load mass flows. The demands of all integration points sum up to 389.72 kWh per working day (usually five working days per week).

	Boiler feed water (supply level)	Boiler make-up water (supply level)	Washing machines (process level)
Volume flow [m^3/d]	4.6	3	1
Process return flow temperautre [°C]	90	20	20
Maximal integration temperature [°C]	110	90	60
Demand [kWh/d]	103.26	240.39	46.07
Demand profile	Continuous during working hours, modulating up to $\dot{v} = 600\,l/h$	Approx. six intervals per day a´ 25 min. at constant mass flow of $\dot{v} = 20\,l/min$	Three washing machines filled randomly approx. once per hour for 30 s. up to $\dot{v} = 300\,l/min$

On high temperature level, the boiler feed water was selected as a solar process heat consumer. At Laguna, rather low feed-water inlet temperatures to the economizer of approx. 90 °C were measured. Typical feed-water temperatures are about 103 °C due to the thermal degassing. A solar discharge plate heat exchanger was installed between feed-water tank and economizer (cp. Figure 5.3). The maximal charging up to 110 °C results from the maximal storage temperature of 120 °C in the SPH system and also from the intention not to affect the efficiency of the economizer. The feed-water demand profile was not measured.

On low-temperature level, the solar heat integration points boiler make-up water and washing machines were selected. The water for both is pre-heated by waste-water heat recovery, but this only results in a temperature level of 20 °C, which is very favorable for ST. The make-up water can be heated up to maximal 90 °C before it enters the feed-water tank (cp. Figure 5.10). This tank has a fill-level control, which results in the described demand profile.

The washing machines are filled with water within 30 seconds. The larger machine needs 125 l per batch, the two smaller ones 62.5 l (cp. Figure 5.2). The temperature levels vary between the washing programs from 25 to 75 °C. The machines mix their hot and cold water inlet to reach the working temperatures and further inject heating steam, if necessary. Using a plate heat exchanger to supply the very short profile of 30 s with its very high power demand would not be reasonable. Thus, a solar pre-heating storage is used for discharge (cp. Figure 5.7). Washing water for the hot connection of the machines always flows through this storage, regardless if it can be solar heated or not.

Within the framework of the project, a comprehensive energy efficiency analysis or process optimization at the laundry was not possible. But the comparably small size of the SPH system (in relation to the heat demand of the connected processes), the integration on supply level, and the use of medium temperature collectors ensure that the system would still work efficiently if the process return flow temperatures increased or the mass flows reduced due to future optimizations or due to a decreasing laundry amount.

System concept: Figure 5.6 shows a simplified hydraulic scheme of the plant. As mentioned above, the size of the system was rather determined by future perspectives than by the heat demands. But also costs played an important role, since the prototypes of the RefleC collectors had to be fabricated with high manual effort.
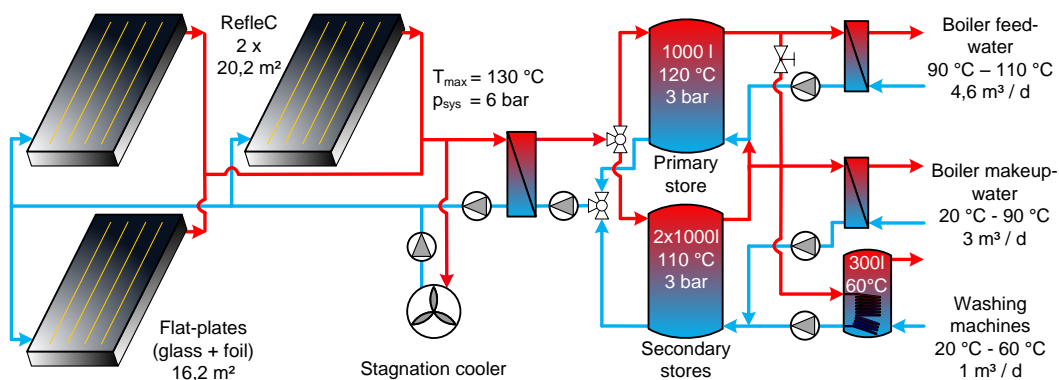
Figure 5.6: Hydraulic scheme of the pilot plant (simplified). Left of the storages are the switching valves for alternating charge; between primary storage and boiler feed water discharge is a manual ball valve to activate or de-activate winter mode (for **detailed hydraulic scheme** with all sensor types and positions **cp. Figure** E.5).

The three parallel sub-fields work at a pressure of 6 bar and a maximum temperature of 130 °C. Either the primary storage or the parallel secondary storages are charged. The storage circuit works at a pressure of 3 bar with a maximum temperature of 120 °C. In "summer-mode", the feed water is heated from the high-temperature primary storage, while make-up water and washing machines are supplied from the secondary storages (manual ball valve closed). In "winter-mode", the feed water is not supplied and both low-temperature processes are supplied by the primary storage. In this case, the return flow always enters the secondaries; from their top it flows to the bottom of the primary. The stores are connected serial in this case. The red switching valves visible in Figure 5.7 between primary (left) and the two hydraulically parallel secondaries (center) control alternated charging. Above the valves is the solar station (black insulated box), including solar loop pump, charging heat exchanger, charging pump, non-return valves and solar loop safety valve connection. The orange vessel on the right is the washing water pre-heating storage. Left of it is the orange expansion vessel of the storage circuit; the other smaller orange expansion vessel of the collector loop is barely visible behind the pre-heating storage. On top and bottom of the primary the feed-water discharge connection is visible; the pumps for make-up water and washing water discharge are in the background on the right of the storage expansion vessel (black insulated).

Charging control: The stores are charged by a so called "switchover threshold control", prioritizing the primary storage. Priority (prio.) 1 is to charge the primary until its top reaches the switchover temperature $T_{tre} = 60\,°C$. Prio. 2 then charges the secondary storages until they also reach T_{tre}. Prio. 3 charges the primary until it reaches its maximum $T_{sto,max}$, prio. 4 does the same for the secondaries. When, at prio. 2 or 4, the temperature in the primary falls below the switchover threshold, short switch offs of the charging pump (all 30 s.) allows to measure the available temperature within the collector loop to check if a switch back to primary storage charging is possible.

Figure 5.7: Centralized components of the RefleC pilot system with monitoring sensors.

Stagnation cooler: A stagnation cooler prevents the collector field from overheating due to stagnation (e.g. at summer weekends). It was also very helpful during optimization of the charging control strategy to effectively handle the incidence angle selective power of RefleC. At 135 °C fluid temperature, the parallel connected device offers a cooling power of 50 kW, at a power consumption of fan and pump of about 290 W each. The cooler is activated when a collector field outlet exceeds $T_{on,RK} = 125\,°C$.

Figure 5.8: Dry stagnation cooler in front of flat-plate subfield. The insulated and aluminum sheet metal coated feed and return flow pipes of the field are routed in a U-shape to compensate thermal expansion. Above them, the rectangular sensor cable duct is visible.

Discharging control: The feed water discharge pump is only activated, if the system runs in summer mode, the feed water pump is on (external signal from boiler fill-level control), and the temperature difference between top primary storage and feed water is sufficient. In this case, the discharge loop is first pre-heated without mass flow through the discharge heat exchanger (i.e. it is bypassed). This avoids undesired heat transfer from the feed-water to the, at first, colder solar discharge loop (cp. detailed hydraulic scheme in Figure E.5 and changeover valve in Figure 5.3).

The discharge to the make-up water is controlled as follows: When a magnetic valve activating the make-up water mass flow opens (external signal from feed-water tank fill-level control) and the temperature difference between solar buffer top make-up water is sufficient, the discharge pump is activated. Due to the constant, very low return flow temperature, the storages are discharged effectively and the collector loop operates at minimal heat losses.

At discharge to the washing water pre-heating storage, this is not always the case. The integrated smooth-pipe heat exchanger and the heating up of this storage over time cause significantly higher return-flow temperatures to the buffer than the make-up water. To prioritize the make-up water discharge, the washing water discharge is only activated if the temperature difference is sufficient and the top buffer storage temperature is above a minimal temperature value (finally set to 50 °C).

Adaptive system operation: The discharge priority order make-up water, washing machine storage and boiler feed water is always valid (with boiler feed water discharge deactivated in winter mode) and also the switchover threshold charging control is the same for winter and summer mode. Together, charging and discharging control aim at only heating the storage volume currently needed. In winter mode, the low-temperature heat consumers are supplied by the primary storage and only this one is heated until it reaches T_{pend}. This results in efficient system operation when the solar gains are significantly lower than the two low-temperature loads. In summer mode, the difference is that in case the primary and the secondaries are charged up to T_{pend}, at prio. 3 operation the primary can indeed supply the feed-water, if the current low-temperature demand is below the solar gains. The hydraulic switch between summer and winter mode is done manually by ball valves near the primary and secondary storages (cp. Figure E.5).

5.1.3 Monitoring System

When the solar thermal plant was constructed, in parallel the monitoring system was installed. This system started operation on 2nd June 2010 and measured the system performance without interruption until it was dismantled on 27th October 2011. During this monitoring phase, for 479 days 47 sensors were logged with a measurement interval of 30 seconds. The raw data volume is approx. 1 MB/day, while each of the automated daily performance evaluation files had around 40 MB/day.

The sensor types and positions are given in Appendix E, Figure E.5. For the whole solar thermal installation, from collector field to charge, storage and discharge, the energy flows were balanced. Pt 100 sensors were used to measure the fluid temperatures, (in immersion sleeves except otherwise specified). The mass flows were determined by magneto-inductive flow sensors (MID). The pressure in the solar loop was measured by a piezo-resistive pressure transmitter to effectively detect stagnation.

The irradiance measurement devices are shown in Figure 5.9. The output of the solar loop was determined at the charging heat exchanger by measuring inlet- and outlet temperatures and mass flow. In the same way, the flat-plate subfield and the RefleC subfield 2 (east) were metered (flow of subfield 2 and cooler calculated from overall flow).

Figure 5.9: Positions of the three pyranometers applied for monitoring (2 CMP 11 and 1 CM 11, shadow band CM 121B). The hemispherical tilted irradiance G_t was measured in the aperture of the flat-plates (the RefleC aperture is in parallel and only centimeters behind, since it starts at the edge of the booster reflectors). The two other pyranometers measure horizontal hemispherical irradiance G and horizontal diffuse irradiance G_d. The axis of the shadow band was positioned east-west and the band was adjusted manually twice per week to shade the sensor from beam during the whole monitoring phase.

Furthermore, ambient temperature and pressure in the field was measured. This way, the instantaneous efficiencies of the three sub-fields and their dynamic behavior at varying irradiance was determined. The direct comparison between RefleC and its receiver without reflectors was of special interest in this regard. But also the energy annually transferred to the charging loop and the collector field utilization ratio was determined.

Another objective of the monitoring was to analyze the dynamic system behavior and to optimize the charging and discharging control concepts explained above. For this purpose, the storages temperatures were measured at different heights to assess the charging and stratification status, also at phases of charge, discharge or stagnation. The heat transferred to the three processes was calculated from temperature differences and mass flows at the discharging heat exchangers. Additionally, the inlet and outlet temperatures of the heated streams on the secondary side were measured to determine the operation time profiles of the supported processes (cp. Figure 5.10).

Figure 5.10: Plate heat exchanger for solar pre-heating of the boiler make-up water. Four Pt 100 temperature sensors measure the temperature differences at the primary side (discharge loop) and the secondary side (make-up water pipe) of the heat exchanger.

All sensor cables are brought together in the monitoring switch cabinet pictured in Figure 5.11. The data were automatically transferred to a monitoring server and from there to the project server. For detailed analyses and daily performance figures, one xls.-file per day was generated. An overall performance analysis file imports the daily results.

Figure 5.11: Monitoring switch cabinet with cable ducts opened. The large box at the cabinet door (right) is a multiplexor, logging sensor signals. The Linux-PC placed on top of the control cabinet processes the signals and transfers the daily data file to a monitoring server of Fraunhofer ISE via the hardware-firewall ASA (Advanced Security Appliance) placed inside at the bottom of the control cabinet.

All sensors were calibrated at Fraunhofer ISE according to the standards of the Test Lab Solar Thermal Systems. The relative measurement uncertainties of all sensors as well as the different maximal uncertainties of the calculated heat amounts resulting from linear error propagation are reported in (Klemke 2011, p. 145 and p. 75).

5.2 Monitoring Results

5.2.1 System Performance

Exemplary weekend: In the following Figure 5.12, the system operation over a weekend is discussed based on daily energy balances.
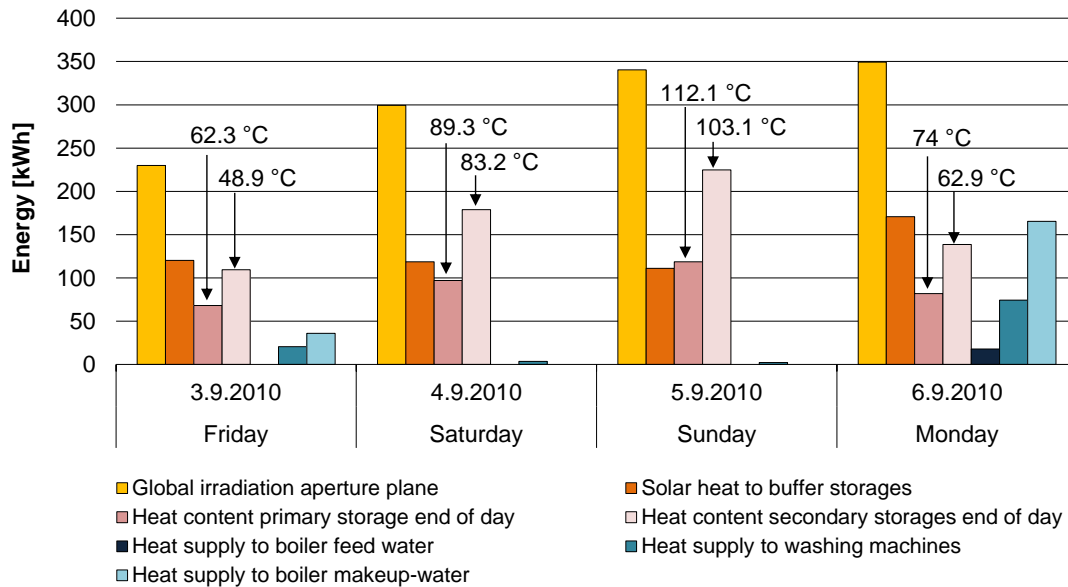
Figure 5.12: Exemplary weekend with daily balances of monitored energies for irradiation, heat charged and discharged as well as energy content and temperature (top) of the storages at the end of the day (last data point 23:59:30 p.m.). The switchover charging was not optimized this time (charging changed frequently between the storages). The system was in winter mode, except for Monday, when summer mode (discharge to feed water) was manually activated at 7 am and de-activated at 9:15 a.m.

During the week, the system was discharged to the low-temperature heat consumers, so Friday night the energy content of the stores is relatively low. During Friday, the low storage bottom temperatures had caused a relatively high solar loop utilization ratio of around 50 % (cp. orange to yellow column). On Saturday and Sunday (laundry not operating), the only discharge is the compensation of the thermal losses of the washing machine's per-heating storage. Due to the increasing storage temperatures, the temperature level of the solar loop is high and the solar loop utilization ratio is low (only 30 % on Sunday). On Sunday evening, the stores are almost maximally charged. Thus, on Monday besides the low-temperature processes, also the boiler feed water can be charged. In spite of the high solar gains, the loads are sufficient to cool down the storages again for effective operation – on Monday and during the whole week. The heat rejector was not active during this weekend.

Monthly operation overview: In **Appendix E**, the monthly energy gains and supplies are shown for all sixteen months of the monitoring in Figure E.1 to Figure E.4. In the captions, information on failures, control configurations and on winter/summer mode operation are given. In these graphs, the heat rejection by the stagnation cooler has a

higher uncertainty than the other energies, because it had to be determined indirectly via the re-cooling temperature sensor and the collector loop energy balance.

Annual solar fractions: From the 16 months of monitoring (06.07.10 to 27.10.11) re-sulted 476 daily data files. Among these days, there were 335 working days with heat demand; the other days are weekends and public holidays. To get annual performance figures, a <u>reference year from 01.10.2010 to 30.09.2011</u> was defined. For this time frame, gap-free monitoring data are available and the system control was usually close to standard-operation. Among the 365 days of the reference year, there was <u>heat de-mand on 256 working days</u>. The following Table 5.2 shows the results.

Table 5.2: Annual system performance figures of the reference year. The demand of the work-ing days (cp. Table 5.1) without weekends and public holidays was considered.

	Boiler feed water (supply level)	Boiler make-up water (supply level)	Washing machines (process level)
Demand within reference year [kWh]	26,435	61,540	11,739
Share of demand [%]	26.5	61.7	11.8
Solar heat supplied [kWh]	115	18,549	4,490
Share of solar heat supplied [%]	0.5	80.1	19.4
Solar fraction [%]	**0.4**	**30.1**	**38.1***
Overall solar fraction [%]		23.2	

* The solar fraction of this process is overestimated, since the discharge to the pre-heating storage on weekends is not included in the heat demand, but correctly counted as heat supplied.

The overall solar fraction was 23.2 %. If only the two low-temperature-processes are considered, 31.4 % of their demand was supplied.

Annual utilization ratios, gains and losses: Within the reference year, the irradiation onto the overall aperture was 66.13 MWh. The collector field was able to convert 49.7 % of this into heat (measured between the subfields inlet and outlet, 32.87 MWh). Of this heat, 3 % had to be rejected by the stagnation cooler; 14.7 % were lost via the solar loop (piping, heat exchanger). The remaining 82.3 % of the heat generated in the collec-tor fields was transferred to the charging circuit of the storages (27.05 MWh). This is the basis for the <u>solar loop utilization ratio</u>, which was <u>40.9 %</u>. The thermal losses of charging circuit, storages and discharging circuits amount to 14.4 %. In sum, 70.4 % of the heat generated by the collectors (calculated from the temperature lift between collec-tor inlet and outlet) was transferred to the processes (23.15 MWh, cp. Table 5.2). Com-paring this useful energy with the irradiance on the aperture gives the performance of the plant within the reference year. This <u>system utilization ratio</u> was <u>35.0 %.</u>

When interpreting these values, the framework conditions reported in Figure E.1 to Fig-ure E.4 as well as the special characteristics of the system and the collectors must be

considered. During the first months of operation, the system control and sensor positions were adapted to high temperature operation of the RefleC collector. Due to minor leakage of a defective cap valve, between 21.04.2011 to 24.06.2011, the maximum storage temperature was restricted to 95 °C and the cooler was activated at $T_{on,RK} = 110$ °C. This significantly reduced the effective storage capacity and made summer mode operation (discharge to the feed water) impossible. In correlation with the extraordinarily good weather conditions during this spring time there was a significant surplus of solar heat, which had to be re-cooled especially on weekends.

The comparably low losses of charging circuit, storages and discharging circuit can be explained by the high room temperatures around the storages. Summer mode was only activated rarely to optimize the high temperature operation of collectors and system. A compromise between solar gain maximization and control strategy development for potential future projects had to be found. For Laguna, the discharge to the boiler feed water is not attractive in its current form. Since $T_{sto,max} = 120$ °C is only little above the integration temperature of 90 °C, the effective storage capacity to support this load is small and so are the operation times of this discharge circuit.

5.2.2 Collector Performance

The following Figure 5.13 shows diurnal variations of the system operation for Saturday, 21.08.2010. This day was selected because it shows high-temperature operation at transversal incidence angles which are advantageous for RefleC. As explained above, the three subfields are parallel and all tilted 55°. This allows for direct performance comparison between flat-plate subfield (aperture area $A_{ap} = 16.18$ m^2) and the RefleC subfield 2 (increased $A_{ap} = 20.22$ m^2 due to reflectors, same number of flat-plates).

High temperature operation: In the morning, the storage top temperature was already around 80 °C, since Friday had been very sunny. The switchover temperature of the charging control was set $T_{tre} = 110$ °C to prioritize boiler feed water discharge and to demonstrate high temperature operation. So in the morning of this Saturday, the primary storage is charged up to T_{tre} (Prio. 1). Since there is no significant process load, the primary reaches T_{tre} already at 10:40. From then, the secondaries are charged (Prio. 2). Every 30 min. the control checks if charging can switch to the primary again (jumps of collector field temperature due to short switchoffs of the charging pump). Prio 1 is indeed shortly activated to compensate the heat losses of the primary. At 13:00, also the secondary storages reach T_{tre}, so after then it is aimed to charge the primary up to 120 °C (Prio 3). This is not fully achieved, since at 13:55 RefleC reaches the stagnation cooler activation temperature $T_{on,RK} = 125$ °C. The cooler is activated four times, with one longer phase between 14:10 and 14:25 (cp. higher mass flow in both fields). From 14:40 to 15:10 the system operates regular again, after 15:10 the collector temperatures resulting from the current irradiance levels are too low or further storage charging.

135
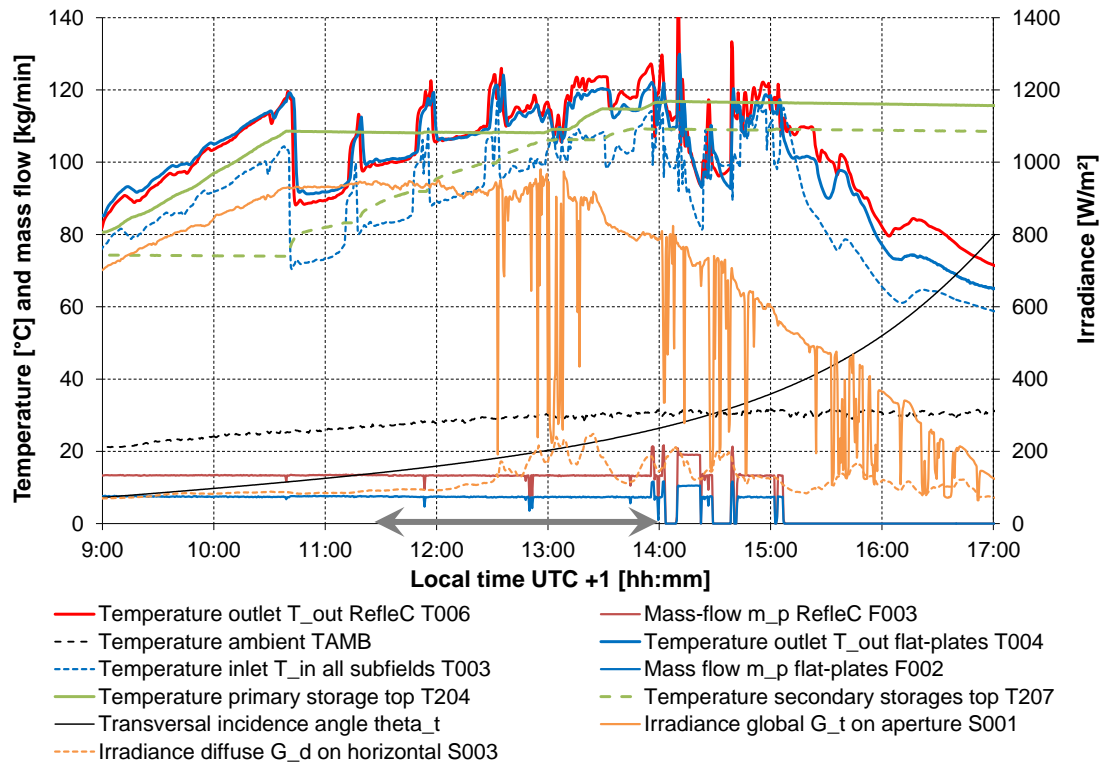
Figure 5.13: Diurnal variation of the pilot plant operation on Saturday, 21.08.2010. In the legend, the identification numbers of the sensors are given (cp. hydraulic scheme with sensors in Figure E.5). The eastern RefleC subfield 2 is compared to the flat-plate sub-field. At RefleC, the mass flow in was 13.3 kg/min or 39.5 kg/(m$_{ap}^2$h), while in the flat-plate subfield it was 7.3 kg/min or 27 kg/(m$_{ap}^2$h). For the time period indicated by the grey arrow, the collector power output is analyzed in detail in Figure 5.15.

In the following, the RefleC performance in comparison to its flat-plate receiver is analyzed for this day. Therefore, Figure 5.14 illustrates the solar incidence angles onto the apertures and the resulting IAM values of both collector types. The sun is within the collector hemisphere from 05:30 to 17:19 ($\theta < 90°$). Due to the field azimuth $\gamma = 21°$ towards east, the sun reaches positive angles θ_t onto the apertures at 06:30 already.

Figure 2.11 shows the IAM values K_b of both collectors along their transversal and longitudinal axes. Since the IAM is influencing collector efficiency directly, the increase in RefleC power output is a factor of 1.4 between $\theta_t = 0$ and it's maximum K_b at $\theta_t = 25°$ (true only if θ_l, thermal losses and K_d were identical). When comparing the field outlet temperatures in Figure 5.13, in addition to K_b also the different field mass flows (RefleC factor 1.9 higher than flat-plates) and the different thermal losses (cp. Figure 3.7) have to be considered. From 09:00 to 11:45, T_{out} of the flat-plates is higher than of RefleC. This is because in the morning T_{in} is comparably low (resulting for the flat-plates in a spread of approx. 15 K between T_{in} and T_{out}), but also due to shading of the analyzed RefleC subfield 2 by its end reflector for irradiance from $\phi < 0°$. From 11:45, due to the higher inlet temperatures (increased thermal losses), the higher transversal incidence angles, and the gains by the end reflector, T_{out} of RefleC is higher (temperature spread of the flat-plates decreases down to 8 K due to reduced efficiency).
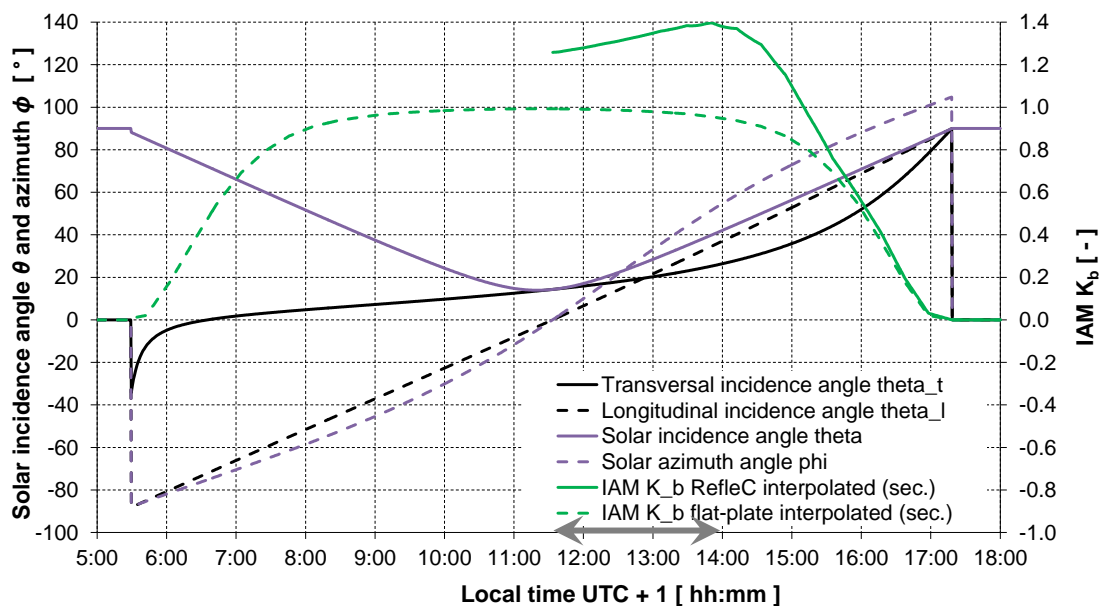
Figure 5.14: Solar incidence angles onto the collector field of the pilot plant on Saturday, 21.08.2010 with resulting current IAM values for beam irradiance of both collector types (green). The incidence angles have been calculated based on Duffie and Beckman (2006, pp. 12-20) for the collector slope of all sub-fields of $\beta = 55°$ and their azimuth $\gamma = -21°$ with the exact coordinates of the collector field in Marburg Wehrda of 50.8440° N, 8.7655° E. For angle conventions cp. Figure 2.7. The grey arrow indicates the time period analyzed in detail in Figure 5.15.

Figure 5.14 shows in the resulting K_b-values during this day, both for RefleC and the flat-plates. For the flat-plate subfield, $K_b(\theta_l, \theta_t)$ was calculated by Eq. 3.15 from the raytraced values given in Figure 2.11. For the RefleC subfield, $K_b(\theta, \phi)$ was interpolated more accurately from a raytraced 3D-IAM. This 3D-IAM was generated for irradiance from the "western" part of the hemisphere of RefleC subfield 2, i.e. for incidence directions $\theta = [0°; 90°]$ and $\phi = [0°; 180°]$ in a resolution of 5°. The longitudinal curve taken from this IAM is shown in Figure 2.39 – its flat shape reveals the additional gains by the eastern trough closure reflector. Since the raytracing of such a 3D-IAM is very time consuming, only K_b-data for this half collector hemisphere were generated. Thus, Figure 5.14 only shows the resulting $K_b(\theta, \phi)$ for incidence from $\phi > 0°$, i.e. from directions where the end-reflector is reflecting irradiance onto the absorber and not shading it (after 11:30 with $\theta_l > 0°$).

After September 2010, the mass flows of the sub-fields were usually related to the aperture area. So the RefleC sub-fields finally have a mass flow of $\dot{m} \approx 35 \text{ kg/(m}^2\text{h)}$, being factor 1.25 higher than that of the flat-plate subfield. Since the system supplies mainly the low-temperature loads, this proved to be a good compromise for adjusting T_{out} of RefleC to that of the flat-plates during day and year. But the data still show that the output of RefleC is much more varying seasonally and during the day than that of a flat-plate due to its unique IAM curve. For a plant exclusively equipped with RefleC collectors, a variable speed pump is recommended for solar loop and charging circuit to achieve constant outlet temperatures for process heat supply.

Measured vs. calculated power output: In Figure 5.15 the measured RefleC and flat-plate power outputs are compared to the theoretical output calculated based on efficiency curve tests and raytracing results.

The "measured" power outputs of the fields were determined by multiplying Eq. 3.1 with the field-apertures. The temperature lifts are $\Delta T = T_{out} - T_{in}$. The mass flow $\dot{m}$ is the MID-measured volume flow $\dot{v}$ multiplied by the density of the fluid ρ_{fl} at the MID-position, represented by T_{in} of the field. The fluid in the solar loop is a mixture of 40 % propylene glycol and 60 % water. From the supplier of the glycol, tabulated values of density and specific heat capacity $\bar{c}_{p,fl}$ from 10 °C to 100 °C in steps of 10 °C were provided to Wagner & Co. They were fitted as follows (Eisenmann 2009):

$$\rho_{fl}(T_{in}) = 1048.7667 - 0.4447 \cdot T_{in} - 0.0027 \cdot T_{in}^2 \quad \text{with } T_{in} \text{ [°C]} \quad (5.1)$$

$$\bar{c}_{p,fl}(T_f) = 3.6060 + 0.0038 \cdot T_f \quad \text{with } T_f \text{ [°C]} \quad (5.2)$$

The "calculated" power output was determined by Eq. 3.12 (cp. also Eq. 3.9) for the same instantaneous T_f and $\dot{m}$ as used for the "measured" values. In addition to the values above, the sensor outputs for ambient temperature T_a, as well as global irradiance onto the aperture G_t, and diffuse irradiance onto the horizontal G_d were used.
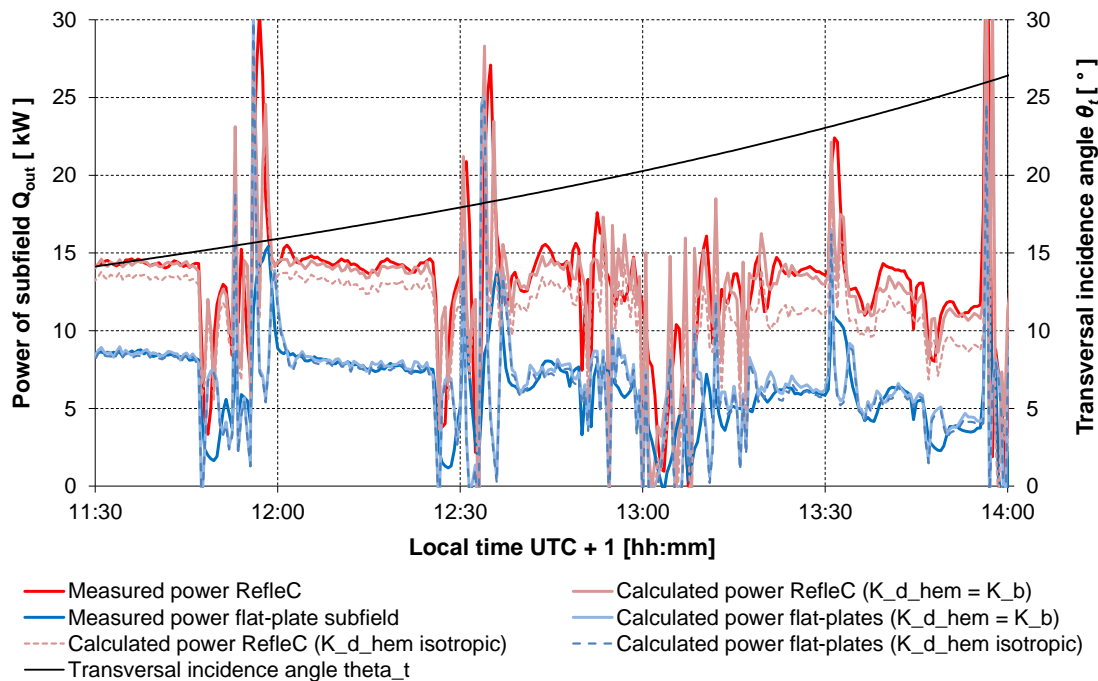
Figure 5.15: Comparison of measured and calculated power of RefleC subfield 2 and flat-plate subfield (both identical number of flat-plates) on Saturday, 21.08.2010. The harsh drop in power output after 13:00 was due to a cloud passing by. For calculation variant $K_{d,hem} = K_b$, all hemispheric irradiance G_t onto the aperture is considered to be beam and weighted by K_b; for variant $K_{d,hem}$ isotropic, the beam irradiance on the tilted plane G_{bt} is indicatively approximated from subtracting the measured horizontal diffuse G_d from the tilted hemispheric G_t. This G_{bt} is then weighted with K_b, while G_{dt} is approximated by G_d and weighted by the IAM for an isotropic collector hemisphere $K_{d,hem}$. The analyzed time period is indicated in Figure 5.13 and Figure 5.14 as grey arrows.

Analyzing the measured power output in Figure 5.15 shows that within the selected time period the RefleC field had a significantly higher power output than the flat-plates. This is due to lower thermal losses at high working temperatures, but also due to the higher K_b-values caused by the reflectors at beneficial transversal incidence angles θ_t. Table 5.3 gives details on the subfield performances.

Table 5.3: Conditions and collector performance on Saturday, 21.08.2010.

Time [hh: mm]	G_t [W/m²]	k^* [−]	f_d^{**} [−]	T_{in} [°C]	Subfield	T_{out} [°C]	$\dot{q}_{out}^{***}$ [kW]	K_b [−]	η [−]	RefleC subfield surplus yield factor (absolute)
11:30	938	0.12	0.10	83.2	Flat-plate	100.3	8.6	0.99	0.57	1.7
					RefleC	99.3	14.0	1.25	0.75	
13:25	916	0.26	0.27	107.3	Flat-plate	119.5	5.9	0.97	0.42	2.3
					RefleC	122.6	13.5	1.38	0.76	
13:50	797	0.19	0.19	110.1	Flat-plate	116.8	3.3	0.96	0.24	3.6
					RefleC	123.4	11.8	1.40	0.68	

* fraction of diffuse on horizontal (horizontal diffuse S003 devided by horizontal hemispheric S002)
** fraction of diffuse on aperutre (indicative estimation; S003 devided by hemispheric on aperture S001)
*** measured power output

At 11:30, the mean fluid temperature was $T_f \approx 92\ °C$ in both fields. Gains and efficiency of RefleC were higher, since θ_t already caused a high value of K_b and the fraction of diffuse f_d was low. The flat-plate subfield had also a high efficiency. At 13:25, the higher working temperatures caused a decrease in efficiency of the flat-plate, while at RefleC the increase in K_b compensated the higher thermal losses. Until 13:50, the irradiance onto the aperture had considerably decreased. But RefleC was at its maximal IAM $K_b = 1.4$ and thus still worked at very satisfying efficiency of $\eta = 0.68$. The flat-plate efficiency collapsed, since lower irradiance and constantly high working temperatures ($T_f \approx 113\ °C$) highly increased the thermal losses. At these conditions, the power output of RefleC was finally 3.6 times higher than that of the flat-plates.

The collector performance values used to calculate the power output are given in the following. The thermal efficiency curves had been determined outdoor at the test laboratory. For the flat-plates, the curve measured at $\dot{m} = 35\ kg/(m^2 h)$ was taken, while for RefleC the curve measured at $\dot{m} = 72\ kg/(m^2 h)$ was used, since the curve at $35\ kg/(m^2 h)$ had not been fully determined (cp. Figure 3.12, no deviation between both mass flows measured for RefleC). The IAM values for beam irradiance K_b of both collectors are shown in Figure 5.14 (for RefleC, as stated above, a raytraced 3D-IAM was used, accurately representing the trough closure reflector effects). The effective thermal capacity of the flat-plates is $c_{eff,fp} = 4.696\ kJ/(m^2 K)$. The factor c_{eff} is related to the aperture, but at RefleC and the reflectors are not thermally connected to their receiver flat-plates. Because of that, the value $c_{eff,R} = c_{eff,fp}/1.25 = 3.757$ was used.

The day selected for the exemplary comparison between measured and calculated collector field output in Figure 5.16 is one with high hemispherical irradiance and highly anisotropic diffuse irradiance. The unshaded pyranometers shown in Figure 5.9 determine the hemispherical irradiance onto horizontal G and aperture G_t. Measurement of diffuse irradiance on the horizontal G_d is done by the shadow band pyranometer and thus less accurate. Neither a pyrheliometer, to determine the exact diffuse irradiance onto horizontal and aperture (by subtracting G_b from DNI-measurement from the respective hemispherical values), nor an albedometer to distinguish between sky and ground reflected diffuse irradiance onto the aperture was available.

Having in mind these limitations, two variants to calculate the power output for a comparison to the measured performance were applied. The **variant "$K_{d,hem} = K_b$"** treats all irradiance onto the aperture as if originating from sun direction. At the very high K_b-values occurring within the investigated time period, this overestimates the influence of diffuse. On the other hand, the measured G_t accurately accounts for the diffuse irradiance from sky and ground received by the collector. Furthermore, due to the high sky anisotropy (cp. horizontal diffuse fraction k in Table 5.3) the major share of diffuse is expected to be brightening around the sun. The **variant "$K_{d,hem}$ isotropic"** aims at distinguishing between beam and diffuse. At the pilot plant, this in principle right intention has the drawback that the diffuse irradiance onto the aperture is not measured. The simplification of using the inaccurately measured horizontal diffuse instead induces very high uncertainties both for G_{dt} and the G_{bt} calculated with it. Since furthermore the distribution of diffuse over the sky dome is not known, the common isotropic approach was taken for comparison to variant "$K_{d,hem} = K_b$". Therefore, for both collectors the IAM for isotropic diffuse irradiance $K_{d,hem}$ from the whole collector hemisphere was needed. For both, the identical values as from the energy gain simulations were used. For the flat-plate, this is $K_{d,hem} = 0.82$; for RefleC it is $K_{d,hem} = 0.66$. Assuming an endless RefleC trough slightly overestimates $K_{d,hem}$ of the pilot plant, but the raytraced 3D-IAM of the RefleC subfield 2 was only valid for the half collector hemisphere with $\phi > 0°$ and could therefore not be used.

The first 15 min in Figure 5.15 are most suitable for the comparison because of the quasi-stationary conditions (almost constant irradiance and T_f, cp. Figure 5.13). For the conditions of this time period, **variant "$K_{d,hem} = K_b$"** predicts the measured power very accurately. At the flat-plates, the measured energy gain of this period is about 0.5 % below the calculated, while for RefleC the measured gain is 0.2 % above. When the time frame is extended to unstationary operation, the deviations are slightly higher. For the flat-plate, IAM values for the whole day are available, so a time period symmetric around $\phi = 0°$ from 09:15 to 13:45 can be used. Here, the measured output is 2 % below the calculated. For the RefleC subfield 2, where no full-day IAM values are available, from 11:30 to 13:45 the measured output is even 2 % above the calculated.

When applying variant "$K_{d,hem}$ isotropic", at the flat-plates almost no difference in calculated output compared to the other variant is observed. This is because at the flat-plates the IAM values for beam and isotropic diffuse are not highly differing and the fraction of diffuse is small (see f_d and cp. $K_{d,hem} = 0.82$ to K_b in Table 5.3). Only at 13:25, because of the higher f_d, the power calculated by variant "$K_{d,hem}$ isotropic" is slightly below that calculated by "$K_{d,hem} = K_b$". For RefleC, there is a high deviation between the variants. The undervaluation by "$K_{d,hem}$ isotropic" increases with increasing f_d and K_b. This is because $K_{d,hem} = 0.66$ is highly differing from K_b, so the acceptance of diffuse is indeed highly influencing the calculated value.

The comparison of the raytracing simulations with measured IAM values at the test laboratory under a very similar incidence angle had already indicated that the isotropic approach significantly underestimates the contribution of diffuse to the output of RefleC (cp. Figure 3.19). Having in mind the measurement uncertainties of the sensors at pilot plant and test laboratory, but also the uncertainties of the raytracing simulations, the calculated power correlates very well with the measured. Further considering that at the pilot plant the uncertainties of the irradiance determination for calculation variant "$K_{d,hem}$ isotropic" are identical for RefleC and the flat-plates, the presented comparison between measured and calculated power confirms that the isotropic approach underestimates the power output of RefleC. Furthermore, the comparison shows that RefleC and flat-plates work as theoretically expected also at a real installation.

Annual additional gains by the reflectors: Figure 5.16 gives a monthly overview on the mean daily irradiance as well as specific flat-plate and RefleC gains of the whole monitoring period. To calculate the additional gain by the reflectors as shown, the measured monthly gross-energy gain of the RefleC subfield 2 was directly compared to that of the flat-plate subfield. In summer 2011, the solar irradiance was low compared to 2010 due to bad weather periods (cp. e.g. variation for July). The additional gains show a sinus-like characteristic – high and stable additional output is observed from April to September. The additional gains in percentage terms mainly depend on the annual sun path; they are fairly independent of the absolute irradiance. This is proved when comparing the additional gains in August, September and October 2010 to the almost identical values in 2011. The reflectors were installed on 9 July 2010, so the values given for this month should not be compared to July 2011. In June and July 2011 the sinus-like shape of the additional gains flattens a bit, since around noon θ_t is often above $35°$, which leads to a decrease in K_b (i.e. the mirrors do not direct beam to the receiver but reflect it back into the sky above the flat-plates).

To allow an indicative comparison between the annual performance of RefleC and its flat-plate at the pilot plant, the reference year from 1 October 2010 to 30 September 2011 as defined above is used. At this comparison, for RefleC again only the measured gains of subfield 2 are used since this subfield had its own mass flow sensor.
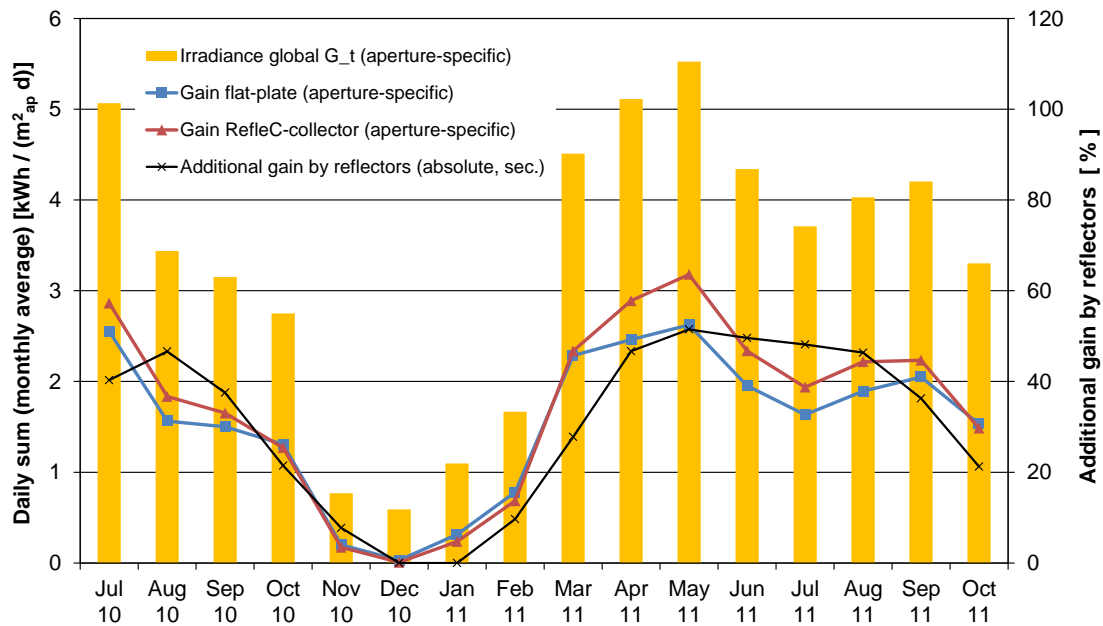
Figure 5.16: Overview on the whole monitoring period of 16 months with irradiance, specific gains of flat-plates and RefleC subfield 2 as well as monthly additional energy gains due to the reflectors. In Dec. and Jan. the flat-plate subfield had higher absolute gains than RefleC because of albedo and shading of the RefleC receiver flat-plates by the front row. But since the absolute gains at this time were very low, these marginal "negative additional gains" are not displayed in the graph.

In the reference year, <u>at</u> field inlet temperatures $\underline{T_{in} > 80\,°C\text{ the measured}}$ cumulated additional gross energy gains of the <u>RefleC</u> subfield 2 were <u>78 % higher than</u> the gains of the <u>flat plate subfield</u>. When all inlet temperatures are considered, RefleC was still 39 % better. Aperture-specific, these cumulated additional gains were 42 % at $T_{in} > 80\,°C$ and 11 % over the whole year. <u>A comparison of these measured gains to the annual simulation results in chapter 4 is not admissible</u> because of the following reasons:

- The simulations are valid for a typical meteorological year in Würzburg with a collector field orientated south; the monitored field is located in Marburg with collector azimuth $\gamma = -21°$ and exposed to current weather and irradiance.
- The monitored flat-plate sub-field is not tilted for maximal energy gain (cp. $\beta = 55°$ at the pilot plant vs. optimized $\beta = 32.5°$ in the simulations.
- In the simulations, the field was operated at constant mass flow and inlet temperatures over the whole year and all positive gains were counted. At the pilot plant, the inlet temperatures were highly variable and mass flow through the field was only activated when a sufficient temperature lift was reached.

To conclude, the monitoring of the pilot plant proved the suitability of the RefleC concept to significantly increase the energy output of double covered flat-plates at working temperatures above 80 °C. The measured annual additional gains by the reflectors will be lower for optimally orientated flat plates, but the detailed look into the monitoring results above revealed that <u>RefleC performs as theoretically expected</u>.

5.3   Economic Assessment of RefleC Boosters

The anisotropic simulations discussed above showed that the additional gain caused by the RefleC booster reflectors is much higher than predicted by isotropic, state of the art modelling (cp. Figure 4.15). This can be of high practical relevance for the ST industry, because it positively influences the cost/performance ratio of the boosters.

Taking the anisotropically calculated booster gains into account, this section aims to estimate up to which investment costs per unit reflector area boosters may be economically attractive for applications similar to the RefleC pilot plant. This estimation starts from the expression of solar heat generation costs K_{sol} (VDI 2004, p. 66):

$$K_{sol} = \frac{K_{inv} \cdot f_a + K_{main}}{Q_{sol}} + K_{op} \qquad (5.3)$$

Therein, K_{inv} is the overall investment costs, f_a is the annuity factor accounting for the annual capital costs, K_{main} and K_{op} are the annual maintenance and operational costs, and Q_{sol} is the annual solar gains. The annuity factor f_a is calculated from the capital interest rate p and the service life T of the boosters (VDI 2004, p. 66):

$$f_a = \frac{(1+p)^T \cdot p}{(1+p)^T - 1} \qquad (5.4)$$

At the RefleC pilot plant, the reflectors are not cleaned and therefore do not cause additional operational or maintenance costs compared to a system of flat plate collectors without reflectors. Thus, because only costs and gains related to the reflector shall be analyzed, K_{op} and K_{main} do not have to be considered and eq. 5.3 can be written as:

$$K_{inv} = \frac{K_{sol} \cdot Q_{sol}}{f_a} \qquad (5.5)$$

First, the additional annual gains by the booster reflectors Q_{sol} have to be quantified. This must be the difference between an optimized system with double-covered flat-plates and a system with RefleC collectors. It was discussed at the end of the last section 5.2.2 that the additional gains measured at the pilot plant do not represent this difference. But because the monitored system worked as theoretically expected, the simulation results for RefleC 6 and LBM 4 GF can be used. These simulations revealed that the absolute additional collector gain caused by the boosters depends on the location, but is similar for both simulated inlet temperatures of 40 °C and 120 °C (cp. Figure 4.14 and Table 4.2). For the following assessment, it is assumed that these temperatures mark the expected working temperature range of stationary collectors with boosters. It is further assumed that the additional gains by the boosters are temperature-independent, so that a mean value of the simulated additional gain can be used. This is in Würzburg 126.0 kWh m_{fp}^{-2} a^{-1} and in Seville 212.5 kWh m_{fp}^{-2} a^{-1} (cp. Table 4.2).

These values do not yet represent the useable heat Q_{sol}, because the simulation results in section 4.3.3 give only the collector gain and do not consider losses within a SPH system. At the RefleC pilot plant, 70.4 % of the heat produced by the collector field was transferred to the processes (cp. p. 134). This measured system efficiency accounts for the whole spectrum of operation temperatures (30 °C up to 130 °C), for the losses caused by the stagnation cooler, and for the non-optimized system control during the first months. Although the system efficiency might be higher at larger SPH systems with boosters, the value of the RefleC pilot plant is used here. Based on this conservative system efficiency and the simulation results, the calculated additional energy supply to the processes caused by the reflectors is in Würzburg $Q_{sol} = 88.7 \text{ kWh m}_{\text{fp}}^{-2} \text{ a}^{-1}$ and in Seville $Q_{sol} = 149.6 \text{ kWh m}_{\text{fp}}^{-2} \text{ a}^{-1}$.

To calculate a minimal selling price for the reflectors by eq. 5.5, acceptable solar heat generation costs K_{sol} for the useful energy from the reflectors have to be estimated. Because the RefleC pilot plant is a laundry, conventional heating costs from the laundry sector are used as a basis for comparison. Beeh and Hess (2014) collected data of 20 laundries, most of them located in Germany and having a gas-fired steam network. When losses of 20 % for heat generation and distribution are taken into account, the typical conventional heating costs at these laundries are about 0.06 EUR/kWh (Beeh and Hess 2014, p. 13). As an example, the following assessment assumes that the application of booster reflectors might be attractive if they generate useful solar heat at two thirds of this price, i.e. $K_{sol} = 0.04$ EUR/kWh. To estimate the capital costs, an interest rate $p = 4 \%$ and a lifetime of the system of $T = 20$ years are assumed. With eq. 5.4 this results in an annuity factor of $f = 0.0736$.

From the estimations and framework conditions discussed above, the resulting investment costs K_{inv}, i.e. the minimal selling price of the reflector for one m^2 of flat-plate receiver aperture can be calculated by eq. 5.5. If the same framework conditions are assumed for both locations, the result is for Würzburg $K_{inv} = 48 \text{ EUR/m}_{\text{fp}}^2$ and for Seville $K_{inv} = 81 \text{ EUR/m}_{\text{fp}}^2$. The RefleC collector as applied at the pilot plant uses the flat-plate collector LBM 8 of Wagner & Co. Solartechnik with four glass panes as receiver. This flat-plate has an overall aperture area $A_{ap} = 8{,}15 \text{ m}^2$ and is equipped with an overall reflector area of 12,57 m² (Kramp 2010).

The exemplary calculation above gives a minimal reflector price for Würzburg of $K_{inv} = 31 \text{ EUR/m}^2$ (or 393 EUR per LBM 8 equipped) and for Seville of $K_{inv} = 53 \text{ EUR/m}^2$ (or 663 EUR per LBM 8). For the customer this would mean a static payback period of approx. nine years (calculated from dividing the investment for the boosters by the annually saved gas costs). It has to be stressed that other framework conditions can result in highly different values. Especially the interest rate has a very high impact on reflector price and amortization period.

6 Conclusions and Perspectives

The findings of this work are summarized and discussed against the state of the art. Suggestions for further research are made.

6.1 Low-Concentrating, Stationary Collectors

External reflectors can highly increase the gain of stationary ST collectors. Boosters between collector rows offer better roof area utilization and acceptance for diffuse irradiance than reflectors on both the upper and lower sides of a collector. CPC reflectors have a higher acceptance angle than flat reflectors. But when reflecting on flat-plates, this advantage is partly compensated by lower transmittance of the reflected rays through the cover(s). CPC reflectors also cause local concentration on the absorber. This reduced the collector efficiency factor F' of the flat-plates tested. The booster of RefleC approximates a half CPC by flat segments, which avoided this decrease.

Simulation results revealed that the RefleC booster increases the annual output of the double-covered flat-plate in Würzburg by 20 % at a constant inlet temperature of 40 °C and by 87 % at an inlet of 120 °C. The absolute increase is largely temperature independent. Simulating with a varying, anisotropic diffuse-IAM is considered to be essential for realistic modelling of instantaneous collector gains and for accurate assessment of the cost-benefit ratio of stationary reflectors. Isotropic modelling undervalued the additional gains from the RefleC booster by 40 % at 40 °C and by 20 % at 120 °C.

Accurate efficiency curve and IAM determination is of special importance for medium temperature collectors. Extrapolation of an efficiency curve to values of $\Delta T / G$ higher than tested overestimates the collector efficiency. Therefore, one operation point with efficiency below 20 % is recommended for collector efficiency tests. The influence of the IAM on efficiency and annual gains increases with increasing thermal losses.

It was shown that the efficiency curve of a stationary collector with external reflector can be estimated without measurements, when the efficiency curve of the collector and raytracing of the receiver-booster combination are available, and when F' does not change. This can be used to assess the effect of optimized external reflectors for existing collectors by annual energy gain simulations. Thus, future work in this field could include theoretical assessments of the performance increase of e.g. standard evacuated tube collectors or evacuated flat-plates due to optimized external booster reflectors.

6.2 IAM for Beam and Diffuse Irradiance

Diffuse irradiance originates from the whole 180° hemisphere of a sloped ST collector, except of a solid angle of approx. 6° diameter around the sun, from where pyrheliometers detect beam. The diffuse radiance is not isotropic, and its anisotropy changes with varying meteorological conditions. The influence of both the IAM for beam and diffuse on efficiency and annual gain increases with increasing thermal losses, so accurate IAM values are of increased relevance for medium temperature collectors.

Beam-IAM curves determined from steady-state outdoor-tests at hemispherical irradiance are considered to describe the IAM of low-concentrating collectors sufficiently within their concentrator acceptance angle, if the diffuse fractions during the test intervals are similar. For irradiance from outside the acceptance angle or for highly different diffuse fractions, "correction" of the diffuse influence as applied in this work is recommended. Such a correction was shown under the simplifying assumption of isotropic diffuse irradiance. A comparative correction calculation with diffuse-IAM values that may reflect the hemispheric anisotropy during the test led to the conclusion that the accuracy of the correction could in the future be improved by considering this anisotropy.

A hemispheric, isotropic diffuse-IAM determined from steady-state outdoor-tests is underestimating the annual diffuse utilization of all ST collectors. Quasi-dynamic tests have not been performed in this work. Such tests identify the diffuse-IAM from measured collector output. Although this is also done assuming an isotropic hemisphere, the identified diffuse-IAM value is expected to better represent the annual diffuse utilization of a collector, since its value also reflects the anisotropic irradiance during the test.

Considering the varying anisotropy of diffuse sky radiance in collector simulation models by a varying, anisotropically calculated diffuse-IAM is considered to be essential for realistic modelling of instantaneous collector gains and for accurate assessment of the cost-benefit ratio of stationary reflectors.

In future research, to determine beam and diffuse IAM data from outdoor measurements, a pyrheliometer and an albedometer should be applied. These two sensors allow for accurately distinguishing between beam, sky diffuse, and ground reflected diffuse irradiance onto the aperture. This makes instantaneous clearness index calculation possible, so that the sky radiance could be anisotropically distributed according to the Brunger model. With this, the instantaneous IAM of a collector for anisotropic diffuse irradiance can be calculated as introduced in this work. Following the test value "correction" approach given, the contributions of the three irradiance components to the measured output and thus the three IAMs of the separated irradiance components could be determined iteratively from a set of incidence angles tested. Highest relevance is expected for stationary, incidence-angle selective collectors like RefleC.

6.3 Simulation Model

Existing collector simulation models do not consider the effect of the varying anisotropy of diffuse irradiance on the diffuse-IAM. They calculate with a constant IAM for isotropic diffuse irradiance. Furthermore, they all use one IAM for diffuse irradiance from the 180° collector hemisphere, not distinguishing between sky and ground.

In the TRNSYS simulation software, the radiation processor considers the sky anisotropy e.g. by applying the Perez-Model to calculate irradiance on a tilted plane from weather data files. But the radiation processor only gives the correct sum of the irradiance, not its distribution. That is why existing collector models can not consider the anisotropy of sky irradiance. The collector simulation model presented in this work calculates separate IAMs for sky diffuse irradiance and ground reflected diffuse irradiance. It uses the model of Brunger and Hooper to generate an anisotropic sky based on the current fraction of diffuse and the clearness index. To calculate an anisotropic diffuse-IAM for sky radiance, the model divides the sky into segments and weights their irradiance with raytraced beam-IAM values for the individual incidence angles of these segments. This is done once per time step. The Brunger distribution is exclusively used to calculate the diffuse-IAM for anisotropic sky irradiance. The IAM for diffuse ground irradiance is calculated with an isotropic approach and is constant during the simulation. The model is also capable of calculating a diffuse-IAM for an isotropic collector hemisphere (state of the art) or separate isotropic diffuse IAMs for sky and ground irradiance. The sums of sky and ground reflected diffuse irradiance onto the aperture are input to the model and taken from the radiation processor as usual.

The model was applied to RefleC and its flat-plate receiver for constant inlet temperatures of 40 °C and 120 °C in Würzburg and Seville. At the anisotropic calculation, in Würzburg for RefleC a daily variation of the diffuse IAM of up to 25 % was observed. Separate IAM calculation for anisotropic sky and isotropic ground instead of the hemispherical isotropic calculation resulted for RefleC at 40 °C inlet in 10 % increased annual gains; at 120 °C the gains were 16 % higher. The flat-plate without reflectors showed an increase of 3 % at 40 °C and 8 % at 120 °C. The undervaluation by isotropic modelling was reduced to about 6.5 % (for RefleC at 120 °C), when separate diffuse-IAMs for sky and ground were calculated. In Seville, due to a lower diffuse fraction, the undervaluation in percent was lower than in Würzburg.

The results indicate that the diffuse-utilization of all non-focusing collectors is undervalued by existing simulation models, when isotropic diffuse-IAMs calculated from raytracing or steady-state tests are used. This is concluded from the irradiation diagram shown and because underestimation was also found for the flat-plate, which is the least incidence angle sensitive collector type. The optimal collector slope was not affected by the anisotropic diffuse-IAM modelling, so current models are sufficient in this respect.

In the future, the simulation comparison between annual output with constant isotropic and varying anisotropic diffuse-IAMs should also be performed using isotropic diffuse-IAM values from quasi-dynamic collector tests. In this case, the error of isotropic modelling is expected to be smaller. Such comparisons for different common collector types would allow assessing the individual relevance of anisotropic diffuse-IAM modelling.

The developed simulation model itself should be further improved. Currently, the specific fluid heat capacity is a constant parameter. Its temperature-dependency must be included to compare simulated output temperatures to measured values accurately. The annual output should be much less sensitive for this. Furthermore, the missing parameters of the dynamic collector model of Perers could be implemented. The model has not been validated yet, and also the reported differences between isotropic and anisotropic modelling results were not determined independently, since the same model was used for both. Future work should therefore first compare the different diffuse-IAM modes of the new model to existing collector simulation models.

The simulations given in this work were only determined for constant collector inlet temperatures and constant mass flow, and every positive gain was counted. Future works should compare this simplified collector gain simulation to more realistic cases by applying the new model for in simulations of complete ST systems.

For a real validation of the model, a setup as described at the end of the last section 6.2 is recommended. The measured irradiance and collector test data could be used as model-input, so that the modeled collector output temperatures could be compared to the measured ones for the variety of sky radiance conditions covered by the Brunger model.

At RefleC and similar collectors, the undervaluation of the annual sky-diffuse utilization by the isotropic IAM might be partly compensated by an overvaluation due to the application of the simplified beam-IAM separation approach of McIntire. This means that it is possible that the undervaluation of real annual gains by the existing simulation models might in reality be smaller than resulting from this work. So, future work should determine the error of this separation approach for RefleC and other stationary collector types by 3D-raytracing and annual simulations. The collector model presented is very suitable for this purpose, since it can directly use a 3D-IAM.

The use of raytraced beam-IAM curves in energy gain simulations has a general limitation. They only represent a collector's IAM correctly, when the thermal loss mechanisms do not change with the incidence angle. Such changes can e.g. be caused by a varying F' resulting from local concentrations varying with the incidence angle.

In the short term, the accuracy of standard simulation tools could be significantly increased by implementing a separate calculation of constant isotropic diffuse-IAMs for sky and ground, as documented in this work. Since such a calculation has to be done only once per simulation, no effect on the simulation time of standard tools is expected.

6.4 Pilot Plant

Process heat generation with the RefleC collector is demonstrated at a laundry in Germany with an innovative, monitored ST system. The system supplies hot water for the washing machines, boiler makeup-water, and boiler feed water. A trough of RefleC collectors was directly compared to a row of double-covered flat-plates without reflectors. For a reference year, the annual solar fraction of the system was determined to be 23.2 %, the solar loop utilization ratio was 40.9 %, and the system utilization ratio was 35 %. The system utilization ratio is particularly satisfying compared to other monitored process heat systems. For future collector fields with booster reflectors, adaptive variable speed pumps are recommended to account for the very incidence angle dependent power output and to avoid too high outlet temperatures.

Comparing all gains within the reference year at inlet temperatures above 80 °C, the RefleC boosters increased the gain of the double-covered reference flat-plates by 78 %. During the whole year, the gain of RefleC was 39 % above that of the double-covered flat-plates. The basis of this comparison is a unit area of flat-plate receiver.

A comparison between measured and calculated collector output showed that the flat-plate as well as the RefleC collector work as theoretically expected. For a representative day with a clear sky, the calculated collector output of RefleC was significantly beyond the measured, when a diffuse-IAM for an isotropic sky was used. Calculation with a diffuse-IAM value increased to the beam-IAM (which is expected to be more realistic at clear sky conditions) reproduced the measured collector output correctly.

During the monitoring sequence analyzed, the influence of the diffuse-IAM on the calculated output of the flat-plate was low, because the values of beam- and diffuse-IAM did not differ much. Thus, anisotropy effects on the flat-plate output could not be clearly reproduced yet and might be within the measurement uncertainty range. But for RefleC the comparison clearly indicates an undervaluation by the isotropic approach. For the calculation of the RefleC output, a raytraced 3D-IAM was used, so that errors of the McIntire interpolation approach can be excluded.

For future monitoring projects with similar collectors, a dedicated analysis tool coupled with a monitoring database is recommended. To effectively analyze the utilization of diffuse irradiance by a collector from monitored data, a pyrheliometer and an albedometer, as discussed in section 6.2 above, should be applied. While test stand measurements only allow for a validation at certain irradiance situations and fluid temperatures, a classification of annually monitored data into intervals of operation temperatures and Brunger distributions would allow for a comprehensive validation of the simulation model discussed within this work.
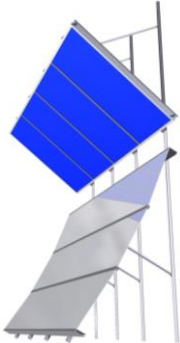
Appendix

A Collector Variants

A.1 RefleC

Table A.1: Parameters of RefleC collectors

Version	Picture	θ_a [-]	C_{geo} [°]	A_{ap} [m²]	Aperture width receiver [mm]	ρ Reflector(s) [-]	Arc length reflector (gap) [mm]	Receiver collector	Purpose
R1 (test sample)		35	1,435	4.380	1618	0.838 Alu sheet Alcan SS-990 (measured)	1145 (two-sided) (gap = 150)	LBM 67 AR	Proof of principle; thermal and optical model validation by efficiency and IAM measurement
R2 G (test sample)		20	1,625	3.867	2080	0.838 Alu sheet Alcan SS-990 (measured)	1435 (two-sided) (gap = 190)	EURO C20 AR	Further increase of thermal efficiency; different receiver collectors; thermography and stagnation temperature
R2 GG (test sample)								EURO C20 AR (glass/glass)	

Version	Picture	θ_a [-]	C_{geo} [°]	A_{ap} [m²]	Aperture width receiver [mm]	ρ Reflector(s) [-]	Arc length reflector (gap) [mm]	Receiver collector	Purpose
R3 (theoretically investigated)		40	1.225	2.928	2080	0.82 SS-990 data sheet	1435 (gap = 190)	EURO C20 AR	Annual energy gain comparison with R2 GG by simulations
R4 (theoretically investigated)		25 … 55	0.97 … 1.42	various	1858	0.82 SS-990 data sheet	various (gap = 400)	LBM 22 AR	Optimization of R3-concept with LBM by energy gain simulations
R5 V1 (test sample)		35	1.257	2.542	1858	0.886 Almirr Larsson 605 (measured)	2700 one side, three segments (gap = 400)	LBM 22 AR GF V1 Foil: 50 μm	Stagnation tests at solar simulator (without reflector)
R5 V2 (test sample)								LBM 23 AR GF V2 Foil: 25 μm	Efficiency curve and IAM measurement
R6 GF (test sample)		35	1.257	5.087	1863	0.886 Almirr Larsson 605 (measured)	2700 one side, three segments (gap = 400)	LBM 4 GFR	Efficiency curve and IAM measurement to determine prototype performance

A.2 Flat-plates

Table A.2: Parameters of receiver flat-plate collectors

Version	Picture	A_{ap} [m^2]	A_{gr} [m^2]	Transparent cover (s)	Backside insulation (mm mineral wool)	Purpose
LBM 67 AR (special construction)		3.05	3.40	Sunarc AR glazing	75	Receiver RefleC 1
EURO C20 AR		2.39	2.61	Sunarc AR glazing	60	Efficiency curve tests for relative comparison between single covered, glass-glass and glass-foil double covered collector
EURO C20 AR GG (glass/glass)				Sunarc AR double glazing		
EURO C20 AR GF (glass/foil)				Sunarc AR and foil (25 μm FEP?)		
LBM 22 AR GF(V1)		2.02	2.28	Sunarc AR and foil (25 μm FEP?)	100 (60 mm mineral wool + 23.5 mm PU-panel)	Stagnation test under sun simulator
LBM 23 AR GF(V2)			2.30	Sunarc AR glass + 50 μm ETFE foil		Efficiency curve and IAM measurement
LBM 4 AR GF		4.05	4.54	Sunarc AR glass + 25 μm ETFE foil	100 (60 mm mineral wool + 23.5 mm PU-panel)	Efficiency curves at different mass flows (72, 35) and IAM measurement

B Collector Test Results

B.1 RefleC

Table B.1: Test results for efficiency curves of the RefleC test samples

Version	Picture	η_0 [-]	c_1 $\left[\frac{W}{m^2K}\right]$	c_2 $\left[\frac{W}{m^2K^2}\right]$	Test facility	Test period	Mass flow $\left[\frac{kg}{m^2h}\right]$	Max. fluid temp. [°C]	IAM measured?	Comment
R1		0.729	1.996	0.0128	Tracker Standard	2007 5.11. - 5.12.	72	95.7	yes	Raytracing validated (single glazed, for efficiency curve testing reflectors left and right, for IAM testing reflectors up and down)
R2 G		0.695	2.733	0.0031	Tracker MTTS	2008 04.-10.07.	300 kg/(h* coll.)	182.6	no	Thermography, mass flow as receiver collector because of uncertain flow through double harp absorber
R2 GG		0.627	1.618	0.0059		2008 02.07.		187.9	no	Maximum thermal efficiency

Version	Picture	η_0 [-]	c_1 $\left[\frac{W}{m^2K}\right]$	c_2 $\left[\frac{W}{m^2K^2}\right]$	Test facility	Test period	Mass flow $\left[\frac{kg}{m^2h}\right]$	Max. fluid temp. [°C]	IAM measured?	Comment
R5 V2		0.723	1.790	0.0054	Tracker Standard	2009 06.08. – 18.08.	72	92.91	yes	Raytracing validated (glass-foil-collector), MTTS defect, LBM 23 AR GF (V2) with wires
		0.726	1.327	0.0247		2009 06.08. – 18.08.	25	84.09 (lift 20 K)	no	Uncertainties at measuring with mass flow 25, less meas. points, possibly capacity influence
R6 GF		0.741	1.761	0.0106	Tracker MTTS	2010 08.10. - 21.10.	72	163.8	yes	Prototype; Reference for pilot plant
		-	-	-		2010 12.10. - 26.10.	35	165.1	yes	Punctual confirmation that efficiency curve does not change at lower mass flow

B.2 Flat-plates

Table B.2: Test results for efficiency curves of the receiver flat-plate collectors

Version	Picture	η_0 [-]	c_1 $\left[\frac{W}{m^2K}\right]$	c_2 $\left[\frac{W}{m^2K^2}\right]$	Test facili-ty	Test period	Mass flow $\left[\frac{kg}{m^2h}\right]$	Max. fluid temp. [°C]	IAM mea-sured?	Comment
LBM 67 AR		0,83	3	0,0180	-	-	-	-	-	Not measured at Fraunhofer ISE, values provided by Wagner & Co. Solartechnik
EURO C20 AR		0,808	3,716	0,0086		2008 03.04.		175.60	no	Mass flow because of uncertainties double harp, small delta T
EURO C20 AR GG		0,782	2,642	0,0091	Indoor simulator MTTS	2008 01.04.	300 kg/(h* coll.)	168.33	no	Not clear if Argon still persistent
EURO C20 AR GF		0,773	2,373	0,0180		2008 31.03.		187.72	no	Transparent distance holders between G and F, Foil type not clear (25ym FEP), sagging and crinkles

Version	Picture	η_0 [-]	c_1 $\left[\frac{W}{m^2K}\right]$	c_2 $\left[\frac{W}{m^2K^2}\right]$	Test facility	Test period	Mass flow $\left[\frac{kg}{m^2h}\right]$	Max. fluid temp. [°C]	IAM measured?	Comment
LBM 22 AR GF(V1)		-	-	-	Indoor simulator standard	2009 08.07.	No flow	Absorber: 196.45	no	Stagnation test foil behavior, sagging determined with wires
LBM 23 AR GF(V2)		-	-	-	-	-	-	-	-	Not measured separately, sagging avoided by wires
LBM 4 AR GF		0,794	1,870	0,0165	Tracker MTTS	2010 11.–22.09.	72	138	no	Serpentine absorber, difference might be small when both turbulent
		0,769	1,559	0,0178		2010 19.09. -6.10.	35	144	no	

B.3 Efficiency Test Plots
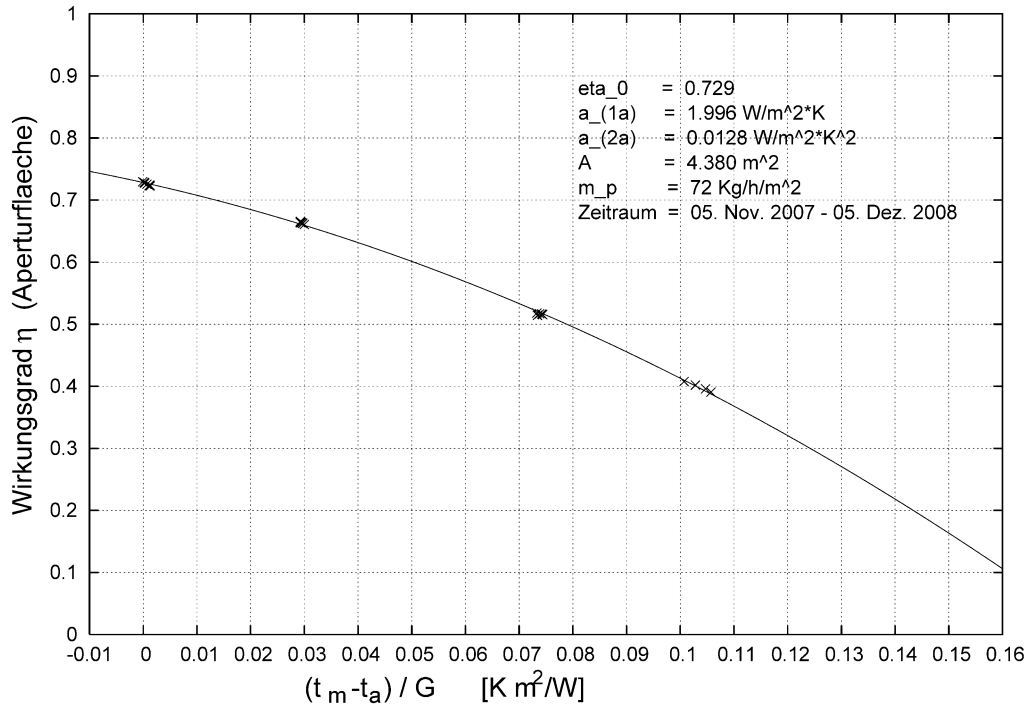
Figure B.1: Efficiency test results (outdoor, standard) of <u>RefleC 1</u>
at $\dot{m} = 72 \text{ kg}/(\text{m}^2\text{h})$
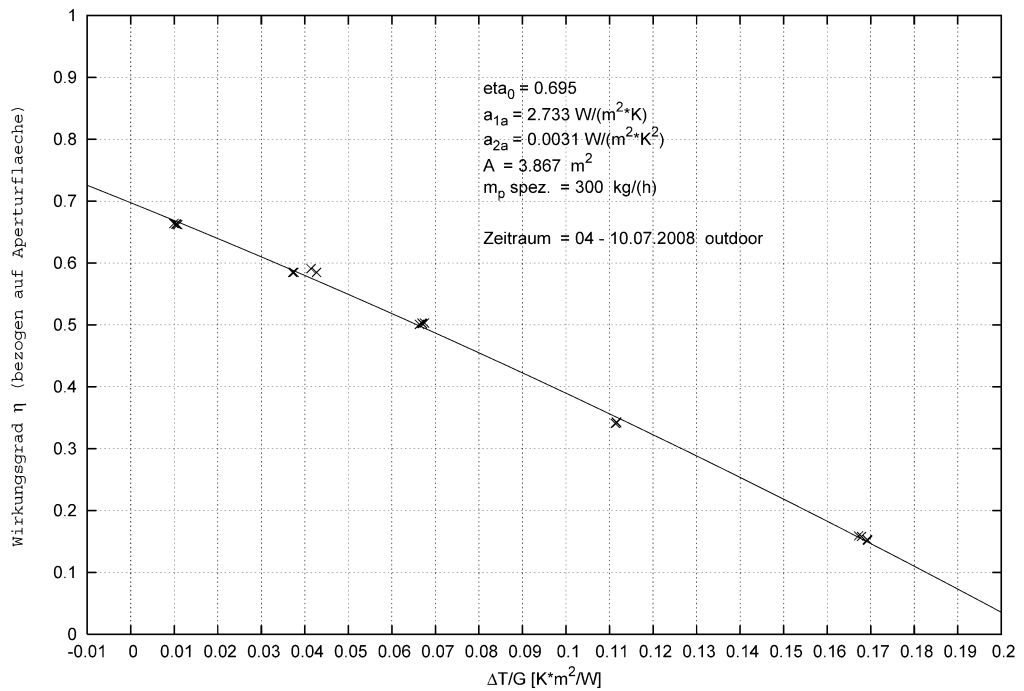
Figure B.2: Efficiency test results (outdoor, MTTS) of <u>RefleC 2 G</u>
at $\dot{m} = 300 \text{ kg}/(\text{coll} \cdot \text{h})$

159
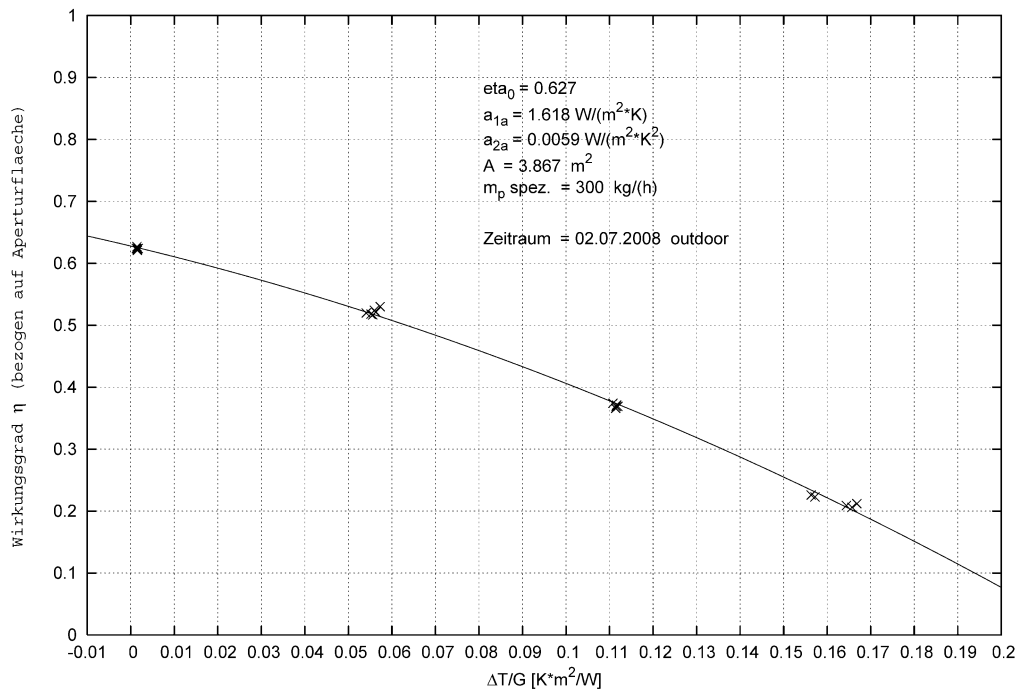
Figure B.3: Efficiency test results (outdoor, MTTS) of <u>RefleC 2 GG</u>
at $\dot{m} = 300 \text{ kg}/(\text{coll} \cdot \text{h})$
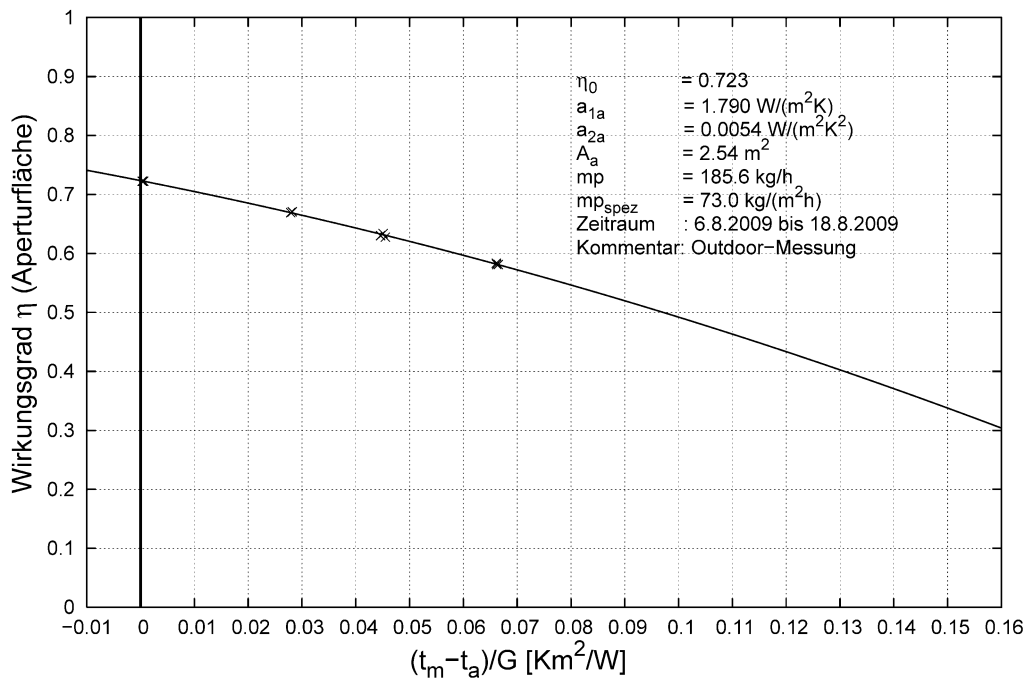
Figure B.4: Efficiency test results (outdoor, standard) of <u>RefleC 5 V2</u>
at $\dot{m} = 72 \text{ kg}/(\text{m}^2\text{h})$
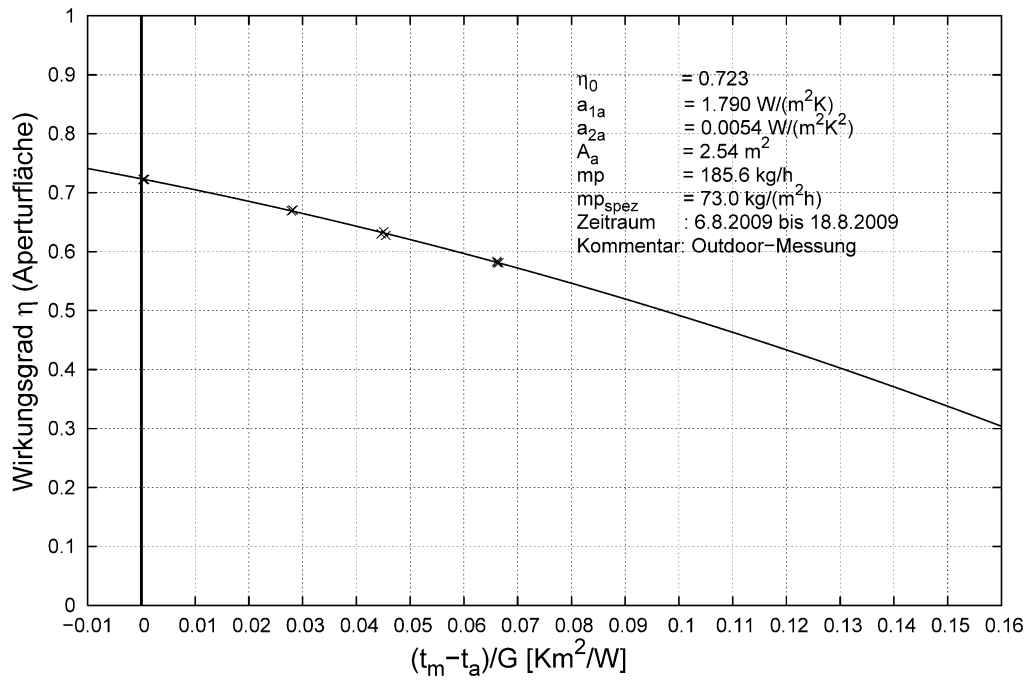
Figure B.5: Efficiency test results (outdoor, standard) of <u>RefleC 5 V2</u>
at $\dot{m} = 26 \, \text{kg}/(\text{m}^2\text{h})$
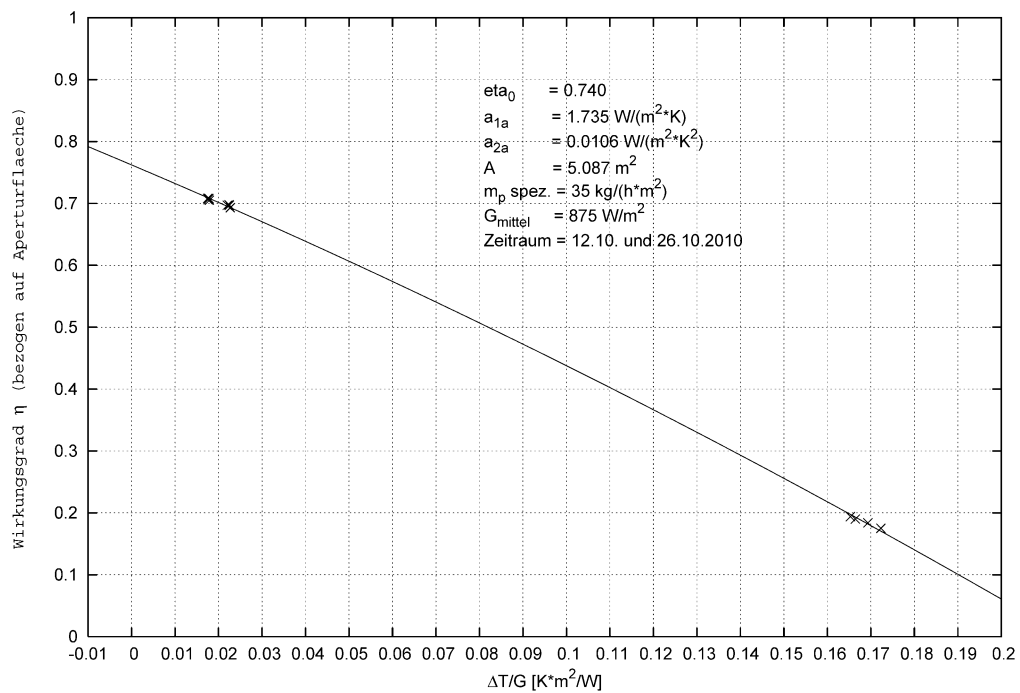
Figure B.6: Efficiency test results (outdoor, standard) of <u>RefleC 6 GF</u>
at $\dot{m} = 35 \, \text{kg}/(\text{m}^2\text{h})$; incomplete efficiency curve
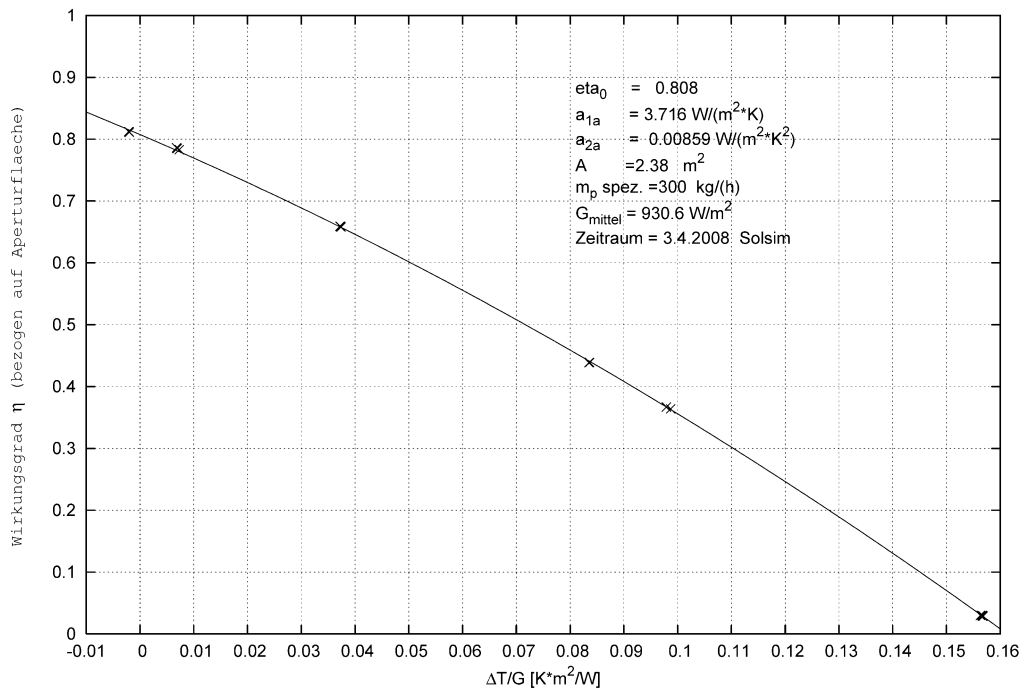
Figure B.7: Efficiency test results (sun simulator, MTTS) of <u>EURO C 20 AR</u>
at $\dot{m} = 300$ kg/(coll $\cdot$ h)
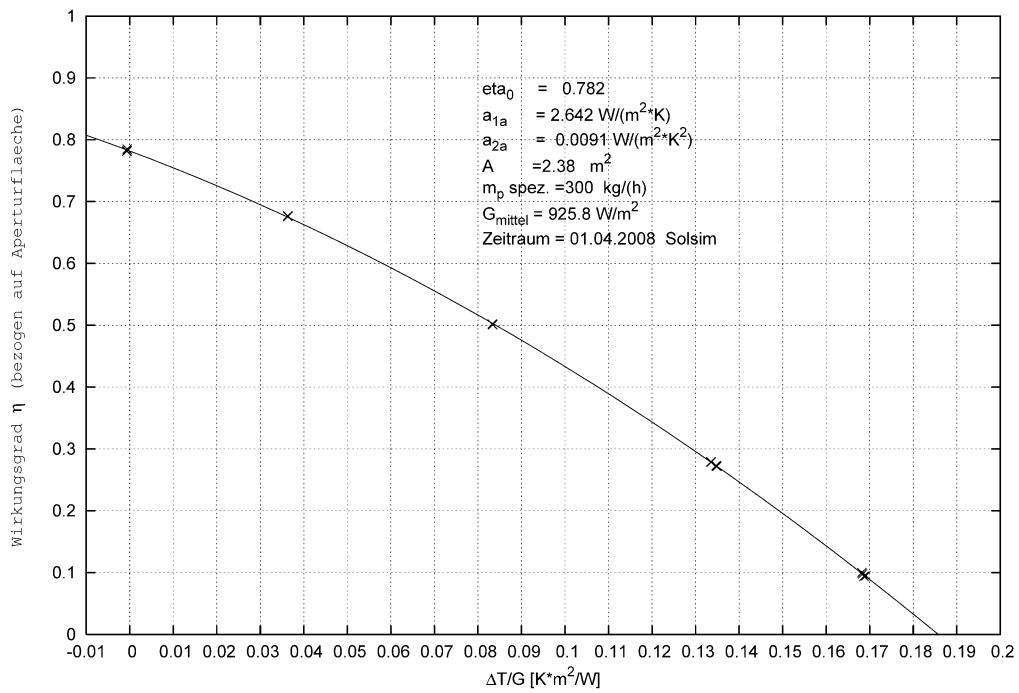
Figure B.8: Efficiency test results (sun simulator, MTTS) of <u>EURO C 20 AR GG</u>
at $\dot{m} = 300$ kg/(coll $\cdot$ h)

eta$_0$ = 0.773
a$_{1a}$ = 2.373 W/(m^2*K)
a$_{2a}$ = 0.01801 W/(m^2*K^2)
A = 2.378 m^2
m$_p$ spez. = 300 kg/(h)
G$_{mittel}$ = 929.9 W/m^2
Zeitraum = 31.03.2008 Solsim
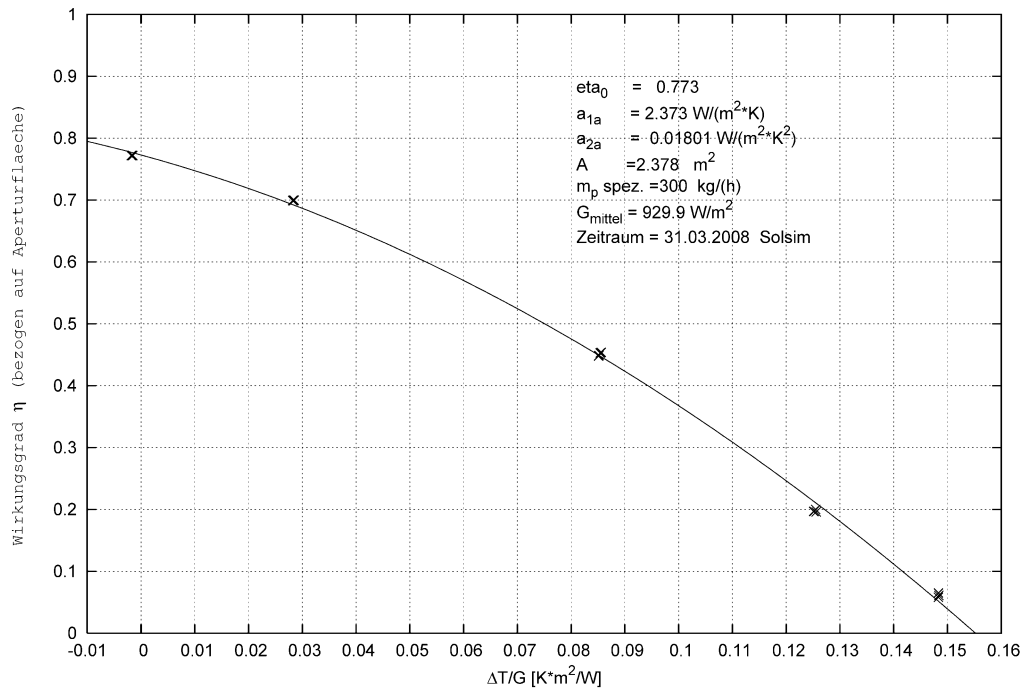
Figure B.9: Efficiency test results (sun simulator, MTTS) of <u>EURO C 20 AR GF</u>
at $\dot{m} = 300 \ \mathrm{kg/(coll \cdot h)}$

eta$_0$ = 0.769
a$_{1a}$ = 1.559 W/(m^2*K)
a$_{2a}$ = 0.0178 W/(m^2*K^2)
A = 4.047 m^2
m$_p$ spez. = 35 kg/(h*m^2)
G$_{mittel}$ = 950 W/m^2
Zeitraum = 19.09. - 06.10.2010
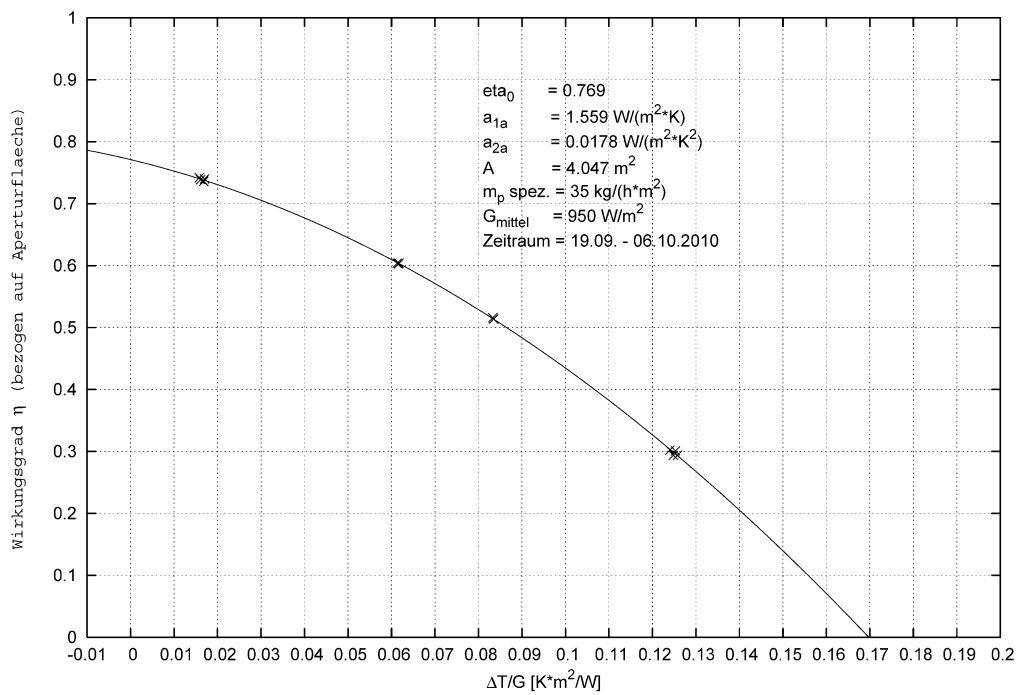
Figure B.10: Efficiency test results (outdoor, MTTS) of <u>LBM 4 GF</u>
at $\dot{m} = 35 \ \mathrm{kg/(m^2 h)}$

C Raytracing Results
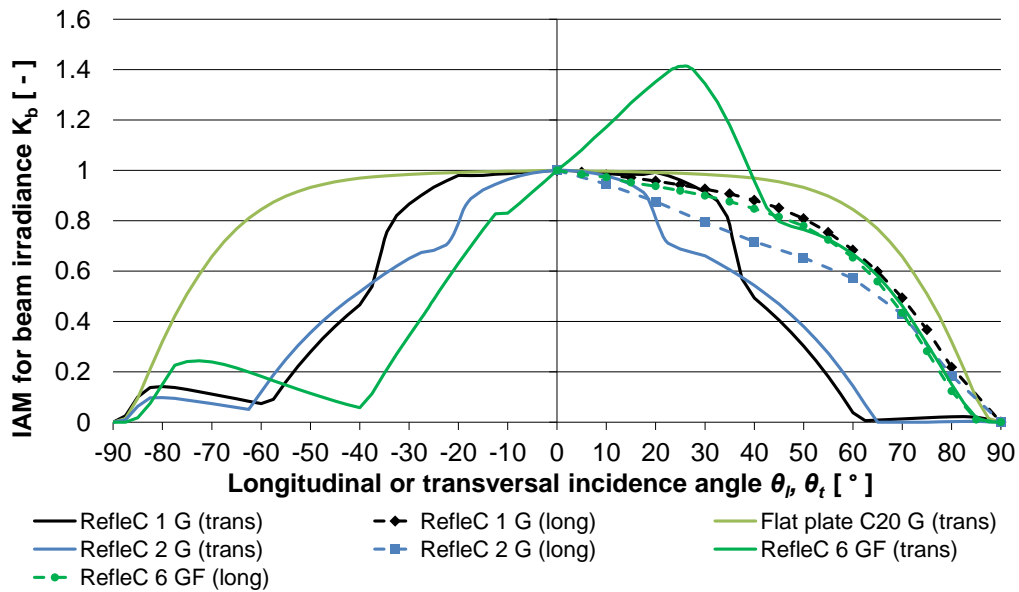
Figure C.1: Raytraced IAM curves of the test samples R1 G, R2 G, R6 GF with losses. For comparison, also C20 G is shown. The longitudinal IAM curves of R1 G, R2 G and R6 GF are symmetric within the longitudinal plane of $\theta_t = [-90°; +90°]$. To improve the graph's clarity, they were displayed for positive incidence angles only. The transversal plane of RefleC is identical to that of the flat-plates (cp. Figure 2.8). Comparing the longitudinal IAMs to that in Figure 2.38 shows the influence of the end losses. R1 G and R6 GF have two glass-panes, R2 G only one.
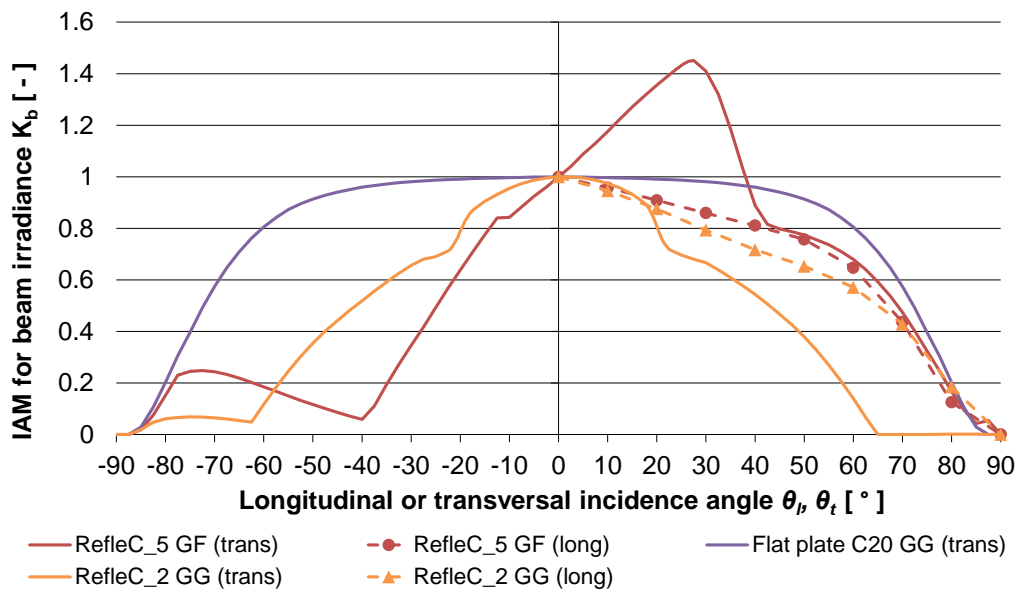
Figure C.2: Raytraced IAM curves of the test samples R2 GG and R5 GF with end losses. For comparison, also C20 G is shown. The longitudinal IAM curves of R2 GG and R5 GF are symmetric within the longitudinal plane of $\theta_t = [-90°; +90°]$. To improve the graph's clarity, they were displayed for positive incidence angles only. The transversal plane of RefleC is identical to that of the flat-plates (cp. Figure 2.8). Comparing the longitudinal IAMs to that in Figure 2.39 shows the influence of the end losses. C_{geo} of R2 GG is higher, so the end losses are higher than at R5 GF.

(a) Perspective view of the setup at $\theta_t = 20°$

(b) $\theta_t = 0°$

(c) $\theta_t = 10°$

(d) $\theta_t = 20°$

(e) $\theta_t = 30°$

(f) $\theta_t = 40°$
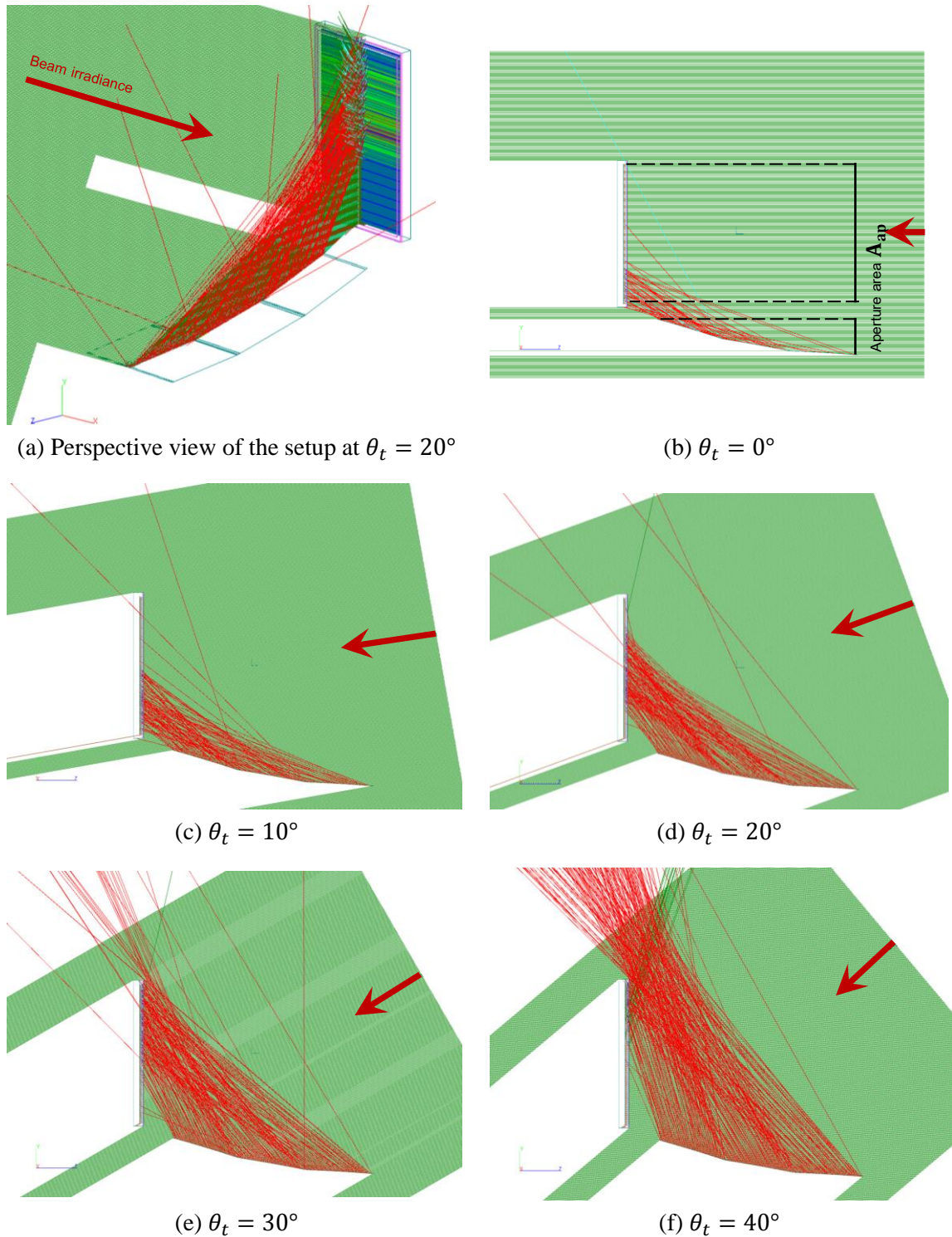
Figure C.3: Screenshots from transversal raytracing analysis of RefleC prototype R6 GF (reflector approximated to acceptance half-angle $\theta_a = 35°$). Simplified setup in Opti-CAD to illustrate the path of reflected rays and local concentrations on the absorber. The radiant power onto the constant aperture area (projected area of flat-plate aperture and reflector, cp. (b)) is constant during the simulation. The resulting transversal IAM K_b is to be found in Figure 2.11.

D Collector Simulation Model Type 154

D.1 Structural Overview
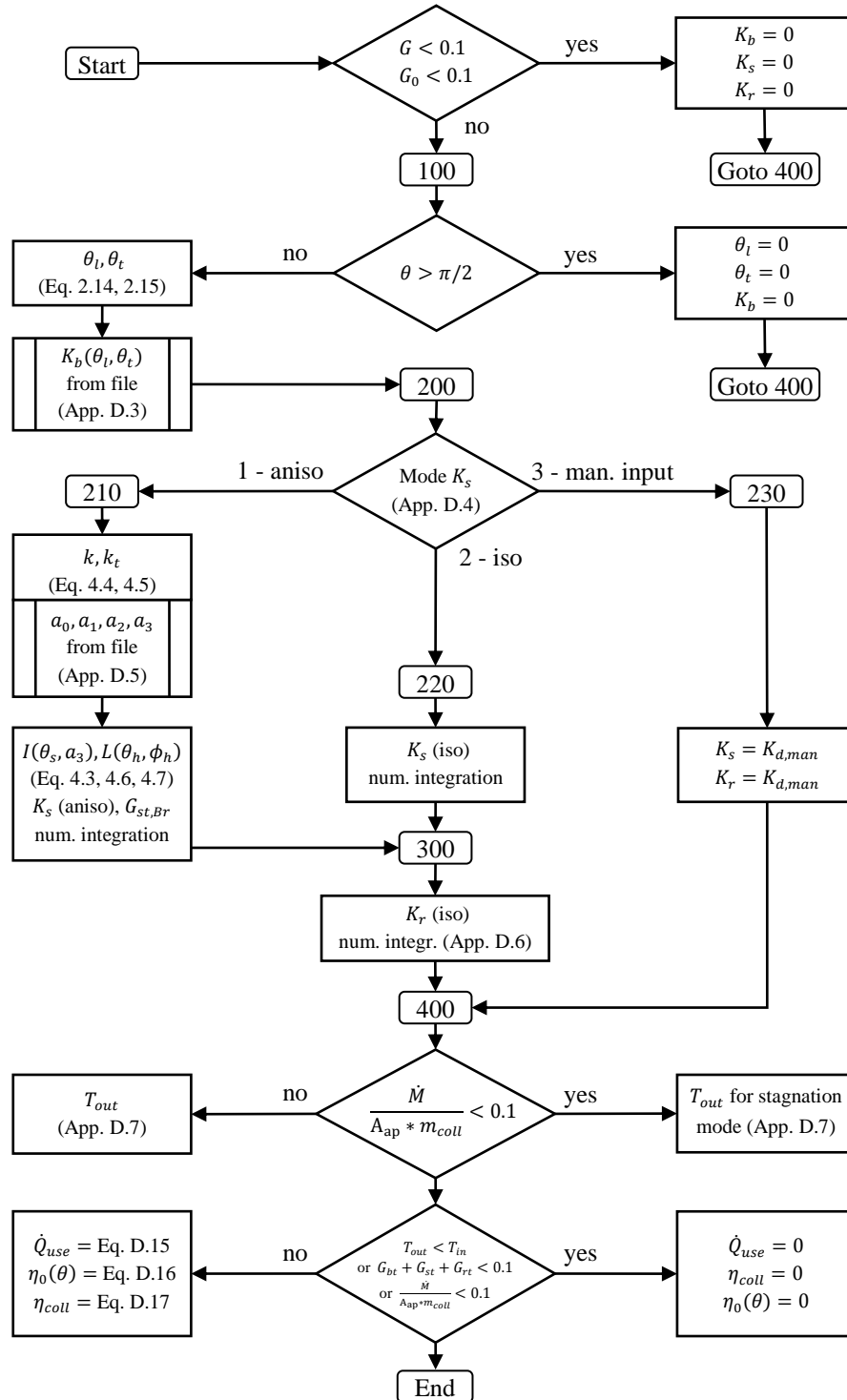
Figure D.1: Overview flow chart of TRNSYS Type 154 with its calculations per time step. The numbers 100 to 400 refer to sections of the Fortran code which can be addressed by jump commands (cp. "Goto 400"). A list of inputs, parameters and outputs is given in Appendix D.2. The modelling is discussed in Appendices D.3 to D.7.

D.2 Model Inputs, Parameters, Outputs and External Data

Table D.1: <u>Input</u> values of Type 154

Nr.	Symbol	Unit	Description	Range	Default
1	T_{in}	°C	Inlet temperature	$[-273.15; \infty]$	25
2	$\dot{M}$	kg/h	Inlet mass flow (absolute)	$[0; \infty]$	72
3	T_a	°C	Ambient temperature	$[-273.15; \infty]$	25
4	G	kJ/(m^2h)	Global irradiance (horizontal)	$[0; \infty]$	0
5	G_0	kJ/(m^2h)	Extraterrestrial irrad. (horizontal)	$[0; \infty]$	0
6	G_b	kJ/(m^2h)	Beam irrad. (horizontal)	$[0; \infty]$	0
7	G_d	kJ/(m^2h)	Diffuse irrad. (horizontal)	$[0; \infty]$	0
8	G_{bt}	kJ/(m^2h)	Beam irrad. (tilted plane)	$[0; \infty]$	0
9	G_{st}	kJ/(m^2h)	Diffuse irrad. from sky (tilted plane)	$[0; \infty]$	0
10	G_{rt}	kJ/(m^2h)	Diffuse irrad. from ground (tilted plane)	$[0; \infty]$	0
11	β	°	Collector slope	$[0; 90]$	0
12	γ	°	Collector azimuth	$[-180; +180]$	0
13	θ_s	°	Solar zenith angle	$[0; 180]$	0
14	ϕ_s	°	Solar azimuth angle	$[-180; +180]$	0
15	θ	°	Solar incidence angle	$[0; 180]$	0

Table D.2: <u>Parameters</u> of Type 154

Nr.	Symbol	Unit	Description	Range	Default
1	n_{coll}	–	Number of collectors (serial)	$[1; 10]$	1
2	m_{coll}	–	Number of collectors (parallel)	$[1; \infty]$	1
3	A_{ap}	m^2	Aperture area of one collector	$[0; \infty]$	2.521
4	$c_{p,fl}$	J/(kg K)	Specific heat capacity of collector fluid	$[0; \infty]$	4190
5	η_0	–	Collector conversion factor	$[0; 1]$	0.695
6	c_1	W/(m^2K)	Collector heat loss coefficient	$[0; \infty]$	2.119
7	c_2	W/(m^2K)	Collector heat loss coefficient	$[0; \infty]$	0.0073
8	c_{eff}	J/K	Effective thermal capacity (one collector and its fluid content)	$[0; \infty]$	9503.4
9	n_{long}	–	Number of longitudinal IAM values in external file	$[2; \infty]$	10
10	n_{trans}	–	Number of transversal IAM values in external file	$[2; \infty]$	19
11	D_{mode}	–	Mode to calculate IAM for diffuse	$[1; 3]$	1
12	$\Delta\theta_{diff}$	°	Width of solid angle ($\Delta\theta_h$ and $\Delta\phi_h$) for numerical integration	$[0; \infty]$	5
13	$K_{d,man}$	–	IAM for diffuse (manual input Mode 3)	$[0; \infty]$	0.647
14	LU_IAM	–	Logical unit IAM	$[10; 999]$	30
15	LU_a0	–	Logical unit a0	$[10; 999]$	31
16	LU_a1	–	Logical unit a1	$[10; 999]$	32

Nr.	Symbol	Unit	Description	Range	Default
17	LU_a2	−	Logical unit a2	$[10; 999]$	33
18	LU_a3	−	Logical unit a3	$[10; 999]$	34

Table D.3: <u>Output</u> values of Type 154

Nr.	Symbol	Unit	Description	Range	Default
1	T_{out}	°C	Outlet temperature	$[-273.15; \infty]$	25
2	$\dot{M}$	kg/h	Outlet mass flow (absolute)	$[0; \infty]$	72
3	$\dot{Q}_{use}$	W	Thermal collector output	$[-\infty; \infty]$	0
4	η_{coll}	−	Collector efficiency	$[0; \infty]$	0
5	$\eta_0(\theta)$	−	Collector conversion factor at θ	$[0; 1]$	0
6	$G_{st,Br}$	W/(m^2)	Diffuse irradiance from sky on tilted plane calculated by the Brunger Model	$[0; \infty]$	0
7	K_b	−	IAM for beam irradiance	$[0; \infty]$	1
8	K_s	−	IAM for sky diffuse irradiance	$[0; \infty]$	0.8
9	K_r	−	IAM for ground reflected diffuse irrad.	$[0; \infty]$	0.4
10	k	−	Fraction of diffuse irrad. (horizontal)	$[0; 1]$	0
11	k_t	−	Atmospheric clearness index	$[0; 1]$	0
12	a_0	−	Brunger coefficient a0	$[-\infty; \infty]$	0
13	a_1	−	Brunger coefficient a1	$[-\infty; \infty]$	0
14	a_2	−	Brunger coefficient a2	$[-\infty; \infty]$	0
15	a_3	−	Brunger coefficient a3	$[-\infty; \infty]$	0
16	$I(\theta_s, a_3)$	−	Function within Brunger model	$[0; \infty]$	0
17	θ_l	°	Projection of θ into longitudinal plane	$[-180; +180]$	0
18	θ_t	°	Projection of θ into transversal plane	$[-180; +180]$	0
19			Saved for later use		
20			Saved for later use		
21	$T_{out,1}$	°C	Outlet temperature first collector (serial)	$[-273.15; \infty]$	25
22	$T_{out,2}$	°C	Outlet temperature second collector (serial)	$[-273.15; \infty]$	25
23	$T_{out,3}$	°C	Outlet temperature third collector (serial)	$[-273.15; \infty]$	25
24	$T_{out,4}$	°C	Outlet temperature fourth collector (serial)	$[-273.15; \infty]$	25
25	$T_{out,5}$	°C	Outlet temperature fifth collector (serial)	$[-273.15; \infty]$	25
26	$T_{out,6}$	°C	Outlet temperature sixth collector (serial)	$[-273.15; \infty]$	25
27	$T_{out,7}$	°C	Outlet temperature seventh collector (serial)	$[-273.15; \infty]$	25
28	$T_{out,8}$	°C	Outlet temperature eighth collector (serial)	$[-273.15; \infty]$	25
29	$T_{out,9}$	°C	Outlet temperature ninth collector (serial)	$[-273.15; \infty]$	25
30	$T_{out,10}$	°C	Outlet temperature tenth collector (serial)	$[-273.15; \infty]$	25

Table D.4: <u>External links</u> of Type 154

Nr.	Description	Default
1	Which file contains the values of IAM K_b?	–
2	Which file contains a0?	$a0.dat$
3	Which file contains a1?	$a1.dat$
4	Which file contains a2?	$a2.dat$
5	Which file contains a3?	$a3.dat$

D.3 100 – IAM for beam irradiance K_b

Input file: The IAM values of an investigated collector are provided to Type 154 for TRNSYS in a tab-spaced text file. This file must be named "filename.dat" and must have the following structure:

```
-90 -80 -72.5 ... 90     !n_long  longitudinal angle component of nodes
-90 -85 -80 ... 90       !n_trans transversal angle component of nodes
Value 1                  !i_long = 1 (-90); i_trans = 1 (-90)
Value 2                  !i_long = 1 (-90); i_trans = 2 (-85)
Value 3                  !i_long = 1 (-90); i_trans = 2 (-72.5)
...
Value n_trans            !i_long = 1 (-90); i_trans = n_trans (90)
Value n_trans+1          !i_long = 2 (-80); i_trans = 1 (-90)
...
Value n_trans*n_long     !i_long = n_long (90); i_trans = n_trans (90)
```

The first two rows contain the incidence angles θ_l and θ_t for which nodes with IAM values are contained in the file. Along both collector planes, values from $[-90°; +90°]$ have to be provided (regardless of the IAM type or shape, cp. section 3.2.2). They do not have to be equidistant. The incidence angle conventions are shown in Figure 2.8 on page 29. From the third row on, each row contains one node $K_b(i_{long}, i_{trans})$ for each combination of the incidence angles listed in row one and two. Thus, the file allows for:

- biaxial, asymmetric shapes of K_b
- a three-dimensional grid of node values $K_b(\theta_l, \theta_t)$ (3D-IAM)

For convenience, the IAM files should be generated within a spreadsheet and then saved as .dat-file. Within the spreadsheet, the values of $K_b(i_{long}, i_{trans})$ can be determined in two ways:

- approximation by separation approach of McIntire (Eq. 3.15)
  (if only values $K_b(i_{long}, 0)$ and $K_b(0, i_{trans})$ are available)
- use of exact 3D-IAM from raytracing

Realization in Type 154: In case there is solar irradiance onto the aperture $(G_0 > 0.1 \text{ W/m}^2 \wedge G > 0.1 \text{ W/m}^2)$ and the sun is visible for the collector at the same time $(\theta < \pi/2)$, K_b is determined for the solar incidence angle components θ_l and θ_t.

In TRNSYS, the programme *DynamicData* calls the file "filename.dat" and imports all provided values $K_b(i_{long}, i_{trans})$ into an array. The searched value $K_b(\theta_l, \theta_t)$ is then linearly interpolated between the four nearest available nodes $K_b(i_{long}, i_{trans})$. *DynamicData* is explained in (Klein et al. 2012b, pp. 7-98 to 7-100).

D.4   200 – IAM for diffuse irradiance from the sky K_s

Via parameter D_{mode}, the user selects one of the three variants to determine K_s. In Mode 1, K_s is re-calculated every time step. Thus, it is the most time consuming mode.

210 - Mode 1 - Anisotropic Sky (Brunger): First, the horizontal diffuse irradiance G_d is distributed over the whole sky as shown in Figure 4.3 using the Brunger distribution. To generate this distribution, k and k_t are calculated and classified into intervals, so that the representative Brunger coefficients a_1 to a_3 can be imported from an external file. This procedure is explained in App. D.5. With this, the function $I(\theta_s, a_3)$ for the Brunger model is calculated by Eq. 4.7. Then, the Brunger distribution $L(\theta_h, \phi_h)$ (cp. Eq. 4.3) can be generated. The sky radiance $L(\theta_h, \phi_h)$ of an infinitesimal sky element $d\Omega$ is located by its angle θ_h from the zenith and its azimuth angle ϕ_h.

The approach for the following calculation of K_s can be understood when considering the diffuse sky irradiance $L(\theta_h, \phi_h)$ as beam irradiance with a certain incidence angle and weighting it with its individual IAM $K_b(\theta_h, \phi_h)$ and individual cosine losses $\cos\theta(\theta_h, \phi_h)$. This is formulated in Eq. D.1 and D.2 (cp. Figure 4.3):

$$K_s = \frac{\int_{\cap} K_b(\theta_h, \phi_h) \cdot L(\theta_h, \phi_h) \cdot \cos\theta(\theta_h, \phi_h)\, d\Omega}{\int_{\cap} L(\theta_h, \phi_h) \cdot \cos\theta(\theta_h, \phi_h)\, d\Omega} \tag{D.1}$$

with $d\Omega = \sin\theta_h\, d\theta_h\, d\phi_h$;   for θ [0; 90°]

$$K_s = \frac{\int_0^{2\pi} \int_0^{\frac{\pi}{2}} K_b(\theta_t(\theta_h, \phi_h), \theta_l(\theta_h, \phi_h)) \cdot L(\theta_h, \phi_h) \cdot \cos\theta(\theta_h, \phi_h) \cdot \sin\theta_h\, d\theta_h\, d\phi_h}{\int_0^{2\pi} \int_0^{\frac{\pi}{2}} L(\theta_h, \phi_h) \cdot \cos\theta(\theta_h, \phi_h) \cdot \sin\theta_h\, d\theta_h\, d\phi_h} \tag{D.2}$$

for θ [0; 90°]

The incidence angle of $d\Omega$ on the collector is $\theta(\theta_h, \phi_h)$. The absorbed diffuse irradiance from the visible collector hemisphere ($\theta(\theta_h, \phi_h) < 90°$) in the numerator is the integral of the irradiance of all visible sky elements $d\Omega$ weighted with their individual IAM $K_b(\theta_h, \phi_h)$ and their individual cosine losses $\cos\theta(\theta_h, \phi_h)$. Division by the overall sky diffuse irradiance onto the aperture gives the IAM for anisotropic diffuse irradiance. The incidence angle $\theta(\theta_h, \phi_h)$ of $d\Omega$ onto the collector aperture can be projected into the collector planes $\theta_t(\theta_h, \phi_h)$ and $\theta_l(\theta_h, \phi_h)$ by Eq. 2.14 and 2.15, since the coordinates of the sun (θ_s, ϕ_s) and of $d\Omega$ (θ_h, ϕ_h) have the same horizontal basis (zenith and south direction). The width of $d\Omega$ increases with $\sin\theta_h$ (cp. Figure 4.3). In Type 154, the integration of Eq. D.2 is solved numerically using the following equation:

$$K_s = \frac{\sum_{i=1}^{n_{\phi_h}} \sum_{j=1}^{n_{\theta_h}} K_b(\theta_{t,ij}, \theta_{l,ij}) \cdot L_{ij}(\theta_{h,ij}, \phi_{h,ij}) \cdot \cos\theta_{ij}(\theta_{h,ij}, \phi_{h,ij}) \cdot \sin\theta_{h,ij} \Delta\theta_h \Delta\phi_h}{\sum_{i=1}^{n_{\phi_h}} \sum_{j=1}^{n_{\theta_h}} L_{ij}(\theta_{h,ij}, \phi_{h,ij}) \cdot \cos\theta_{ij}(\theta_{h,ij}, \phi_{h,ij}) \cdot \sin\theta_{h,ij} \Delta\theta_h \Delta\phi_h} \tag{D.3}$$

for θ_{ij} [0; 90°]

A model parameter $\Delta\theta_{\text{diff}}$, which is a user input, defines $\Delta\theta_h$ and $\Delta\phi_h$ for the numerical integration. The default angular width of one sky element is $\Delta\theta_{\text{diff}} = \Delta\theta_h = \Delta\phi_h = 5°$. For the integration, a double counting loop with the loop variables i and j is used, as shown in Figure D.2. Note again that θ_h and ϕ_h are coordinates of sky elements on a horizontal basis (cp. Figure 4.3).

(a) Numerical integration steps along θ_h
($n_{\theta_h} = 18$ for $\Delta\theta_{\text{diff}} = 5°$)

(b) Numerical integration steps along ϕ_h
($n_{\phi_h} = 72$ for $\Delta\theta_{\text{diff}} = 5°$)
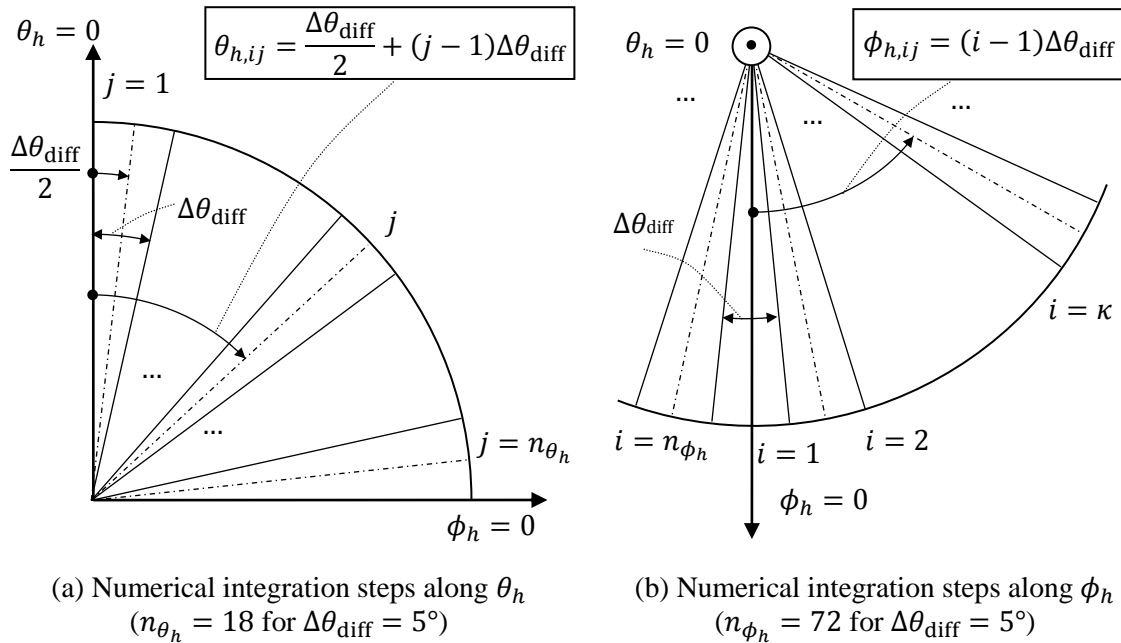
Figure D.2: Numerical integration steps to calculate the IAM for diffuse irradiance from the sky K_s. The coordinate system is based on the horizontal, i.e. the azimuth angles ϕ_h are coincident with the horizontal plane, the angle $\theta_h = 0$ is the zenith perpendicular to the horizontal. The calculation of $\theta_{h,ij}$ and $\phi_{h,ij}$ as shown ensures that the coordinates represent the center of the considered sky element. Adapted from (Raucher 2009, p. 49).

The addition limits n_{θ_h} and n_{ϕ_h} are:

$$n_{\theta_h} = \frac{\pi}{2} \cdot \Delta\theta_{\text{diff}} \tag{D.4}$$

$$n_{\phi_h} = n_{\theta_h} \cdot 4 \tag{D.5}$$

To calculate Eq. D.3, in every loop run (i.e. for every sky element considered) the following values are calculated chronologically:

- $\theta_{h,ij}$ and $\phi_{h,ij}$, the spherical coordinates of sky element as shown in Figure D.2
- θ_{ij}, $\theta_{t,ij}$ and $\theta_{l,ij}$, the incidence angles of the sky element onto the collector, are calculated substituting θ_s and ϕ_s by $\theta_{h,ij}$ and $\phi_{h,ij}$ in Eq. 2.13 to 2.15. If $\theta_{ij} > 90°$, the current loop run ends and the next is started.
- $K_b(\theta_{t,ij}, \theta_{l,ij})$ as described in Appendix D.3
- $\Psi(\theta_{ij}, \phi_{ij})$ by Eq. 4.6

- $L(\theta_{h,ij}, \phi_{h,ij})$, i.e. the radiance of the sky element when the known horizontal diffuse irradiance G_s, is distributed according to the Brunger Model by Eq. 3.31.
- $K_{s,num}= K_{s,num}$ + current numerator of Eq. D.3 (adding up the numerator)
- $K_{s,den}= K_{s,den}$ + current denominator of Eq. D.3 (adding up the denominator)

The loop abortion criterion $\theta_{ij} > 90°$ ensures that only the sky visible for the collector aperture is considered. The numerical addition is performed along $\theta_{h,ij}$ and $\phi_{h,ij}$ until the integration limits $j = n_{\theta_h}$ and $i = n_{\phi_h}$ are reached.

Finally, after all loop runs, the IAM for anisotropic sky diffuse irradiance is $K_s = K_{s,num} / K_{s,den}$. The denominator from Eq. D.3 gives $G_{st,Br}$, i.e. the sky diffuse irradiance calculated with the Brunger model from summing up the sky elements with $\theta_{ij} < 90°$. This value is only informative and used to calculate K_s; for calculation of the collector output, always the current value of G_{st} from the weather data reader is used.

To conclude, anisotropic determination of K_s by Eq. D.3 in the way described needs 1296 loop runs per time step (18 runs in direction θ_h and 72 in direction ϕ_h). This is highly increasing the simulation time, so $\Delta\theta_{\mathrm{diff}}$ and STEP must be chosen carefully.

220 – Mode 2 – Isotropic Sky: K_s for an isotropic sky is independent of the actual irradiance, it only depends on the K_b-values and on β. This allows for a major difference compared to Mode 1: Its calculation is performed only once per simulation, within the first time step. This is extremely reducing simulation time.

For convenience, Mode 2 follows the calculation procedure of Mode 1, solving Eq. D.3 as well. For the numerator and denominator, a constant value of $L_{ij}(\theta_{h,ij}, \phi_{h,ij}) = 1 \, \mathrm{W/(m^2 sr)}$ is used, since the generation of the Brunger distribution can be omitted in the isotropic case. The scan width is set to $\Delta\theta_{\mathrm{diff}} = \Delta\theta_h = \Delta\phi_h = 2.5°$, which results in $n_{\theta_h} = 36$ and $n_{\phi_h} = 144$ (i.e. 5184 loop runs). Because of this high resolution, the value of K_s represents a collector's acceptance for isotropic sky radiance very accurately, if K_b-values of high resolution are provided.

230 – Mode 3 – Manual Input for Collector Hemisphere: Mode 3 represents the simplest case to account for a collector's acceptance for diffuse irradiance. No difference between G_{st} and G_{rt} is made, so K_s is independent of the collector orientation and thus can be assigned to the collector as a constant parameter. In collector test reports, this parameter is called K_d, the acceptance for irradiance from an isotropic collector hemisphere.

Within Type 154, $K_{d,man}$ is an input value, which is only used when Mode 3 is active. To assure the desired behaviour, in the first simulation time step it is set that $K_s = K_r = K_{d,man}$, so the collector output calculations do not have to be changed.

D.5 Brunger Coefficients

Input files: For each of the Brunger coefficients a_0, a_1, a_2 and a_3, an individual input file "a0.dat", "a1.dat", "a2.dat" and "a3.dat" must be placed in the same folder as the simulated TRNSYS deck. These files contain the values of the Brunger coefficients shown in Table 4.1 on page 103. The structure of the four files is identical to the external IAM file. To give an example, "a1.dat" looks like this:

```
0.05  0.15  0.25  0.35  0.45  0.55  0.65  0.75  0.85        !k_t
0.15  0.25  0.35  0.45  0.55  0.65  0.75  0.85  0.95        !k
0.3360              !k_t = 0,05 k = 0,15
0.3417              !k_t = 0,05 k = 0,25
0.3162              !k_t = 0,05 k = 0,35
...
0.3162              !k_t = 0,45 k = 0,35
0.2822              !k_t = 0,45 k = 0,45
0.2816              !k_t = 0,45 k = 0,55
0.2713              !k_t = 0,45 k = 0,65
0.2019              !k_t = 0,45 k = 0,75
...
0.2060              !k_t = 0,85 k = 0,95
```

Brunger and Hooper provide 49 sets of coefficients. They are valid for all combinations of k and k_t which occurred during model calibration (Brunger and Hooper 1993, p. 56). It is ensured that the simulation does not stop in the potentially rare case a combination should occur, for which no coefficients are provided. Therefore, to generate the coefficient input files, the Brunger table was completely filled (81 sets). This was done by inserting the nearest available coefficient set in k_t-direction, when none was given (e.g. the value `0.3360` in the third line above is originally given for $k = 0.15$ and $k_t = 0.65$).

Realization in Type 154: To read the coefficients out of these files, the same procedure as for reading the K_b-file (cp. section D.3) is used. Prior to that, the appropriate set out of the 49 sets of coefficients is identified, i.e. the current k and k_t are classified into the Brunger categories by Eq. D.6 and D.7. The result is e.g. $k = 0.45 := [0.4; 0.5[$. To achieve this, a rounding down-function resulting in the next smaller integer-value is used in the following classification functions:

$$k = \frac{\lfloor 10 \cdot k \rfloor + 0.5}{10} \qquad (\text{D.6})$$

$$k_t = \frac{\lfloor 10 \cdot k_t \rfloor + 0.5}{10} \qquad (\text{D.7})$$

This classification before reading avoids that *DynamicData* interpolates the values to be selected.

D.6 300 – IAM for ground reflected diffuse K_r

The part of the visible collector hemisphere located below the horizon is assumed to have an isotropic radiance. Thus, K_r is calculated similar to the isotropic K_s (i.e similar to Mode 2 in Appendix D.4). K_r is as well independent of the current irradiance, it only depends on the K_b-values and on β. It is calculated once per simulation using the coordinate system shown in Figure D.3.
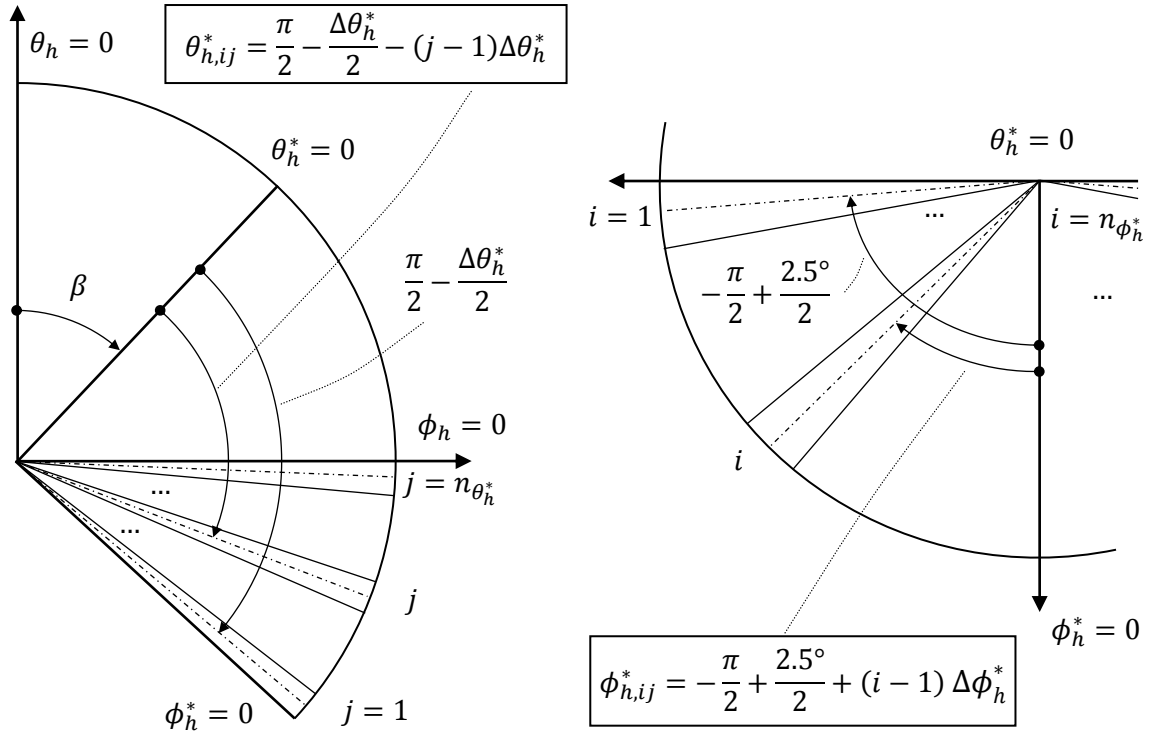
(a) Numerical integration steps along θ_h^*
($n_{\theta_h^*} = 36$, with $\Delta\theta_h^* = \beta/36$)

(b) Numerical integration step along θ_h^*
($n_{\phi_h^*} = \pi/\Delta\phi_h^* = 72$, with $\Delta\phi_h^* = 2.5$)

Figure D.3: Numerical integration steps to calculate the IAM for isotropic diffuse irradiance from the ground K_r. The **coordinate system is sloped by β from the horizontal**, i.e. it is based on the collector aperture. Its zenith angle $\theta_h^* = 0$ is orientated normal to the collector aperture and $\phi_h^* = 0$ perpendicular to it. The orientation of zenith and azimuth is the same as in Figure 4.3. The calculation of $\theta_{h,ij}^*$ and $\phi_{h,ij}^*$ as shown ensures that the coordinates represent the center of the considered ground element. Adapted from (Raucher 2009, p. 57).

Based on the considerations which resulted in Eq. D.3, K_r is numerically integrated using Eq. D.8 below. In order to provide the same accuracy as the calculation of K_s with Mode 2, the width of a considered ground element should be 2.5°. But since the basis of the coordinate system depends on the user input β, which can be an odd number, it must be ensured that in direction θ_h^* the ground irradiance is represented by equal, integer segments, covering exactly θ_h^* [90°; 90° − β]. This is realized by setting the integration steps to $n_{\theta_h^*} = 36$ and $n_{\phi_h^*} = 72$. The orientation of zenith and azimuth is the same as in Fig. 4. For the numerical integration, the angular width is set to $\Delta\phi_h^* = 2.5°$ (72 segments) and $\Delta\theta_h^* = \beta/36$ (maximum 2.5° for $\beta = 90°$).

$$K_r = \frac{\sum_{i=1}^{n_{\phi_h^*}} \sum_{j=1}^{n_{\theta_h^*}} K_b(\theta_{t,ij}, \theta_{l,ij}) \cdot \cos \theta_{ij}(\theta_{h,ij}^*, \phi_{h,ij}^*) \cdot \sin \theta_{h,ij}^* \Delta\theta_h^* \Delta\phi_h^*}{\sum_{i=1}^{n_{\phi_h^*}} \sum_{j=1}^{n_{\theta_h^*}} \cos \theta_{ij}(\theta_{h,ij}^*, \phi_{h,ij}^*) \cdot \sin \theta_{h,ij}^* \Delta\theta_h^* \Delta\phi_h^*} \qquad (D.8)$$

for $\theta_{h,ij}^*[0; 90°]$

With the coordinate system of Figure D.3 the incidence angle of a ground element is:

$$\theta_{ij} = \theta_{h,ij}^* \qquad\qquad (D.9)$$

Its transversal and longitudinal components are calculated according to Eq. 2.17 and 2.18 as follows:

$$\theta_{t,ij} = -\tan^{-1}[\tan \theta_{h,ij}^* \cdot \cos \phi_{h,ij}^*] \qquad\qquad \forall\, \theta_t \in\ ]-90; +90[\quad (D.10)$$

$$\theta_{l,ij} = -\tan^{-1}[\tan \theta_{h,ij}^* \cdot \sin \phi_{h,ij}^*] \qquad\qquad \forall\, \theta_t \in\ ]-90; +90[\quad (D.11)$$

To calculate K_r from numerically integrating Eq. D.8, in every loop run (i.e. for every ground element considered), the following values are determined chronologically:

- $\theta_{h,ij}^*$ and $\phi_{h,ij}^*$, the spherical coordinates of sky element as shown in Figure D.3
- θ_{ij}, $\theta_{t,ij}$ and $\theta_{l,ij}$ according to Eq. D.9 to D.11
- $K_b(\theta_{t,ij}, \theta_{l,ij})$ as described in Appendix D.3
- $K_{r,num} = K_{r,num}$ + current numerator of Eq. D.8 (summing up the numerator)
- $K_{r,den} = K_{r,den}$ + current denominator of Eq. D.8 (summing up the denominator)

A loop abortion criterion $\theta_{ij} > 90°$ is not necessary, since the calculation of $\theta_{h,ij}^*$ and $\phi_{h,ij}^*$ already ensures that only radiance from the hemispheric segment covered by the ground is considered. After all 2592 loop runs, the IAM for isotropic diffuse irradiance from the ground is $K_r = K_{r,num} / K_{r,den}$.

D.7 400 – Outlet Temperature, Energy Gain, Efficiency and Stagnation Temperature

Thermally, Type 154 allows for calculation of the outlet temperature T_{out} of up to ten serially connected collectors ($n_{coll} = [1; 10]$). An unlimited number of collectors can be connected in parallel ($m_{coll} = [1; \infty]$). Optically, the model does not account for any interference between collectors or collector rows (shading, reflections).

Following the flow chart in Figure D.1, the first check of every time step is if the specific mass flow rate through the collector field $\dot{m} < 0.1$ kg/(m²h). If this is the case, the stagnation temperature of the collector field T_{stag} is calculated (discussed later below). If not, the outlet temperatures $T_{out,i}$ of the collectors in series and the field outlet temperature T_{out} are calculated. From equating Eq. 3.1 and Eq. 3.12 we get:

$$\dot{m} \cdot \bar{c}_{p,fl} \cdot (T_{out} - T_{in}) = \dot{q}_{gain} - c_{eff} \cdot \frac{dT_f}{dt} \tag{D.12}$$

The change of the arithmetic mean fluid temperature T_f with the overall thermal capacity of the collector c_{eff} can for finite time steps Δt be described as:

$$\frac{dT_f}{dt} \approx \frac{\frac{T_{out} + T_{in}}{2} - T_f(t - \Delta t)}{\Delta t} \tag{D.13}$$

Solving equation D.12 for T_{out} gives:

$$T_{out} = \frac{\dot{m} \cdot \bar{c}_{p,fl} \cdot T_{in} - \frac{c_{eff}}{2\Delta t} \cdot T_{in} + \dot{q}_{gain} + \frac{c_{eff}}{\Delta t} \cdot T_f(t - \Delta t)}{\dot{m} \cdot \bar{c}_{p,fl} + \frac{c_{eff}}{2\Delta t}} \tag{D.14}$$

The specific solar gains $\dot{q}_{gain}$ calculated by Eq. 3.9 depend on the mean fluid temperature T_f in the current time step, while T_{out} of the current time step depends on the mean fluid temperature of the last step $T_f(t - \Delta t)$, as seen from Eq. D.14. Thus, the calculation of T_{out} is an iterative process and it takes a few steps, until realistic collector performance is reached.

The outlet temperatures $T_{out,i}$ of n_{coll} serially connected collectors are calculated at every time step by a loop with the loop variable i. At the start of a simulation, the starting fluid temperature for the loop $T_{f,start}$ is set to 25 °C and the collector inlet temperature for the loop calculation $T_{in,l}$ is set to the field inlet temperature T_{in}. Within a time step, the loop runs until $i > n_{coll}$ as follows:

- $\dot{q}_{gain,l}$ is calculated for $T_{f,start}$ by Eq. 3.9
- $T_{out,i}$ is calculated for $T_{f,start}$ by Eq. D.14 using $\dot{q}_{gain,l}$
- $T_{f,end} = (T_{out,i} + T_{in,l})/2$

- $T_{f,start} = T_{f,end}$ (mean fluid temperature for next loop run, i.e. for next serial collector)

- $T_{in,l} = T_{out,i}$ (inlet temperature for next loop run, i.e. for next serial collector)

Herein, only $T_{out,i}$ are model output values. The other variables mentioned are exclusively used within the loop calculations. After $i > n_{coll}$ is reached, i.e. the outlet temperatures $T_{out,i}$ of up to 10 serially connected collectors are calculated, the field outlet temperature is set to the outlet temperature of the last collector $T_{out} = T_{out,n_{coll}}$. Now the useful field output $\dot{Q}_{use}$, conversion efficiency $\eta_0(\theta)$ and the overall efficiency of the field η_{coll} considering optical and thermal losses can be calculated:

$$\dot{Q}_{use} = \dot{M} \cdot c_{p,fl} \cdot (T_{out} - T_{in}) \tag{D.15}$$

$$\eta_0(\theta) = \eta_0(\theta_l, \theta_t) = \eta_0 \cdot \frac{G_{bt} \cdot K_b(\theta_l, \theta_t) + G_{st} \cdot K_s + G_{rt} \cdot K_r}{G_{bt} + G_{st} + G_{rt}} \tag{D.16}$$

$$\eta_{coll} = \frac{\dot{Q}_{use}}{(G_{bt} + G_{st} + G_{rt}) \cdot A_{ap} \cdot m_{coll} \cdot n_{coll}} \tag{D.17}$$

Herein, $\dot{M}$ is the overall absolute mass flow rate of the field.

In the case of $\dot{m} < 0.1 \, \mathrm{kg/(m^2 h)}$, i.e. in case of no mass flow, the collector field stagnation temperature T_{stag} has to be determined. For this purpose, the collector field outlet temperature T_{out} is calculated with the same loop described above, but independent of how many collectors are connected serially. In stagnation mode, a defined specific mass flow of $\dot{m} = 0.1 \, \mathrm{kg/(m^2 h)}$ is used, and the number of loop runs is set to $i = 10$. At the end, it is set $T_{stag} = T_{out,10}$. The 10 collectors in series and the selected mass flow ensure that mathematically $\eta_{coll} = 0$ is reached before the 10th collector is reached, so that $T_{out,i}$ cannot increase further and indeed the output of the last collector is the stagnation temperature.

If the collector field outlet temperature is below inlet or the irradiance on the tilted plane is below $G_t < 0.1 \, \mathrm{W/m^2}$ or in case of $\dot{m} < 0.1 \, \mathrm{kg/(m^2 h)}$, $\dot{Q}_{use}$, $\eta_0(\theta)$, and η_{coll} are set zero.

E   Monitoring Scheme and Results
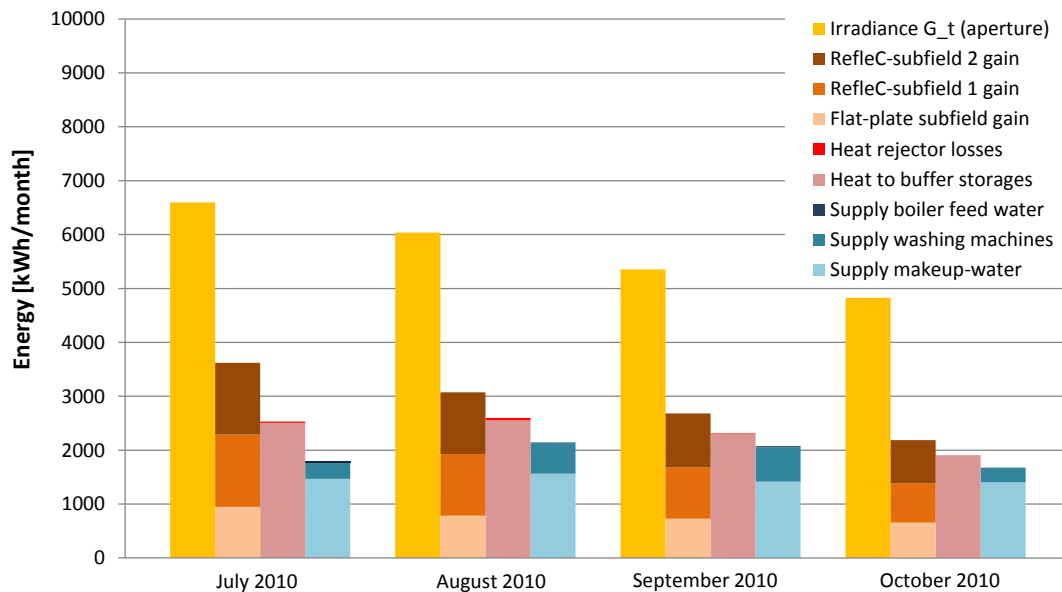
Figure E.1: Monthly system energies calculated from monitoring (July to October 2010). Collector gains logged from 03.07.10, all other energies from 06.07.10. Reflectors installed on 09.07.10. For 15./16.07.10 no gains counted because of system tests. Solar loop pipes insulated from 22.07.10. Frequent changes of control parameters. Usually winter mode, summer mode with feed water discharge rarely activated on Mondays (manually).
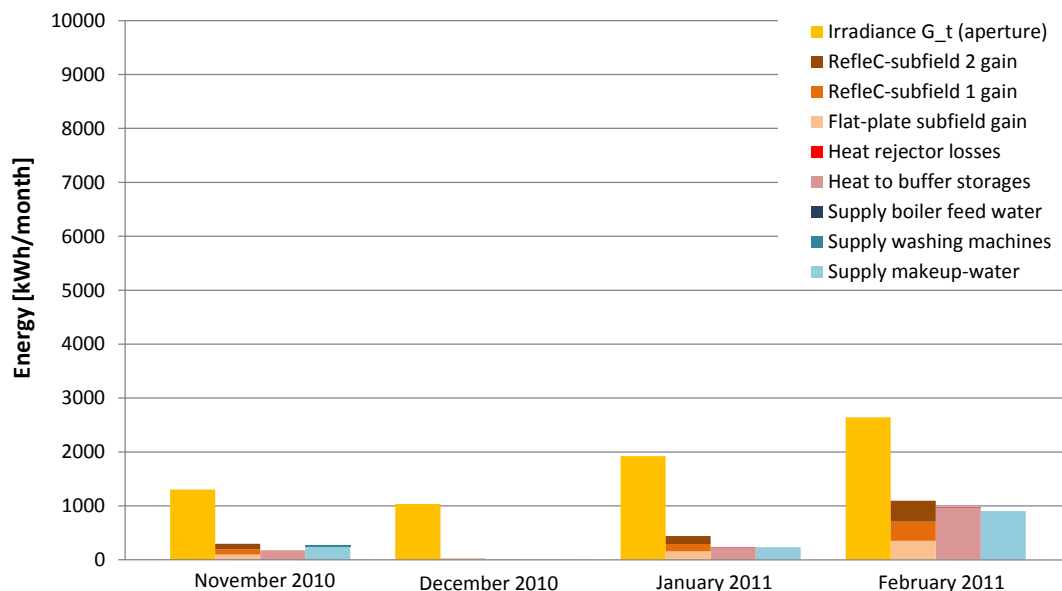
Figure E.2: Monthly system energies calculated from monitoring (Nov. 2010 to Feb. 2011). From 27.10.10 to 10.02.11 the collector pump was only started at $\Delta T = 45$ K between coll. outlet and storage bottom (pump off at $\Delta T = 40$ K). From 01.11.10 discharge to make-up water was prioritized among the low-temperature loads; discharge to the washing machines storage only activated at buffer storage top temperatures above $T_{sto} > 50$ °C. In November 2010 the process-supply was higher than the heat transferred to the buffers. This is due to the fact that there is heat transfer from the indoor air (approx. 30 °C at working hours) to the buffer storage water. From 11.02.11 on, normal operation with collector pump on at $\Delta T = 4$ K, pump off at $\Delta T = 2$ K. Exclusively winter mode.

179
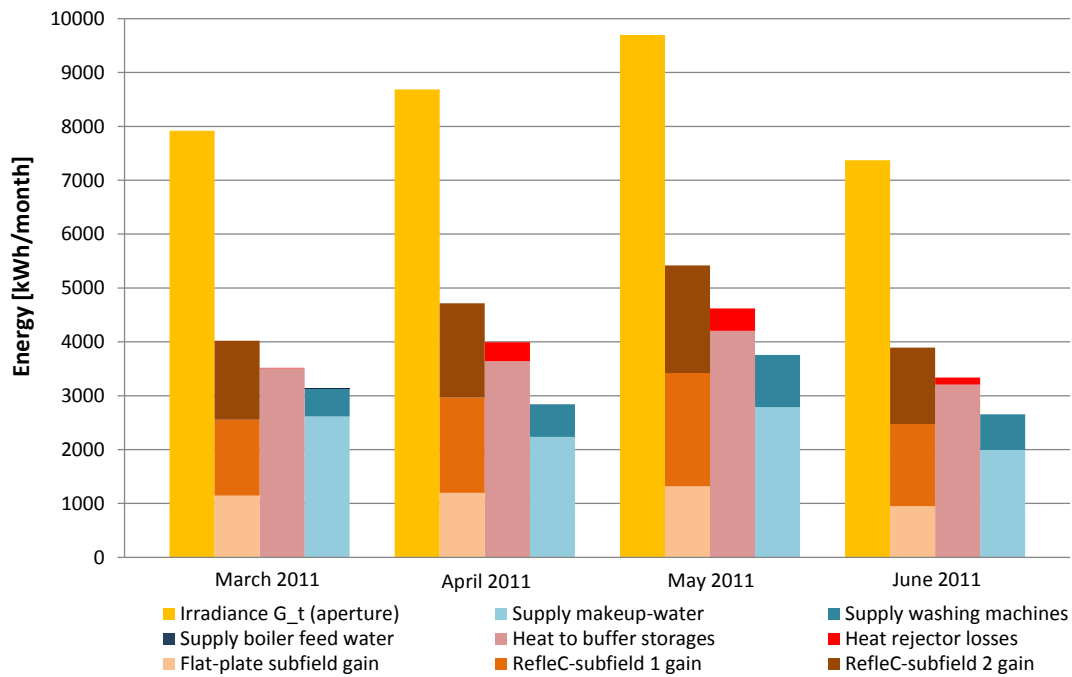
Figure E.3: Monthly system energies calculated from monitoring (March to June 2011). On 21.04 a defect of a cap valve occurred at the solar station. Thus, from 21.04. to 24.06.11 the max. temperature $T_{sto,max}$ of all buffers was limited to 95 °C (before primary 115 °C, secondary 110 °C), and the turn-on threshold of the heat rejector was decreased from 125 °C down to $T_{on,RK} = 100$ °C (increased heat rejector losses). On 24.06.11 the defect cap valve was replaced and the old control parameters were restored. Exclusively winter mode.
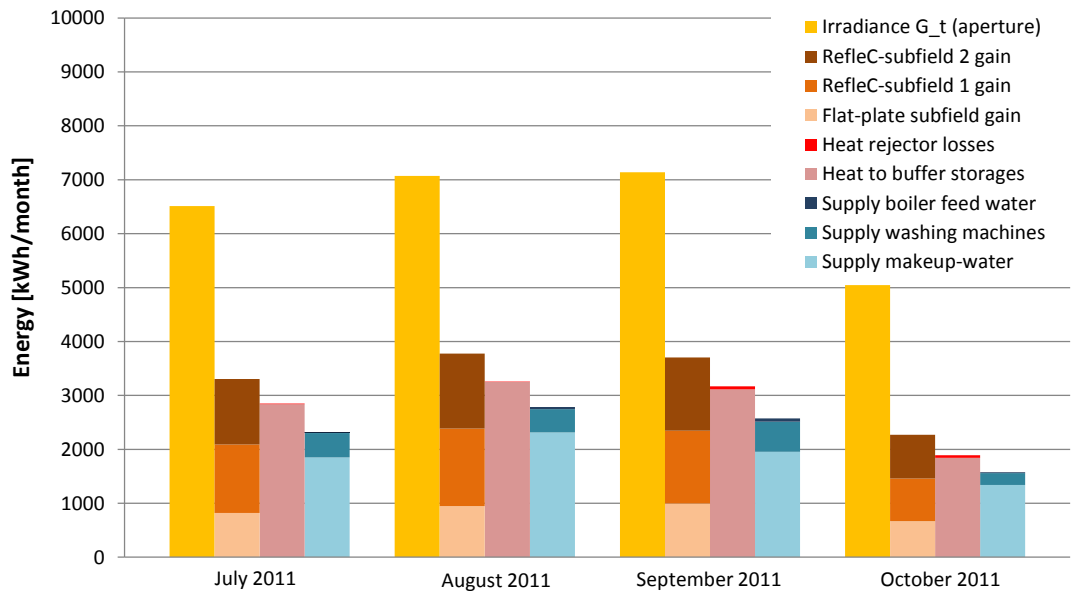
Figure E.4: Monthly system energies calculated from monitoring (July to Oct. 2011). On 19.07.11 the bottom of the buffer storages has been insulated, which reduced storage losses (especially in summer mode). From 25.06.11 to 24.08.11 exclusively winter mode because of bad weather conditions. From 25.08. to 19.09. exclusively summer mode. On 31.08. the switchover threshold of the secondary was changed finally from 50 °C to 60 °C (secondaries are charged higher to also effectively support the washing machines). From 20.09.11 winter mode. On 28.10.11 the monitoring system was removed.
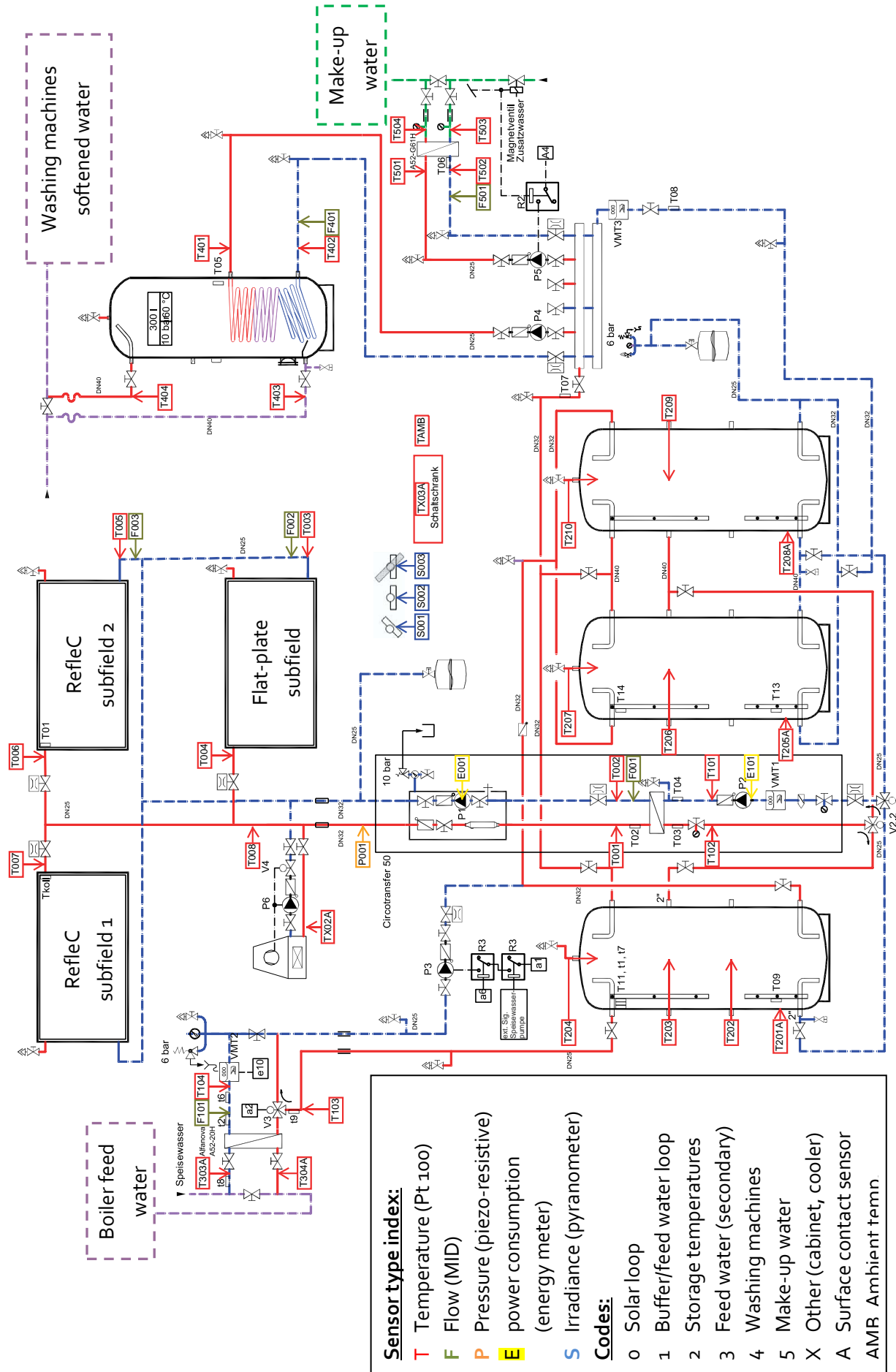
Figure E.5: Hydraulic scheme of the RefleC pilot plant (scheme of Wagner & Co. Solartechnik complemented by monitoring sensors)

Figures

Tables

Publications

Selected Publications with Relation to this Work

Hess, S. and Hanby, V. I. (2014). "Collector Simulation Model with Dynamic Incidence Angle Modifier for Anisotropic Diffuse Irradiance." Energy Procedia 48(0): 87-96.

Hess, S., Oliva, A., et al. (2012). Ergebnisse des IEE-Projekts SO-PRO: Auslegung von Solaranlagen für vier ausgewählte industrielle Prozesse. 22. OTTI-Symposium Thermische Solarenergie. Bad Staffelstein.

Hess, S., Klemke, M., Oliva, A., Di Lauro, P., Hermann, M., Stryi-Hipp, G., Kramp, G., von Bodungen, O., Eisenmann, W. and Hanby, V. (2011). Pilotanlage mit RefleC Kollektoren: Anlagenkonzept und Monitoring-Ergebnisse. 21. OTTI-Symposium Thermische Solarenergie. Bad Staffelstein: 124-129.

Hess, S., Oliva, A., Hermann, M., Stryi-Hipp, G. and Hanby, V. (2011). Solar Process Heat – System Design for Selected Low-temperature Applications in the Industry. Solar World Congress 2011. Kassel.

Hess, S. and Oliva, A. (2010). Guide to Solar Thermal System Design for Selected Industrial Processes. URL: www.solar-process-heat.eu/guide.

Hess, S., Oliva, A., Di Lauro, P., Klemke, M., Hermann, M., Kramp, G., Eisenmann, W. and Hanby, V. (2010). Solar Heat for Industrial Processes: RefleC Collector Development and System Design. EuroSun 2010. Graz.

Hess, S., Oliva, A., Di Lauro, P., Klemke, M., Hermann, M., Stryi-Hipp, G., Kallwellis, V., Kramp, G., Eisenmann, W. and Hanby, V. (2010). Flachkollektor mit externen Reflektoren (RefleC): Entwicklungserfahrungen. 20. OTTI-Symposium Thermische Solarenergie. Bad Staffelstein: 150-155.

Hess, S., Di Lauro, P., Oliva, A. and Hanby, V. (2009). RefleC – A new Collector for Solar Cooling Applications with Operating Temperatures up to 150 °C. 3rd International OTTI-Conference on Solar Air-Conditioning. Palermo: 393-398.

Hess, S., Di Lauro, P., Oliva, A. and Hanby, V. (2009). RefleC – Ein verbesserter Flachkollektor mit externen Reflektoren zur Erzeugung von Prozesswärme bis 150 °C. 19. OTTI-Symposium Thermische Solarenergie. Bad Staffelstein: 116-117.

Hess, S., Di Lauro, P., Rose, S. and Rommel, M. (2008). Comparison of Medium Temperature Collectors for the Generation of Process Heat. EuroSun 2008. Lisbon: paper 513.

Hess, S., Rommel, M., Di Lauro, P. and Rose, S. (2008). Raytracing-Untersuchungen für die Entwicklung von Prozesswärmekollektoren. 18. OTTI-Symposium Thermische Solarenergie. Bad Staffelstein: 416-421.

Hess, S. (2007). Application of Medium Temperature Collectors for Solar Air-Conditioning. 2nd International Conference on Solar Air-Conditioning. Tarragona: 118-123.

Theses of Students Supervised during this Work

Schmid, M. (2014). Identifikation und Bewertung von Systemkonzepten zur Integration solarer Prozesswärme in Wäschereien. Diploma Thesis. Universität Kassel.

Klemke, M. (2011). Monitoring einer solarthermischen Demonstrationsanlage zur Bereitstellung von Wärme für industrielle Prozesse. Diploma Thesis. Fachhochschule Gießen-Friedberg.

Oliva, A. (2009). Einbindung der Energie eines konzentrierenden solarthermischen Flachkollektors in industrielle Prozesse. Diploma Thesis. Technische Universität Hamburg-Harburg.

Raucher, C. (2009). Untersuchungen zur Einbindung der Energie eines konzentrierenden solarthermischen Flachkollektors in industrielle Prozesse. Master Thesis. Universität Kassel.

Rose, S. (2008). Untersuchungen zur Entwicklung einer Zweifachabdeckung für einen Prozesswärme-Flachkollektor mit externen Reflektoren. Diploma Thesis. Hochschule Ulm.

Di Lauro, P. (2008). Untersuchungen zum einstrahlwinkelabhängigen Wirkungsgrad eines Prozesswärme-Flachkollektors mit externen Reflektoren. Diploma Thesis. Hochschule Ulm.

Bibliography

Adsten, M. (2002). Solar Thermal Collectors at High Latitudes-Design and performance of nontracking concentrators. Uppsala University.

Adsten, M., Helgesson, A., et al. (2005). "Evaluation of CPC-collector designs for stand-alone, roof- or wall installation." Solar Energy 79(6): 638-647.

Adsten, M., Hellström, B., et al. (2004). "Measurement of radiation distribution on the absorber in an asymmetric CPC collector." Solar Energy 76(1–3): 199-206.

AEE INTEC (2014). "Database for applications of solar heat integration in industrial processes." Retrieved 05.09.2014. URL: http://www.ship-plants.info/.

Aidonis, A., Drosou, V., et al. (2005). PROCESOL II - Solar thermal plants in industrial processes. Design and Maintenance Guidelines. Centre for Renewable Energy Sources. Pikermi. URL: http://www.aee-intec.at/0uploads/dateienEnglisch124.pdf.

Ambrosetti, P. and Keller, J. (1985). Das neue Bruttowärmeertragsmodell für verglaste Solarkollektoren. Eidgenössisches Institut für Reaktorforschung. Würlingen (CH).

Badescu, V. (2008). Modeling Solar Radiation at the Earth's Surface: Recent Advances. Berlin, Springer Verlag.

Beeh, M. and Hess, S. (2014). Bericht zu Screenings und Fallstudien in SoProW. Bönnigheim.

BMWi (2014). Energiedaten: Gesamtausgabe. Stand: April 2014. URL: http://www.bmwi.de/DE/Themen/Energie/Energiedaten-und-analysen/Energiedaten/gesamtausgabe,did=476134.html.

Bollentin, J. W. and Wilk, R. D. (1995). "Modeling the solar irradiation on flat plate collectors augmented with planar reflectors." Solar Energy 55(5): 343-354.

Bosanac, M. and Nielsen, J. E. (1997). "In situ check of collector array performance." Solar Energy 59(4–6): 135-142.

Brandemuehl, M. J. and Beckman, W. A. (1980). "Transmission of diffuse radiation through CPC and flat plate collector glazings." Solar Energy 24(5): 511-513.

Brogren, M. (2004). Optical Efficiency of Low-Concentrating Solar Energy Systems with Parabolic Reflectors. Dissertation. Uppsala University.

Brogren, M., Helgesson, A., et al. (2004a). "Optical properties, durability, and system aspects of a new aluminium-polymer-laminated steel reflector for solar concentrators." Solar Energy Materials and Solar Cells 82(3): 387-412.

Brogren, M., Karlsson, B., et al. (2004b). "Analysis of the effects of outdoor and accelerated ageing on the optical properties of reflector materials for solar energy applications." Solar Energy Materials and Solar Cells 82(4): 491-515.

Brunger, A. P. and Hooper, F. C. (1993). "Anisotropic sky radiance model based on narrow field of view measurements of shortwave radiance." Solar Energy 51(1): 53-64.

Burckhart, H. J., Audinet, F., et al. (2014). "Application of a Novel, Vacuum-insulated Solar Collector for Heating and Cooling." Energy Procedia 48(0): 790-795.

Buttinger, F., Beikircher, T., et al. (2010). "Development of a new flat stationary evacuated CPC-collector for process heat applications." Solar Energy 84(7): 1166-1174.

Calderoni, M., Aprile, M., et al. (2012). "Solar Thermal Plants for Industrial Process Heat in Tunisia: Economic Feasibility Analysis and Ideas for a New Policy." Energy Procedia 30(0): 1390-1400.

Carvalho, M. J., Collares-Pereira, M., et al. (1995). "Optical and thermal testing of a new 1.12X CPC solar collector." Solar Energy Materials and Solar Cells 37(2): 175-190.

Carvalho, M. J., Horta, P., et al. (2007). Incidence angle modifiers: A general approach for energy calculations. ISES Solar World Congress, September 18-21. D. Y. Goswami and Y. Zhao. Beijing, China, Springer 608-612.

Chaves, J. (2008). Introduction to Nonimaging Optics (Optical Science and Engineering). Boca Raton, CRC Press Inc.

Clement, C. (2004). Verfahren zur optischen und thermischen Auslegung von konzentrierenden Solarkollektoren für Prozesswärmeanlagen. Dissertation. Technische Universität München.

Corporation, O. (2009). OptiCAD - Optical Analysis Program - User´s Guide version 10.046. Santa Fe. URL: www.opticad.com.

Cotrado, M., Dalibard, A., et al. (2014). "Design, Control and First Monitoring Data of a Large Scale Solar Plant at the Meat Factory Berger, Austria." Energy Procedia 48(0): 1144-1151.

Duff, W. S. and Daosukho, J. (2011). Evaluation of the Reliability of a Novel ICPC Solar Collector Installation: Incorporating the Diffuse Radiation Component into the Analysis and Its Impact on the Comparison between Measured and Predicted Performance. ISES Solar World Congress. Kassel.

Duff, W. S., Winston, R., et al. (2004). "Performance of the Sacramento demonstration ICPC collector and double effect chiller." Solar Energy 76(1–3): 175-180.

Duffie, J. A. and Beckman, W. A. (2006). Solar Engineering of Thermal Processes. 3rd Edition. New Jersey, John Wiley & Sons, inc.

Duffie, J. A. and Beckman, W. A. (2013). Solar Engineering of Thermal Processes. 4th Edition. New Jersey, John Wiley & Sons, Inc.

Ebert, V., Günther, R., et al. (2012). Fahrplan Solarwärme. Strategie und Maßnahmen der Solarwärme-Branche für ein beschleunigtes Marktwachstum bis 2030. Berlin. URL: http://www.solarwirtschaft.de/fileadmin/media/pdf/120854_bsw_studie_st.pdf.

Egger, C. (2011). Solar Process Heat So-Pro. Publishable, result-orientated report. Final project report. Linz. URL: www.solar-process-heat.eu/report.

Eisenmann, W. (2009). Physical properties of solar fluid DC20 in a mixture with 60 % water. Fit functions determined from tabulated values between 10 °C and 100 °C in steps of 10 °C sent by Mr. Krakat, Fragol GmbH to Mr. Eisenmann, Wagner & Co. on 30.10.2009.

Eisenmann, W., Hess, S., et al. (2011). Entwicklung eines leistungsgesteigerten Flachkollektors mit Reflektoren für die Gewinnung von Prozesswärme bis 150 °C. Final project report. TIB Hannover. URL: http://edok01.tib.uni-hannover.de/edoks/e01fb11/668455144.pdf.

Eisenmann, W., Vajen, K., et al. (2004). "On the correlations between collector efficiency factor and material content of parallel flow flat-plate solar collectors." Solar Energy 76(4): 381-387.

EN 12975-2:2006 Thermal solar systems and components - Solar collectors - Part 2: Test methods. Brussels, European Committee for Standardization.

Eurostat (2014a). "Energy statistics - final energy consumption by sector - annual data (tsdpc320)." URL: http://epp.eurostat.ec.europa.eu/tgm/table.do?tab=table&init=1&plugin=1&language=en&pcode=tsdpc320.

Eurostat (2014b). "Energy statistics - supply, transformation, consumption - all products - annual data (nrg_100a)." URL: http://appsso.eurostat.ec.europa.eu/nui/show.do?dataset=nrg_100a&lang=en.

Evseev, E. G. and Kudish, A. I. (2009). "The assessment of different models to predict the global solar radiation on a surface tilted to the south." Solar Energy 83(3): 377-388.

Faber, C., Anthrakidis, A., et al. (2011). Barriers to Solar Process Heat Applications. ISES Solar World Congress 2011. Kassel.

Bibliography

Fasulo, A., Odicino, L., et al. (1987). "Development of a CPC with low thermal losses." Solar & Wind Technology 4(2): 157-162.

Fischer, S. (2011). Dynamische Prüfung von Sonnenkollektoren unter besonderer Berücksichtigung der Einfallswinkelkorrektur und der Reduzierung der Prüfdauer. Dissertation. Universität Stuttgart.

Fischer, S. (2012). Proposal for Definition of Temperature Ranges and Terminology. IEA-Task 49, 2nd Expert Meeting, 6.09.-7.09.12, Graz.

Fischer, S., Heidemann, W., et al. (2004). "Collector test method under quasi-dynamic conditions according to the European Standard EN 12975-2." Solar Energy 76(1–3): 117-123.

Fraidenraich, N., Tiba, C., et al. (2008). "Analytic solutions for the geometric and optical properties of stationary compound parabolic concentrators with fully illuminated inverted V receiver." Solar Energy 82(2): 132-143.

Frei, U., Brunold, S., et al. (1998). Langzeit-Alterungsuntersuchungen an Abdeckungsmaterialien für thermische Sonnenkollektoren. Institut für Solartechnik Prüfung Forschung SPF. Rapperswil. URL: http://www.solarenergy.ch/fileadmin/daten/publ/abde.pdf.

Frein, A., Calderoni, M., et al. (2014). "Solar Thermal Plant Integration into an Industrial Process." Energy Procedia 48(0): 1152-1163.

Frey, R., Frei, U., et al. (1997). Bestimmung des Kollektorwirkungsgradfaktors F' an flüssigkeitsführenden Solarabsorbern. Rapperswil. URL: http://www.spf.ch/fileadmin/daten/publ/fstrich.pdf.

Fuller, R. J. (2011). "Solar industrial process heating in Australia - Past and current status." Renewable Energy 36: 216-221.

Georg, A. (2007). Simulated absorpance values for Cermet selective coating. Fraunhofer ISE, unpublished values.

Goswami, D. Y., Kreith, F., et al. (1999). Principles of Solar Engineering. 2nd. Philadelphia, Taylor & Francis.

Gueymard, C. A. (2009). "Direct and indirect uncertainties in the prediction of tilted irradiance for solar engineering applications." Solar Energy 83(3): 432-444.

Häberle, A. (1999). Vermessung und Modellierung von stationären, konzentrierenden Kollektoren. Dissertation. Universität Freiburg.

Haller, M., Perers, B., et al. (2013). TRNSYS Type 832 v5.01 - Dynamic Collector Model by Bengt Perers - Updated Input-Output Reference. URL: http://www.solarenergy.ch/Type-832-Kollektormodell.223.0.html?&no_cache=1&L=0&no_cache=1.

Harrison, A. W. (1991). "Directional sky luminance versus cloud cover and solar position." Solar Energy 46(1): 13-19.

Hay, J. E. (1979). "Calculation of monthly mean solar radiation for horizontal and inclined surfaces." Solar Energy 23(4): 301-307.

Heinzen, R., Zaß, K., et al. (2011). Integration of Solar Thermal Systems into Gas Pressure Regulating Stations. ISES Solar World Congress. Kassel.

Helgesson, A. (2004). Optical Characterization of Solar Collectors from Outdoor Measurements. Dissertation. Lund University.

Hellstrom, B., Adsten, M., et al. (2003). "The impact of optical and thermal properties on the performance of flat plate solar collectors." Renewable Energy 28(3): 331-344.

Hess, S. (2007). Untersuchungen zur Entwicklung eines Prozesswärme-Flachkollektors mit externen Reflektoren. Diploma Thesis. Fachhochschule Augsburg.

Hess, S. and Hanby, V. I. (2014). "Collector Simulation Model with Dynamic Incidence Angle Modifier for Anisotropic Diffuse Irradiance." Energy Procedia 48(0): 87-96.

Hess, S. and Oliva, A. (2010). Guide to Solar Thermal System Design for Selected Industrial Processes. Linz. URL: www.solar-process-heat.eu/guide.

Hess, S., Oliva, A., et al. (2011). Solar Process Heat – System Design for Selected Low-temperature Applications in the Industry. Solar World Congress 2011. Kassel.

IEA (2012). IEA Technology Roadmap Solar Heating and Cooling. International Energy Agency. Paris. URL: http://www.iea.org/publications/freepublications/publication/Solar_Heating_Cooling_Roadmap_2012_WEB.pdf.

Igawa, N., Koga, Y., et al. (2004). "Models of sky radiance distribution and sky luminance distribution." Solar Energy 77(2): 137-157.

Iqbal, M. (1983). An Introduction to solar Radiation. New York, Academic Press, Inc.

ISO 9806:2013 Solar energy — solar thermal collectors — test methods, edition 2013-11.

Ivancic, A., Mugnier, D., et al. (2014). RHC Solar Heating and Cooling Technology Roadmap. Renewable Heating and Cooling Platform. Brussels. URL: http://www.rhc-platform.org/publications/.

Jiang, L. and Winston, R. (2014). "Progress on Integrated Compound Concentrator Design." Energy Procedia 48(0): 114-122.

Kalogirou, S. (2003). "The potential of solar industrial process heat applications." Applied Energy 76(4): 337-361.

Kalogirou, S. A. (2004). "Solar thermal collectors and applications." Progress in Energy and Combustion Science 30(3): 231-295.

Karagiorgas, M., Botzios, A., et al. (2001). "Industrial solar thermal applications in Greece Economic evaluation, quality requirements and case studies." Renewable and Sustainable Energy Reviews 5: 157–173.

Kasper, B.-R., Weyers-Borchert, B., et al. (2012). Solarthermische Anlagen: Leitfaden für das SHK-, Elektro- und Dachdeckerhandwerk, Fachplaner, Architekten, Bauherrn und Weiterbildungsinstitutionen. 9th Edition. Berlin, DGS, Deutsche Gesellschaft für Sonnenenergie.

Kim, Y. S., Balkoski, K., et al. (2013). "Efficient stationary solar thermal collector systems operating at a medium-temperature range." Applied Energy 111(0): 1071-1079.

Kittler, R. (1985). "Luminance distribution characteristics of homogeneous skies: a measurement and prediction strategy." Lighting Research and Technology 17(4): 183-188.

Klein, S. A., Beckman, W. A., et al. (2006). Trnsys 16 - a transient system simulation program, Solar Energy Laboratory, University of Wisconsin-Madison.

Klein, S. A., Beckman, W. A., et al. (2012a). Trnsys 17 - a TRaNsient SYstem Simulation program. Mathematical Reference, Solar Energy Laboratory, University of Wisconsin-Madison.

Klein, S. A., Beckman, W. A., et al. (2012b). Trnsys 17 - a TRaNsient SYstem Simulation program. Programmer´s Guide, Solar Energy Laboratory, University of Wisconsin-Madison.

Klein, S. A., Beckman, W. A., et al. (2012c). Trnsys 17 - a TRaNsient SYstem Simulation program. Standard Component Library Overview, Solar Energy Laboratory, University of Wisconsin-Madison.

Klemke, M. (2011). Monitoring einer solarthermischen Demonstrationsanlage zur Bereitstellung von Wärme für industrielle Prozesse. Diploma Thesis. Fachhochschule Gießen-Friedberg.

Kramer, K. (2006). Aufbau und Einsatz eines Teststandes zur Messung der Wirkungsgradkennlinien von Prozesswärme-Solarkollektoren. Diploma Thesis. Fachhochschule Augsburg.

Bibliography

Kramp, G. (2010). Technical drawing of final RefleC collector as used for the pilot plant. STEP construction data of Wagner & Co. Solartechnik GmbH, received per email on 19.02.2010.

Krueger, D., Lichtenhaeler, N., et al. (2011). Solar Steam Supply: Initial Operation of a Plant. ISES Solar World Congress. Kassel.

Lauterbach, C. (2014). Potential, system analysis and preliminary design of low-temperature solar process heat systems. Dissertation. Kassel University.

Lauterbach, C., Rad, J. S., et al. (2011a). Feasibility Assessment of Solar Process Heat Applications. Solar World Congress. Kassel.

Lauterbach, C., Schmitt, B., et al. (2012). "The potential of solar heat for industrial processes in Germany." Renewable and Sustainable Energy Reviews 16(7): 5121-5130.

Lauterbach, C., Schmitt, B., et al. (2011b). Das Potential solarer Prozesswärme in Deutschland. Teil 1 des Abschlussberichts zum Forschungsvorhaben SOPREN, Solare Prozesswärme und Energieeffizienz Kassel. URL: http://solar.umwelt-uni-kassel.de/downloads.de.html.

Lauterbach, C., Schmitt, B., et al. (2014). "System analysis of a low-temperature solar process heat system." Solar Energy 101(0): 117-130.

Lindseth, I., Bardal, A., et al. (1999). "Reflectance measurements of aluminium surfaces using integrating spheres." Optics and Lasers in Engineering 32(5): 419-435.

McIntire, W. R. (1982). "Factored approximations for biaxial incident angle modifiers." Solar Energy 29(4): 315-322.

McIntire, W. R. and Reed, K. A. (1983). "Orientational relationships for optically non-symmetric solar collectors." Solar Energy 31(4): 405-410.

Mills, D. R., Monger, A., et al. (1994). "Comparison of fixed asymmetrical and symmetrical reflectors for evacuated tube solar receivers." Solar Energy 53(1): 91-104.

Motta, M. (2010). MEDiterranean food and agro Industry applications of Solar COoling technologies. Milano. URL: http://cordis.europa.eu/documents/documentlibrary/124585001EN6.pdf.

Müller, T., Weiss, W., et al. (2004). Produzieren mit Sonnenenergie: Potenzialstudie zur thermischen Solarenergienutzung in österreichischen Gewerbe- und Industriebetrieben. Wien.

Muschaweck, J., Spirkl, W., et al. (2000). "Optimized reflectors for non-tracking solar collectors with tubular absorbers." Solar Energy 68(2): 151-159.

Neumann, A., Witzke, A., et al. (2002). "Representative Terrestrial Solar Brightness Profiles." ASME Journal of Solar Energy Engineering Vol. 124: 198-204.

Nilsson, J., Leutz, R., et al. (2007). "Micro-structured reflector surfaces for a stationary asymmetric parabolic solar concentrator." Solar Energy Materials and Solar Cells 91(6): 525-533.

Nkwetta, D. N. and Smyth, M. (2012). "Performance analysis and comparison of concentrated evacuated tube heat pipe solar collectors." Applied Energy 98(0): 22-32.

Nkwetta, D. N., Smyth, M., et al. (2013). "Experimental performance evaluation and comparative analyses of heat pipe and direct flow augmented solar collectors." Applied Thermal Engineering 60(1–2): 225-233.

Nkwetta, D. N., Smyth, M., et al. (2012). "Optical evaluation and analysis of an internal low-concentrated evacuated tube heat pipe solar collector for powering solar air-conditioning systems." Renewable Energy 39(1): 65-70.

Norton, B., Ed. (2012). Industrial and Agricultural Applications of Solar Heat. Comprehensive Renewable Energy. Oxford, Elsevier.

Nostell, P., Roos, A., et al. (1998). "Ageing of solar booster reflector materials." Solar Energy Materials and Solar Cells 54(1–4): 235-246.

NREL (2013, 07.11.2013). "ASTM G173-03 Reference Spectra - derived from SMARTS v. 2.9.2." URL: http://rredc.nrel.gov/solar/spectra/am1.5/.

Oliva, A. (2009). Einbindung der Energie eines konzentrierenden solarthermischen Flachkollektors in industrielle Prozesse. Diploma Thesis. Technische Universität Hamburg-Harburg.

Pereira, M. C., Carvalho, M. J., et al. (2003). New Low Concentration CPC Type Collector with Convection Controlled by a Honeycomb TIM Material. ISES Solar World Congress 2003. Göteborg. URL: http://www.psa.es/webeng/aquasol/files/Congresos/ISES2003_O3_13_Aquasol.pdf.

Perers, B. (1995). Optical Modelling of Solar Collectors and Booster Reflectors under Non Stationary Conditions. Dissertation. Uppsala University.

Perers, B. and Karlsson, B. (1993). "External reflectors for large solar collector arrays, simulation model and experimental results." Solar Energy 51(5): 327-337.

Perez, R., Ineichen, P., et al. (1990). "Modeling daylight availability and irradiance components from direct and global irradiance." Solar Energy 44(5): 271-289.

Perez, R., Seals, R., et al. (1987). "A new simplified version of the perez diffuse irradiance model for tilted surfaces." Solar Energy 39(3): 221-231.

Perez, R., Seals, R., et al. (1993). "All-weather model for sky luminance distribution— Preliminary configuration and validation." Solar Energy 50(3): 235-245.

Perez, R., Stewart, R., et al. (1986). "An anisotropic hourly diffuse radiation model for sloping surfaces: Description, performance validation, site dependency evaluation." Solar Energy 36(6): 481-497.

Perez, R., Stewart, R., et al. (1988). The Development and Verification of the Perez Diffuse Radiation Model.

Quaschning, V. (2007). Regenerative Energiesysteme. 5th Edition. München, Hanser Verlag.

Rabl, A. (1976a). "Comparison of Solar Concentrators." Solar Energy Vol. 18: 93-111.

Rabl, A. (1976b). "Optical and thermal properties of compound parabolic concentrators." Solar Energy 18(6): 497-511.

Rabl, A. (1985). Active Solar Collectors and Their Applications. New Jork, Oxford University Press.

Rabl, A., O'Gallagher, J., et al. (1980). "Design and test of non-evacuated solar collectors with compound parabolic concentrators." Solar Energy 25(4): 335-351.

Raucher, C. (2009). Untersuchungen zur Einbindung der Energie eines konzentrierenden solarthermischen Flachkollektors in industrielle Prozesse. Master Thesis. Universität Kassel.

Reindl, D. T., Beckman, W. A., et al. (1990). "Evaluation of hourly tilted surface radiation models." Solar Energy 45(1): 9-17.

Remund, J., Müller, S., et al. (2007a). Meteonorm: Global Meteorological Database, Part 1: Software, Version 7. Bern, Meteotest.

Remund, J., Müller, S., et al. (2007b). Meteonorm: Global Meteorological Database, Part 2: Theory, Version 7. Bern, Meteotest.

Rommel, M. (2005). Medium Temperature Collectors for Solar Process Heat up to 250°C. Second European Solar Thermal Energy Conference. Freiburg.

Rommel, M. (2008). Solarthermie 2000plus: Kollektorentwicklung und –testung für Solare Prozesswärme im Bereich von 80 bis 250 °C. TIB Hannover. Freiburg. URL: https://getinfo.de/app.

Rönnelid, M. and Karlsson, B. (1996). "Experimental investigation of heat losses from low-concentrating non-imaging concentrators." Solar Energy 57(2): 93-109.

Rönnelid, M. and Karlsson, B. (1997). "Irradiation distribution diagrams and their use for estimating collectable energy." Solar Energy 61(3): 191-201.

Rönnelid, M. and Karlsson, B. (1999). "The Use of Corrugated Booster Reflectors for Solar Collector Fields." Solar Energy 65(6): 343-351.

Rönnelid, M., Perers, B., et al. (1996). "Construction and testing of a large-area CPC-collector and comparison with a flat plate collector." Solar Energy 57(3): 177-184.

Rönnelid, M., Perers, B., et al. (1997). "On the factorisation of incidence angle modifiers for CPC collectors." Solar Energy 59(4–6): 281-286.

Rose, S. (2008). Untersuchungen zur Entwicklung einer Zweifachabdeckung für einen Prozesswärme-Flachkollektor mit externen Reflektoren. Diploma Thesis. Hochschule Ulm.

Ruesch, F. and Brunold, S. (2008). Langzeitalterungsuntersuchung an Abdeckungsmaterialien für thermische Sonnenkollektoren. Ergebnisse einer 20jährigen Freibewitterungsstudie. Schlussbericht für Bundesamt für Energie. Rapperswil. URL: http://www.solarenergy.ch/fileadmin/daten/publ/Freibewitterung_Bericht_16-07-2008.pdf.

Sanner, B., Angelino, L., et al. (2013). RHC Strategic Research and Innovation Agenda for Renewable Heating & Cooling. Renewable Heating and Cooling Platform. Brussels. URL: http://www.rhc-platform.org/publications/.

Sanner, B., Kalf, R., et al. (2011). RHC Common Vision for the Renewable Heating & Cooling sector in Europe. European Union. Brussels. URL: http://www.rhc-platform.org/publications/.

SCEnOCalc (2014). SCEnOCalc v4.06 (Solar Collector Energy Output Calculator), a program for calculation of annual solar collector energy output, SP Technical Research Institute of Sweden. URL: http://www.sp.se/en/index/services/solar/ScenoCalc/Sidor/default.aspx.

Schmitt, B. (2014). Integration thermischer Solaranlagen zur Bereitstellung von Prozesswärme in Industriebetrieben. Dissertation. Universität Kassel.

Schmitt, B., Lauterbach, C., et al. (2012a). Branchenkonzept Solare Prozesswärme für Brauereien. Teil 2 des Abschlussberichts zum Forschungsvorhaben "SOPREN - Solare Prozesswärme und Energieeffizienz". Universität Kassel. Kassel. URL: http://solar.umwelt-uni-kassel.de/downloads.de.html.

Schmitt, B., Lauterbach, C., et al. (2012b). Leitfaden zur Nutzung solarer Prozesswärme in Brauereien. Universität Kassel. Kassel. URL: http://solar.umwelt-uni-kassel.de/downloads.de.html.

Schramm, S. and Adam, M. (2014). "Storage in Solar Process Heat Applications." Energy Procedia 48(0): 1202-1209.

Schweiger, H. (2001). POSHIP: The Potential of Solar Heat in Industrial Processes. Final Project Report. Barcelona.

Schweiger, H., Mendes, J. F., et al. (2000). The Potential of Solar Heat in Industrial Processes. A State of the Art Review for Spain and Portugal. EuroSun Copenhagen, Denmark.

Siala, F. M. F. and Hooper, F. C. (1990). "A model for the directional distribution of the diffuse sky radiance with an application to a CPC collector." Solar Energy 44(5): 291-296.

Silva, R., Cabrera, F. J., et al. (2014). "Process Heat Generation with Parabolic Trough Collectors for a Vegetables Preservation Industry in Southern Spain." Energy Procedia 48(0): 1210-1216.

Smyth, M. and Russell, J. (2009). "'From graft to bottle'—Analysis of energy use in viticulture and wine production and the potential for solar renewable technologies." Renewable and Sustainable Energy Reviews 13(8): 1985-1993.

Solarkeymark (2014). "The Solar Keymark Database." Retrieved Jan. 4th, 2014. URL: http://solarkey.dk/solarkeymarkdata/qCollectorCertificates/ShowQCollectorCertificates Table.aspx.

Souka, A. F. and Safwat, H. H. (1966). "Determination of the optimum orientations for the double-exposure, flat-plate collector and its reflectors." Solar Energy 10(4): 170-174.

Spirkl, W., Ries, H., et al. (1998). "Nontracking solar concentrators." Solar Energy 62(2): 113-120.

SRCC (2014). "Ratings Summary Page." Retrieved Jan. 4th, 2014. URL: https://secure.solar-rating.org/Certification/Ratings/RatingsSummaryPage.aspx.

Stryi-Hipp, G., Weiss, W., et al. (2012). RHC Strategic Research Priorities for Solar Thermal Technology. Brussels. URL: http://www.rhc-platform.org/publications/.

SU (2013). "Stellenbosch University Solar Resource and Weather Stations." URL: http://blogs.sun.ac.za/sterg/files/2013/04/Brochure-Sonbesie1.pdf.

Sunarc (n.a.). Test Report Anti Reflection Coating of Uppsala University, Sweden. URL: http://www.sunarc.net/images/billeder/pdf/report%20sarc.pdf.

SUNNY (2014). "Changzhou SUNNY Solar Technology Co., Ltd." Retrieved 16 July 2013. URL: http://www.solarpower-waterheater.com/.

Tabor, H. (1958). "Stationary mirror systems for solar collectors." Solar Energy 2(3–4): 27-33.

Tesfamichael, T. and Wäckelgård, E. (2000). "Angular solar absorptance and incident angle modifier of selective absorbers for solar thermal collectors." Solar Energy 68(4): 335-341.

Theunissen, P. H. and Beckman, W. A. (1985). "Solar transmittance characteristics of evacuated tubular collectors with diffuse back reflectors." Solar Energy 35(4): 311-320.

Tiwari, G. N. (2002). Solar Energy - Fundamentals, Design, Modelling and Applications. Narosa Publishing House.

Tripanagnostopoulos, Y., Yianoulis, P., et al. (2000). "CPC Solar Collectors With Flat Bifacial Absorbers." Solar Energy 69(3): 191-203.

Uecker, M. (2000). Zur Vermessung, Simulation und Langzeituberwachung großer solarintegrierter Warmeversorgungsanlagen. Philipps-Universität Marburg

Valentin (2014). T*SOL Pro Version 5.5 User Manual. URL: www.valentin-software.com/en/downloads.

Vannoni, C., Battisti, R., et al. (2008). Potential for Solar Heat in Industrial Processes. CIEMAT. Madrid. URL: http://task33.iea-shc.org/publications.

VDI (2004). VDI 6002 Part 1: Solar heating for domestic water: General principles, system technology and use in residential building. Berlin, Beuth Verlag.

Velasolaris (2013). "Polysun Version 5.10 User Manual."

Vittoriosi, A., Fedrizzi, R., et al. (2014). "Monitoring of a MW Class Solar Field Set up in a Brick Manufacturing Process." Energy Procedia 48(0): 1217-1225.

Weiss, W. and Biermayr, P. (2009). Potential of Solar Thermal in Europe. European Solar Thermal Industry Federation (ESTIF). Brussels. URL: http://www.aee-intec.at/0uploads/dateien758.pdf.

Weiss, W. and Mauthner, F. (2014). Solar Heat Worldwide: Markets and Contribution to the Energy Supply 2012. Gleisdorf. URL: http://www.iea-shc.org/solar-heat-worldwide.

Weiss, W. and Rommel, M. (2008). Process Heat Collectors: State of the Art. AEE Intec, Gleisdorf. URL: http://task33.iea-shc.org/publications.

Welford, W. T. and Winston, R. (1978). The Optics of Nonimaging Concentrators: Light and Solar Energy. San Diego, London: Academic Press, Inc.

Wilbert, S., Pitz-Paal, R., et al. (2012). Circumsolar Radiation and Beam Irradiance Measurements for Focusing Collectors. ES1002: Workshop May 22nd - 23rd 2012.

Bibliography

Winston, R. (1974). "Principles of solar concentrators of a novel design." Solar Energy 16(2): 89-95.

Winston, R., Minano, J. C., et al. (2005). <u>Nonimaging Optics</u>. Oxford, Elsevier.

Wutzler, M., Schirmer, U., et al. (2011). Solar Process Heat Application at the Hofmuehl Brewery at Eichstätt / Germany. ISES Solar World Congress. Kassel.